# Molecular characterisation of bacterial proteins that interact with sulfur or nitrogen compounds

**Daniel Grabarczyk**

Department of Biochemistry

and

Worcester College

University of Oxford

A thesis submitted in partial fulfilment of the requirements for the degree of Doctor of Philosophy at the University of Oxford

Trinity Term 2014

42,500 words

# Molecular characterisation of bacterial proteins that interact with sulfur or nitrogen compounds

Daniel Grabarczyk

Department of Biochemistry and Worcester College, University of Oxford

Submitted in partial fulfilment for the degree of Doctor of Philosophy at the University of Oxford

Trinity Term 2014

## Abstract

Many bacteria use inorganic nitrogen and sulfur compounds for energy metabolism. These compounds are often toxic and so bacteria must adapt to survive their deleterious effects. Bacteria use specific proteins in order to metabolise, sense and detoxify these compounds. In this thesis protein interactions with inorganic nitrogen and sulfur compounds are examined at the mechanistic level.

Intermediates in the Sox sulfur oxidation pathway are covalently attached to a cysteine on the swinging arm of the substrate carrier protein SoxYZ. An interaction between the Sox pathway enzyme SoxB and the carrier protein SoxYZ is demonstrated. A crystal structure of a trapped SoxB-SoxYZ complex at 3.3 Å resolution identifies two sites of interaction, one between the SoxYZ carrier arm and the SoxB active site channel and the other at a patch distal to the active site. The presence of a distal interaction site suggests a mechanism for promiscuous specificity in the protein-protein interactions of the Sox pathway. Using biophysical methods it is shown that SoxB distinguishes between the substrate and product forms of the carrier protein through differences in interaction kinetics and that the carrier arm-bound substrate group is able to out-compete the adjacent C-terminal carboxylate for binding to the SoxB active site.

The thiosulfate dehydrogenase TsdA has an unusual His/Cys coordinated heme. TsdA catalyses oxidative conjugation of two thiosulfate molecules to form tetrathionate. Mass spectrometry and UV/visible spectroscopy are used to identify an S-thiosulfonate reaction intermediate which is covalently attached to the cysteine heme ligand. A catalytic mechanism for TsdA is proposed using a crystal structure of TsdA at 1.3 Å resolution alongside site-directed mutagenesis of active site residues.

Nitric oxide is produced by the mammalian immune response to kill bacterial pathogens. Part of the killing mechanism occurs through the reaction of nitric oxide with protein-bound iron-sulfur clusters. However, the same type of reaction is also exploited by nitric oxide-sensing bacterial proteins. An infrared spectroscopy approach is developed to detect the products of iron-sulfur protein nitrosylation. Using this methodology it is shown that the presence of trace $O_2$ strongly impacts which products are formed in these nitrosylation reactions. These observations are of physiological relevance because bacteria are often exposed to NO under aerobic conditions during an immune response.

Some of the work detailed in Chapter 5, particularly Section 5.4, has been published as:

**“Infrared Spectroscopy Provides Insight into the Role of Dioxygen in the Nitrosylation Pathway of a [2Fe2S] Cluster Iron–Sulfur Protein”**

Daniel B. Grabarczyk, Philip A. Ash and Kylie A. Vincent.

*Journal of the American Chemical Society*, **136**, 11236-11239 (2014)

# Acknowledgements

I would like to thank Ben Berks for being extremely quick and helpful during my thesis writing process and for his critical analysis and suggestions throughout my DPhil. I would like to thank Kylie Vincent for giving me the opportunity to work on a project outside of my comfort zone and for her constant enthusiasm and ideas during an often dispiriting project.

Many thanks to Susan Lea, Pietro Roversi, Steve Johnson and particularly Paul Chappell for performing all of the crystallographic data collection and analysis as well as for their help and supervision with crystallisation trials, and to Steve for performing SEC-MALS experiments.

Thanks to Philip Ash for help in writing this thesis, assistance with experiments and experimental setup, and general discussion and amusement. Thanks to Martin Krehenbrink for training, ideas and his inspiring scientific attitude. Thanks to Bianca Eisel for her hard work at the start of the TsdA project without which I would have been too discouraged to continue and to Lucie Dearlove for assistance with many of the technically challenging experiments in Chapter 5. A special thanks to Will Myers for his tireless dedication in collecting EPR data.

Thanks to everyone in the general 10-042 lab area, particularly Despoina Mavridou, Shilpa Bali, Felicity Alcock and Marta Wojnowska for help with various protocols. And thanks to everyone in the Vincent group for help and some interesting nights out. Particular thanks to Ian McPherson and Charlie McKenna for experimental help. Thanks to Lukas Stelzl for help with molecular dynamics, and sharing his scripts with me, and to Mark Sansom for giving me the opportunity to learn some new skills in his lab. I would also like to acknowledge assistance from Monika Kalde and Sarah McCraw from Plants Sciences; PTCL workshops; Rob Jacobs and the surface analysis facility; David Staunton and the biophysics facility; and Jason Crack and Nick Le Brun at UEA, Norwich.

I am very grateful for financial support from the BBSRC as well as Worcester College, FEMS, the Biochemical Society, and the Keith Prout Crystallography Fund.

I would like to thank my parents for their support, particularly my mum for her endless encouragement during my entire education.

Finally, I am grateful to Esmé for her support and encouragement throughout my DPhil. I am happy to have had many adventures together, which were much-needed distractions from work, and am also thankful for her help with thesis formatting.

# Table of contents

## Chapter 3: Specificity and promiscuity in a substrate-carrier protein/enzyme system from the sulfur cycle ........................................................................ 56

## Chapter 4: Mechanism of oxidative thiosulfate conjugation catalysed by cysteine-ligated cytochromes ........ 90

## Chapter 5: Optimising an IR spectroscopic method to provide insight into the mechanism of iron-sulfur protein nitrosylation ........142

# List of figures

# List of tables

# List of Abbreviations

| | |
|---|---|
| **APS** | Adenosine 5′-phosphosulfate |
| **ATP** | Adenosine triphosphate |
| **ATR** | Attenuated total reflectance |
| **AU** | Absorbance units |
| **bNOS** | Bacterial nitric oxide synthase |
| **CO** | Codon-optimised |
| **CW** | Continuous wave |
| **DNA** | Deoxyribonucleic acid |
| **DNIC** | Dinitrosyl iron complex |
| **DNR** | Dissimilatory nitrate respiration regulator |
| **DMSO** | Dimethyl sulfoxide |
| **DTT** | Dithiothreitol |
| **EDTA** | Ethylenediaminetetraacetic acid |
| **EPR** | Electron paramagnetic resonance |
| **ESI-MS** | Electrospray ionisation-mass spectrometry |
| **FAD** | Flavin adenine dinucleotide |
| **Fd** | Spinach ferredoxin I |
| **FMN** | Flavin mononucleotide |
| **FNR** | Fumarate and nitrate reductase regulator |
| **GSH** | Glutathione |
| **HEPES** | 4-(2-hydroxyethyl)-1-piperazineethanesulfonic acid |
| **HiPIP** | High potential iron-sulfur protein |
| **IFN** | Interferon |
| **IL** | Interleukin |
| **iNOS** | Inducible nitric oxide synthase |
| **IPTG** | Isopropyl β-D-1-thiogalactopyranoside |
| **IR** | Infrared |
| **ITC** | Isothermal titration calorimetry |
| **LB** | Lysogeny broth |
| **MALS** | Mult-angle light scattering |
| **Mb** | Myoglobin |

| | |
|---|---|
| **MCD** | Magnetic circular dichroism |
| **MD** | Molecular dynamics |
| **MES** | 2-(N-morpholino)ethanesulfonic acid |
| **MNIC** | Mononuclear iron complex |
| **MQ** | Menaquinone |
| **NAD** | Nicotinamide adenine dinucleotide |
| **NADP** | Nicotinamide adenine dinucleotide phosphate |
| **NNR** | Nitrate and nitrite reductase regulator |
| **NO** | Nitric oxide |
| **NRVS** | Nuclear resonance vibrational spectroscopy |
| **PAGE** | Polyacrylamide gel electrophoresis |
| **PCR** | Polymerase chain reaction |
| **PDB** | Protein databank |
| **PEG** | Polyethylene glycol |
| **RBS** | Ribsomal binding site |
| **RBS** | Roussin's black salt |
| **RMSD** | Root mean squared deviation |
| **RNS** | Reactive nitrogen species |
| **ROS** | Reactive oxygen species |
| **RRE** | Roussin's red rester |
| **rRRE** | Reduced Roussin's red ester |
| **RRS** | Roussin's red salt |
| **SDS** | Sodium dodecyl sulfate |
| **SEC** | Size-exclusion chromatography |
| **SEM** | Standard error of the mean |
| **sGC** | Soluble guanate cyclase |
| **SHE** | Standard hydrogen electrode |
| **SOR** | Sulfur oxygenase reductase |
| **SPR** | Surface plasmon resonance |
| **SQR** | Sulfide quinone oxidoreductase |
| **Tat** | Twin-arginine translocase |
| **TCA** | Tricarboxylic acid |
| **TCEP** | tris(2-carboxyethyl)phosphine |
| **TFA** | Trifluoroacetic acid |

| | |
|---|---|
| **TNF** | Tumour necrosis factor |
| **Tris** | tris(hydroxymethyl)aminomethane |
| **UQ** | Ubiquinone |
| **UV** | Ultraviolet |
| **WT** | Wild-type |

# Chapter 1: Introduction

## 1.1 The interactions of bacteria with nitrogen and sulfur compounds

The interior of the Earth is rich in nitrogen and sulfur. Abiotic and biotic processes have resulted in speciation of these elements and dissemination of the species throughout the lithosphere and atmosphere. Therefore, a range of inorganic nitrogen and sulfur compounds are prevalent in the biosphere. These compounds exhibit many oxidation states and so can be used by bacteria as a source of electrochemical energy. They are often very reactive towards biological materials, including metals in proteins. Many bacteria have evolved proteins which specifically interact with these inorganic nitrogen and sulfur compounds, usually through cysteine residues or metallocofactors. Some of these proteins metabolise these compounds, whilst others exist to sense the presence of these compounds so that bacteria can express genes to utilise them or protect themselves against the toxic effects of such compounds.

## 1.2 Microbial sulfur metabolism

Sulfur exists in a range of formal oxidation states from -2 to +6 (Table 1.1). Prokaryotes can therefore use a wide range of inorganic sulfur compounds as either electron donors or acceptors in energy metabolism. The redox couples for the reactions of inorganic sulfur compounds have negative standard electrochemical potentials (Table 1.2). This means that they are poor terminal electron acceptors relative to oxygen, and so organisms using oxygen as a terminal electron acceptor have a competitive advantage over prokaryotes using oxidised sulfur compounds. Other bacteria oxidise reduced sulfur compounds with oxygen or nitrate as an electron acceptor. Here, the sulfur oxidation redox couples are generally not sufficient to reduce $NAD^+$, and electrons enter the respiratory chain at the level of cytochrome *c* or ubiquinone. In general sulfur compounds are not as energy dense as organic matter. Furthermore, reduced sulfur compounds such as sulfide and sulfite are very toxic to cells and so bacteria are restricted to environments with low concentrations of the compounds, which reduces the driving force for oxidation of these compounds.

**Table 1.1 – The oxidation state of sulfur species used in bacteria energy metabolism. The oxidation state refers to the sulfur atom(s) highlighted in red.**

| **Sulfur oxidation state** | **Sulfur species** |
|---|---|
| -2 | Sulfide ($H\mathbf{S}^-$)<br>Thiocyanate ($\mathbf{S}CN-$)<br>Cysteine ($Cys\mathbf{SH}$) |
| -1 | Cysteine persulfide ($Cys\mathbf{SS}^-$)<br>Disulfide ($^-\mathbf{S}-\mathbf{S}^-$)<br>Thiosulfate ($^-\mathbf{S}-SO_3^-$)<br>Polysulfides ($^-\mathbf{S}-S_{(n)}-\mathbf{S}^-$) |
| 0 | Elemental sulfur ($\mathbf{S}^o$)<br>Polythionates ($^-O_3S-\mathbf{S}_{(n)}-SO_3^-$)<br>Polysulfides ($^-S-\mathbf{S}_{(n)}-S^-$) |
| +4 | Sulfur dioxide ($\mathbf{S}O_2$)<br>Sulfite ($H\mathbf{S}O_3^-$) |
| +5 | Polythionates ($^-O_3\mathbf{S}-S_{(n)}-\mathbf{S}O_3^-$)<br>Thiosulfate ($^-S-\mathbf{S}O_3^-$) |
| +6 | Sulfate ($\mathbf{S}O_4^{2-}$) |

**Table 1.2 – Redox potentials of couples involved in bacterial metabolism (Thauer et al., 1977)**

| **Redox couple** | **Redox potential, $E^{o/}$ (mV)** |
|---|---|
| $SO_4^{2-}/HSO_3^-$ | -516 |
| $H^+/H_2$ | -414 |
| $^-S-SO_3^-/HS^- + HSO_3^-$ | -402 |
| Ferredoxin ox/red | -371 |
| $NAD^+/NADH$ | -320 |
| $S^o/HS^-$ | -270 |
| $HSO_3^-/HS^-$ | -116 |
| $MQ/MQH_2$ | -74 |
| $APS/AMP + HSO_3^-$ | -60 |
| $HSO_3^-/S^o$ | -38 |
| $^-O_3S-S-S-SO_3^-/^-S-SO_3^-$ | +24 |
| $O_2/H_2O$ | +818 |

Life evolved in an environment with very little organic matter and oxygen. The only metabolic substrates arose from volcanic activity and included $CO_2$, $H_2$ and inorganic sulfur compounds. Therefore, the first organisms are thought to have been chemoautotrophic (Martin and Russell, 2003), meaning that they derived their energy from the transfer of electrons between inorganic compounds, and also used these electrons to fix $CO_2$. It has been proposed that the metabolism of these first organisms may have involved the reduction of sulfite and the disproportion of elemental sulfur ($S^o$) and disulfide (Sousa et al., 2013).

In the present-day environment, organic matter and oxygen are abundant. However, many niches still exist where micro-organisms can gain a significant competitive advantage through dissimilatory metabolism of inorganic sulfur compounds (Lengeler et al., 1998). Such niches usually arise at the interface between oxic and anoxic conditions. In these interfaces anaerobic bacteria use oxidised compounds, such as sulfate, as their terminal electron acceptors rather than oxygen. This results in the production of reduced sulfur compounds, which can then be used as the energy source for aerobic bacteria using oxygen as their terminal electron acceptor. This process regenerates sulfate which can be reduced by the anaerobic bacteria. Other niches for chemotrophs are areas rich in inorganic sulfur compounds, such as mining sites and hydrothermal vents. Sulfur metabolising bacteria are often extremophiles able to survive at the very high temperatures close to thermal vents, the very low pH of mining drainage sites or the high sulfide concentrations in stratified lakes.

### 1.2.1 The biogeochemical sulfur cycle

Sulfur is present in amino acids and many cofactors and is therefore essential to life. Hydrogen sulfide and sulfur dioxide are potent pollutants produced both naturally and by human activity. Many metals are locked up as sulfidic ores. For these reasons there is great interest in understanding the biotic and abiotic processes which result in the transformation of sulfur compounds and the influence of humanity upon this (Ivanov and Freney, 1983).

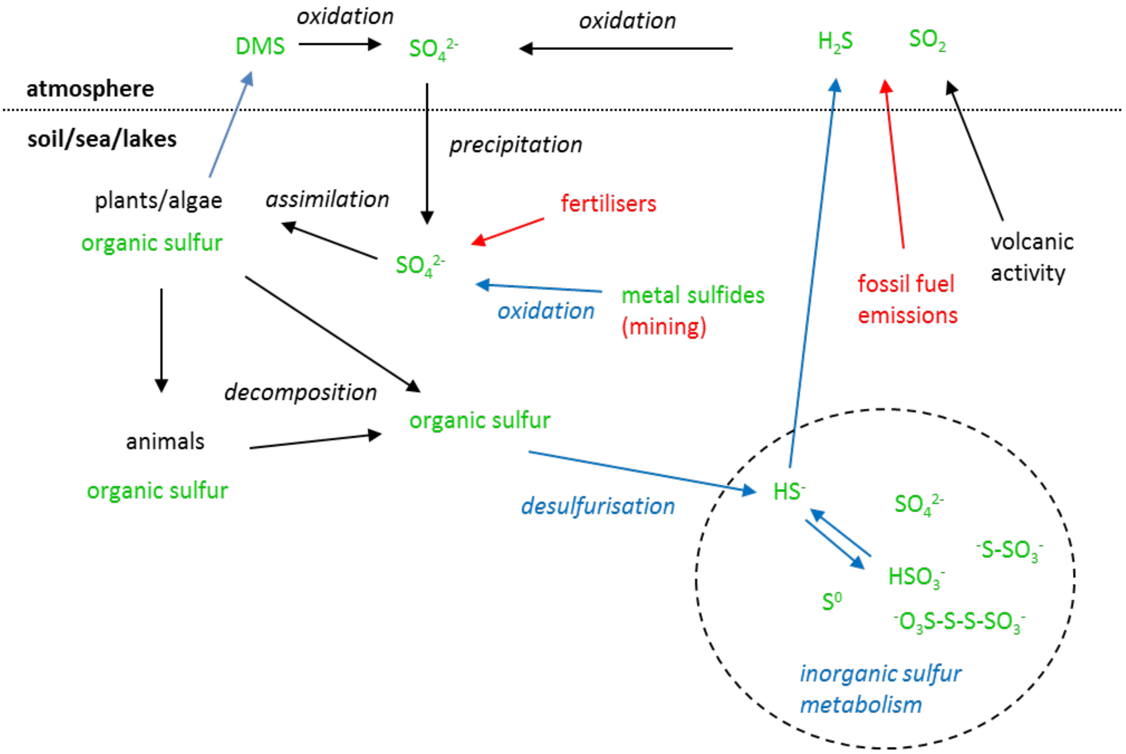

**Figure 1.1 – The biogeochemical sulfur cycle.** Transformations which are due to dissimilatory bacterial metabolism are shown in blue, whilst the effects of human activity are shown in red. The inorganic sulfur transformations described in this chapter are shown in the dashed circle, but note that these inorganic sulfur compounds are present elsewhere in the cycle but not included in the dashed circle for simplicity.

The biogeochemical sulfur cycle is summarised in Figure 1.1. Sulfur dioxide, hydrogen sulfide and dimethyl sulfide are released into the environment through volcanic activity, the burning of fossil fuels and biotic processes. Sulfur dioxide and hydrogen sulfide are oxidised to sulfuric acid and return to the earth as acid rain, resulting in an increase in sulfate in soil and water reservoirs. Sulfate is also present in the Earth’s crust as gypsum ($CaSO_4$) and further introduced by the use of fertilisers in agriculture. Another route for sulfate formation is microbial oxidation of metal sulfides, also present in the Earth’s crust. This sulfate is assimilated by plants and micro-organisms and transferred to other organisms as organic sulfur. These organic sulfur compounds undergo biotic desulfuration resulting in inorganic sulfur compounds which are cycled by micro-organisms. Sulfur is released to the atmosphere as hydrogen sulfide during the cycling of inorganic compounds.

### 1.2.2 Industrial and environmental importance of microbial sulfur metabolisers

There has been much interest in exploiting the sulfur transformation processes performed by sulfur oxidising bacteria. This often relates to attempting to reduce the impact of human activity on the environment. Fossil fuels contain varying quantities of sulfur and so their combustion releases hydrogen sulfide and sulfur dioxide into the environment. There is therefore interest in using sulfur oxidising bacteria to either oxidise and remove the metal sulfides found in fossil fuels before combustion (Schippers et al., 2014) or to oxidise hydrogen sulfide gas to solid $S^o$ after combustion. Sulfur oxidising bacteria are also employed in the mining industry to mobilise metals from low-grade sulfidic ores (Rawlings and Johnson, 2007). Metals such as nickel, copper and iron are present in sulfidic ores. A consortium of bacteria is able to mobilise this metal by converting it to its soluble sulfate form. Part of this process involves bacterial oxidation of the sulfide to sulfuric acid. When uncontrolled, bacterial production of sulfuric acid at exposed metal sulfide sites is an environmental problem. Bacterial metal leaching can also be used to recycle metals present in low concentrations in industrial waste (Brandl, 2008).

Unlike the exploitation of sulfur oxidising bacteria, much effort has been put into preventing the activity of sulfur reducing bacteria. As well as producing the pollutant, hydrogen sulfide, these bacteria can use iron as an electron donor in anoxic environments and are responsible for corrosion of steel structures in the sea, which is rich in sulfate (Enning et al., 2012). This corrosion is also an issue in the anoxic interior of steel pipelines. Sulfur reducing bacteria are used in biotechnology to prevent the entry of metal and sulfate waste produced by the textile, tannery, paper and other industries into the environment (Liamleam and Annachhatre, 2007). The sulfate is reduced and precipitated as insoluble metal sulfide.

### 1.2.3 Metabolic pathways in sulfur reducing prokaryotes

Various sulfur reducing bacteria and archaea can use sulfate, sulfite, $S^o$ or thiosulfate as electron acceptors (Grein et al., 2013). Reduction of sulfate to sulfite is thermodynamically unfavourable with biological electron donors (see Table 1.2) and so sulfate is first activated by reaction with ATP to form adenosine 5’-phosphosulfate (APS) (Equation 1.1). Dissimilatory sulfate reducing bacteria, typified by *Desulfovibrio* species, then reduce this activated sulfate to sulfite using the APS reductase complex, AprAB (Equation 1.2). The sulfite is then reduced to sulfide by the dissimilatory sulfite reductase (Dsr) system (Equation 1.3). The sulfite is first reduced to $S^o$ by the sulfite reductase DsrAB and transferred as a persulfide to a cysteine residue of DsrC (Venceslau et al., 2014). The structure of DsrC bound to DsrAB has been solved (Oliveira et al., 2008). DsrC has two cysteines on the end of a carrier arm which is inserted into the DsrAB siroheme/[4Fe4S] active site. After persulfuration of one cysteine on the carrier arm, it is thought that the unmodified cysteine nucleophilically attacks the cysteine persulfide to release sulfide and form a cysteine disulfide. It is anticipated that this cysteine disulfide is reduced by the DsrMKJOP membrane-bound complex. The electrons for the reduction of APS and sulfite are believed to come from menaquinol through the respective membrane-bound complexes QmoABC (Pires et al., 2003) and DsrMKJOP (Pires et al., 2005). It has been suggested that menaquinol would not have sufficient reducing power *in vivo* to reduce sulfite to sulfide or APS to sulfite. It has been proposed that QmoABC and DsrMKJOP use heterodisulfide reductase-like domains to catalyse an electron confurcation reaction (Grein et al., 2013). An electron confurcation reaction is where oxidation of a low potential single electron donor drives the oxidation of a higher potential electron donor. The two-electron acceptor would have a potential between the low and high potential donors. An FAD group would be at the centre of the confurcation for QmoABC and DsrMKJOP. An electron from an unknown low potential electron donor would reduce FAD to form a flavosemiquinone. This flavosemiquinone would then pull an electron from menaquinol. The resulting $FADH_2$ could then reduce APS. Electron bifurcation, which can also involve a heterodisulfide reductase, is the reverse process where a high potential electron acceptor drives reduction of a low potential electron acceptor. Electron bifurcation is thought to be an important feature of hydrogen oxidation in ancient metabolism (Buckel and Thauer, 2013).

Equation 1.1 $SO_4^{2-} + ATP \rightarrow APS + PP_i$ *ATP sulfurylase*

Equation 1.2 $APS + 2H^+ + 2e^- \rightarrow SO_3^{2-} + AMP + H_2O$ *APS reductase*

Equation 1.3 $SO_3^{2-} + 7H^+ + 6e^- \rightarrow HS^- + 3H_2O$ *Sulfite reductase*

Many bacteria can reduce polysulfide, tetrathionate and/or thiosulfate using one of the members of a family of reductase enzymes related to formate dehydrogenase (Hensel et al., 1999; Jormakka et al., 2008; Stoffels et al., 2012) (Reactions 1.4-1.6). These enzymes contain three subunits, are membrane-bound and contain a molybdopterin cofactor and several iron-sulfur clusters. In *Salmonella enterica* electrons for thiosulfate reductase come from menaquinol, which does not have sufficient reducing power to reduce thiosulate (Stoffels et al., 2012). This enzyme therefore uses the proton-motive force to drive thiosulfate reduction. Some bacteria can grow by disproportionating thiosulfate to sulfide and sulfate (Finster, 2008). Here, thiosulfate reductase is coupled to the oxidation of the sulfite product to sulfate by the reverse of the APS pathway (Equation 1.1-1.2). Sulfite and $S^o$ can also be disproportionated to sulfide and sulfate.

Equation 1.4 ${}^{-}S\text{-}S_{(n)}\text{-}S^{-} + 2e- + H+ \rightarrow {}^{-}S\text{-}S_{(n-1)}\text{-}S^{-} + HS^{-}$ *Polysulfide reductase*

Equation 1.5 $^{-}S\text{-}SO_3^{-} + MQH_2 \rightarrow HSO_3^{-} + HS^{-} + MQ$ *Thiosulfate reductase*

Equation 1.6 $^{-}O_3S\text{-}S\text{-}S\text{-}SO_3^{-} + 2e^{-} \rightarrow {}^{-}S\text{-}SO_3^{-} + {}^{-}S\text{-}SO_3^{-}$ *Tetrathionate reductase*

Equation 1.7 $^{-}S\text{-}SO_3^{-} + H_2O \rightarrow SO_4^{2-} + HS^{-} + H^{+}$ *Thiosulfate disproportionation*

### 1.2.4 Sulfur oxidising bacteria and archaea

Sulfur oxidising bacteria use the electrons derived from sulfur oxidation either for respiration or photosynthesis (Ghosh and Dam, 2009). Chemotrophic sulfur oxidisers are usually aerobic and use oxygen as a terminal electron acceptor. However, some chemotrophic species such as *Thiobacillus denitrificans* can grow anaerobically and use nitrate as an electron acceptor for sulfur oxidation (Beller et al., 2006). Electrons from oxidation of sulfur compounds enter the electron transport chain either at the level of quinone or cytochrome *c*.

Phototrophic sulfur oxidisers will respire sulfur compounds using oxygen when under aerobic conditions, but under anaerobic conditions they will use the electrons from sulfur oxidation for photosynthesis. Different phototrophic sulfur oxidisers use different photosynthetic approaches (Brune, 1989). Green sulfur bacteria can perform non-cyclic photosynthetic electron flow, with excited electrons going from the reaction centre to ferredoxin to $NAD^{+}$. Rather than the next electron coming from water splitting as in plants and cyanobacteria, electrons instead come from oxidation of sulfur compounds *via* a cytochrome *c*. Purple bacteria do not excite electrons to a low enough potential to directly reduce $NAD^{+}$, but instead are limited to cyclic photosynthetic electron transport to generate a proton-motive force. The oxidation of sulfur compounds generates electrons which are too high in potential to reduce $NAD^{+}$, so the endergonic reduction of $NAD^{+}$ by sulfur compounds occurs by the reverse electron transport chain. The NADH is used to fix $CO_2$ through the Calvin cycle. Green non-sulfur bacteria use an approach which is similar but distinct from purple bacteria (Bruce et al., 1982).

### 1.2.5 The Sox sulfur oxidation pathway

The central sulfur oxidation pathway in most chemotrophic and phototrophic sulfur oxidising bacteria (but not archaea) is the Sox pathway (Ghosh and Dam, 2009). This pathway is used for the complete oxidation of thiosulfate, tetrathionate and sulfide to form sulfate (Chandra and Friedrich, 1986; Mukhopadhyaya et al., 2000; Appia-Ayme et al., 2001), or in some cases incomplete oxidation to form $S^o$ (Hensen et al., 2006). The Sox pathway is found in all proteobacterial classes and the model organisms are usually proteobacteria. However, the pathway is also present in members of *Deinococcus-Thermus*, *Aquificae*, *Chlorobi* (green sulfur bacteria) and *Chloroflexi* (green non-sulfur bacteria). It is thought that rather than being a particularly ancient pathway like the Dsr pathway, the Sox pathway evolved in chemotrophic proteobacteria and was passed by horizontal gene transfer to other phyla (Meyer et al., 2007). Despite its widespread nature, the Sox pathway is notably absent from some sulfur oxidising bacteria, such as *Acidithiobacillus ferrooxidans* (Valdes et al., 2008), which has a sulfur oxidising system more related to archaea.

A model has been proposed for the Sox cycle (Friedrich et al., 2001) based on work performed on *Paracoccus pantotrophus* (Chandra and Friedrich, 1986) and *Paracoccus versutus* (Kelly et al., 1994). Intermediates of the Sox pathway are covalently attached to a cysteine on the C-terminal carrier arm of the SoxYZ heterodimeric carrier protein (Figure 1.2) (Lu et al., 1985; Friedrich et al., 2001; Quentmeier and Friedrich, 2001; Sauvé et al., 2007). The diheme or triheme cytochrome *c* SoxAX protein is thought to catalyse oxidative attachment of substrates to the SoxYZ carrier arm cysteine (Friedrich et al., 2000; Bamford et al., 2002). SoxAX is reviewed in more depth in Chapter 4. The dimanganese hydrolase SoxB is thought to hydrolyse cysteine-$S_n$-

sulfonate groups to generate sulfate and Cysteine-$S_n^-$ (Lu and Kelly, 1983a; Friedrich et al., 2001; Sauvé et al., 2009). The SoxB-catalysed reaction is covered in more depth in Chapter 3. The Sox pathway then diverges in different bacteria. In the complete *Paracoccus*/*Rhodovulum* Sox pathway, the sulfane dehydrogenase SoxCD is thought to catalyse oxidation of cysteine-$S_n$-persulfane to cysteine-$S_n$-sulfonate (Lu and Kelly, 1984; Wodara et al., 1997; Quentmeier et al., 2000; Zander et al., 2011). SoxCD is related to sulfite oxidases, but does not display any sulfite dehydrogenase activity *in vitro* without the presence of SoxB, SoxAX and SoxYZ. The SoxCD and SoxB enzymes will work in sequence until the original unmodified cysteine is regenerated (Friedrich et al., 2001). The reconstituted core Sox pathway (SoxABCDXYZ) will oxidise thiosulfate with the release of 8 electrons, sulfite with 2 electrons and sulfide with 4 electrons (Friedrich et al., 2000). When SoxCD is not included in the assay the electron yield drops to two electrons regardless of the substrate. The Sox pathway model shown in Figure 1.2 (Friedrich et al., 2001) was derived from three pieces of evidence. Firstly, the electron yields from each substrate. Secondly, the homology of the Sox enzymes to those of known function. Thirdly, the observation that SoxYZ purified from *P. pantotrophus* grown on thiosulfate is modified with $-SO_3^-$, $-SSO_3^-$ and $-SSSO_3^-$ (Quentmeier and Friedrich, 2001). It is not clear why oxidation of sulfide releases 4 electrons rather than 8 electrons as the model would predict.

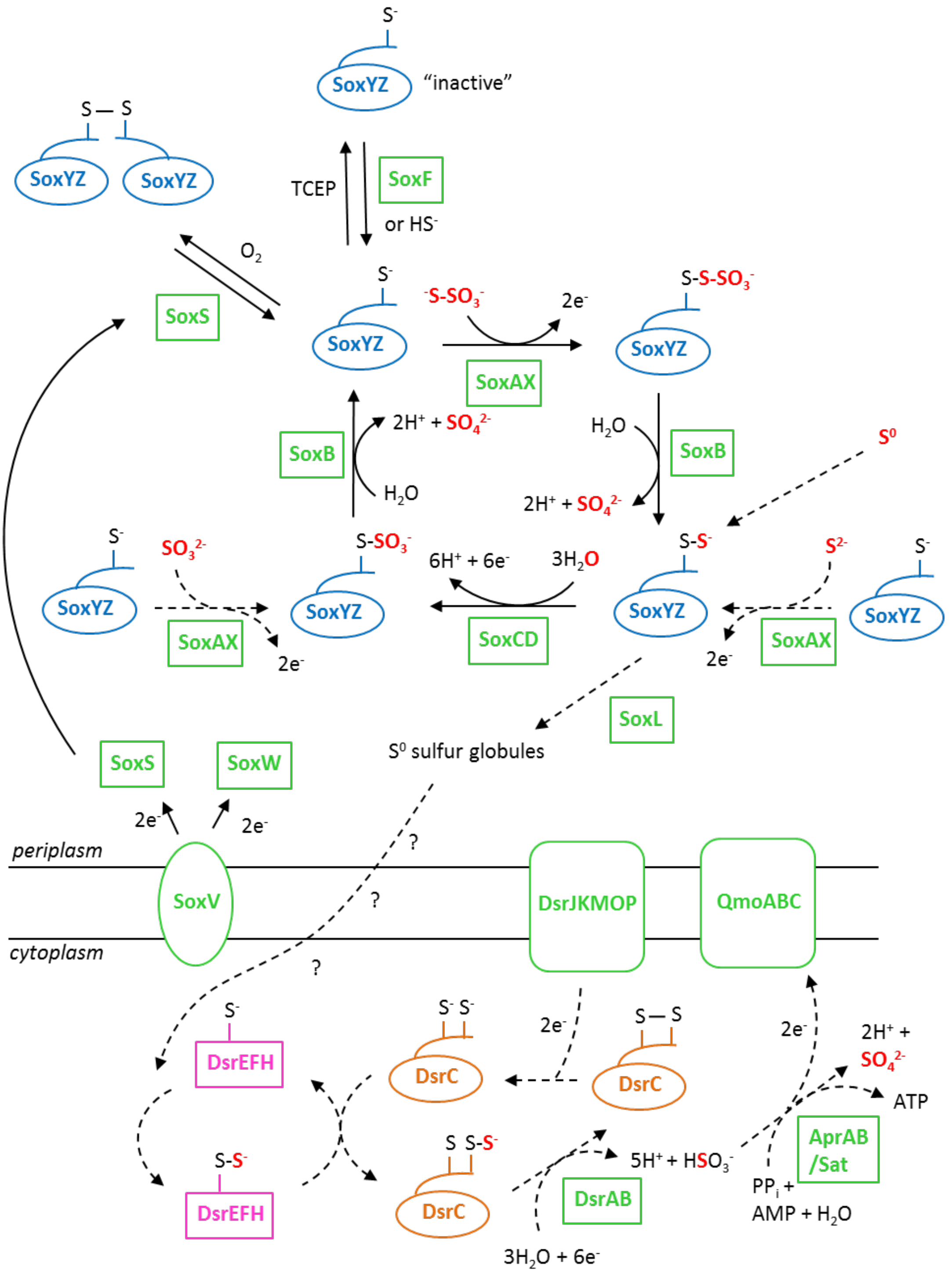

**Figure 1.2 – The Sox pathway in *P. pantrotrophus* and *A. vinosum*.** The thiosulfate oxidising system from *P. pantotrophus* is shown in solid lines, whilst deviations from this standard system are shown with dashed lines. One deviation is the entry point for oxidation of other substrates – sulfite, sulfide and S$^o$. The other deviation is the branched Sox pathway in *A. vinosum*. Here sulfur chains from SoxYZ are thought to be transferred to sulfur globules by SoxL. It is not known how this sulfur is transferred to the cytoplasm onto DsrEFH. Much of the cytoplasmic pathway is speculative. TCEP is a non-phsyiological disulfide bond reductant.

Some organisms with the *soxABXYZ* genes do not have the genes for *soxCD*. This attribute correlates with the formation of either intracellular or extracellular sulfur globules and the presence of the *Dsr* gene cluster discussed in Section 1.2.3. The existence of a branched Sox pathway has been demonstrated in the green sulfur bacterium *Chlorobium tepidum* (Hanson and Tabita, 2003) and the purple sulfur bacterium *Allochromatium vinosum* (Figure 1.2) (Hensen et al., 2006). In *A. vinosum* it is thought that the rhodanese-like protein SoxL removes the sulfane sulfur from SoxYZ and transfers this as $S^o$ to sulfur globules (Welte et al., 2009). The sulfur is transported to the cytoplasm and oxidised to sulfate by the reversal of the sulfate-reducing reactions described in Section 1.2.3 (Pott and Dahl, 1998). The difference in the reverse direction is the existence of a DsrEFH complex, which has been shown to interact with DsrC (Cort et al., 2008). This system is related to the sulfur transferring thiouridine synthesis Tus pathway in *Escherichia coli* (Ikeuchi et al., 2006).

There are several *Sox* genes other than the core *Sox* genes described above. There has been much interest in the role of the flavoprotein SoxF, which is present in all organisms with a full or branched Sox pathway, and which was first assumed to be a sulfide:cytochrome *c* dehydrogenase (Kusai and Yamanaka, 1973). Deletion of *soxF* results in a reduced rate of *P. pantotrophus* thiosulfate oxidation *in vivo* but not *in vitro* and does not affect the electron yield (Bardischewsky et al., 2006b). *P. pantotrophus* SoxYZ can be activated by incubation with sulfide before mixing with the other Sox components (Quentmeier et al., 2007; Quentmeier et al., 2008). This activation can also be achieved by using SoxF in place of sulfide (Friedrich et al., 2008). SoxF also activates *C. tepidum* SoxYZ when this SoxYZ is heterologously expressed in *E. coli*, but not when it is purified from *C. tepidum* (Ogawa et al., 2010). The activated form of *P. pantotrophus* SoxYZ can be inactivated with the non-sulfur reducant tris(2-carboxyethyl)phosphine (TCEP). Our preliminary data suggest that the cysteine in the active form of SoxYZ is modified with a persulfide or polysulfane, but this will not be discussed in this work.

SoxV is a transmembrane protein which is essential for *in vivo* thiosulfate oxidation and uses cytoplasmic reducing equivalents to reduce the periplasmic thioredoxins SoxW and SoxS (Appia-Ayme and Berks, 2002; Bardischewsky et al., 2006a). It is thought that this system reductively activates inactive heterotetrameric forms of SoxYZ where two SoxYZ complexes are bridged via a disulfide formed between their carrier arm cysteines (Figure 1.2). The thioredoxin SoxW is not essential. However, the other thioredoxin SoxS is essential and deletion of SoxS results in an increase of oxidatively inactivated SoxYZ (Friedrich et al., 2008). Deletion of SoxV or SoxS in *P. pantotrophus* can be complemented by addition of DTT to reduce disulfide bonds. Other Sox proteins such as SoxG and SoxH are not commonly encoded in the *Sox* gene cluster. SoxG and SoxH are $\beta$-lactamase-like hydrolases which are not essential for thiosulfate oxidation (Rother et al., 2001; Rother and Friedrich, 2002).

## 1.2.6 Other sulfur oxidation pathways

### 1.2.6.1 Thiosulfate oxidation

Aside from the Sox pathway, two other pathways exist for thiosulfate oxidation. These pathways oxidise thiosulfate to tetrathionate in a simple two electron disulfide bond formation reaction (the reverse of Equation 1.6). The resulting tetrathionate can then be hydrolysed to form sulfate, thiosulfate and elemental sulfur (Equation 1.8) (de Jong et al., 1997).

Equation 1.8 $^{-}O_3S\text{-}S\text{-}S\text{-}SO_3^{-} + H_2O \rightarrow SO_4^{2-} + {}^{-}S\text{-}SO_3^{-} + S^{o} + 2H^{+}$ *Tetrathionate hydrolase*

Tetrathionate-forming thiosulfate dehydrogenases were for a long time thought to be a very diverse group of periplasmic or membrane-bound enzymes, each large and containing various numbers of subunits (Visser et al., 1996). Recently it has become clear that the periplasmic pathway involves a single subunit *ca.* 27 kDa diheme *c*-type cytochrome thiosulfate dehydrogenase, TsdA, which in some organisms co-purifies with its downstream diheme electron acceptor TsdB (Denkmann et al., 2012). TsdA also operates in the reverse direction to catalyse tetrathionate reduction in enteric bacteria (Liu et al., 2013). *A. vinosum* uses the Sox pathway to oxidise thiosulfate at neutral to mildly basic pH values, but at lower pH values instead oxidises thiosulfate using TsdA (Hensen et al., 2006). The properties of TsdA are discussed in more detail in Chapter 4.

The membrane-bound thiosulfate dehydrogenase is unrelated to the periplasmic TsdA. This protein has been best-characterised in the archaeal species *Acidianus ambivalens* and is thought to be a heterotetramer composed of two subunits, DoxA and DoxD (Müller et al., 2004). This protein transfers electrons to membrane quinones, and is therefore called thiosulfate quinone oxidoreductase. No mechanistic information is available for this protein. Interestingly, as well as being present in some other species of the *Sulfolobales* order of archaea, this complex may also be used for thiosulfate oxidation by the eubacterium *A. ferrooxidans*, which does not possess TsdA or the Sox pathway (Müller et al., 2004).

#### 1.2.6.2 Sulfite oxidation

Three pathways for the oxidation of sulfite to sulfate exist. One is the reverse of the APS reductase reaction described for sulfate-reduction in Section 1.2.3. This pathway is found in diverse sulfur oxidising bacteria and archaea. The second pathway involves members of the sulfite oxidase family which directly oxidise sulfite to sulfate using a molybdopterin cofactor (Equation 1.9) (Kappler, 2011). Members of this enzyme family are found in all three domains of life, and include the sulfane dehydrogenase, SoxCD, discussed earlier. The sulfite oxidase used for dissimilatory sulfite oxidation is known as SorAB. The enzyme from *Starkeya novella* has been intensely studied (Kappler et al., 2000) and contains a cytochrome *c* domain, which accepts electrons from the molybdopterin domain. Some members of this family have no cytochrome *c* domain, including the sulfite dehydrogenase from *Thermus thermophilus* (Di Salle et al., 2006).

Equation 1.9 $HSO_3^- + H_2O \rightarrow SO_4^{2-} + 3H^+ + 2e^-$ *Sulfite dehydrogenase*

For *A. vinosum* it has been shown that APS reductase is not essential and this organism instead uses SoeABC to oxidise sulfite (Dahl et al., 2013). SoeABC contains a molypdopterin cofactor, but has no homology to the sulfite oxidase family. It additionally has five [4Fe4S] iron-sulfur clusters and is anchored to the cytoplasmic side of the membrane. Interestingly, SoxYZ, but not the other Sox pathway enzymes, has been implicated in SoeABC-mediated sulfite oxidation (Dahl et al., 2013). Indeed, SoxYZ is present in purple-sulfur bacteria with no Sox pathway. SoxYZ is periplasmically located so its role in these organisms has been suggested to be transport of sulfite to a transmembrane transporter.

#### 1.2.6.3 Sulfide and $S^o$ oxidation

The Sox and reverse Dsr pathways for sulfide and $S^o$ oxidation have already been discussed. It is unlikely that the SoxF-like flavocytochrome is directly involved in sulfide oxidation *in vivo* despite having sulfide dehydrogenase activity *in vitro* (Reinartz et al., 1998). In photosynthetic organisms, such as *A. vinosum* and *Rhodobacter capsulatus*, there is a clear role for the membrane-bound flavoprotein sulfide quinone oxidoreductase (SQR) in the oxidation of sulfide to $S^o$ (Equation 1.10) (Reinartz et al., 1998; Schütz et al., 1999). SQR is also present in non-photosynthetic bacteria such as *P. pantotrophus* (Schütz et al., 1998). However, this organism shows no sulfide oxidation when the Sox pathway is knocked out (Chandra and Friedrich, 1986), so the role of SQR is not clear in this case. The structure of *A. ambivalens* SQR shows two cysteines next to an FAD cofactor, with a chain of sulfur atoms bridging the two cysteines (Brito et al., 2009).

Equation 1.10 $(n)H_2S + (n-1)Q \rightarrow H_2S_{(n)} + (n-1)QH_2$ *Sulfide quinone oxidoreductase*

A specialised $S^o$ oxidation system is present in members of *Acidithiobacillus* and *Acidiphilum*. This enzyme can oxidise $S^o$ to sulfite using glutathione and so is named glutathione-dependent sulfur dioxygenase (Rohwerder and Sand, 2003). The glutathione is thought to non-enzymatically react with $S^o$ to generate a persulfide adduct, and this glutathione persulfide is the substrate of the enzyme (Equation 1.11). This enzyme is periplasmic and the persulfide carrier *in vivo* is likely to be a protein cysteine residue rather than glutathione, making this system in some way analogous to SoxCD-catalysed oxidation of $SoxYZ\text{-}S\text{-}S^-$ and DsrAB-catalysed oxidation of $DsrC\text{-}S\text{-}S^-$.

Equation 1.11 $G\text{-}S\text{-}S^- + O_2 + H_2O \rightarrow HSO_3^- + GSH$ *Glutathione-dependent sulfur dioxygenase*

A distinct $S^o$ oxidation system is found in sulfur-oxidising archaea, some *Acidithiobacillus* species and *Aquifex aeolicus*. The cytoplasmic sulfur oxygenase reductase (SOR) involved in this pathway has been functionally and structurally characterised from *A. ambivalens* (Urich et al., 2006). This enzyme is a large homo-24-mer, with a mononuclear non-heme iron centre in each subunit next to a cysteine with a persulfide adduct. This enzyme catalyses the oxidation and disproportionation of $S^o$ to sulfite and sulfide (Equation 1.12 - 1.14). It is thought that a rhodanese-like enzyme may supply sulfur chains to SOR (Aussignargues et al., 2012) as well as polysulfide reductase (Section 1.2.3). Rhodanese enzymes catalyse the cleavage of thiosulfate into sulfite and a persulfide stored on the rhodanese active site cysteine (Equation 1.15) (Gliubich et al., 1996). These enzymes have been thought to be involved in sulfur metabolism for a very long time, but are thought not to be directly involved in dissimilatory thiosulfate metabolism (Lu and Kelly, 1983b). Rhodanese enzymes are also implicated in the oxidation of sulfide in mitochondria, which is the only inorganic substrate used in human energy metabolism (Goubern et al., 2007). Here an SQR enzyme oxidises sulfide to sulfur and this sulfur is transferred to glutathione as a glutathione persulfide (Libiad et al., 2014). Rhodanese then catalyses the reverse of Equation 1.15 to generate thiosulfate from glutathione persulfide and sulfite.

Equation 1.12 $S^o + O_2 + H_2O \rightarrow HSO_3^- + H^+$ *SOR oxygenase reaction*

Equation 1.13 $3S^o + 3H_2O \rightarrow HSO_3^- + 2HS^- + 3H^+$ *SOR disproportionation reaction*

Equation 1.14 $S^o + HSO_3^- \rightarrow {}^-S\text{-}SO_3^- + H^+$ *SOR non-enzymatic*

Equation 1.15 $\text{rhodanese-SH} + {}^-S\text{-}SO_3^- \rightarrow \text{rhodanese-S-}S^- + HSO_3^-$ *Rhodanese*

## 1.3 Bacteria and nitric oxide

### 1.3.1 Exposure of bacteria to nitric oxide

The anti-bacterial effect of nitric oxide (NO) has been exploited for thousands of years with the use of saltpetre ($Ca(NO_3)_2$) to preserve meats (Binkerd and Kolari, 1975). It is now known that the nitrate in saltpetre is reduced to NO, which kills bacteria and binds to the myoglobin in meat resulting in the characteristic pink colour of cured meats. This antimicrobial effect is enhanced by ascorbic acid (vitamin C), which reduces nitrite to NO. The use of nitrite as a preservative has been instrumental in largely eradicating botulism, a disease caused by spores of the gram-positive bacterium *Clostridium botulinum* in meat products (Pierson et al., 1983). It was subsequently suggested that the mode of action of nitrite against *C. botulinum* was the irreversible reaction of NO with metabolically important iron-sulfur clusters (Reddy et al., 1983).

Bacteria are also exposed to NO under physiological conditions as NO can be formed as an intermediate of bacterial nitrogen metabolism (Gayon and Dupetit, 1886). However, most interest has been garnered by the relatively recent discovery that the mammalian immune response attacks bacteria by using the enzyme, inducible NO synthase (iNOS), to generate NO (Marletta et al., 1988).

### 1.3.2 Denitrification

In anaerobic environments bacteria cannot use $O_2$ as a terminal electron acceptor. As described in Section 1.2.3, some bacteria reduce oxidised sulfur compounds, but these have redox couples with low potentials so are not good electron acceptors. Other bacteria instead reduce oxidised nitrogen compounds such as nitrate. Nitrate is either reduced to ammonia in a process called ammonification, or to $N_2$. The reduction of nitrate to $N_2$ is known as denitrification, because it results in the loss of nitrate from the soil and the formation of $N_2$ which is lost to the atmosphere. Nitrate is an important nutrient which plants assimilate to generate organic nitrogen sources and so denitrification is of great importance to agriculture. The denitrification pathway passes through the gaseous intermediates NO and nitrous oxide. Nitrous oxide is a potent greenhouse gas, whilst NO is oxidised in the atmosphere to higher nitrogen oxides, which are highly toxic pollutants that also cause acid rain. Use of nitrogen-based fertilisers in agriculture is a serious environmental problem partly because of the denitrification of these fertilisers resulting in an increase in the amount of nitrous oxide and NO released to the atmosphere. This adds to the NO released to the atmosphere from the burning of fossil fuels, where the temperatures are high enough for $N_2$ oxidation to occur.

The denitrification pathway has been well characterised in the $\alpha$-proteobacterium *P. denitrificans*, which is closely related to *P. pantotrophus*, a model organism for sulfur oxidation. The denitrification pathway of *P. denitrificans* is illustrated in Figure 1.3 (Simon and Klotz, 2013). Nitrate is reduced by NarGHI, which is related to the thiosulfate/tetrathionate/polysulfide reductases described in Section 1.2.3, and accepts electrons from menaquinol (Bertero et al., 2003). NarG is cytoplasmic so the nitrate and nitrite transporter NarK is required to link nitrate reduction to the rest of the denitrification pathway which is periplasmic (Goddard et al., 2008). NarK from *P. denitrificans* has a nitrate/proton symporter domain which is suggested to allow initial import of nitrate into the cytoplasm. When nitrite is produced in the cytoplasm, its export is coupled to nitrate import by a distinct NarK nitrate/nitrite antiporter domain, which decreases the use of the proton-motive force for nitrate import. There is also a distinct periplasmic nitrate reductase, NapAB, which accepts electrons from the membrane-bound NapC. The catalytic domain, NapA, is related to NarG. NapAB is expressed under aerobic conditions as an energy dissipating system (Richardson et al., 2001). The nitrite reductase, cytochrome $cd_1$, which contains an unusual $d_1$ heme, catalyses the one electron reduction of nitrite to NO (Fülöp et al., 1995). NO is reduced by the NO reductase NorBC. This is a transmembrane enzyme related to cytochrome *c* oxidase but with a non-heme iron instead of a copper atom (Hino et al., 2010). Finally nitrous oxide is reduced to $N_2$ by nitrous oxide reductase, NosZ. The catalytic site of this enzyme is an unusual [4Cu2S] cluster (Pomowski et al., 2011). The last three enzymes in the chain are periplasmic and accept electrons from cytochrome $bc_1$ through monoheme cytochrome *c* or pseudoazurin.

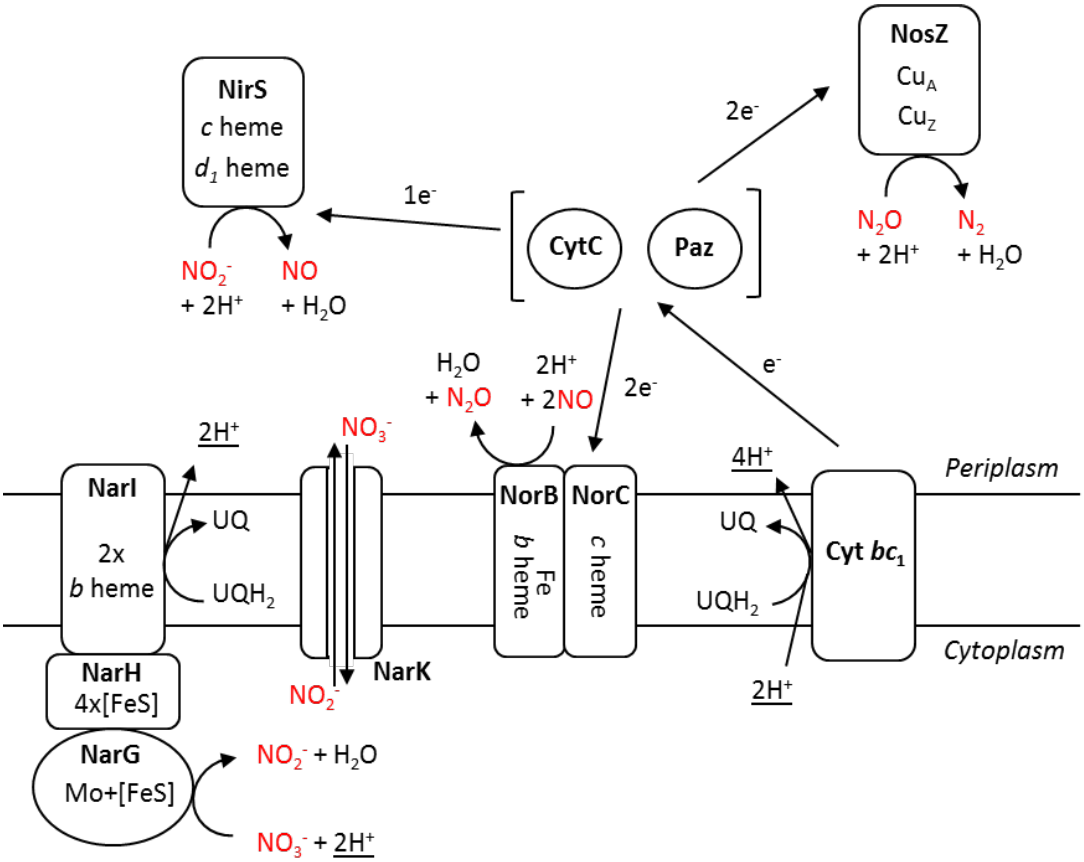

**Figure 1.3 – A simple model of the *P. denitrificans* denitrification pathway in anerobic conditions (Simon and Klotz, 2013).** Protons which contribute to the proton-motive force are underlined. Paz – pseudoazurin.

### 1.3.3 Nitric oxide synthase

In the late 80s it was discovered that the mysterious unstable signalling molecule, endothelium-derived relaxing factor, was in fact NO (Palmer et al., 1987). At the same time it was also shown that macrophages induced with *Escherichia coli* lipopolysaccharide produced NO as a cytotoxic agent (Marletta et al., 1988). In each case the NO was synthesised by NO synthase using L-arginine as a precursor (Palmer et al., 1988; Moncada et al., 1989).

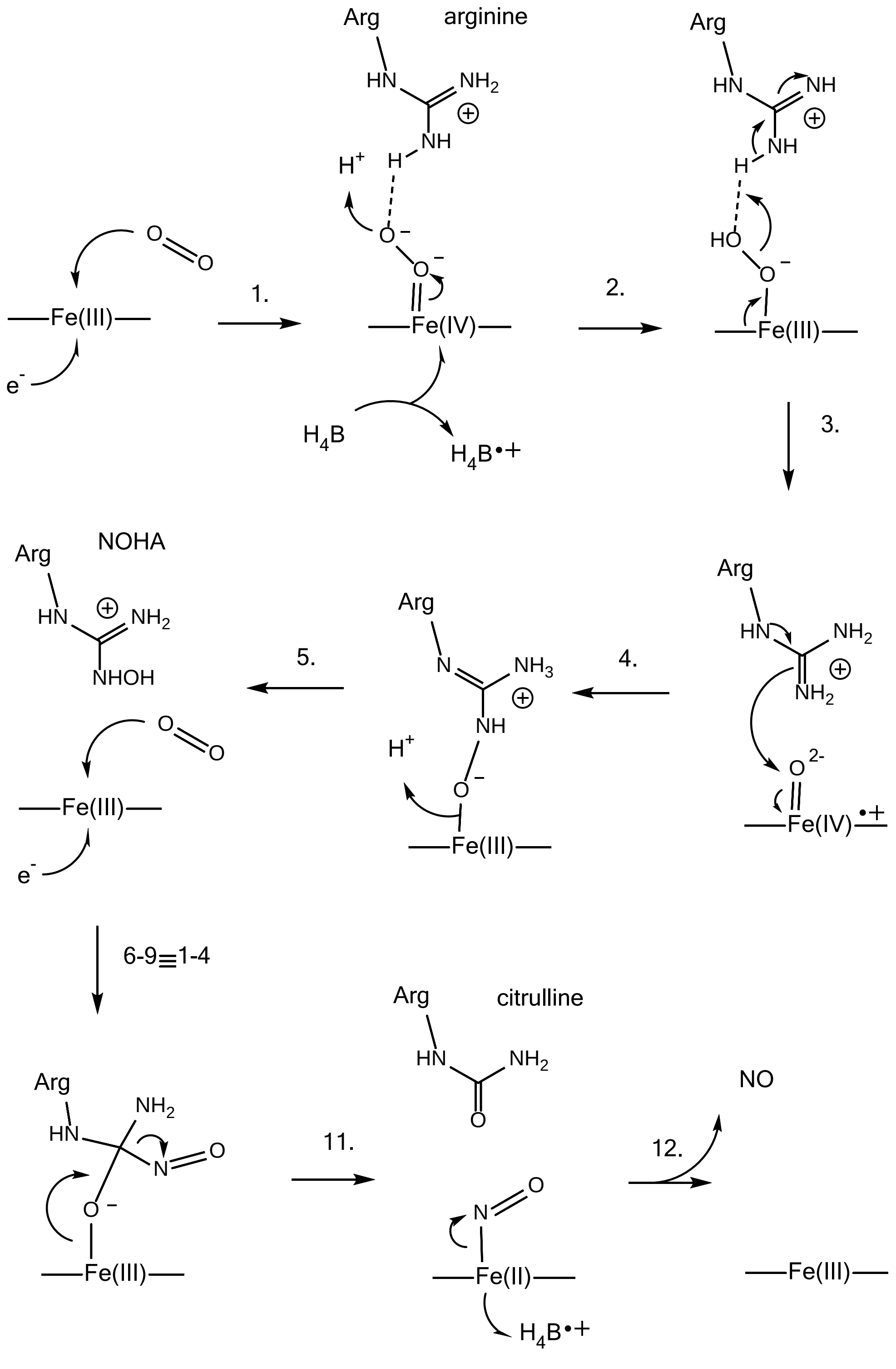

**Figure 1.4 – A possible catalytic mechanism for NO synthase (Daff, 2010).** Steps 6-9 are not shown to conserve space, but these steps are analogous to steps 1-4, except that the double bond formed in step 3 is between the secondary amine and the central carbon, and the electrons which attack the oxyferryl species in step 4 derive from the hydroxylamine oxygen, resulting in an N=O double bond and oxygen from the oxyferryl species added to the central carbon. Arg is used to identify the equivalent amino acid backbone of the substrate, intermediate and product regardless of whether this is an arginine or not. NOHA - $N^{\omega}$-hydroxy-L-arginine; $H_4B$ – tetrahydropterin cofactor.

NO synthase catalyses the reductive oxygenation of L-arginine to $N^{\omega}$-hydroxy-L-arginine and then the subsequent reductive oxygenation of this product to form L-citrulline and NO (Figure 1.4) (Daff, 2010). The oxygenase domain contains a cytochrome P450-like heme which is proposed to perform similar oxygenation chemistry to a standard cytochrome P450 (Crane et al., 1997). The oxygenase domain is otherwise unrelated to cytochrome P450. A tetrahydropterin cofactor mediates the radical chemistry (Figure 1.4) (Wei et al., 2003). Electrons come from NADPH through the FMN-and FAD-containing reductase domain. The enzyme is regulated through control of the association of the oxygenase and reductase domains by a calmodulin domain (Abu-Soud and Stuehr, 1993).

### 1.3.4 Nitric oxide in macrophages

Macrophages use phagocytosis to engulf pathogens. The engulfed pathogens are compartmentalised into phagosomes, which fuse with lysosomes to create phagolysosomes (Figure 1.5). Here, the pathogens are killed by exposure to reactive oxygen species (ROS), reactive nitrogen species (RNS) and recycled by hydrolytic enzymes. ROS derive from superoxide, which is largely generated by NADPH phagocyte oxidase (Babior et al., 2002), whilst RNS stem from NO, which is generated by iNOS (Figure 1.6). iNOS is present in macrophages in both phagolysosomes and the cytoplasm (Fang, 2004). However, NO can freely diffuse through membranes, so it is not clear if this compartmentalisation of iNOS is important. Despite the presence of a calmodulin domain, iNOS is not regulated by calcium, but instead at the level of transcription (Nathan and Xie, 1994). iNOS expression is induced by immune system signals, such as IFN-$\gamma$, IL-1$\beta$ and TNF-$\alpha$, in combination with the recognition of pathogenic epitopes on the bacterium, such as lipopolysaccharide (Assreuy et al., 1994). The regulation of ROS and RNS production is distinct, and these species are often but not always produced with temporal distinction. NADPH oxidase is regulated post-translationally, meaning that ROS are generated earlier than RNS. It is thought that the ROS response is for rapid killing, whilst RNS are generated later for sustained killing (Vazquez-Torres et al., 2000; Chakravortty and Hensel, 2003). Superoxide and NO are highly reactive and will react with each other or oxygen to produce a range of species (Figure 1.6).

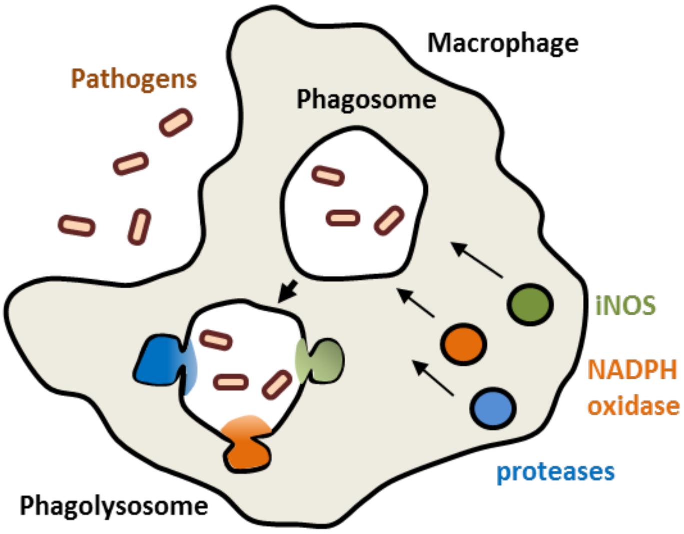

**Figure 1.5 – Simplistic model for the role of macrophages in innate immunity (Fang, 2004).** The vesicles containing iNOS, NADPH phagocyte oxidase and proteases are likely to fuse with the phagosome at different times in response to different signals. iNOS is also present in the cytoplasm, and the diffusion of NO is not restricted by membranes.

The role of NO in innate immunity has been studied in mice and in macrophages derived from humans and mice. Mice with iNOS knocked out are susceptible to infection by *Campylobacter jejuni* (Iovine et al., 2008), *Rhodococcus equi* (Darrah et al., 2000), *Mycobacterium tuberculosis*, *Staphylococcus aureus*, *Chlamydia pneumonia*, *Listeria monocytogenes*, *Leishmania spp.* and *Salmonella enterica* (Nathan and Shiloh, 2000). Although many pathogens are not killed by NO, this is not because of the limited bactericidal effect of NO, but because these pathogens have resistance mechanisms. When these resistance mechanism are knocked out, then pathogens such as *Neisseria meningiditis* (Stevanin et al., 2005), *Pseudomonas aeruginosa* (Kakishima et al., 2007), *Vibrio cholerae* (Stern et al., 2012) and *E. coli* (Shimizu et al., 2012) all become sensitive to NO-mediated killing by macrophages. Thus, the majority of infectious pathogens – including bacteria, eukaryotic parasites, viruses and fungi – must survive macrophage-derived NO. Understanding the antimicrobial action of NO and how bacteria sense and respond to NO is an extremely important area of medical research. Additionally, NO is important in the killing of cancer cells (Xu et al., 2002).

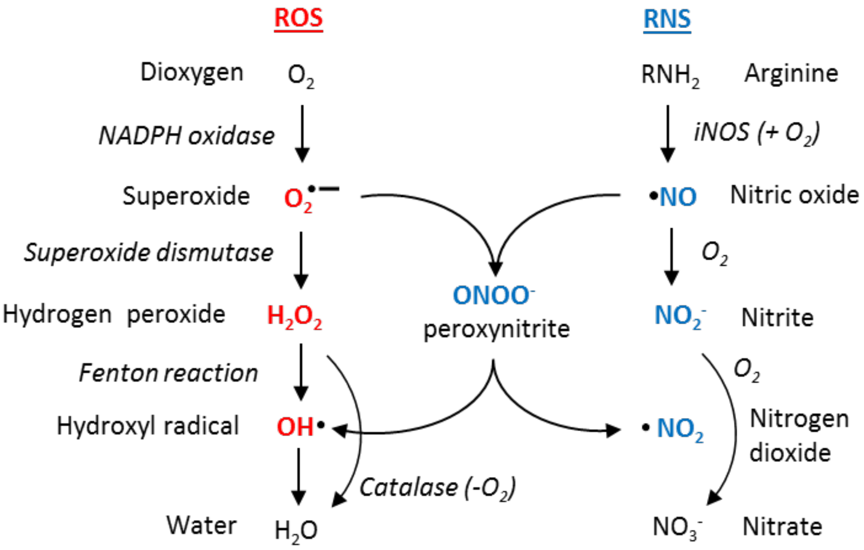

**Figure 1.6 – Inorganic nitrogen and oxygen species during macrophage-mediated killing of bacteria (Fang, 2004).** Macrophages synthesise NO and superoxide. These react together to form peroxynitrite which decomposes upon protonation to form nitrogen dioxide and a hydroxyl radical. Superoxide is deactivated by conversion to hydrogen peroxide using superoxide dismutase. However, Fenton chemistry, using redox active metals, cofactors or thiolates, can convert hydrogen peroxide to a hydroxyl radical and a hydroperoxyl radical (not shown). Hydrogen peroxide can also be deactivated by catalase to form water. NO is rapidly oxidised by $O_2$ in solution to form nitrite and nitrate. Nitrogen dioxide will also react with NO and $O_2$ to form $N_2O_3$ and other reactive $N_xO_x$ species (not shown). The RNS and ROS in each column are ordered by the oxidation state of the nitrogen or oxygen rather than by the actual transformations.

Early reports suggested that NO is strongly produced in mouse macrophage models, but not in human macrophages (Schneemann et al., 1993). However, it later became clear that regulation of iNOS is very different in mice and humans (Taylor and Geller, 2000). When the correct induction procedures are followed, iNOS is expressed and active in human macrophages (Weinberg, 1998). Furthermore, the upregulation of iNOS and the presence of NO has been detected in the tissues of infected humans (Choi et al., 2002).

### 1.3.5 The mode of action of RNS

The antimicrobial effect of ROS is thought to largely be caused by the reactivity of ROS with DNA (Imlay and Linn, 1988). This damage is caused by the extremely reactive hydroxyl radical. Formation of hydroxyl radicals from superoxide by the Fenton reaction is dependent on free ferrous iron. Superoxide and peroxide react with iron-sulfur clusters which results in the release of free iron. ROS can also react with protein side chains and lipids.

The antimicrobial effect of RNS is more complex. NO is very reactive with iron-sulfur clusters, and this is discussed in depth in Chapter 5. This reaction can release iron into the cell and so catalyse Fenton chemistry, increasing the damage done by ROS. Furthermore, many metabolically important proteins contain reactive iron-sulfur clusters. It has been shown *in vivo* using *E. coli* that <240 nM NO will cause irreversible inhibition to the TCA cycle enzyme, aconitase. Aconitase has a catalytic iron-sulfur cluster which readily binds NO during its catalytic cycle (Gardner et al., 1997). One study has shown that NO has a bacteriostatic effect on *E. coli* when they are grown in minimal media without branched chain amino acids. This was shown to be due to the reactivity of NO with dihydroxyacid dehydratase, an iron-sulfur protein involved in branched chain amino acid biosynthesis (Ren et al., 2008). NO also inhibits several non-iron-sulfur protein TCA cycle steps in *S. enterica* by inhibiting lipoamide dehydrogenase (Richardson et al., 2011)

Another mechanism of NO toxicity involves reversible inhibition of the respiratory chain (Stevanin et al., 2000). Here, NO reversibly binds to heme iron centres in proteins in the respiratory chain, such as cytochrome *c* oxidase, preventing binding of the true substrates. NO also inhibits certain enzymes, such as ribonucleotide reductase, by reacting with important tyrosine radical reaction intermediates (Lepoivre et al., 1991). Inhibition of ribonucleotide reductase decreases the availability of substrates for DNA repair enzymes. It has also been shown that NO will S-nitrosylate cysteines in zinc-binding motifs (Schapiro et al., 2003). This results in inhibition of several enzymes involved in DNA repair. Inhibition of DNA repair will exacerbate oxidative damage of DNA by ROS and RNS.

Another important antimicrobial RNS is peroxynitrite, which is formed from the reaction of NO and superoxide (Figure 1.6). This molecule decomposes to form the very reactive hydroxyl radical ROS species discussed above. Peroxynitrite is itself reactive and will nitrosylate protein tyrosine and cysteine residues, as well as DNA (Wink et al., 1991), resulting in oxidative damage related to that caused by ROS.

The potency of ROS, NO and peroxynitrite varies depending on the organism and their mechanisms of resistance. For example *Rhodococcus equi* is sensitive to peroxynitrite, but not NO (Darrah et al., 2000). *M. tuberculosis* is resistant to peroxynitrite but sensitive to NO, whilst the avirulent vaccination strain *M. bovis* BCG is sensitive to peroxynitrite (Yu et al., 1999). ROS-production but not RNS-production is extremely important for the survival of mice infected with *Aspergillus fumigatus* (Morgenstern et al., 1997).

### 1.3.6 Bacterial nitric oxide sensing systems

To resist attack by ROS and RNS, bacteria must first sense the presence of these species so that they can induce responses. Nitric oxide sensing and defence systems have been studied intensively in *E. coli*, *S. enterica*, *M. tuberculosis* and *St. aureus*. *E. coli* and *S. enterica* sense oxidative stress using SoxR (Greenberg et al., 1990) and OxyR (Zheng et al., 1998). SoxR is activated by superoxide which causes a one electron oxidation of a [2Fe2S] cluster inside the protein. OxyR senses peroxide through its reaction with a cysteine to form a cysteine sulfenic acid. These oxidation reactions alter the conformation of these proteins and result in upregulation of genes involved in the oxidative stress response. NO also reacts with SoxR and OxyR, but to form different products compared to the reactions of these proteins with ROS. The iron-sulfur cluster of SoxR reacts with NO to form a dinitrosyl iron complex, whilst the cysteine of OxyR reacts with NO to form a cysteine-S-nitrosyl group (Hausladen et al., 1996; Ding and Demple, 2000). NO causes similar transcriptional activation of these regulatory proteins as is caused by ROS.

SoxR and OxyR were the first NO-sensing proteins which were identified. However, later transcriptomics studies in *E. coli* have shown that SoxR and OxyR have minor roles in NO sensing *in vivo* (Mukhopadhyay et al., 2004). Instead the non-heme iron proteins Fur and NorR were shown to be important. NorR is activated by binding NO reversibly to form a mononitrosyl iron species (D'Autreaux et al., 2005). NorR is important for the *in vivo* survival of pathogens exposed to macrophage-produced NO (Stern et al., 2012). Fur is activated by reacting irreversibly with NO to form a range of dinitrosyl iron complexes – species with iron coordinated by two NO molecules and two other ligands (D'Autréaux et al., 2004). Whilst NorR is likely to be a specific NO-sensor, the activation of Fur is strongly dependent on the concentration of chelated iron in the medium, and is only activated by NO in iron-depleted media (Flatley et al., 2005), suggesting that Fur links redox regulation and NO sensing to iron homeostasis.

Fumarate and nitrite reductase regulator (FNR), which controls the anaerobic/aerobic switch of many bacteria, is also regulated by NO (Cruz-Ramos et al., 2002). FNR-repressed promoters are found before genes involved in NO detoxification. FNR contains a [4Fe4S] cluster which is broken down by $O_2$ to form a [2Fe2S] cluster, or reacts with NO to form dinitrosyl iron complexes. NO up-regulates genes with FNR promoters (Spiro, 2007). However, many FNR-regulated genes are not up-regulated by NO, suggesting that FNR works in concert with other NO-sensors. Nitrate and nitrite reductase regulator (NNR) is related to FNR, but appears to be more specific to NO rather than $O_2$ (Hutchings et al., 2000). NNR and the related dissimilatory nitrate respiration regulator (DNR) are thought to sense NO using non-covalently bound heme rather than a [4Fe4S] cluster (Giardina et al., 2008).

NsrR is an NO-specific sensor found in many bacteria which is unrelated to FNR but usually has a promoter within the same region as FNR and is thought to be more important than FNR for the NO-specific response (Tucker et al., 2010). NsrR is related to the iron-sulfur cluster biogenesis regulator IscR. There have been conflicting reports on whether NsrR contains a [2Fe2S] cluster (Tucker et al., 2008) or a [4Fe4S] cluster (Yukl et al., 2008), but the cluster, whether [2Fe2S] or [4Fe4S], certainly reacts with NO to form dinitrosyl iron complexes. NsrR has been shown to be important in *S. enterica* pathogenesis (Karlinsey et al., 2012). *St. aureus* does not have NsrR, and instead uses SsrA to control expression of NO resistance genes (Kinkel et al., 2013). SsrA is thought to sense a build-up of menaquinol, the reduced form of menaquinone, resulting from inhibition of the respiratory chain caused by NO.

*M. tuberculosis* does not have genes for the classical redox/NO regulators described above (Bhat et al., 2012). The [4Fe4S] cluster containing WhiB-like (Wbl) proteins, of which there are seven in *M. tuberculosis*, are thought to be important for redox and NO sensing, as well as possibly functioning as thioredoxins in their apoprotein form (Chim et al., 2014). The [4Fe4S] clusters of Wbl proteins are sensitive to both NO and $O_2$. However, the clusters in different Wbl proteins display differences in their sensitivity to NO and $O_2$. WhiB4 is sensitive to both gases (Chawla et al., 2012), WhiB3 reacts relatively slowly with $O_2$ (Singh et al., 2007) and WhiB1 is more sensitive to NO than $O_2$ (Smith et al., 2010).

A well-characterised NO-sensing system in *M. tuberculosis* is the Dos system, a two/three component system involving membrane tethered histidine kinases. These proteins regulate the expression of genes which are specifically involved in the entry of the dormancy phase of the *M. tuberculosis* pathogenic life cycle (Boon and Dick, 2002). The sensing proteins are DosS and DosT, whilst DosR is the response regulator (Figure 1.7). DosS and DosT are closely related proteins which both bind heme. DosS is mainly thought to sense the redox state of the cell through the redox state of the heme (Honaker et al., 2010), whilst DosT senses $O_2$ binding to the ferrous state of the heme. The strong binding of NO locks DosS or DosT in the ferrous state and prevents the sensing of $O_2$ or oxidising conditions (Kumar et al., 2007; Sousa et al., 2007). Thus, either the presence of NO in aerobic conditions or hypoxic conditions regardless of NO can activate *M. tuberculosis* dormancy.

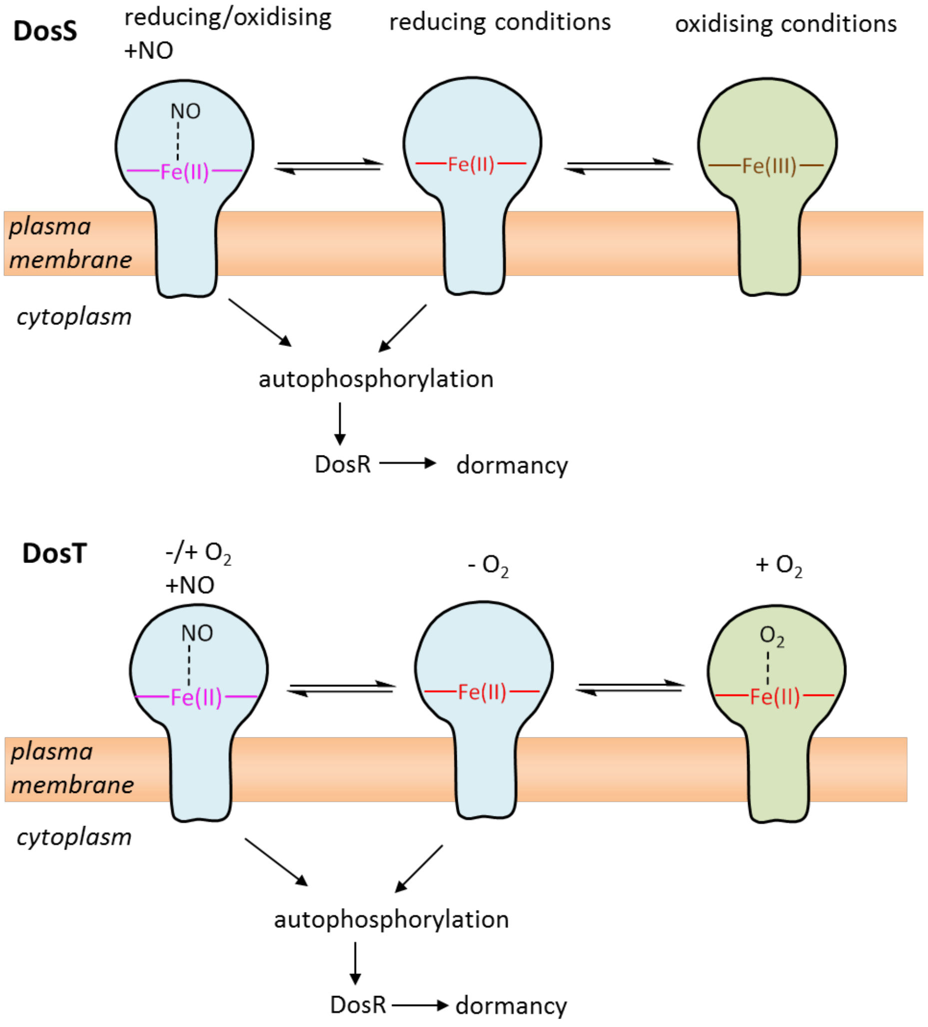

**Figure 1.7 – Regulation of dormancy in *M. tuberculosis* (Bhat et al., 2012).** The *b*-type heme in the GAF-A domain of DosS and DosT is shown as empty when pentacoordianted or water-bound, or with the 6th ligand indicated when bound to $O_2$ or NO. The heme of DosS is in the ferric state under aerobic conditions which results in inactivation of the histidine kinase domain. Under anaerobic conditions the electron transport chain will become more reducing and reduce the heme of DosS to the ferrous state, which in turn activates the histidine kinase domain. NO can only bind to the ferrous form of DosS and so will lock the protein in the reduced active form. Unlike DosS, the ferrous heme of DosT binds to $O_2$ under aerobic conditions, and this state inactivates the histidine kinase domain. Under anaerobic conditions the $O_2$ molecule dissociates and the kinase domain is activated. NO will outcompete $O_2$ for heme binding and so the presence of NO will lock the protein in the activated state.

### 1.3.7 Microbial nitric oxide defence systems

The NO sensing systems described in the previous section result in the up-regulation of many defence systems. The simplest defence is detoxification. This is similar to the overexpression of superoxide dismutase induced by SoxR to combat the superoxide generated by macrophage NADPH oxidase (Greenberg et al., 1990). Two enzymes are used to detoxify NO – the flavohemoglobin HmpA and the flavorubredoxin NorV. In *E. coli* and *S. enterica*, HmpA is induced by NsrR (Karlinsey et al., 2012), whilst NorV is induced by NorR (Mukhopadhyay et al., 2004). HmpA is an NO dixoygenase, which converts NO to $NO_3^-$ using NADH and $O_2$ (Hausladen et al., 2001). It is thought that NO binds to the ferrous heme as a nitroxyl species which then reacts with $O_2$, resulting in oxidation of the heme and formation of $NO_3^-$. The dependence on $O_2$ means that this enzyme only contributes to NO detoxification under aerobic conditions (Gardner et al., 2002). NorV, on the other hand, is oxygen sensitive and only contributes to NO detoxification under anaerobic conditions (Gardner et al., 2002). This enzyme contains a non-heme di-iron centre which catalyses the reduction of NO to $N_2O$ using NADH (Gomes et al., 2002).

Bacteria may also synthesise small molecule scavengers to soak up NO, and up-regulate enzymes which recycle these scavenger molecules (Fang, 2004). One example is glutathione, which reacts with NO to form S-nitrosoglutathione. This is then recycled by glutathione-dependent formaldehyde dehydrogenase (Liu et al., 2001). The methionine biosynthesis pathway is up-regulated during nitrosative stress (Flatley et al., 2005). Methionine and the methionine biosynthesis pathway intermediate homocysteine will react with peroxynitrite and NO respectively. Oxidised methionine can be recycled by methionine sulfoxide reductase (John et al., 2001). However, rather than being a protective measure, the up-regulation of the methionine biosynthesis pathway may be to overcome methionine deficiency caused by the NO reactivity of methionine and homocysteine (Flatley et al., 2005).

A recently discovered protein from *V. cholerae*, NnrS, has been characterised which specifically protects iron-sulfur cluster proteins, such as aconitase, from the effects of NO (Stern et al., 2013). However, the details of this process are not known.

An alternative approach to RNS resistance is to avoid the effects of RNS entirely by disrupting macrophage signalling pathways. *S. enterica* secrete effector molecules through the SPI2 type III secretion system. These effector molecules can prevent the targeting of vesicles containing iNOS and NADPH oxidase to the phagosome (Chakravortty et al., 2002). As NO can diffuse through membranes, it is thought that this mechanism exists to prevent formation of peroxynitrite, which cannot diffuse through membranes. Adenovirus E1A protein prevents the expression of iNOS by inhibiting binding of transcriptional regulators to the iNOS promoter (Cao et al., 2003).

Because NO inhibits many important metabolic enzymes, bacteria can alleviate NO toxicity by altering their metabolic flux. One example is up-regulation of glucose-6-phosphate dehydrogenase, which increases flux through the pentose phosphate pathway (Lundberg et al., 1999). This pathway is not inhibited by NO and generates reducing equivalents, which can be used to reduce NO or NO-damaged molecules, as well as providing ribose to generate nucleotide precursors to repair DNA damage. *St. aureus* possesses an NO-inducible lactate dehydrogenase (Richardson et al., 2008). Upon NO-exposure, respiring or fermenting *St. aureus* only produce lactate rather than acetate, ethanol or formate. This trait is not present in non-pathogenic *Staphylococcus* strains. It is known that NO inhibits respiratory enzymes as well as pyruvate dehydrogenase (Figure 1.8) (also see Section 1.3.6). By fermenting glucose to form lactate, these inhibited metabolic pathways are avoided (Figure 1.8). Much NO sensing relates to denitrifying bacteria and consequently a lot of NO sensors regulate the different steps of the denitrification pathway to prevent the build-up of endogenously-produced NO (Spiro, 2007). *M. tuberculosis* specifically up-regulates the nitrate reductase NarGHI and nitrate channel NarK when inside phagolysosomes (Jung et al., 2013). The NO produced by macrophages is abiotically oxidised to $NO_3^-$. It is thought that *M. tuberculosis* then uses this nitrate as its terminal electron acceptor. This results in the build-up of millimolar concentrations of nitrite, itself a RNS (Cunningham-Bussel et al., 2013).

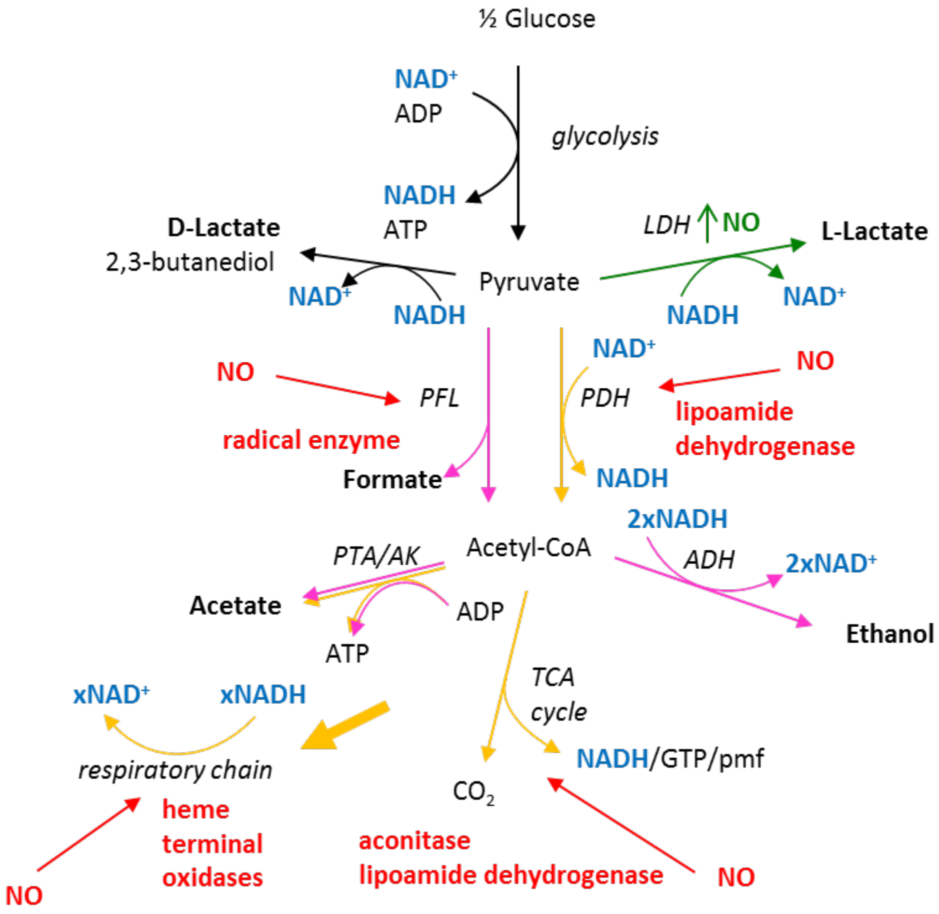

**Figure 1.8 – Effect of NO on the aerobic and anerobic metabolism of *St. aureus* (Richardson et al., 2008).** Products which were quantified are shown in bold type. Under anaerobic conditions (pink) glucose is fermented to form lactate or ethanol, formate and acetate. Under aerobic conditions (yellow) glucose is respired to form acetate during the exponential growth phase. In stationary phase or under glucose-limited conditions the acetate is converted back to acetyl-CoA and respired using the TCA cycle. Electrons from both aerobic processes are used in the respiratory chain. The inhibitory effects of NO are shown in red. The specific target of NO is described in red. Under nitrosative stress, the only viable route for glucose catabolism is by fermentation with lactate or 2,3-butanediol as products. NO up-regulates L-lactate dehydrogenase (LDH) through an unknown mechanism (green), such that this is the major product upon NO exposure in both aerobic and anaerobic conditions. Formation of the D-lactate stereoisomer is neither decreased nor increased upon NO exposure under anaerobic conditions. Formation of 2,3-butanediol was not investigated. PDH – pyruvate dehydrogenase; PFL – pyruvate formate lyase; LDH – lactate dehydrogenase; ADH – alcohol dehydrogenase; AK – acetate kinase; PTA – phosphotransacetylase; TCA cycle – tricarboxylic acid cycle.

### 1.3.8 Bacteria produce their own NO

NO instantaneously protects *Bacillus subtilis* from oxidative stress (Gusarov and Nudler, 2005). This is thought to be because NO inhibits thioredoxins which maintain cysteine in the reduced state. *B. subtilis* uses cysteine instead of glutathione to control the redox potential of the cytoplasm. Keeping cysteine in the oxidised state has two effects. Firstly, it prevents cysteine-mediated conversion of peroxide into the hydroxyl radical by the Fenton reaction. Secondly, it prevents inhibition of catalase, which detoxifies peroxide, by cysteine. A similar mechanism was also demonstrated for *St. aureus* in the same paper. *B. subtilis* and many other Gram-positive bacteria have their own nitric oxide synthase (bNOS) (Sudhamsu and Crane, 2009) and so are able to induce NO-mediated cytoprotection before macrophages produce NO. The importance of bNOS for the survival and virulence of pathogens *in vivo* has been shown for *B. anthracis* (Shatalin et al., 2008) and *St. aureus* (van Sorge et al., 2013). These bNOS proteins are also thought to contribute to protection from antibiotics (Gusarov et al., 2009).

The main NO sensor in mammals is the soluble guanylate cyclase (sGC), which detects the binding of NO to its heme. This sensor is extremely sensitive to non-lethal nanomolar concentrations of NO. It is now clear that bacteria use related proteins, called H-NOX proteins, which are related to sGC and detect sub-nanomolar NO concentrations (Plate and Marletta, 2013). H-NOX proteins are thought to be important in quorum sensing in *Vibrio harveyi* (Henares et al., 2012) and biofilm formation in *Legionella pneumophila* (Carlson et al., 2010). The bacteria which sense NO are not the same as those which generate NO, so it is thought that NO is an interspecies signal. For example, *V. fischeri* establish a symbiotic relationship with the squid *Euprymna scolopes* and this process is mediated by H-NOX proteins which sense NO produced by the squid (Wang et al., 2010).

## 1.4 Aims of this work

The general aim of this thesis is to understand some of the chemistry and mechanistic detail of the microbiology described in this introduction through the analysis of the interaction of proteins with inorganic sulfur and nitrogen compounds. One chapter will be dedicated to each of the following specific aims:

1. I aim to understand how covalently attaching substrates to carrier proteins affects the enzymology of sulfur oxidation. Substrate-carrier proteins are a prevalent theme in sulfur metabolism, but I will solely focus on the Sox pathway. Specifically, I will study the interaction of the carrier protein SoxYZ with one of its enzyme partners, SoxB.

2. I aim to study an example of an enzyme which uses a catalytic cysteine to interact with inorganic sulfur compounds, which is another common theme in bacterial sulfur enzymology. I will use the thiosulfate dehydrogenase TsdA as a paradigm for understanding the mechanism of a family of enzymes with a reactive cysteine heme ligand.

3. I aim to study the reaction of NO with protein-bound iron-sulfur clusters. These reactions are important for both the antimicrobial activity of NO and the sensing of NO by pathogens and denitrifying bacteria. The environment in which bacteria are exposed to NO can be anaerobic, at a low pH or filled with other RNS and ROS. I will determine how these factors affect the reactivity of iron-sulfur clusters with NO. To gain new insight I will develop infrared spectroscopy as a tool for studying this reactivity.

# Chapter 2: Materials and methods

## 2.1 Chemicals used in this thesis and general considerations

Sodium trithionate was synthesised by reacting sodium thiosulfate with hydrogen peroxide (Kelly et al., 1994) according to Equation 2.1. Sodium sulfate was removed by crystallisation on ice. Sodium trithionate was purified by crystallisation in ethanol. Sodium trithionate crystals were washed with ethanol and acetone and then dried.

$$2Na_2S_2O_3 + 4H_2O_2 \rightarrow Na_2S_3O_6 + Na_2SO_4 + 4H_2O \qquad \text{Equation 2.1}$$

For experiments with purified gases, 10% NO gas in $N_2$ (BOC) was first passed through a stainless steel column packed with Ascarite® II (20-30 mesh, Sigma Aldrich) to remove higher oxide impurities. Pure $N_2$ gas (BOC) was passed through an Agilent Gas-Clean filter to remove trace $O_2$ (outlet < 50 ppb $O_2$). Experiments using 0.5% NO were performed using a cylinder of 0.5% NO in $N_2$ (BOC). Other concentrations of gas were prepared by mixing 10% NO with pure $N_2$ using mass flow controllers (Brooks Instruments).

$^{15}$N-labelled NO was synthesised by mixing 1 mL of 0.1 M ascorbic acid (Sigma-Aldrich) and 1 mL of 0.1 M $^{15}$N-sodium nitrite (Sigma-Aldrich).

All other chemicals were purchased as indicated in the text, and used without further purification.

Anaerobic experiments were performed in a $N_2$-filled anaerobic glove-box (<1 ppm $O_2$, Glove Box Technology Ltd. or MBRAUN). All gas-lines were composed of gas-tight tubing, fittings, valves and taps purchased from Swagelok.

## 2.2 Molecular biology

### 2.2.1 Plasmids used in this work

Most plasmids used in this work had either already been made or were generated by standard restriction cloning as described in Section 2.2.2. However, two plasmids contain codon optimised versions of the *Thermus thermophilus* SoxB and SoxYZ-expressing plasmids previously constructed by Veronique Sauvé (Sauvé et al., 2009). These codon optimised versions were synthesised by GenScript USA Inc. and have the sequences shown in Figure 2.1. *T. thermophilus* DNA has a high GC content and a lot of secondary structure, so codon-optimised genes were synthesised to increase the ease of mutagenesis and other genetic manipulation.

SoxB$_{co}$

**GAATTC**ATTAAAGAGGAGAAATTAACTATGGCCTCGTGGTCGCATCCGCAGTTTGAAAAAGGTGCCCTGGAAGACCCGCG
CTCGCTGTATGATCTGCCGCCGTATGGTGACGCAACCCTGCTGTACTTTTCCGATCTGCATGGCCAGGCTTTTCCGCACTA
TTTCATGGAACCGCCGAACCTGATCGCACCGAAACCGCTGATGGGTCGTCCGGGTTATCTGACCGGTGAAGCGATTCTGC
GCTATTACGGCGTGGAACGTGGTACGCCGCTGGCCTATCTGCTGTCTTACGTGGATTTTGTTGAACTGGCACGTACCTTCG
GTCCGATCGGCGGTATGGGTGCACTGACGGCACTGATTCGCGACCAGAAAGCTCGTGTCGAAGCGGAAGGCGGTAAAGC
ACTGGTGCTGGATGGCGGTGACACCTGGACGAACAGCGGCCTGTCTCTGCTGACCCGCGGTGAAGCGGTGGTTCGTTGG
CAAAATCTGGTCGGCGTGGATCATATGGTGTCTCACTGGGAATGGACGCTGGGTCGTGAACGCGTTGAAGAACTGCTGGG
CCTGTTTCGCGGTGAATTTCTGAGTTATAATATCGTGGATGACCTGTTTGGCGATCCGCTGTTCCCGGCTTACCGCATTCAT
CGTGTTGGTCCGTATGCTCTGGCAGTCGTGGGTGCAAGTTATCCGTACGTTAAAGTCAGTCACCCGGAATCCTTTACCGAA
GGTCTGTCCTTCGCCCTGGATGAACGTCGCCTGCAGGAAGCAGTGGACAAAGCCCGCGCAGAAGGCGCTAACGCGGTTG
TCCTGCTGTCACATAATGGTATGCAACTGGATGCGGCCCTGGCGGAACGTATTCGCGGCATCGATCTGATTCTGTCGGGT
CATACCCACGACCTGACGCCGCGTCCGTGGCGTGTGGGTAAAACCTGGATCGTTGCCGGCAGCGCAGCTGGTAAAGCAC
TGATGCGTGTGGATCTGAAACTGTGGAAAGGCGGTATTGCTAACCTGCGTGTGCGCGTTCTGCCGGTTCTGGCGGAACAC
CTGCCGAAAGCTGAAGATGTCGAAGCGTTTCTGAAAGCTCAGCTGGCGCCGCATCAAGACCACCTGTTCACCCCGCTGGC
CGTTAGCGAAACGCTGCTGTATAAACGCGATACCCTGTACTCTACGTGGGACCAGCTGGTTGGTGAAGCCGTCAAAGCAA
TCTACCCGGAAGTCGAAGTGGTTTTTAGCCCGGCAGTGCGTTGGGGCACCACGATCCTGCCGGGTCAGGCTATTACCTGG
GATCATCTGTATGCGTACACCGGCTTTACGTATCCGGAACTGTACCTGTTTTATCTGCGCGGTGCCCAAATCAAAGCAGTT
CTGGAAGACATTGCCTCAAACGTCTTTACCTCGGATCCGTTCTACCAGCAAGGCGGTGACGTCAGTCGCGTGTTTGGCCT
GCGTTATGTGCTGGATCCGGACGCACCGACGGGTGAACGTGTTCGCGAAGTCGAAGTGGGCGGTCGTCCGCTGGATCCG
AATCGTCGCTATCTGGCAGCAGCATACGGTGGTCGTCTGCAGCGTGTGGGTGAAGCCAAACCGGGTTATGAACCGCGCC
CGATTTACGAAGTGCTGGCAGAATATCTGCGTAGCGTTGGCCGTGTTCGCGTCCGTCCGGAACCGAATGTGAAAGTGATT
GGTCGCAACTATCGCCTGCCGGAAGTGACGGGCTAA**GGTACC**

SoxYZ$_{co}$

**GGATCC**CAAGGCCTGGAAGGCGAAGACCTGGAACATCTGGAACAAGCACTGAAAGAAGTTTTTGGTAAAGGTTTTAAAGA
CCTGACCCCGTCGGATGCGGTGAAACTGAACATGCCGGCGATTGCCGAAAGCGGCGCGAATGTTCCGGCCGAAGTCGAA
GTGGCCCTGCCGAAAGAACAGGTCAAAGCAATTCACCTGTTTGCTGACAAAAACCCGACCCCGCACATCCTGGCATTCAT
GCCGATGAAAGCGGAACCGTATTACGCCACCCGTGTTCGCCTGGCTGAAACCACGGCAATCCGTGCTGTGGTTGAAACGC
AAGATGGCAAACTGCTGCTGGCGTCTGCTTCAACCCGTGTGACCGTGGGCGGCTGCGGCTGAGGTACCATTAAAGAGGA
GAAATTAACTATGCCGTTCCGCACCATTGCCCGTCTGAATCCGGCCAAACCGAAAGCAGGCGAAGAATTCCGTCTGCAAG
TCGTCGCACAACATCCGAACGAACCGGGCACCCGTCGCGATGCAGAAGGTAAACTGATTCCGGCCAAATACATCAACCTG
GTGGAAGTTTACTTCGAAGGCGAAAAAGTCGCAGAAGCACGTCCGGGTCCGAGCACGTCTGCAAACCCGCTGTATGCCTT
TAAATTCAAAGCAGAAAAAGCTGGCACCTTCACGATTAAACTGAAAGATACGGACGGTGATACGGGCGAAGCAAGTGTGAA
ACTGGAACTGGCGTGA**AAGCTT**

**Figure 2.1 – Sequences of SoxB$_{CO}$ and SoxYZ$_{co}$.** Restriction sites to increase the ease of cloning are shown in bold type. GAATTC – EcoRI, GGTACC – KpnI, GGATCC – BamHI, AAGCTT – HindIII.

**Table 2.1 – Plasmids used in this work.** Plasmids encoding variant proteins are described in Table 2.5, and derive from pQE-SoxB$_{CO}$, pQE-SoxYZ$_{CO}$ or pQE80AvTsdA-strep.

| **Plasmid name** | **Description** | **Source** |
|---|---|---|
| pQE80L | Expression vector with IPTG-inducible T5 promoter, Amp$^R$ | QIAGEN |
| pVS048 | PQE80L-derivative for expressing *Tt* SoxB with a Strep(II) tag replacing the Tat signal peptide | (Sauvé et al., 2009) |
| pVS056 | PQE80L-derivative for expressing *Tt* SoxYZ with a hexahistidine tag replacing the Tat signal peptide on SoxY | (Sauvé et al., 2009) |
| pQE-SoxB$_{CO}$ | As pVS048 but with a codon-optimised *soxB* gene | Figure 2.1 |
| pQE-SoxYZ$_{CO}$ | As pVS056 but with codon-optimised *soxYZ* genes | Figure 2.1 |
| pQE-SoxYZ$_{CO\Delta Zloop}$ | For expression of *Tt* SoxYZ without the Z-loop (SoxZ residues 29-46) | Section 2.2.3 |
| pRARE | Cam$^R$; constitutively expresses 6 rare tRNAs | Novagen |
| pEC86 | Cam$^R$; constitutively expresses the *E. coli* cytochrome *c* maturation genes *ccmABCDEFGH* | (Arslan et al., 1998) |
| pTZ19R | High copy cloning vector, Amp$^R$ | Thermo Scientific |
| pTZAvTsdA | The *Av tsdA* gene with its native signal peptide in the pTZ19R cloning vector | Section 4.2.2 |
| pQEAvTsdA-strep | pQE80L-derivative for expressing *Av* TsdA with its native signal peptide and a C-terminal Strep(II) tag | Section 4.2.2 |
| pASK-IBA-13+ | Expression vector with a *tet* promoter encoding a strep(II) tag N-terminal to MCS, Amp$^R$ | IBA |
| pASK-strepFd | pASK-IBA-13+ derivative for expressing spinach ferredoxin I with an N-terminal strep tag replacing its chloroplast targeting sequence | Section 5.3.2 |

## 2.2.2 PCR, mutagenesis and cloning

PCR reactions were performed either using a PTC-150 MiniCycler (MJ Research) or a MyCycler (Bio-Rad). PCR reactions were generally performed using KOD Hot Start Polymerase (Novagen), but Pfu Ultra II Polymerase (Agilent) was used for mutagenesis in Chapter 4. The reaction mixtures were prepared according to the manufacturer's instructions. When the primer DNA had a GC content above 60% then 5% DMSO was added to the reaction. The cycling parameters which were used are summarised in Tables 2.2-2.4. When amplifying fragments for cloning, primers were designed with a $T_m$ of *ca.* 60°C using the formula, $T_m = 81.5 + 0.41x\%CG - 675/n$

(Stratagene QuikChange manual). Mutagenesis was performed using the QuikChange method (Stratagene) as described in the manual.

**Table 2.2 – Amplifying fragments for cloning using KOD Hot Start Polymerase**

| Initial denaturation | Denaturation | Annealing | Extension | Final Extension |
|---|---|---|---|---|
| 95°C<br>2 min | 95°C<br>30 s | 50 - 60°C<br>30 s | 68°C<br>1 min/kb | 68°C<br>10 min |
| | x25 | | | |

**Table 2.3 – Mutagenesis using KOD Hot Start Polymerase**

| Initial denaturation | Denaturation | Annealing | Extension | Final Extension |
|---|---|---|---|---|
| 95°C<br>2 min | 95°C<br>30 s | 50 - 60°C<br>1 min | 68°C<br>1 min/kb | 68°C<br>10 min |
| | X17 | | | |

**Table 2.4 – Mutagenesis using Pfu Ultra II**

| Initial denaturation | Denaturation | Annealing | Extension | Final Extension |
|---|---|---|---|---|
| 95°C<br>2 min | 95°C<br>20 s | 50 - 60°C<br>20 s | 68°C<br>30 s/kb | 68°C<br>10 min |
| | x25 | | | |

All cloning was performed using restriction sites. Fragments were amplified with restriction sites added in the sequence of the primers. The amplified sequence was purified using the QIAquick purification kit (QIAGEN) as described in the manual, and was added to the vector at a ratio of approximately 5:1. Double digests were performed using restriction enzymes from New England Biolabs for one hour at 37°C. The mixture was purified using the QIAquick purification kit and T4 DNA ligase (New England Biolabs) was added for one hour at room temperature. XL-I competent cells were transformed with 1 μL of the resulting solution. Colonies were screened by colony

PCR. Positive colonies from either cloning or mutagenesis were grown in LB overnight with the appropriate antibiotics, and the plasmid was purified using the MiniPrep kit (QIAGEN) and sequenced using the service provided by Source Bioscience.

When required, PCR products were visualised using electrophoresis with ethidium bromide staining. Electrophoresis was performed using 1% agarose gels in a buffer which contained 40 mM Tris, 20 mM acetic acid, 1 mM EDTA, pH 8.5.

### 2.2.3 List of primers used in this thesis

**Table 2.5 – List of primers used for mutagenesis in this thesis.** Mismatching bases are shown in red. The reverse primer is not shown as it is the reverse complement of the forward primer. SoxY$_{\Delta Arm}$Z (where SoxY is missing residues $^{145}$RVTVGGCG) was generated using SoxYZ$_{CO}$ *Y*R145[stop].

| **Variant** | **Forward primer** |
|---|---|
| SoxYZ$_{WT}$ *Y*C151S | 5'-CACCGTGGGGGGCTCCGGTTAAGGTACC-3' |
| SoxYZ$_{CO}$ *Y*R145[stop] | 5'-CGTCTGCTTCAACCTGAGTGACCGTGGGCGGC-3' |
| SoxB$_{CO}$ R416G | 5'-GCCCGGCAGTGGGTTGGGGCACCACG-3' |
| SoxB$_{CO}$ D207R | 5'-GGATGACCTGTTTGGCCGTCCGCTGTTCCCGGC-3' |
| SoxB$_{CO}$ F205S | 5'-CGTGGATGACCTGTCTGGCGATCCGCTG-3' |
| SoxB$_{CO}$ W175C | 5'-CATATGGTGTCTCACTGCGAATGGACGCTGG-3' |
| TsdA R119A | 5'-CCTCATCACGCTCGAACAGGCCATCGGCGATTGTTTCG-3' |
| TsdA R109A | 5'-CCGCAGTACAGCGCCGCACATGGCCGCCTC-3' |
| TsdA R224A | 5'-CGCGGGGATGAACGCTCAGGCCACGGCCG-3' |
| TsdA S127A | 5'-CGATTGTTTCGAGCGCGCTCTCAACGGTCGAGCG-3' |

**Table 2.6 – List of primers used for cloning in this thesis.** SoxYZ$_{\Delta Z\text{-loop}}$ was generated by inverse PCR using primers which did not include SoxZ residues 29-46. A BamHI site was introduced on each end of the fragment to allow recircularisation by restriction digest and ligation resulting in -gly-ser-gly- replacing residues 29-46. Subcloning of SoxB$_{CO}$ and SoxYZ$_{CO}$ from the pUC4K plasmid in which they were provided by GenScript used standard M13 primers, which are not listed here.

| **Primer name** | **Sequence** |
|---|---|
| BamHI_SoxYZ$_{\Delta Z\text{-loop}}$_F | 5'-ACGGCTGGATCCGGTTACATCAACCTGCTGGAAG-3' |
| BamHI_SoxYZ$_{\Delta Z\text{-loop}}$_R | 5'-ACGGCTGGATCCATGTTGTGCGACGACTTG-3' |
| XbaI_AvTsdA_F | 5'-CAAGACTCTAGAATGCGCGGTGATGTAAGG-3' |
| XbaI_AvTsdA_R | 5' ACTTACTCTAGATCAGTCACCCGTCGGC-3' |
| EcoRI_RBS_AvTsdA_F | 5'-CAGGACGAATTCATTAAAGAGGAGAAATTAACTATGCGCGGTGATGTAAGG-3' |
| HindIII_strep_AvTsdA_R | 5'-ACTTACAAGCTTTCATTTTTCGAACTGCGGGTGGCTCCAGCTAGCGTCACCCGTCGGCTC-3' |
| SacII_Spinach_FdI_F | 5'-CAGGACCCGCGGTGCTGCCTACAAGGTAACCTTGG-3' |
| KpnI_Spinach_FdI_R | 5'-ACGGCTGGTACCTTAGGCAGTAAGCTCCTCTTCC-3' |

## 2.3 Bacterial growth

**Table 2.7 – List of *E. coli* strains used in this thesis.**

| **Strain** | **Comments** | **Source/reference** |
|---|---|---|
| BL21 star | DE3 expression strain with increased mRNA stability<br>F$^-$ *ompT hsdS*$_B$ ($r_B^-m_B^-$) *gal dcm rne131* (DE3) | Invitrogen |
| C41 | BL21(DE3) derivative for decreasing toxicity of protein overexpression<br>F$^-$ *ompT hsdS*$_B$ ($r_B^-m_B^-$) *gal dcm* (DE3) | (Miroux and Walker, 1996) |
| C43 | C41 derivative for decreasing toxicity of protein overexpression | (Miroux and Walker, 1996) |
| L56 | Unpublished Lemo21 (DE3) derivative selected for high-level expression of membrane proteins | (Rollauer et al., 2012; Tarry et al., 2012) |
| JM109 | Cloning strain which can be used for expression<br>e14$^-$ (McrA$^-$) *recA1 endA1 gyrA96 thi-1 hsdR17* ($r_K^-$ $m_K^+$) *supE44 relA1* Δ(*lac-proAB*) [F′ *traD36 proAB lacIq ZΔM15*]. | (Yanisch-Perron et al., 1985) |
| XL-I | Cloning strain with mutations to increase DNA stability and allow blue-white screening<br>*recA1 endA1 gyrA96 thi-1 hsdR17 supE44 relA1 lac* [F′ *proAB lacI*$^q$ *ZΔM15* Tn*10* (Tet$^r$)] | Stratagene (Agilent) |

All bacterial growth described in this thesis was performed using lysogeny broth (LB) (Bertani, 1951), either in the liquid phase or in the solid phase with 2% agar. LB contained 10 g tryptone, 5 g yeast extract and 10 g NaCL per litre. Unless otherwise specified, bacterial growth was performed aerobically in a shaking incubator at 185 rpm at 37°C. Ampicillin was used at a final concentration of 100 μg/mL and chloramphenicol at 25 μg/mL.

## 2.4 Protein expression and purification

All chromatography steps were performed using an ÅKTA FPLC system (GE Healthcare).

### 2.4.1 *T. thermophilus* SoxYZ$_{\text{(WT and CO)}}$ and variants

The BL21 star *E. coli* expression strain (Table 2.7) was transformed with plasmid pVS056 or pQE-SoxYZ$_{\text{CO}}$ or mutagenised derivatives (Table 2.5). Starter cultures were grown overnight at 37°C and 185 rpm in LB-Amp media. Expression was performed in 750 mL (LB-Amp) cultures in 2.5 L baffled flasks. Cultures were inoculated with 7.5 mL of the starter culture and grown at 37°C and 185 rpm. At an $A_{600}$ of *ca.* 0.6 cultures were induced with 0.1 mM IPTG and grown for a further 4 hours under the same conditions. Cells were harvested by centrifugation at 9000 x *g* in a JLA8.1000 rotor (Beckman) operated in a J-25X Avanti centrifuge (Beckman). The cell pellet was stored at -80°C until required.

The pellet was thawed and resuspended in 50 mM Tris-HCl pH 8.0, 500 mM NaCl with a few crystals of DNAse I and lysozyme (both Sigma-Aldrich) and one EDTA-free protease inhibitor tablet (Roche). Cells were then lysed by two passages through a French Press (Thermo Scientific) at 65-100 MPa. Cell debris was removed by centrifugation at 200000 x *g* for one hour at 4°C. The soluble fraction was heat-treated for 30 minutes at 65°C to precipitate non-thermophilic proteins. Precipitated proteins were removed by centrifugation at 10000 x *g* for 25 minutes. The soluble fraction was purified by Ni-NTA affinity chromatography by loading on a 5 mL His-trap HP column (GE Healthcare) equilibrated in 50 mM Tris-HCl pH 8.0, 500 mM NaCl, 1 mM imidazole. The loaded column was washed with 10 column volumes of the same buffer but with 25 mM imidazole, and then SoxYZ was eluted with a 25-210 mM imidazole gradient over 10 column volumes. SoxYZ elutes in the first peak whilst free SoxY elutes in the second peak. The first peak was pooled and concentrated to 500 μL by ultrafiltration using a 30 kDa cut-off concentrator (Millipore). Final purification of SoxYZ was by size-exclusion chromatography (SEC) using a Superdex 75 10/300 (GE Healthcare) equilibrated in 30 mM Tris-HCl pH 8.0, 200 mM NaCl. SoxYZ elutes as a single peak. The purity of the preparation was analysed by 15% SDS-PAGE. For expression of SoxYZ constructs with their native carrier arm cysteine, 2 mM DTT (Sigma Aldrich) was added to all buffers during purification until the final SEC step.

### 2.4.2 *T. thermophilus* SoxB$_{\mathrm{(WT\ and\ CO)}}$ and variants

A BL21 strain with a pRARE plasmid (Table 2.1) was transformed with SoxB$_{\mathrm{WT}}$, whilst a BL21 star strain was transformed with SoxB$_{\mathrm{CO}}$ and variants. Expression, cell lysis and heat-treatment were performed similarly to SoxYZ, except the cell pellet was resuspended in 100 mM Tris-HCl pH 8.0, 200 mM NaCl, and heat treatment was only performed for 20 minutes. DTT was not used in the purification buffers, even for the cysteine-containing variant SoxB$_{\mathrm{W175C}}$. The soluble fraction after heat-treatment was loaded on a 5 mL streptactin (IBA) column and washed with 5 column volumes of 100 mM Tris-HCl 200 mM NaCl, and then eluted with five column volumes of the same buffer with 2.5 mM desthiobiotin. Further purification by SEC was performed as for SoxYZ.

### 2.4.3 *A. vinosum* TsdA and Spinach ferredoxin I

TsdA was expressed and purified as discussed in Section 4.2.2 whilst Spinach ferredoxin I was expressed and purified as discussed in Section 5.3.2. Purification protocols were similar to SoxB but with extra steps in place of the heat-treatment step. Strains expressing Fd were induced with 200 ng/L anhydrotetracycline.

### 2.4.4 Protein modification

The cysteine-S-thiosulfonate derivative of SoxYZ (SoxY($SSO_3$)Z) was generated by reacting SoxYZ with 50 mM potassium tetrathionate (Fluka) at room temperature for one hour as previously described (Sauvé et al., 2009). Tetrathionate was added to SoxYZ immediately after removal of DTT by the SEC step in the standard purification protocol. The S-carboxymethyl SoxYZ derivative (SoxY(Ac)Z) was generated by reaction of SoxYZ in 100 mM Tris-HCl pH 8.0, 200 mM NaCl, 2 mM DTT with 20 mM sodium iodoacetate (Sigma Aldrich) at 37°C for one hour (Crankshaw and Grant, 2001). Unreacted iodoacetate was quenched with β-mercaptoethanol. Using the same protocol, the S-carboxyamidomethyl SoxYZ derivative (SoxY(Am)Z) was generated by reaction of SoxYZ with sodium iodoacetamide (Sigma Aldrich). Following derivatisation, small molecules were removed from SoxYZ by SEC using a Superdex 75 10/300 column (GE Healthcare). Electrospray ionisation-mass spectrometry (ESI-MS) was used to confirm that SoxYZ samples had been correctly and quantitatively derivatised.

The disulfide-linked SoxB-SoxYZ complex was generated by incubating 50 μM $\text{SoxB}_{\text{W175C}}$ with 50 μM SoxY($SSO_3$)Z in 30 mM Tris-HCl pH 8.0, 200 mM NaCl for one hour at 70°C. Precipitate was removed by centrifugation at 16000 x *g*, and the complex was purified away from unreacted SoxB by Ni-NTA affinity chromatography using a 1 mL HisTrap HP column (GE Healthcare) essentially as described for purification of SoxYZ. Purification of the complex from unreacted SoxYZ was achieved by SEC using a Superdex 200 10/300 column (GE Healthcare) equilibrated in 30 mM Tris-HCl pH 8.0. For crystallography the buffer was diluted to 10 mM Tris-HCl pH 8.0 using water. The sample was then concentrated to 93 μM for crystallography using an Amicon Ultra 2 mL 10000 MWCO spin concentrator (Millipore). ESI-MS and SDS-PAGE were used to confirm successful purification of the SoxB-SoxYZ complex.

## 2.5 Protein biochemistry

### 2.5.1 Electrophoresis

Protein electrophoresis was performed in polyacrylamide gels using standard buffers and methods (Laemmli, 1970). Gels were made without sodium dodecyl sulfate (SDS), and so could be used for both native polyacrylamide gel electrophoresis (PAGE) or SDS-PAGE, depending on the running buffer used during electrophoresis. A 15% gel was prepared as shown in Table 2.8. Other percentage gels were prepared by scaling the amount of acrylamide and water added accordingly. Running buffer contained 14.4 g of glycine and 3.03 g of Tris per litre. For SDS-PAGE, 1 g of SDS was added to the running buffer. Samples were prepared in sample buffer. 2x sample buffer contained 0.125 M Tris-HCl pH 6.8, 20% glycerol and a few crystals of bromophenol blue. 4% SDS was added to the 2x sample buffer used for SDS-PAGE. For reducing SDS-PAGE, 100 mM DTT was added to the 2x sample buffer.

**Table 2.8 – Recipe for polyacrylamide gels.**

| Ingredient | 15% Resolving gel | Stacking gel |
|---|---|---|
| 1 M Tris-HCl pH 8.8 | 3.25 mL | - |
| 1 M Tris-HCl pH 6.8 | - | 0.625 mL |
| 30% (v/v) acrylamide<br>0.8% (w/v) bisacrylamide | 5 mL | 0.5 mL |
| 10% ammonium persulfate | 100 μL | 50 μL |
| tetramethylethylenediamine | 10 μL | 5 μL |
| water | 1.64 mL | 3.82 mL |

### 2.5.2 Protein concentration determination

Protein concentration was determined in one of four ways. Some proteins, such as spinach ferredoxin, have published extinction coefficients in the visible region of the spectrum. Concentration for these proteins was determined by simply measuring the absorption at the wavelength of the published extinction coefficient.

SoxB and SoxYZ were initially quantified by dilution 3 in 100 into 6 M guanidinium-hydrochloride and their absorption at $A_{280}$ compared to calculated extinction coefficients of 105 $mM^{-1}cm^{-1}$ for SoxB and 7.45 $mM^{-1}cm^{-1}$ for SoxYZ. However, SoxYZ has weak absorbance as it has no tryptophans and many of the SoxYZ cysteine modifications discussed will absorb at $A_{280}$. Therefore, once the concentration had been determined spectroscopically for the native proteins, these proteins were used as standards to generate a calibration curve for a Bradford assay (Biorad). All protein concentration determination for SoxB and SoxYZ was performed using the Bradford assay in triplicate using the instruction manual provided by the manufacturer.

The concentration of TsdA was determined from the heme concentration using the pyridine hemochrome method (Tervoort et al., 1981). TsdA was dissolved in 19% pyridine, 0.15 M NaOH. The protein was then reduced with a few crystals of sodium dithionite. The absorbance at 535 nm was subtracted from the absorbance at 550 nm. The concentration of heme was calculated using an $\varepsilon_{(550\text{-}535)}$ of 22.1 $mM^{-1}cm^{-1}$. The concentration of TsdA is half the total heme concentration.

## 2.5.3 Enzyme assays

### 2.5.3.1 Analysis of trithionate hydrolysis

SoxB trithionate hydrolysis assays were performed in 10 mM HEPES-NaOH at 70°C, pH 6.8 (pH 7.5 at 25°C). Activities were corrected for the rate of non-enzymatic hydrolysis. Trithionate and thiosulfate concentrations were quantified by cyanolysis using sodium thiosulfate standards of known concentration (Kelly et al., 1994). Sulfate concentrations were determined using the barium sulfate assay calibrated with sodium sulfate standards of known concentration (Kolmert et al., 2000).

Michaelis-Menten parameters were determined using 0.5 µM SoxB. Initial velocities were estimated from measuring the thiosulfate concentration by cyanolysis after a 10 minute trithionate hydrolysis assay as above. $K_M$ and $k_{cat}$ values were determined by non-linear curve-fitting to the standard Michaelis-Menten equation using OriginPro 8.5.1 (OriginLab).

The activities of SoxB variants were assessed as sulfate production from 5 mM sodium trithionate in 10 minutes, determined by the barium sulfate method, with other conditions and corrections as above.

### 2.5.3.2 TsdA thiosulfate oxidation assays with ferricyanide as electron acceptor

The reduction of ferricyanide was monitored by the decrease in absorption at 420 nm. A molar absorbitivity difference between the reduced and oxidised forms of ferricyanide at 420 nm of 1.09 $mM^{-1}cm^{-1}$ was used to quantify reduction. The rate of reaction was calculated from the initial rate of decrease of $A_{420}$. Reactions typically contained 1 nM TsdA, 100 mM ammonium acetate pH 4.25, 8 mM sodium thiosulfate and 1 mM potassium ferricyanide. To prevent auto-activation behaviour where the rate increased over time, and to obtain maximal activity, all components apart from ferricyanide were pre-mixed for 30 seconds and reactions were then initiated with ferricyanide. TsdA and thiosulfate are mildly unstable at pH 4.25, so the time that these components spent at low pH was minimised as much as possible.

### 2.5.4 Protein crystallography, X-ray data collection, structure solution, and refinement

I performed all protein crystallisation. However, all data collection, structure solution and refinement were performed by Paul Chappell, Steven Johnson and Susan Lea using the methods described below.

#### 2.5.4.1 SoxBYZ

Crystals of the disulfide-linked SoxB-SoxYZ complex were obtained by the vapour-diffusion method using 0.55 µL sitting drops containing 70% protein solution (93 µM) and 30% mother liquor (100 mM Tris-HCl, 200 mM $(NH_4)_2SO_{4,}$ 8.55% PEG 8000, pH 8.3). Drops were incubated at 20$^{o}$C and equilibrated against 120 µL of mother liquor.

A single crystal was cryoprotected in 30% ethylene glycol and 70% mother liquor and flash cooled in liquid nitrogen. Diffraction data were collected at 100K to 3.28 Å on the i04 beamline at the Diamond Light Source, Oxfordshire, England. Automatic data processing was carried out with the Xia2 package (Winter, 2010). Molecular replacement utilised Phaser (McCoy et al., 2007) with search models derived from *T. thermophilus* SoxB (PDB: 2WDF), *T. thermophilus* SoxZ (PDB: 1V8H) and *P. pantotrophus* SoxYZ (PDB:2OX5).

Cycles of refinement and rebuilding were carried out using the computer graphics program Coot (Emsley et al., 2010) and the autoBUSTER (Global Phasing) refinement package, and targeting the structure to the previously determined structures of the individual components of the complex (Blanc et al., 2004). The structure has been deposited in the Protein Data Bank under the code (PDB:4UWQ). Structural figures were produced using the PyMol Molecular Graphics System, Version 1.3 (Schrödinger, LLC).

### 2.5.4.2 TsdA

This section provides details of the co-crystallisation and structure solution of TsdA with tetrathionate. The structures of native TsdA, TsdA-DTT and S-carboxymethylated TsdA have not been fully refined due to difficulty in unambiguously assigning active site electron density. Crystallisation of TsdA was carried out using the sitting drop, vapour-diffusion method. Drops of 0.2 µL were incubated at 20°C and equilibrated against 120 µL of mother liquor. Crystals grew overnight and were obtained from conditions containing 70% protein solution (380 µM TsdA and 2 mM sodium tetrathionate) and 30% mother liquor (100 mM ammonium acetate pH 4.6, 7.5% PEG 10K). A single crystal was cryoprotected in 30% ethylene glycol and 70% mother liquor and flash cooled in liquid nitrogen. Diffraction data were collected at 100K to 1.29 Å on the i03 beamline at the Diamond Light Source, Oxfordshire, England. Automatic data processing was carried out with the Xia2 package (Winter, 2010). Molecular replacement was carried out using MolRep (Vagin and Teplyakov, 2010) with search models derived from the C-terminal domain of *R. sulfidophilum* reduced SoxAX (PDB:1H32) and the C-terminal region of *P. haloplanktis* nitrite reductase (PDB:2ZOO). Auto-building was carried out with ARP/wARP (Langer et al., 2008) and subsequent refinement and rebuilding cycles were carried out using the computer graphics programs Coot (Emsley et al., 2010) and Refmac (Murshudov et al., 1997). Structural figures were produced using the PyMol Molecular Graphics System, Version 1.3 (Schrödinger, LLC).

## 2.6 Biophysical techniques

### 2.6.1 Electrospray-ionisation mass spectrometry

Electrospray-ionisation mass spectrometry (ESI-MS) was used in Chapter 3 to confirm that SoxYZ samples had been correctly and quantitatively derivatised, and to confirm successful formation of the disulfide linked SoxB-SoxYZ complex. Prior to ESI-MS, samples were desalted into 50% v/v acetonitrile/water, 0.1% formic acid using a $C_4$ ZipTip (Millipore) according to the manufacturer's instruction. ESI-MS analysis was performed on a Micromass LCT (Waters) operated in positive ion mode. The mass accuracy was ±0.1%.

ESI-MS was also performed in Chapter 5, as described in the main text. For these measurements, samples were prepared by dilution in 0.1% TFA, and then desalted using in-line reverse phase chromatography before loading on a LCT Premier (Waters) in positive ion mode in 50% v/v acetonitrile/water, 0.1% formic acid.

All spectra were analysed using MassLynx software (Waters Software).

### 2.6.2 Surface plasmon resonance

All surface plasmon resonance (SPR) experiments were performed on a Biacore T200 (GE Healthcare) at 25°C. SoxB was immobilized to a CM5 chip using amine coupling chemistry. SoxB in sodium acetate pH 5.5 at 1 or 10 µg/mL was immobilised at a density of 100 and 200 response units, respectively. For each comparison a control reaction without SoxB was performed in an adjacent flow cell and the response subtracted from that of the SoxB-containing test cell. The sensogram from an injection of buffer onto the sensor chip was also subtracted from each sample. Experiments were performed in 10 mM HEPES-NaOH, 150 mM NaCl, 0.005% Tween-20, pH 7.4. Analytes were injected in a randomized order for 30 seconds at a flow rate of 75 µL/min, and allowed to dissociate over 360 seconds. No regeneration step was required due to the fast dissociation rates. For each analyte loading density data were acquired for duplicate two-fold serial dilutions with 9 concentrations from 30 µM to 0.12 µM. Equilibrium data from duplicate runs were simultaneously fit to a 1:1 binding model using the Biacore T200 software (GE Healthcare). The $k_{\mathrm{off}}$ rates were determined by fitting the dissociation phase at each concentration as an exponential decay function using OriginPro. The specific approaches used are described in Figure 3.7.

### 2.6.3 Isothermal titration calorimetry

All ITC experiments were performed on a MicroCal $\mathrm{iTC_{200}}$ at 25°C with a reference power of 3 cal/s and a stirring speed of 1000 rpm. Experiments were carried out with SoxB in the cell and SoxYZ as the titrant. Both proteins were in 30 mM Tris-HCl pH 8.0, 200 mM NaCl. For each protein variant control experiments were carried out to confirm that sample dilution did not cause systematic deviation from a flat baseline. Traces were integrated using OriginPro and then two replicate experiments were simultaneously fitted to a hetero-association model ($A + B \leftrightarrow AB$) with ΔH and $K_D$ as fitting parameters using SEDPHAT (Houtman et al., 2007). When the inflexion point was clear, inactive protein fractions were included as fitting parameters to account for small errors in protein concentration determination.

### 2.6.4 Size-exclusion chromatography – multi angle light scattering (SEC-MALS)

SEC-MALS separates samples by size and shape, like standard SEC. However, rather than an in-line UV detector, the eluate is analysed by scattering methods. This allows determination of the average molecular weight of eluted peaks. Samples were loaded on a Superdex 200 10/300 column (GE Healthcare) equilibrated in 30 mM Tris-HCl, 150 mM NaCl pH 8.0 and analysed by an in-line Dawn Heleos-II light scattering detector (Wyatt Technologies) and an Optilab-rex refractive index monitor (Wyatt Technologies). Molecular mass calculations were performed using ASTRA 5.3.4.14 (Wyatt Technologies) assuming a standard refractive index increment (dn/dc) for a protein containing no carbohydrate of 0.186 mL $g^{-1}$ (Wen et al., 1996). This value is not affected by the sequence of the protein.

### 2.6.5 Molecular dynamics simulations

Molecular dynamics (MD) simulations used an AMBER 99SB force-field (Hornak et al., 2006) with a TIP3P water model (Jorgensen et al., 1983) run on GROMACS v4.5.6 (Hess et al., 2008). Previously described AMBER parameters were used for the manganese (II) ions (M. Bradbrook et al., 1998). Cysteine-S-thiosulfonate partial charges were generated by quantum mechanical calculations using AmberTools13 (Case et al., 2012) and Gaussian 03 (Frisch et al., 2004), and bond length, angle and dihedral parameters for the sulfonate group were taken from the AMBER GAFF force-field (Wang et al., 2004).

## 2.7 Spectroscopy

### 2.7.1 UV/visible spectroscopy

UV/visible spectroscopy in Chapters 3 and 4 was performed using an Ultrospec 2100 Pro photospectrometer (GE Healthcare). Spectra requiring either low volumes or measurement of UV absorption were performed using a 80 μL quartz cuvette (Optiglass Ltd.) with a 10 mm path-length. Spectra were recorded at 250 nm $min^{-1}$ versus a buffer blank. All other UV/visible measurements, such as enzyme kinetic assays and protein concentration determination, were performed with this spectrometer.

UV/visible spectroscopy in Chapter 5 was performed using a Cary 60 UV-visible spectrophotometer (Agilent) housed entirely inside a glove box (< 1 ppm $O_2$, Glove Box

Technology Ltd.). Samples were measured inside a quartz cuvette (Hellma) with a 10 mm pathlength. Spectra were recorded at 300 nm min$^{-1}$ versus a buffer blank.

The scale for UV/visible spectra is occasionally given in absorbance units (AU). 1 mAU is equivalent to a difference in absorbance, $\Delta \ln(I/I_o)$, at any wavelength of 0.001, where $I_o$ is the intensity of the light before absorption and I is the intensity which is transmitted.

### 2.7.2 Fourier-transform infrared spectroscopy

Rather than using a monochromator to scan across the wavelengths of the infrared spectrum and measure absorbance at each wavelength, a Fourier-transform infrared spectrometer detects polychromatic light and uses an interferometer to provide wavelength-specific information. The infrared light is split towards two different mirrors and then recombined into a single beam. One of these mirrors is fixed whilst the other oscillates, creating a periodic path-length difference between the two portions of light. This means that a pattern of constructive and deconstructive interference will occur which will depend on the position of the oscillating mirror. In the absence of absorbing sample, the transmitted intensity at each mirror position will be a superposition of the interference from all component wavelengths of the incident light, modulated by the emission profile of the light source. However, if some wavelengths are absorbed by a sample, there will be changes in this pattern of interference. A Fourier transform of the interferogram will convert the data from the time (in the oscillation cycle) domain to the frequency domain, and these data can be converted into a standard absorption spectrum by normalisation to a spectrum of the spectrometer in the absence of a sample. These calculations were all performed by the spectrometer software – Varian Resolutions Pro 4.0.

When spectroscopy was performed outside a glove box, ATR-IR measurements were recorded using a Varian FTS-7000 spectrometer coupled to a DurasamplIR II accessory (SensIR technologies) with a single-bounce diamond prism.

When spectroscopy was performed inside a glove box, ATR-IR measurements were recorded using the external beam of a Varian 680-IR spectrometer coupled to a customised ATR accessory (GladiATR, PIKE Technologies) with a five-bounce silicon prism (Crystal GMBH) and MCT detector liquid nitrogen-cooled to 77 K in a $N_2$-filled glove box (<1 ppm $O_2$, <-85 °C dew point, Glove Box Technology Ltd.). Spectra were recorded at 4 $cm^{-1}$ resolution with an acquisition time of 325 s. Any differences in water vapour were subtracted away using a water vapour spectrum and a reference point away from peaks of interest.

### 2.7.3 Electron paramagnetic resonance (EPR) spectroscopy

All EPR spectroscopy was performed by Dr. Will Myers. Continuous wave (CW)-EPR spectra were collected in the Centre for Advanced Electron Spin Resonance (CAESR). X-band measurements were performed with a Bruker-Biospin EMXplus spectrometer equipped with a PremiumX microwave bridge, a cylindrical TE011 mode resonator (SHQE-W), an ESR-900 cryostat operating with liquid nitrogen, and an ITC-503s temperature controller (Oxford Instruments). EPR simulations were performed with matrix diagonalisation, using the EasySpin routines (Stoll and Schweiger, 2006). Spin quantitation was obtained by double integration and comparison to a 1 mM Cu(II)EDTA standard.

# Chapter 3: Specificity and promiscuity in a substrate-carrier protein/enzyme system from the sulfur cycle

## 3.1 Introduction and aims

### 3.1.1 Substrate carrier-proteins

Sometimes intermediates in metabolic pathways are covalently attached to a carrier protein to enhance their solubility, raise their local concentration, alter their reactivity or prevent side-reactions. The intermediate is usually attached to the carrier protein by a long flexible protein or cofactor arm which can enter the active sites of the various partner enzymes in the metabolic pathway (Perham, 2000). In some cases all the enzymes and the carrier protein are part of the same permanent complex, such as the Type I Fatty Acid Synthase complex (Maier et al., 2008), biotin carboxylases (Tong, 2013) and the mitochondrial α-keto acid dehydrogenases (Perham, 2000). The loosely tethered substrate-carrier protein is expected to swing between the various enzymatic domains or subunits (Gipson et al., 2010). In other systems, the enzymes form no single stable complex and the substrate-carrier is not tethered to the other components of the pathways, such as type II fatty acid synthesis and polyketide synthesis. Here, the substrate-carrier protein transiently interacts with each enzyme in turn. Much work has focused on the role of the carrier protein beyond simply carrying the substrate (Crosby and Crump, 2012; Masoudi et al., 2014), particularly the mechanism of substrate protection and release to each enzyme (Nguyen et al., 2014), the way the substrate can be directed to the next enzyme module in an assembly line mechanism (Frueh et al., 2008) and the ability of the carrier protein to control the reactivity of the substrate (Cryle and Schlichting, 2008).

Substrate carrier proteins are also often used in sulfur metabolism pathways. In these cases, carrier proteins often act as sulfur shuttles (Mueller, 2006; Leimkühler et al., 2011), storing sulfur in the form of either cysteine persulfide or thiocarboxylated cysteine persulfide, so it can be transferred to or removed from the substrate. In these cases the carrier protein also has an active role in directing the stored sulfur into the correct enzyme active site (Sasaki et al., 2014). A similar situation is seen in the Dsr pathway in sulfate reducing bacteria and some sulfur oxidising bacteria (see Chapter 1.2.3), where DsrC carries sulfur as a persulfide (Venceslau et al., 2014).

### 3.1.2 SoxB and SoxYZ

The Sox system (Section 1.2.5) is a carrier protein system involved in sulfur metabolism. However, the carrier protein, SoxYZ, does not simply transfer sulfur, but carries distinct intermediates between enzymes similarly to the non-sulfur carrier protein systems discussed above. Intermediates are attached to SoxY via a cysteine which is the penultimate residue of the flexible C-terminal carrier arm (Sauvé et al., 2007). The structures of SoxB, SoxCD and SoxAX have all been solved (Bamford et al., 2002; Sauvé et al., 2009; Zander et al., 2011), and show a wide channel able to accommodate this carrier arm. The reaction mechanisms of individual Sox enzymes have not been studied in depth, largely due to difficulties with observing enzymatic activity for isolated Sox enzymes. The simplest reaction is catalysed by the putative thiosulfohydrolase SoxB. A mechanism for this reaction has been proposed based on crystal structures of *T. thermophilus* SoxB bound to the substrate analogue, thiosulfate, and product, sulfate, as well as homology to 5' nucleotidases (Figure 3.1) (Sauvé et al., 2009). The carrier protein, SoxYZ, was assumed to have a passive role in this reaction. Sauvé and co-workers developed an assay using *T. thermophilus* SoxB and its putative substrate cysteine-S-thiosulfonated SoxYZ. They showed that incubation of the substrate with SoxB resulted in the inability to detect the substrate by ESI-MS. However, no product could then be detected by ESI-MS. Previously, Friedrich and co-workers had shown that *P. pantotrophus* SoxB can exchange disulfides with SoxYZ (Quentmeier et al., 2003), but the relevance of this study is unclear in light of evidence that disulfide-linked SoxYZ is inactive (Quentmeier et al., 2008) and that the SoxZ cysteine which was involved is buried in the SoxYZ complex (Sauvé et al., 2007) and would only be exposed when the protein is unfolded in SDS.

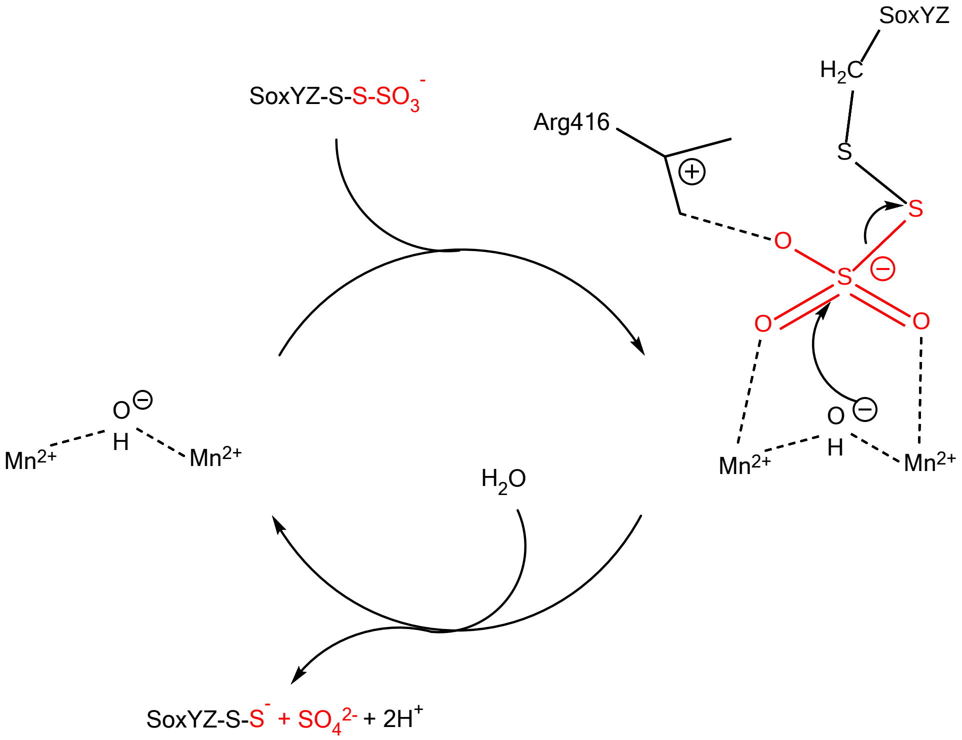

**Figure 3.1 – Simplified possible mechanism of SoxB (Sauvé et al., 2009)**. SoxB Arg416 and SoxY Cys151 are shown and refer to residue numbering from *T. thermophilus*.

### 3.1.3 Aims of chapter

Carrier protein systems are a biotechnologically interesting and useful way to carefully regulate and direct metabolic pathways in a module based design. We wanted to use the relatively simple Sox system to gain detailed insight into how carrier protein systems can function. It is likely that SoxB evolved from 5' nucleotidases, which work on small-molecule substrates (Knofel and Strater, 1999), to work on a carrier protein substrate. Therefore, by understanding how SoxB hydrolyses its physiological substrate-carrier protein-attached substrate, we can begin to understand what adaptations are required to overcome issues associated with having a carrier protein substrate. This information could help the design of modules in synthetic carrier protein systems.

## 3.2 SoxB has thiosulfohydrolase activity

To understand the enzymology of SoxB a quantitative enzyme assay is needed. Attempts to assay hydrolysis of the physiological SoxYZ-conjugated substrate proved unsuccessful. The ESI-MS assay used previously by our group (Sauvé et al., 2009) could not be reproduced. We next used infrared (IR) spectroscopy to detect the SoxB-catalysed removal of the terminal sulfonate of cysteine-S-thiosulfonated *T. thermophilus* SoxYZ. Cysteine-S-thiosulfonate has characteristic IR absorptions with a broad peak at 1220 cm$^{-1}$ and a sharp peak at 1032 cm$^{-1}$ (Church and Evans, 2008). Unmodified SoxYZ and SoxYZ-cysteine-S-thiosulfonate ('SoxY($SSO_3$)Z') were prepared and dialysed into the same buffer, and then both concentrated to 0.47 mM. Both buffer and amide absorb in the region of interest (Figure 3.2A), so care was taken to prevent differences in buffer and protein concentration. A difference spectrum of SoxY(SSO3)Z minus unmodified SoxYZ shows the characteristic peaks at 1220 cm$^{-1}$ and 1020 cm$^{-1}$ (Figure 3.2B black line). These are at different positions to the sulfonate bands arising from HEPES buffer (Figure 3.2A). There is a small increase in the amide peaks due to unavoidable minor error in protein concentration determination, but subtraction of the spectrum of SoxYZ from the spectrum of the SoxY($SSO_3$)Z difference spectrum shows that these amide peaks do not significantly affect the region of interest (Figure 3.2B red line). Incubation of 650 $\mu$M SoxY($SSO_3$)Z with 2 $\mu$M SoxB for 120 minutes at 70°C (the growth temperature of *T. thermophilus*) did not result in any changes in these bands (Figure 3.2C). The expected product of this reaction, sulfate, has a single broad peak at 1121 cm$^{-1}$. The only new peak is at 1045 cm$^{-1}$, and this can be assigned to an increase in buffer concentration due to sample evaporation. Note that the buffer peaks (Figure 3.2A) are much larger than the cysteine-S-thiosulfonate peaks (Figure 3.2B), so the actual change in concentration is approximately 3% and would not be noticed for the cysteine-S-thiosulfonate peaks. Thus, SoxB appears not to catalyse significant conversion of SoxY($SSO_3$)Z to unmodified SoxYZ and sulfate under these conditions.

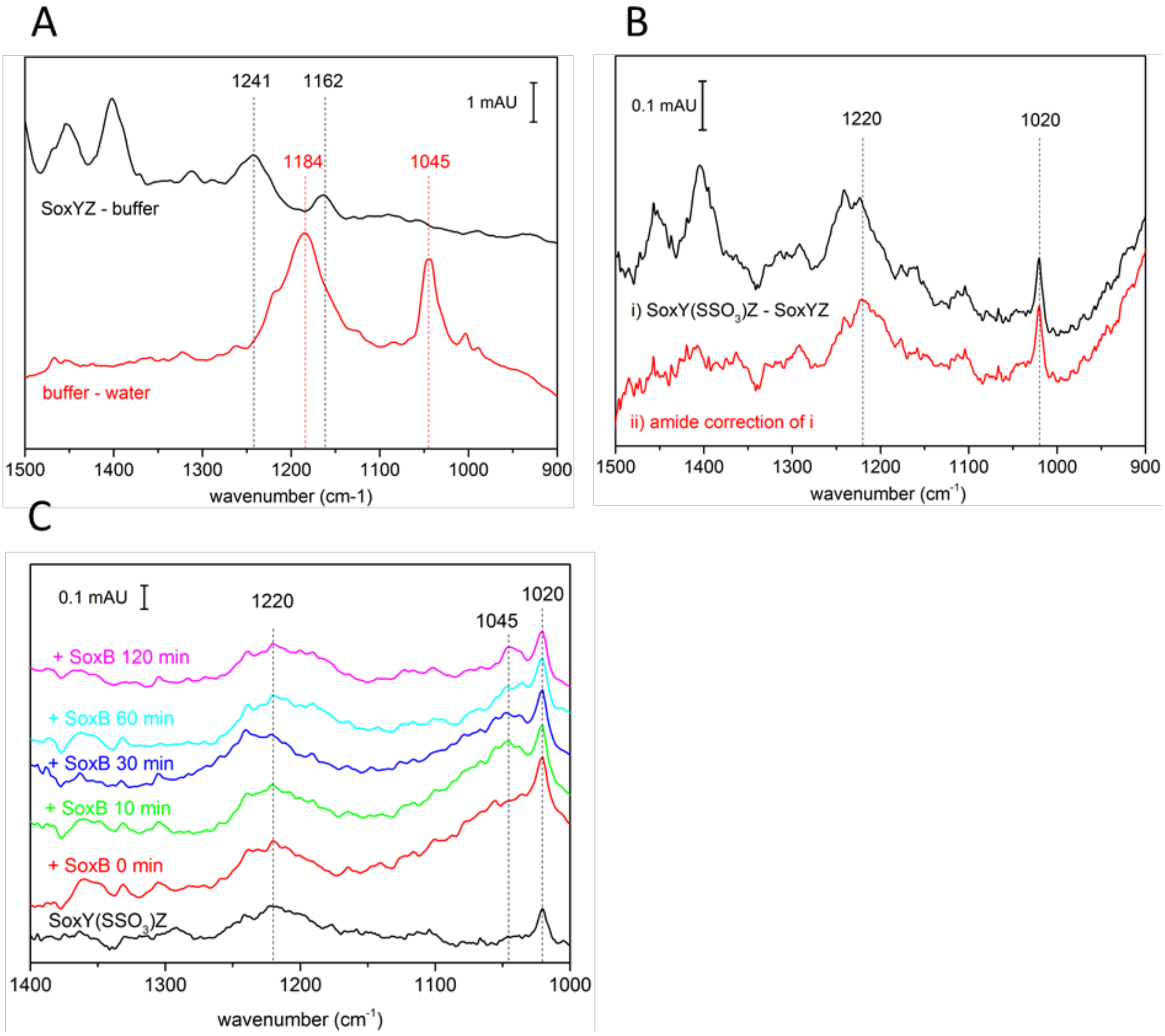

**Figure 3.2 – IR spectroscopy of SoxY(SSO$_3$)Z.** All spectra were recorded using the diamond ATR setup described in Sections 2.7.2 and 5.3.4 and (A) Spectra of buffer (15 mM HEPES-NaOH 150 mM NaCl pH 7.5) and SoxYZ (0.47 mM) show that HEPES and amide features overlap with the region of interest. (B) The black spectrum shows the difference spectrum of SoxY(SSO$_3$)Z minus unmodified SoxYZ. Dialysis removed buffer differences, but it is impossible to measure protein concentration accurately enough to remove all amide differences. Subtraction of the unmodified SoxYZ spectrum (from panel A) using the bands outside of the region of interest as guides results in the red spectrum. (C) The black spectrum is identical to the red spectrum in panel B. The other spectra show SoxY(SSO$_3$)Z incubated with SoxB for the times indicated at 70$^{o}$C in a PCR machine to prevent evaporation before loading on the diamond ATR prism. Increases at 1045 and 1162 cm$^{-1}$ result from an increase in buffer concentration due to evaporation. All spectra have the same correction as the spectrum of SoxY(SSO$_3$)Z shown in black.

We also attempted to use native PAGE, free thiolate and persulfide determination and kinetic mode ITC and these all showed no SoxB activity. Like SoxAX (see Section 4.1.2), it appears that

SoxB is unable to catalyse its proposed physiological reaction without the presence of the other Sox components, SoxAX and SoxCD. However, we plan to perform similar experiments with *P. pantotrophus* SoxB and SoxYZ, which we know are active in the reconstituted Sox system assay. *T. thermophilus* SoxCD and SoxAX have never been isolated so we cannot reconstitute the *T. thermophilus* Sox system and therefore cannot demonstrate that this system is functional.

We next explored whether the predicted thiosulfohydrolase activity of SoxB (Equation 3.1) could be detected using trithionate ($^{-}O_3S\text{-}S\text{-}SO_3^{-}$) as a small molecule analogue of the physiological SoxY conjugate (Equation 3.2). The products of trithionate hydrolysis are unreactive and thus readily analysed.

$$\text{SoxY-S-}\mathbf{S\text{-}SO_3}^{-} + H_2O \rightarrow \text{SoxY-S-}\mathbf{S}^{-} + \mathbf{SO_4}^{2-} + 2H^{+} \qquad \text{(Equation 3.1)}$$

$$^{-}O_3S\text{-}\mathbf{S\text{-}SO_3}^{-} + H_2O \rightarrow {}^{-}O_3S\text{-}\mathbf{S}^{-} + \mathbf{SO_4}^{2-} + 2H^{+} \qquad \text{(Equation 3.2)}$$

SoxB was able to catalyse the stoichiometric conversion of trithionate to thiosulfate and sulfate (Figure 3.3). SoxB is a member of the metallophosphatase superfamily and contains a pair of Mn(II) ions at the active site (Sauvé et al., 2009). Trithionate hydrolase activity decreased in the presence of the metal chelator EDTA but was increased when the assay mix was supplemented with $Mn^{2+}$ or $Zn^{2+}$ ions. This behaviour is consistent with the SoxB active site metal ions being involved in catalysing the reaction. Trithonate hydrolase activity followed Michaelis-Menten kinetics with a $K_M$ of 2.20±0.15 mM (95% confidence limit, n=3), and a $k_{cat}$ of 2±0.1 $s^{-1}$ (SEM, highest activity preparation).

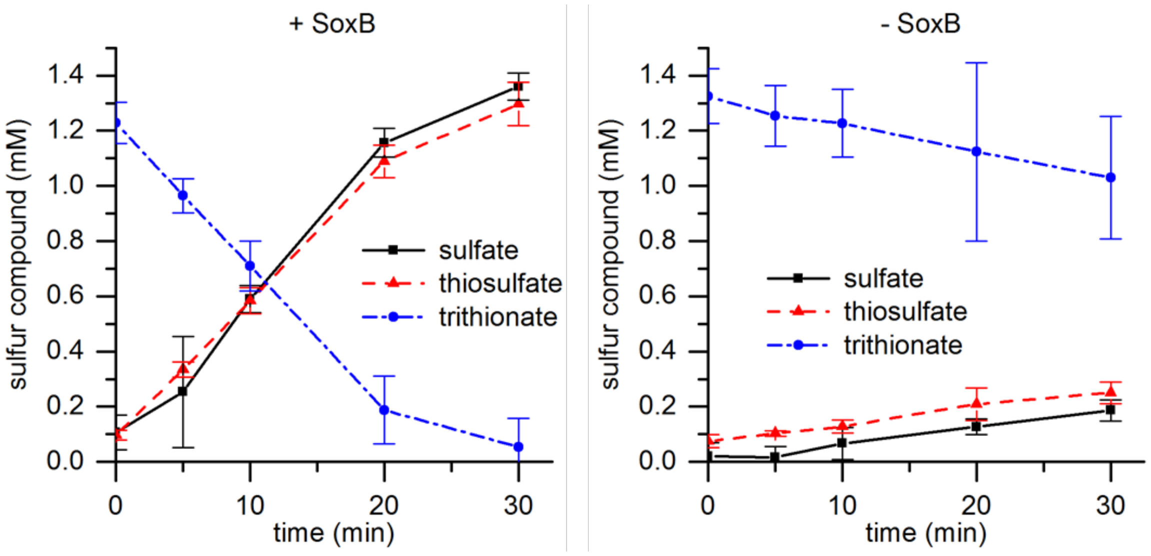

**Figure 3.3 – *T. thermophilus* SoxB possesses trithionate hydrolase activity**. Reactions were carried out at 70°C and contained 1.3 mM trithionate, 10 mM HEPES-NaOH pH 6.8, 1 mM $MnCl_2$. Non-enzymatic hydrolysis is shown in the left panel, while hydrolysis in the presence of 0.5 $\mu$M SoxB is shown in the right panel. Error bars show confidence limits ($p = 0.05$) from 3 experiments.

A previously-determined crystal structure of SoxB in complex with the non-hydrolysable substrate analogue thiosulfate suggests that active site residue Arg416 is involved in substrate binding and transition-state stabilisation (Sauvé et al., 2009). In agreement with this hypothesis we found that an Arg416Gly variant had undetectable trithionate hydrolase activity.

## 3.3 Protein-protein interactions between SoxB and SoxYZ

SoxB exhibits a millimolar $K_M$ for the substrate analogue trithionate (above). By contrast, the reconstituted Sox system of *P. pantotrophus* has a low micromolar $K_M$ for the SoxYZ protein to which the physiological SoxB substrate is bound (Welte et al., 2009). This three order of magnitude difference in Michaelis constants suggests that protein-protein interactions between SoxYZ and SoxB increase the affinity of SoxB for its substrate. We investigated this idea by directly analysing the interactions between the two proteins. In these experiments we used a SoxYZ variant in which the carrier arm cysteine residue had been substituted with a serine

(SoxY$_{C151S}$Z). This variant allowed us to assess the protein-protein interactions between SoxB and SoxYZ independent of the contribution from the substrate-binding residue on the carrier protein.

Complex formation between SoxB and SoxY$_{C151S}$Z was observed at room temperature by both native PAGE (Figure 3.2A) and size-exclusion chromatography in-line with multi-angle light scattering (SEC-MALS) (Figure 3.2B). The absolute molecular mass of the complex determined by MALS was concentration dependent such that even at the highest protein concentration tested (40 μM of each protein) the measured mass of 68 kDa was lower than the 90 kDa mass calculated for a 1:1 SoxB:SoxYZ complex. This behaviour indicates that the complex is unstable and partially dissociates during chromatography.

Isothermal titration calorimetry (ITC) was used to quantify the interaction between SoxB and SoxY$_{C151S}$Z. The binding isotherm was well fit by a simple 1:1 association model with a $K_D$ of 3 μM (Figure 3.3A). To determine the contribution that the SoxYZ-bound substrate makes to the interaction between SoxB and SoxYZ the ITC experiment was repeated using SoxY(SSO$_3$)Z (Figure 3.3B). Addition of the thiosulfonate group made no significant difference to the affinity of SoxB for SoxYZ (compare Figures 3.3A and B) confirming the dominant contribution of protein-protein interactions to the affinity of complex formation between the two proteins. However, there was a large difference in the $\Delta H$ of the interaction, changing from exothermic (-3 kcal/mol) for SoxY$_{C151S}$Z to endothermic for SoxY(SSO$_3$)Z (+10 kcal/mol). This enthalpy change was balanced by a change in T$\Delta S$ from -5.2 kcal/mol to -17.4 kcal/mol. These observations suggest that conjugation of substrate to SoxYZ alters the mechanism of interaction with SoxB.

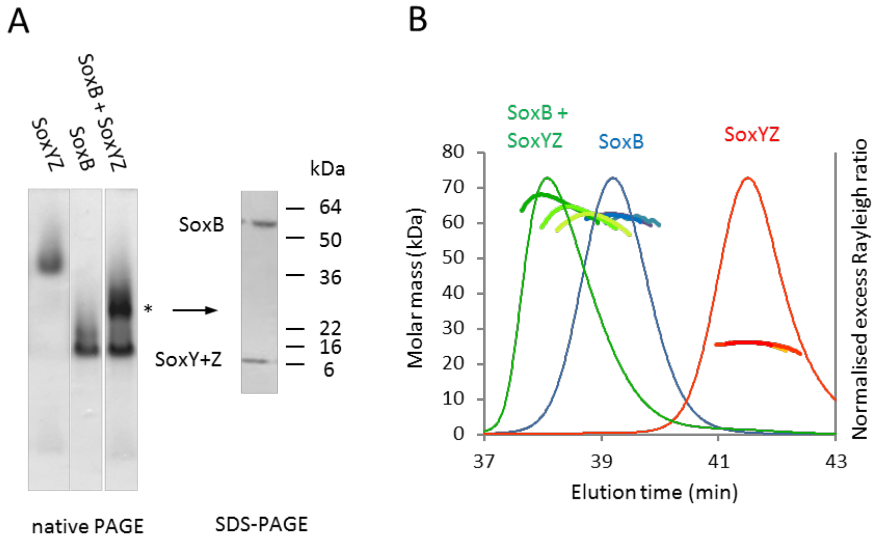

**Figure 3.4 – SoxYZ forms a weak complex with SoxB.** (A) Comparative native PAGE analysis of SoxY$_{C151S}$Z, SoxB, or a mixture of the two proteins (left). Each sample analysed contained 10 µM (per component) protein. A major band present only in the mixed sample is indicated with *. The polypeptide composition of this band was determined by excising the band, dehydrating the gel slice in acetonitrile followed by boiling in SDS-containing buffer and analysis on an SDS-PAGE gel (right). Note that *T. thermophilus* SoxY and SoxZ have identical electrophoretic mobilities in SDS-PAGE. (B) SEC-MALS analysis of SoxY$_{C151S}$Z, SoxB, or mixtures of the two proteins. Measured average molar masses are shown for loading concentrations (per protein component) of 10 µM, 20 µM and 40 µM (thick lines, changing from light to dark as the protein concentration increases). The excess Rayleigh ratio is shown for the 40 µM concentration samples only (thin lines).

To further probe the influence that the group bound to the carrier arm of SoxYZ has on interactions with SoxB we repeated the ITC analysis with SoxYZ conjugated either to an S-carboxymethyl group ('SoxY(Ac)Z') or to its amide derivative ('SoxY(Am)Z'). The carboxymethyl group (-CH$_2$-CO$_2^-$) has physicochemical similarity to S-thiosulfonate. By contrast, amidating this species produces a functional group (-CH$_2$-CONH$_2$) that would be unable to act as a bidentate ligand to the active site manganese ions. SoxY(Ac)Z exhibits an endothermic enthalpy change on interaction with SoxB that is identical to that measured for SoxY(SSO$_3$)Z (Figure 3.3B,C) while SoxY(Am)Z shows an exothermic enthalpy change that is very close to that observed with SoxY$_{C151S}$Z (Figure 3.3A,D). Thus, there is an apparent correlation between the thermodynamic characteristics of the SoxYZ-SoxB interaction and the ability of the SoxY-conjugated group to act as a bidendate ligand to the di-manganese centre.

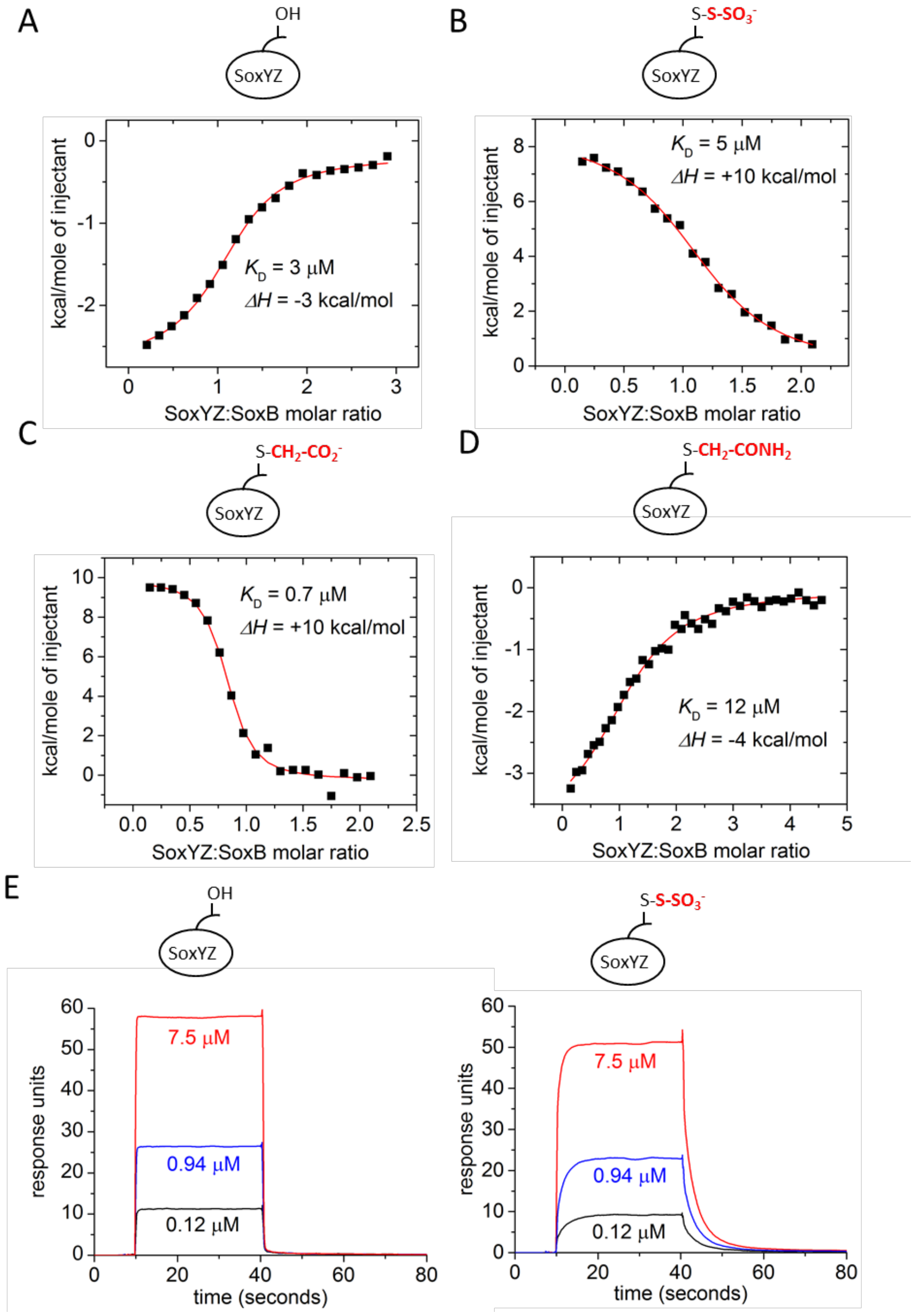

**Figure 3.5 – Biophysical analysis of the interaction between SoxYZ and SoxB.** For ITC experiments, integrated heats from a representative experiment are shown. The fit to the data and corresponding $K_D$ and enthalpy change values are from duplicate experiments. Experiments differ in the derivatisation of the SoxY carrier arm cysteine residue as shown schematically at the top of each panel. (A) SoxY$_{C151S}$Z titrated into 47 µM SoxB. (B) SoxY(SSO$_3$)Z titrated into 50 µM SoxB. (C) SoxY(Ac)Z titrated into 50 µM SoxB. (D) SoxY(Am)Z titrated into 58 µM SoxB. (E) Representative surface plasmon resonance sensograms showing the kinetics of the association and dissociation of SoxY$_{C151S}$Z (left panel) or SoxY(SSO$_3$)Z (right panel) to a SoxB-coated sensor chip. The concentrations of injected SoxYZ samples are indicated.

The similar affinity of SoxB for its putative substrate, SoxY($SSO_3$)Z, and product analogue, SoxY$_{C151S}$Z, was unexpected and raised the question of how SoxB avoids strong product inhibition. We investigated the possibility of kinetic discrimination between substrate and product using surface plasmon resonance (SPR). Equilibrium SPR experiments measured dissociation constants of 2.4 µM for the SoxB-SoxY($SSO_3$)Z substrate complex and 2.7 µM for the SoxB-SoxY$_{C151S}$Z product complex (Figure 3.4). These are close to the values of 5 µM and 3 µM determined for the same complexes by ITC showing that the SPR technique reproduces the binding interactions seen in solution.

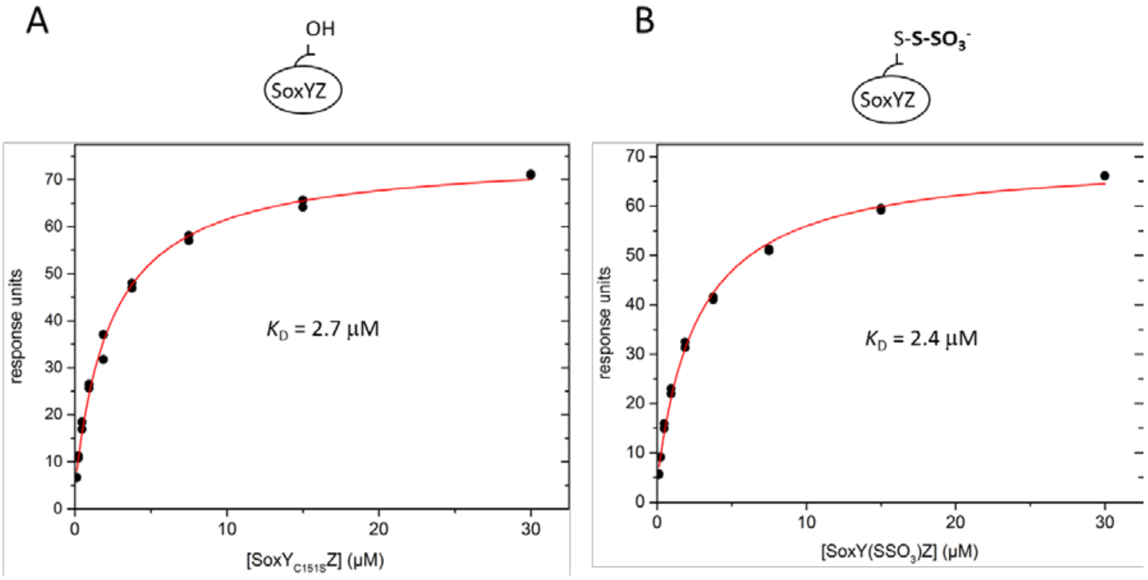

**Figure 3.6 – Affinities of SoxB-SoxYZ interactions determined by equilibrium SPR.** (A) The SoxY$_{C151S}$Z variant was used. (B) The SoxY($SSO_3$)Z adduct was used

Binding of the product analogue SoxY$_{C151S}$Z to SoxB was extremely rapid with association and dissociation complete within 0.5 seconds at all concentrations (Fig 3.5E, left panel). By contrast, the kinetics of both association and dissociation between SoxB and the putative substrate, SoxY($SSO_3$)Z were markedly slower with association and dissociation now occurring over ten seconds (Figure 3.5E, right panel). The same behaviour was seen at multiple SoxB loading densities, suggesting it is not a mass-transfer artefact. The dissociation kinetics for this complex showed a small burst phase (Figure 3.7A). While this burst phase may indicate a two-step dissociation mechanism it more likely corresponds to the rapid dissociation of a small subpopulation of underivatized SoxYZ molecules. For both types of SoxB-SoxYZ complexes the association and dissociation phases were too fast to allow reliable extraction of kinetic parameters using standard multiple parameter fitting methods. However, the dissociation phase kinetics could be fitted using simple exponential decay models giving a rate constant of 5.7 ± 0.8 $s^{-1}$ for dissociation of the SoxB-SoxY$_{C151S}$Z complex (Figure 3.7C,D) and rate constants of 0.34 ± 0.01 $s^{-1}$ and 4.5 ± 0.7 $s^{-1}$, respectively, for the major dissociation phase and minor burst phase of the SoxB-SoxY(SSO$_3$)Z complex (Figure 3.7B). The corresponding association rate constants calculated from the relationship $K_D = k_{off}/k_{on}$ are 1.4 x $10^5$ $M^{-1}$ $s^{-1}$ for the formation of the substrate complex (calculated using the major phase dissociation rate constant) and 2.1 x $10^6$ $s^{-1}$ for formation of the product complex. These figures reinforce the qualitative conclusion that $k_{on}$ and $k_{off}$ are both significantly slower for the interaction involving the putative substrate. Thus SoxB is able to discriminate in favour of the substrate form of SoxYZ because it forms longer-lived complexes with this substrate than it does with the product.

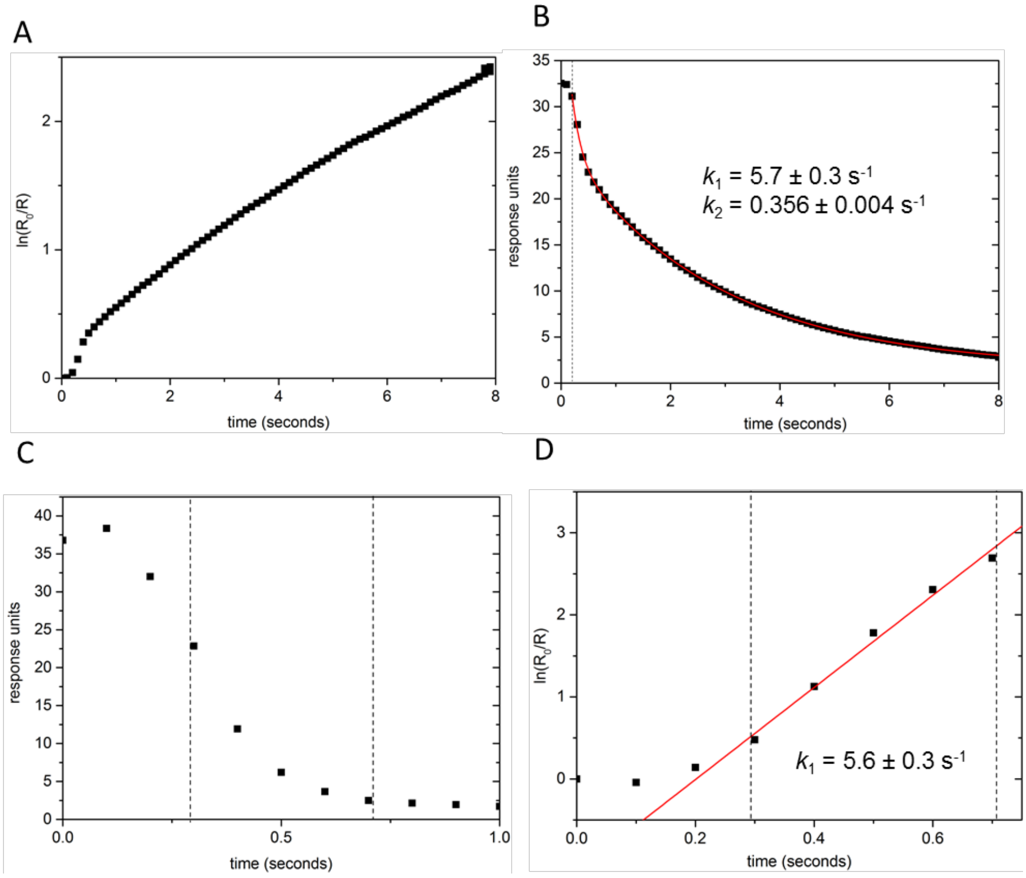

**Figure 3.7 – Representative SoxB-SoxYZ complex dissociation phase data showing the fitting methods used.** Analysis of the SoxB-SoxY(SSO$_3$)Z complex is shown in (A,B) and analysis of the SoxB-SoxY$_{C151S}$Z complex in (C,D). The SoxYZ concentration in both cases was 1.88 µM. (A) A log plot of the dissociation phase for the SoxB-SoxY(SSO$_3$)Z complex shows deviation from linearity indicating biphasic behaviour with a burst phase before 0.5 seconds. The burst phase is associated with the dissociation of a minor proportion of the complexes and most likely arises from a small proportion of underivatized or incorrectly-derivatized SoxYZ in the sample. (B) The data in (A) were fit as a sum of two exponential decay processes using the equation:

$$Y = Y_0 + A_1.e^{k_1(x-x_o)} + A_2.e^{k_2(x-x_o)}$$

Here $k_1$ and $k_2$ represent the kinetic rate constants of each decay, and $A_1$ and $A_2$ the starting amplitude of each decay. The data is unreliable around the injection point. Therefore the fit does not include points on either side of the injection, and the time of injection is floated as the $x_0$ parameter. The $A_1$ and $k_1$ parameters are defined by only a few points and so are heavily influenced by injection artefacts. By contrast, the $k_2$ parameter can be robustly fit across different analyte concentrations and loading densities. The values of the kinetic rate constants given in the main text are the means and 95% confidence intervals of the fitted values at every concentration and their duplicates. The values shown in this figure derive from the fit to the single curve shown here. (C) The dissociation of the SoxB-SoxY$_{C151S}$Z complex is rapid and a significant proportion of the curve is affected by injection artefacts making it difficult to fit the data by non-linear regression fitting. (D) Consequently, a log plot was used to fit the $k_1$ value using only that part of the curve not influenced by the injection noise. The $k_1$ value in the text is the mean with 95% confidence intervals fitted at every concentration for two technical replicates.

## 3.4 Preparation of a disulfide-linked SoxB-SoxYZ complex for crystallography

To identify the specific molecular contacts involved in the interaction between SoxYZ and SoxB it was necessary to determine the structure of the SoxYZ-SoxB complex. This would provide insight into the kinetic specificity and different thermodynamic binding modes discussed in Section 3.3, as well as how SoxYZ could have specific but promiscuous interactions with its partner proteins. Crystallization trials with the purified complex were unsuccessful, most likely due to the relatively low affinity and fast dynamics of the interaction between the components. To overcome this problem we developed a strategy to covalently link the two proteins through formation of a disulfide bond between the cysteine of the SoxY carrier arm and a cysteine residue engineered into the SoxB active site. The rationale behind this approach was that a covalent linkage at the active site would prevent dissociation of the complex but would not interfere with protein-protein interactions outside the active site.

We targeted SoxB active site residue Trp175 for cysteine substitution. Trp175 stabilizes the sulfane group of the substrate analogue thiosulfate in the previously determined SoxB-thiosulfate complex structure (Sauvé et al., 2009) and so was inferred to be close to the carrier arm cysteine sulfur atom in the native SoxYZ-SoxB complex. To provide a leaving group in the disulfide bond-forming reaction and prevent formation of SoxYZ-SoxYZ complexes we used the S-thiosulfonate derivative of the partner SoxYZ protein (Equation 3.3).

$$\text{SoxY-S-S-SO}_3^- + \text{SoxB-SH} \rightarrow \text{SoxY-S-S-SoxB} + {}^-\text{S-SO}_3^- + \text{H}^+ \qquad \text{(Equation 3.3)}$$

Incubation of the SoxB Trp175Cys variant at 70$^{o}$C with the S-thiosulfonate derivative of SoxYZ resulted in a high yield of disulfide-linked SoxYZ-SoxB complexes (Figure 3.8). Mass spectrometry of the crosslinked product before and after incubation with the reductant DTT confirmed the expected disulfide linkage between SoxYZ and SoxB.

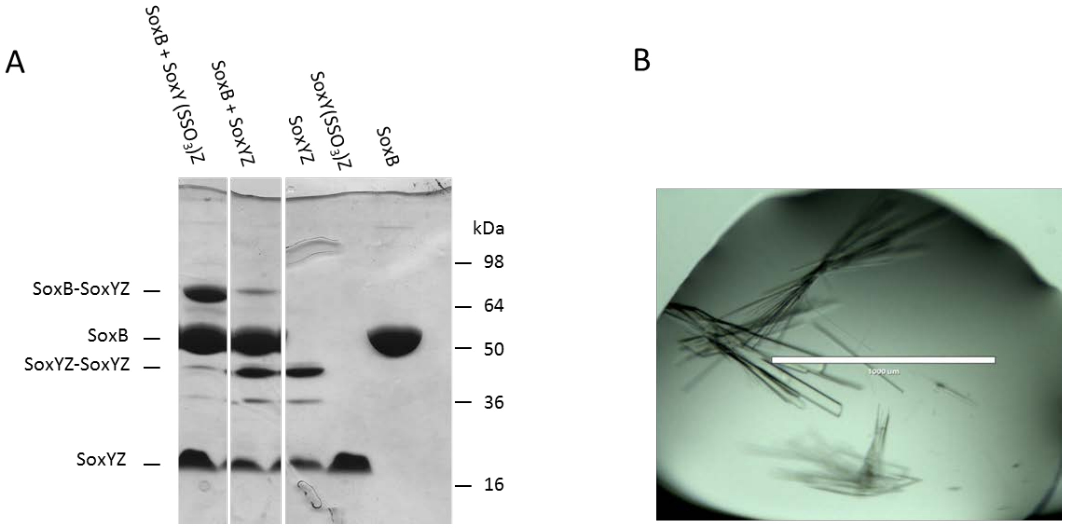

**Figure 3.8 – Disulfide cross-linking of SoxB and SoxYZ for crystallography.** (A) Either 20 µM SoxYZ or SoxY($SSO_3$)Z were incubated with 20 µM $SoxB_{W175C}$ at 70°C for one hour. Cross-linking was visualised using a 12% SDS-PAGE gel without reductant or heating. Under these conditions the native SoxYZ complex does not dissociate. (B) Crystals of the disulfide cross-linked SoxB-SoxYZ complex grown in 100 mM Tris-HCl, 200 mM $(NH_4)_2SO_4$, 8.55% PEG 8000, pH 8.3. The scale bar shows 1 mm.

## 3.5 Structural insight into the SoxB-SoxYZ protein-protein interactions

### 3.5.1 Structure of a disufide-linked SoxB-SoxYZ complex

The cross-linked SoxB-SoxYZ complex was crystallized using the sitting drop vapour-diffusion method. Initial trials resulted only in bunches of needle-shaped crystals. However, after multiple rounds of optimisation, large singular crystals were obtained in a number of conditions. Crystals in space-group $P_1$ obtained using 100 mM Tris-HCl, 200 mM $(NH_4)_2SO_4$, 8.55% PEG 8000, pH 8.3 as mother liquor diffracted to the best resolution of 3.3 Å (Figure 3.8B). The structure of the cross-linked SoxB-SoxYZ complex was solved by Paul Chappell in the group of Susan Lea, using molecular replacement with the non-complexed proteins as models. All four SoxB subunits in the asymmetric unit were well ordered and displayed interpretable electron density. By contrast, the SoxY and SoxZ subunits exhibited high B-factors and more ambiguous electron density in all but one copy of the complex. Nevertheless, all copies of the complex showed the same overall structure (Figure 3.9A).

**Table 3.1 – SoxB-SoxYZ X-ray data collection statistics**

| | |
|---|---|
| X-ray source | Diamond - i04 (0.99990 Å) |
| Space group | P1 |
| Cell dimensions | *a* = 70.2 Å, *b* = 116.0 Å, *c* = 120.9 Å<br>α = 86.51°, β = 83.21°, γ = 89.77° |
| Resolution (Å) | 59.81-3.28 (3.37-3.28) |
| Total reflections | 112492 |
| Number of unique reflections | 57115 |
| Completeness (%) | 98.7 (98.4) |
| Multiplicity | 2.0 |
| $R_{merge}$ | 0.088 (0.302) |
| I / δ (I) | 7.9 (1.9) |
| **Refinement statistics** | |
| R (%) | 26.96 (27.76) |
| $R_{free}$ (%) | 27.47 (30.04) |
| **Root mean square deviation from idealized covalent geometry** | |
| Bond length (Å) | 0.007 |
| Bond angles (°) | 0.84 |
| Average B value ($Å^2$) | 92.77 |
| Ramachandran outliers (%) | 0.24 |
| Residues modelled | 2952 |
| Non-protein molecules | 11 waters, 8 $Mn^{2+}$ (100% occupancy) |
| Molprobity score | 1.48 |

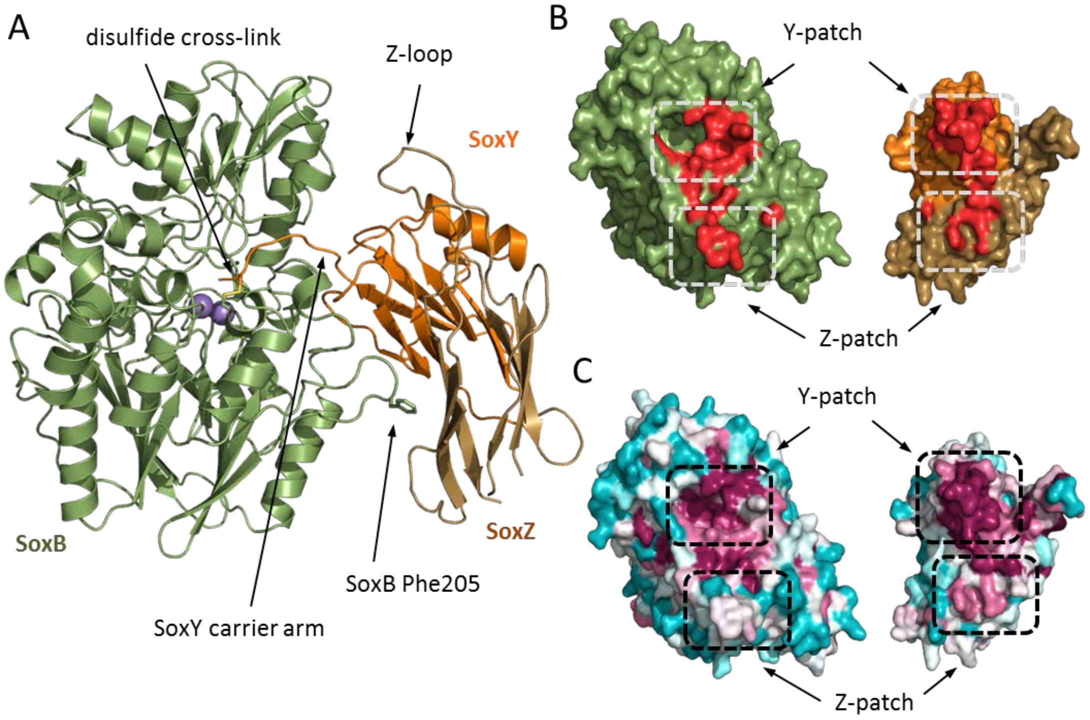

**Figure 3.9** – **Structure of a disulfide-linked SoxYZ-SoxB complex.** (A) Overall structure of the complex with proteins in cartoon representation and the manganese ions shown as purple spheres. Stick representation is used to show the disulfide bond between the SoxY carrier arm cysteine and SoxB Cys175, and for SoxB residue Phe205 that contributes to the Z-patch. SoxB is coloured green, SoxY orange, and SoxZ brown. (B) Surface representation of the interacting faces of the SoxB and SoxYZ proteins coloured as in (A). The interacting surfaces are shown in red. (C) The same views of the SoxB and SoxYZ proteins as in (B) but with the surface coloured according to sequence conservation using the program Consurf (Celniker et al., 2013). Magenta indicates areas of highest sequence conservation and cyan the most variable sequences. Note that the Z-patch conservation in SoxB and SoxYZ is probably under reported due to alignment difficulties caused by insertions and deletions in adjacent sequences in the proteins from Purple Sulfur Bacteria and Green Sulfur Bacteria.

The interface between SoxYZ and SoxB buries a surface area of 1220 Å$^2$ (Figure 3.9B). The relatively small size of this interface is consistent with the low stability of the complex (Lange and Hunte, 2002). The binding interface shows two main sites of interaction (Figure 3.9B). One site involves an interaction between the base of the SoxY carrier arm, as well as the arm itself, with the area around the active site channel of SoxB. This we term the ‘Y-patch’. The other area, which we term the ‘Z-patch’, involves contacts between a SoxB surface loop and the face of a β-sheet in SoxZ. These interaction surfaces contain most of the conserved surface residues of both proteins (Figure 3.9C).

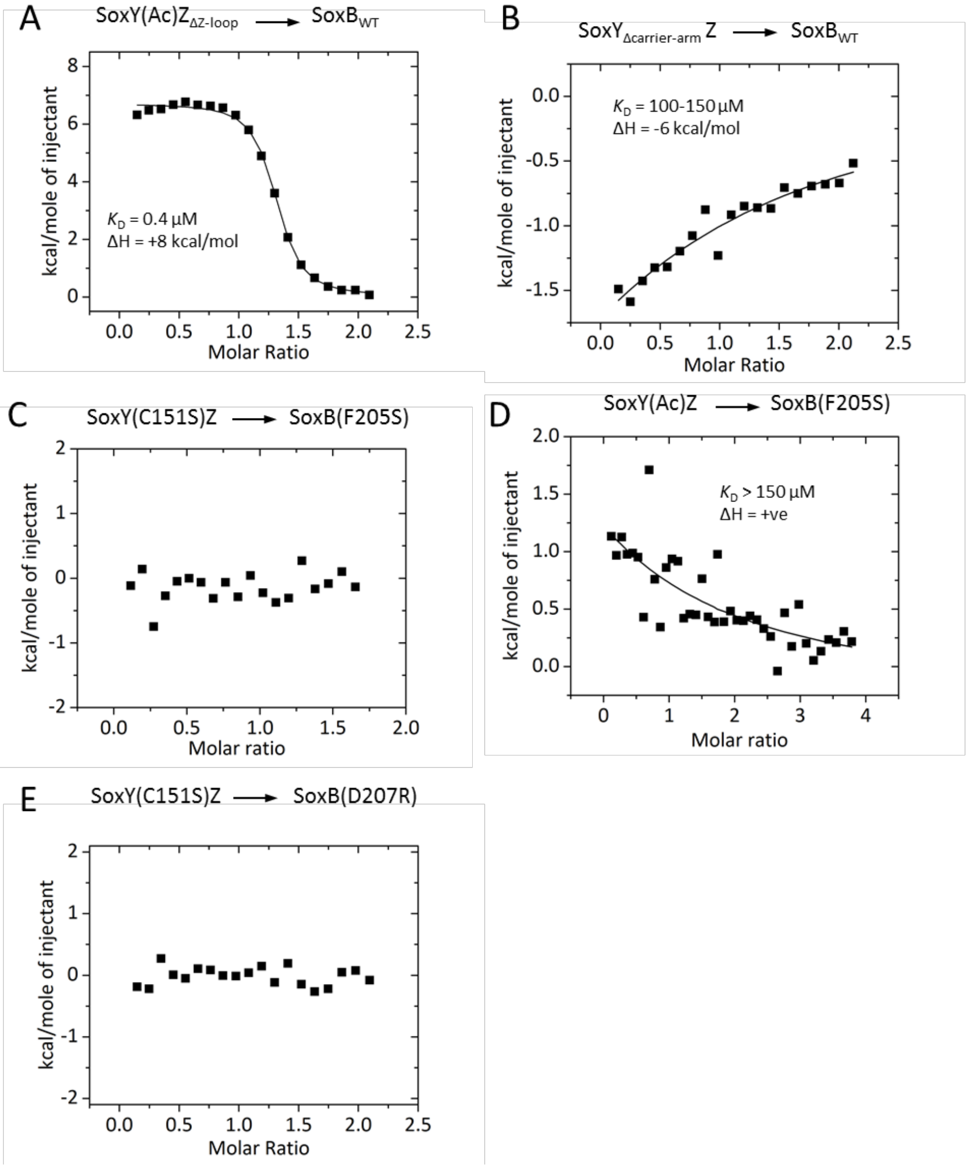

**Figure 3.10 – ITC titrations of SoxB and SoxYZ variants with manipulation of residues involved in complex formation.** The ITC titrations that were performed are shown above each panel. Figures show a representative integrated titration, whilst values are derived from simultaneously fitting duplicate titrations. Each variant is described in the main text. (C-E) are SoxB variants with mutations in the Z-patch.

SoxZ contains a large polypeptide loop (the ‘Z-loop’) that was previously predicted to be involved in interactions with SoxYZ partner proteins (Sauvé et al., 2007). However, in the SoxYZ-

SoxB complex structure the Z-loop is positioned well away from SoxB and does not participate in inter-protein contacts (Fig 3.9A). There was no decrease in the affinity of SoxYZ for SoxB when the Z-loop was deleted (Figure 3.10A) in agreement with the structural data that the Z-loop is not involved in this interaction.

### 3.5.2 Interactions between SoxZ and SoxB

The Z-patch on SoxZ is formed from the outward facing side chains of strands β1, β2 and β5. A hydrophobic pocket is formed by Ile6, Val25, and Leu74 (Figure 3.11A). Two arginine residues, SoxZ Arg8 and SoxY Arg117, are positioned at the edge of the pocket and the non-polar portion of their side chains contribute to the hydrophobicity of the pocket. The interacting surface on SoxB is formed from a surface loop with the sequence $^{202}$DDLFGD$^{207}$. This loop creates a hydrophobic bulge surrounded by negatively charged residues that is complementary to the structure of the Z-patch on SoxZ. The non-polar SoxB residues Leu204 and Phe205 insert into the hydrophobic pocket of the SoxZ Z-patch while SoxB Asp207 forms a salt-bridge with SoxZ Arg8 (Figure 3.11A). It is conceivable that the other charged residues at the interface could form alternative salt bridges if there is some plasticity in the SoxYZ-SoxB interaction or could provide long range electrostatic interactions to aid docking as the interacting sites have opposite charges (Figure 3.11B). The importance of long range electrostatic interactions is well-established in the case of the interactions of cytochrome *c* with its partners (Koh et al., 2003). The salt bridge and the presence of an aromatic residue at position 205 in SoxB are conserved in SoxB and SoxZ proteins from the distantly related model organism *P. pantotrophus*, as expected if these interactions are of biological relevance (Figure 3.11C). Additionally, the basic electrostatic potential of the Z-patch is conserved in the structure of SoxYZ from *P. pantotrophus* (Figure 3.11B).

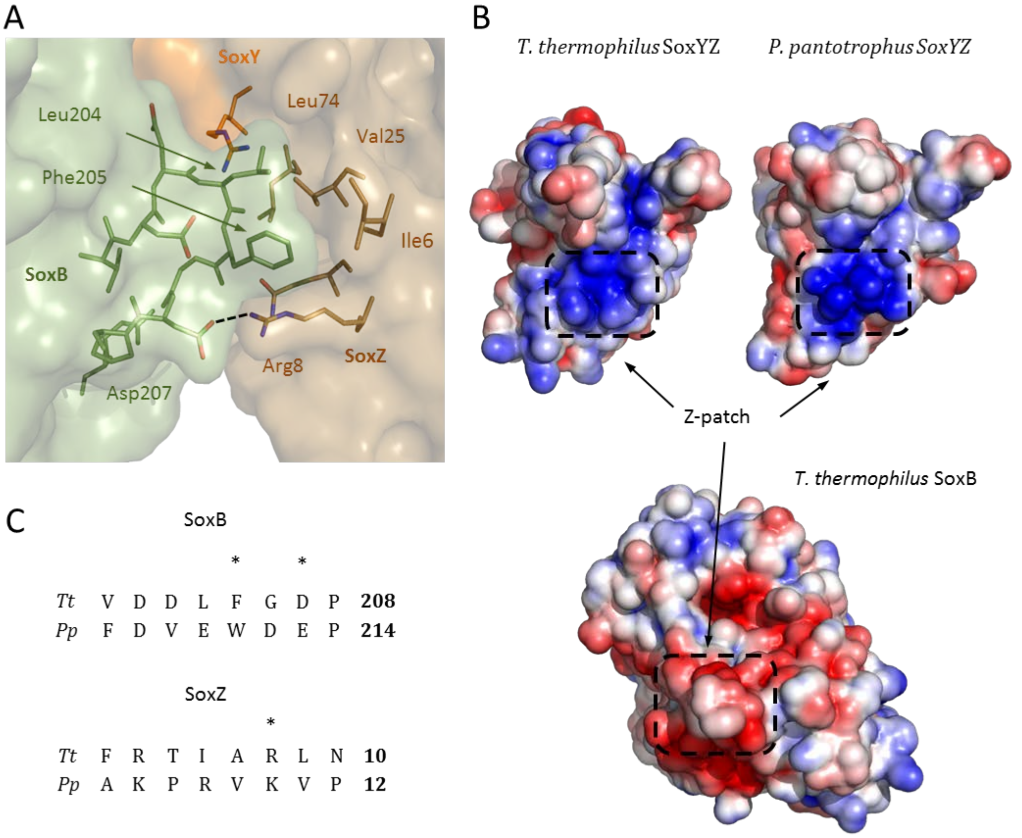

**Figure 3.11 – The SoxZ-SoxB interface.** (A) Molecular details of the SoxZ-SoxB interface. The SoxB surface is coloured green, the SoxY surface orange, and the SoxZ surface brown. Residues involved in the interaction are shown in stick representation with the carbon atoms given the same colours as the subunit to which they belong. (B) The surface potentials around the Z-patch in the SoxYZ proteins of *T. thermophilus* (from the SoxB-SoxYZ complex) and *P. pantotrophus* (2OX5), and around the Z-patch of *T. thermophilus* SoxB. The surface potential was calculated using Adaptive Poisson-Boltzmann Solver (Baker et al., 2001). (C) Sequence comparisons for the Z-patch loop in SoxB and the Z-patch region in SoxZ for proteins from different sulfur-oxidising organisms. Residues directly involved in interactions are highlighted by asterisks above the alignment. Alignments were generated using ClustalX2. Tt – *T. thermophilus* HB27, Pp – *P. pantotrophus* GB17

To validate the Z-patch interaction seen in the crystal structure we designed SoxB variants that would disrupt the interface and then assessed their interaction with SoxYZ by ITC. Correct folding of the SoxB variants was verified by measuring their trithionate hydrolase activity using the barium sulfate assay. For all variants described, apart from Arg416Gly, the activity was indistinguishable from the wild-type within the error of the experiment (data not shown). Either a Phe205 to Ser substitution or an Asp207 to arginine substitution abolished binding to SoxY$_{C151S}$Z (Figure 3.10C,E). Binding of SoxB$_{F205S}$ to SoxY(Ac)Z was also abolished (Figure 3.10D) suggesting that SoxYZ binds via the Z-patch irrespective of the species conjugated to the carrier arm.

### 3.5.3 Interaction between SoxY and the SoxB substrate channel

The structure of *T. thermophilus* SoxYZ in the SoxYZ-SoxB complex can be compared with that of isolated *P. pantotrophus* SoxYZ (Figure 3.12A). This comparison suggests that the only significant structural change in the protein on complex formation is that the SoxY carrier arm moves from a pocket formed between SoxY and SoxZ to the SoxB active site channel where the reactive cysteine is disulfide-bonded with the engineered Cys175 of SoxB (Figure 3.12B). The C-terminal carboxylate of the SoxY polypeptide lies at the end of the carrier arm and co-ordinates the active site manganese ions in a similar way to the sulfonate group of the substrate analogue thiosulfate (Sauvé et al., 2009). The SoxB active site channel is relatively large compared to the SoxY carrier arm, which runs along one side of the channel leaving the other side largely empty (Figure 3.12B). There are two small pockets on the side of the channel where the swinging arm rests (Figure 3.12B).

The SoxB channel accommodates the C-terminal $^{147}$TVGGCG-COO$^{-}$ portion of the SoxY carrier arm. SoxY residues Arg145, Ser143, and the loop comprising residues $^{66}$AIAES$^{70}$ contact the surface of SoxB around the mouth of the active site channel (Figure 3.12C). Residues Ala66 and Ile67 rest in a pocket formed by SoxB residues Tyr232, Val235, Asn463, Tyr471 and Gln473, together with SoxY Thr147 (Figure 3.12C). Apart from this pocket, and the manganese coordination, the interaction surface between SoxY and SoxB is formed by a sparse hydrogen bonding network involving six direct interactions (Figure 3.12C). Additional hydrogen bonding interactions are probably mediated by waters not seen at this resolution. Removing the C-terminal carrier arm from SoxY increased the $K_D$ of the SoxB-SoxYZ interaction 50-fold (Figure

3.10B) showing that contacts involving the carrier arm contacts are important for association with SoxB in spite of the small number of interactions involved.

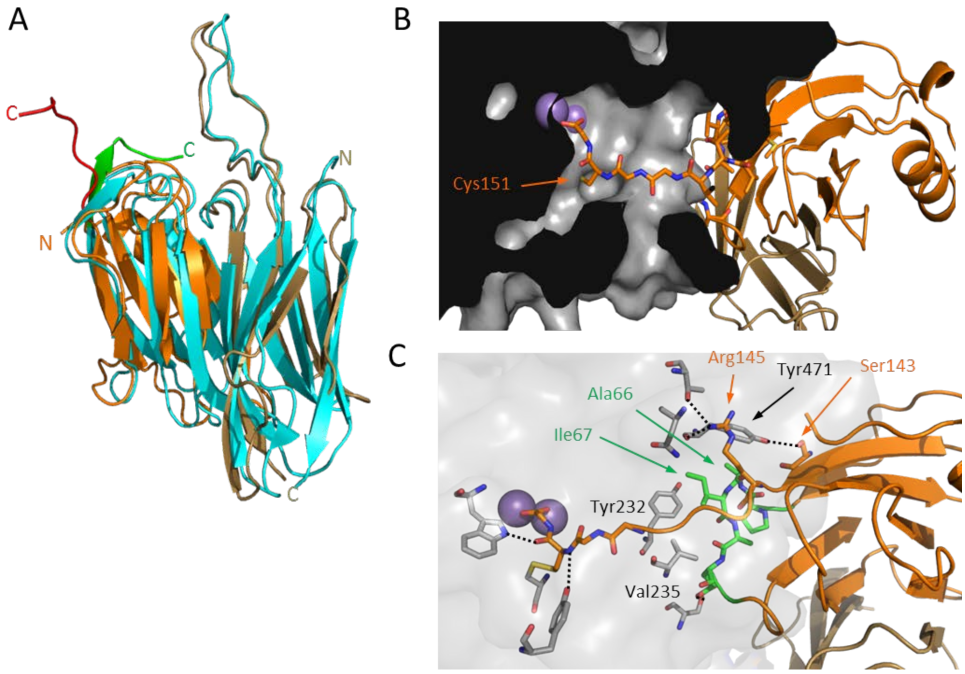

**Figure 3.12 – The SoxY-SoxB interface.** (A) Backbone alignment of *T. thermophilus* SoxYZ from the SoxYZ-SoxB complex (SoxY orange; SoxZ brown; carrier arm red) with P. pantotrophus SoxYZ (PDB: 2OX5; cyan, SoxY carrier arm in green). The N and C-termini of SoxY and SoxZ are marked. (B) Position of the SoxY carrier arm within the SoxB active site channel. SoxY (orange) and SoxZ (brown) are shown in ribbon representation with the carrier arm in sticks representation. SoxB is shown as a section through a space-filling model. The manganese atoms are shown as purple spheres. (C) Molecular details of the interactions between SoxY and SoxB with relevant residues shown in stick representation and the manganese atoms as purple spheres. The SoxY $^{65}$PAIAES$^{70}$ loop is highlighted in green.

### 3.5.4 Conformational changes in the SoxB mobile loop

Previous structural work (Sauvé et al., 2009) has shown that binding of the substrate analogue thiosulfate to SoxB is associated with widening of the active site channel through movement of a loop (residues 463 to 478) containing the highly conserved $^{472}$QQGGD$^{476}$ motif (Figure 3.13A). This conformational change is mediated through mobile loop residue Asp476. In the unliganded SoxB structure the side chain of Asp476 forms a salt bridge with the catalytically important residue Arg416, anchoring the mobile loop close to the active site (Figure 3.13B, left hand panel). However, in the thiosulfate complex Arg416 co-ordinates the sulfonate part of thiosulfate in preference to Asp476 which, in turn, now forms a salt bridge with Arg385 (Figure 3.13B, right panel). This switch in Asp476 bonding interactions causes the mobile loop to move away from the active site.

A change in the conformation of the mobile loop is also seen in the SoxB-SoxYZ complex (Figure 3.13A). However, this movement is small and in a different direction to the displacement induced by thiosulfate binding. This SoxYZ-induced structural change most likely results from the alleviation of a number of steric clashes that would otherwise exist between SoxY and the SoxB mobile loop, namely SoxY Ile67 with SoxB Gln473, SoxY Ala66 with SoxB Tyr471, and SoxY Arg145 and Thr147 with SoxB Asn463 (Figure 3.13C).

The SoxYZ-SoxB complex structure shows that binding of SoxYZ perturbs the interaction between SoxB Asp476 and SoxB Arg416. Although the structure of unliganded SoxB was used in the molecular replacement, in the final refined structure of the SoxYZ-SoxB complex the electron densities of Arg416 and Arg385 have moved towards the positions found in the SoxB-thiosulfate structure (Figure 3.13D). While the exact side chain positions of these amino acids are not fully defined at this resolution it is clear that Arg416 has rotated so that it is no longer forming a salt bridge with Asp476 and that Arg385 has moved away from Glu59 towards Asp476. As Arg416 has not formed a new hydrogen bonding interaction, it is apparent that it is distortion of the mobile loop which has broken the Asp476-Arg416 interaction, positioning Arg416 where it would be able to ligate a sulfonate moiety if one were present. The interaction between Arg416 and the sulfonate group would stabilise the position of the moving loop which does not sterically clash with SoxY. Thus, the structures suggest a molecular basis for the observed kinetic discrimination of binding between the substrate and product forms of SoxYZ (Figure 3.5E).

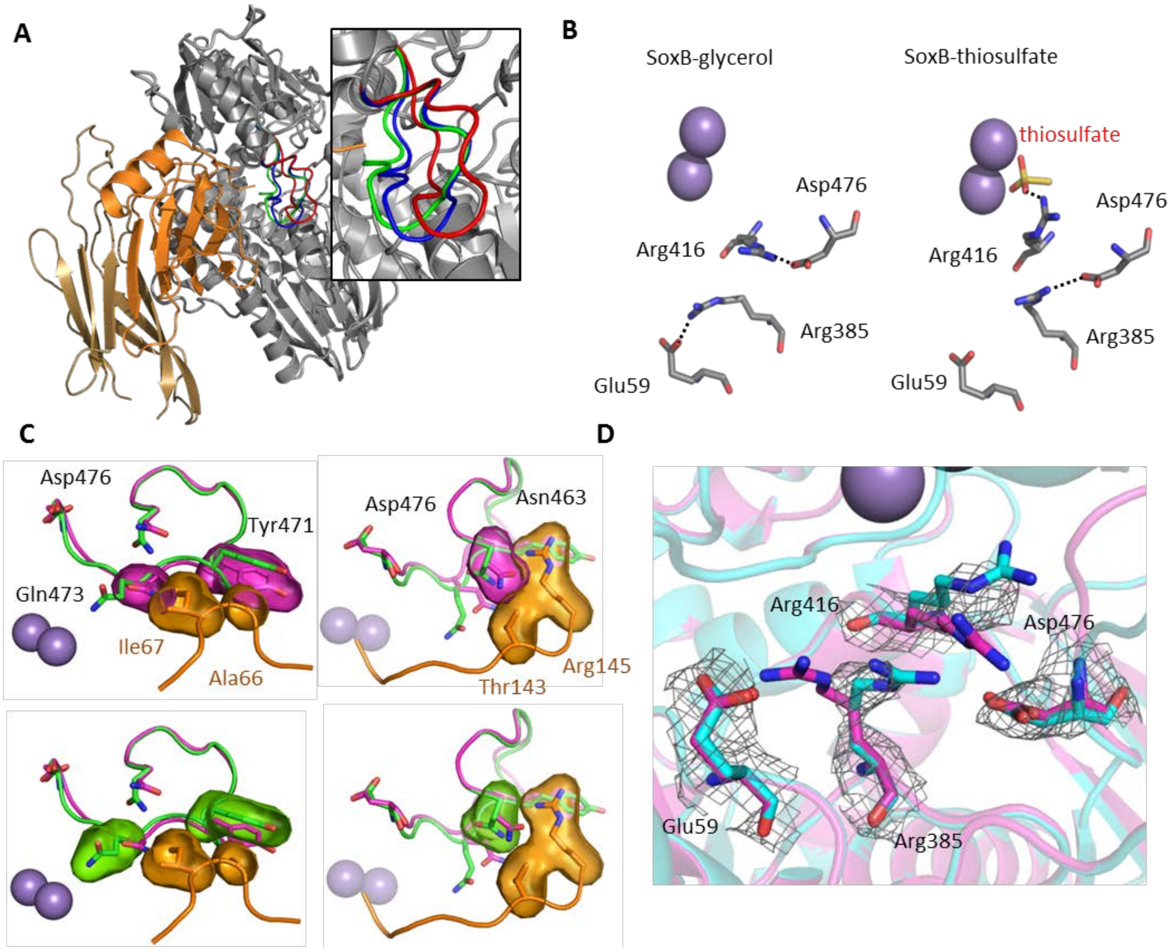

**Figure 3.13 – Conformational changes related to the SoxB mobile loop.** (A) Backbone alignment of SoxB (grey) bound to SoxYZ (orange/brown), or to thiosulfate (2WDE), or with glycerol in the active site (2WDC), with the SoxB mobile loop highlighted in green, red, and blue respectively. (B) The mobile loop-interacting salt-bridge network in the three structures shown in (A). Thiosulfate and relevant amino acid residues are shown in stick representation where carbon is grey in SoxB and green in SoxY, oxygen is red, nitrogen blue, and sulfur yellow. The manganese ions are represented by purple spheres. (C) Alterations in SoxB side chain orientations that alleviate steric clashes with SoxY. Comparative positions of SoxB residues are shown in the presence (green) or absence (magenta; glycerol structure) of SoxY amino acids (orange). Calculated surfaces are shown in surface representation. (D) 2F-Fo electron density map of the SoxYZ-SoxB complex shown at 1.0 σ contour level overlaid with the structures of SoxB bound to thiosulfate (cyan) and with glycerol in the active site (magenta).

### 3.6 Basis for the selective binding of sulfonate to the active site manganese ions

For SoxB catalysis to occur the sulfonate group of the substrate molecule must co-ordinate the active site manganese ions. However, the C-terminal carboxylate of the SoxY carrier arm is also present in the active site channel and will compete with the sulfonate group for binding to the metal ions. Indeed, active site co-ordination by the C-terminal carboxylate is seen in the SoxB-SoxYZ complex structure (Figure 3.12B,C). To gain insight into how SoxB is able to resolve this competition in favour of sulfonate ligation we produced models of the physiological thiosulfonated SoxYZ-SoxB complex. Starting from the disulfide-linked structure, we restored native SoxB Trp175 in place of the introduced Cys residue with the native Trp175, and added an S-thiosulfonate group onto the SoxY carrier arm Cys. In one model we manually positioned the S-thiosulfonate group to co-ordinate the manganese ions using the position of thiosulfate in the previously-determined SoxB-thiosulfate structure as a guide (Sauvé et al., 2009). In a second model the SoxY C-terminal carboxylate ligation seen in the SoxB-SoxYZ structure was retained. These models were solvated and then subjected to energy minimisation and position restrained molecular dynamics equilibration. Comparison of the two models (Figure 3.14) shows that the different binding configurations place chemical groups of different character in contact with a ring of aromatic and non-polar residues that provide access to the manganese ions. When the SoxY C-terminal carboxylate coordinates the metal ions, the C-terminal SoxY Cys-Gly peptide is within the aromatic ring and participates in hydrogen-bonding interactions with the ring residues and solvent (Figure 3.14A). However, in the substrate complex, it is the hydrophobic side chain of cysteine-S-thiosulfonate that is within the aromatic ring and the interaction is now non-polar in nature (Figure 3.14B). These different modes of interaction of the carrier arm with the SoxB aromatic ring provide a plausible mechanism for the change from net enthalpic to net entropic association between SoxB with SoxYZ observed following substrate conjugation to the SoxY carrier arm (Figure 3.5A,B). This is because the hydrogen bonding interactions seen with the C-terminal carboxylate interaction are enthalpically driven, while the non-polar interactions seen with the cysteine-S-thiosulfonate side chain are entropically driven.

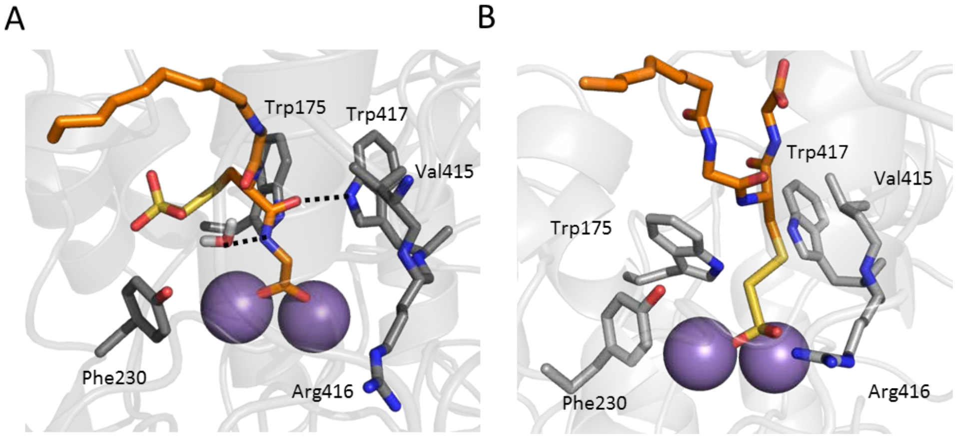

**Figure 3.14 – Energy-minimised models of the active site of the SoxB-SoxYZ-S-thiosulfonate complex**. The carbon atoms of SoxB are shown in grey and of SoxY in orange. Water is shown by its elemental colours. Oxygen atoms are red, nitrogen atoms blue, and sulfur atoms yellow. The manganese ions are represented by purple spheres. (A) Complex with the SoxY C-terminal carboxylate co-ordinating the SoxB dimanganese ions. The interaction of SoxB with the SoxY C-terminal Cys-Gly peptide is stabilised by hydrogen bonding. (B) Complex with the S-thiosulfonate group co-ordinating the manganese ions. The interaction of SoxB with the cysteine-S-thiosulfonate is stabilised by an arc of hydrophobic residues.

In our structural models the S-thiosulfonate group and C-terminal carboxylate both use two terminal oxygen atoms to provide bi-dentate co-ordination to the manganese ions (Figure 3.14). However, the S-thiosulfonate has an additional terminal oxygen atom which forms bonding interactions with SoxB Arg416 (Figure 3.14B). To investigate whether this interaction plays a role in the selective binding of the S-thiosulfonate group by the active site we investigated the effect of substituting SoxB Arg416 with Gly on the thermodynamics of the interaction between SoxB and S-thiosulfonated SoxYZ. The mode of association changed from entropic to enthalpic (Figure 3.15A,B). Given the correlation between binding mode and thermodynamics outlined above this indicates that the carrier arm no longer ligates the active site through the thiosulfonate group but instead binds the metal ions by the C-terminal carboxylate. Thus, Arg416 is critical for correct positioning of the substrate group at the active site. However, this effect cannot be mediated entirely by the interaction between Arg416 and the sulfonate oxygen atom because a similar change in the thermodynamics of binding is seen with SoxY(Ac)Z (Figure

3.15C) which has a carboxylate group and no extra oxygen atom to interact with Arg416. In this case the discrimination between the SoxY C-terminal carboxylate and Cys-S-carboxymethyl must be due to differences in polarity alone. This suggests that the aliphatic portion of the Arg416 side chain provides a significant functional contribution to the hydrophobic environment inside the SoxB aliphatic ring (Figure 3.14B).

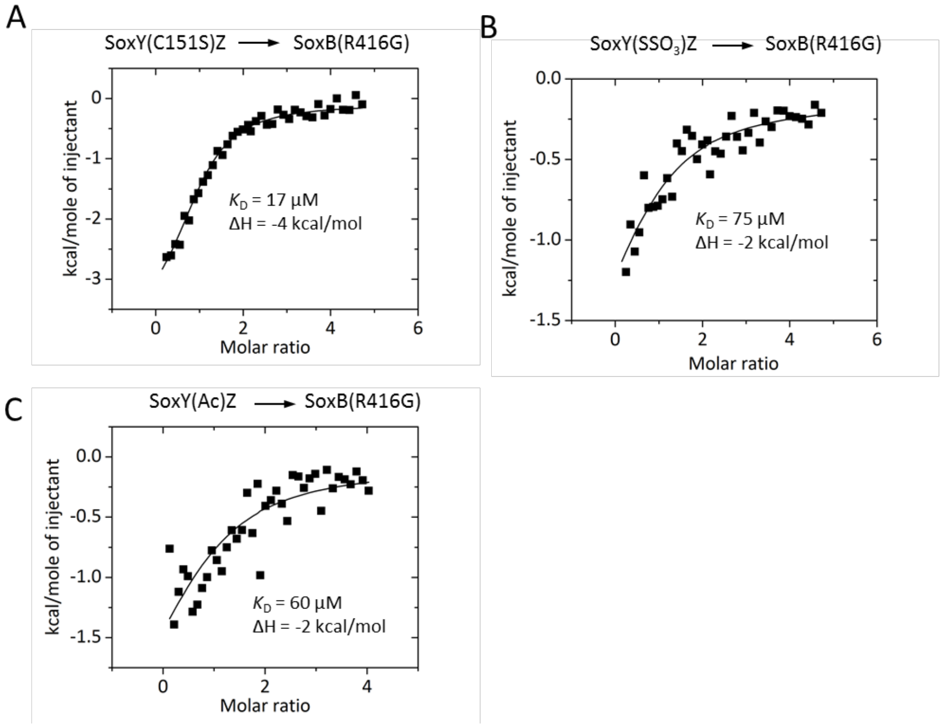

**Figure 3.15 – Effect of Arg416Gly substitution on the thermodynamics of the interaction of SoxB with different forms of SoxYZ.** The ITC titrations that were performed are shown above each panel. Figures show a representative integrated titration, whilst values are derived from simultaneously fitting duplicate titrations.

## 3.7 The Sox carrier protein system

In this chapter we have discovered and characterised the first instance of protein-protein interactions in the Sox system. Our in-depth biophysical and structural analysis allows us to provide insight into some issues which arise when an enzyme evolves to work on a carrier protein-conjugated substrate and how these are overcome in this case.

### 3.7.1 Promiscuous pseudospecificity in a carrier protein-enzyme interaction

For SoxB to have evolved to act on a SoxYZ-bound substrate, it needed to gain a specific protein-protein interaction surface. Conversely, it is likely that SoxYZ evolved to specifically interact with several unrelated enzymes – SoxB, SoxAX, SoxCD and probably SoxF – and so needed to evolve promiscuous pseudospecific interactions with each of these enzymes. By considering the nature of the molecular contacts of the Z-patch and Y-patch we can understand how the interaction interfaces could fulfil these criteria.

The Z-patch interaction involves a small motif on a surface loop of SoxB, and a pocket in the β-sheet of SoxZ. The interactions here are few and specific: a salt bridge and insertion of an aromatic residue into a hydrophobic pocket. We show by mutagenesis that this salt bridge and aromatic residue are crucial for formation of a SoxB-SoxYZ complex. Modifying a surface loop is the easiest way to introduce new functionality without affecting the overall fold of an enzyme. It is likely that the sole function of SoxZ is to mediate protein-protein interactions with the Sox pathway enzymes, so it was free for more complex evolution to gain a pocket complementary to this loop. With this Z-patch pocket, SoxYZ would be able to form similar contacts with unrelated enzymes, as long as they have a surface loop with the same physicochemical properties as the SoxB loop at the right distance from the active site. This allows interactions to be specific but promiscuous. A similar strategy is employed by the MAP kinase family. These protein kinases gain specificity for many different substrate proteins by recognising small distal motifs such as the D motif and FxFP motif (Tanoue and Nishida, 2003). The UshA 5' nucleotidase family, the closest relatives to SoxB, contain a loop in exactly the same place as the Z-patch motif, but with no sequence conservation and a low probability of aromatic and acidic residues.

The Y-patch interaction has different properties to the Z-patch interaction. The contact surface area is much larger than for the Z-patch interaction but there are no salt-bridges or specific hydrophobic interactions. Most of the Y-patch interactions are probably mediated by water molecules not seen at the resolution of our structure. This lack of specific interactions, along with the inherent flexibility of the SoxY C-terminal carrier arm, means that the SoxY carrier arm is not restricted to bind to each Sox enzyme by the same mechanism, which is ideal for promiscuous pseudospecificity. An extreme example of this approach is used by the promiscuous electron transferring flavoprotein, ETF, and shown by the interaction with one of its redox partners, trymethylamine dehydrogenase (Leys et al., 2003). Here, the two proteins are anchored by specific distal interactions, with very weak interactions and high conformational flexibility at the active site.

### 3.7.2 Competition between the substrate and similar chemical groups on the carrier protein

A protein-protein interaction between enzyme and substrate-carrier protein effectively increases the local concentration of the substrate conjugated to the carrier protein. In the case of SoxB and SoxYZ, the affinity of the protein-protein interaction is so strong that the actual binding of the substrate thiosulfonate moiety to the dimanganese centre can be very weak. However, the effective concentration of all other functional groups on the SoxY C-terminal carrier arm is also increased. In particular, the C-terminal carboxylate has physicochemical similarity to the substrate thiosulfonate moiety, and in our complex structure this carboxylate is co-ordinating the dimanganese centre similarly to thiosulfate in the SoxB-thiosulfate structure (Sauvé et al., 2009). So, rather than the system needing to adapt to bind to its substrate with high affinity, it must instead be able to discriminate the substrate group from any other functional groups on the carrier protein. This is particularly the case when there is inherent flexibility in the active site interaction, as discussed in the previous section.

From our ITC data and computational models of the SoxB active site with SoxY($SSO_3$)Z bound, it appears that this competition is resolved in favour of the thiosulfonate group by an arc of hydrophobic residues above the active site (Figure 3.14). The cysteine-S-thiosulfonate side chain is largely hydrophobic apart from the head-group, whilst the C-terminal carboxylate peptide chain is hydrophilic in nature. The catalytic residue Arg416 in particular is ideally suited for this role, as it has a non-polar chain leading to a head-group which can bind to the extra oxygen which is displayed by the thiosulfonate moiety (Figure 3.14), but is not present in the carboxylate moiety. Indeed, Arg416 is necessary for this discrimination (Figure 3.15). The role of Arg416 is especially of interest as it is sequestered in the non-substrate-bound state of the enzyme (see below).

### 3.7.3 A kinetic selectivity model for SoxYZ in the Sox system

A standard model for an enzyme-catalysed reaction, particularly in a system designed to go in one direction, would be that the enzyme would have a weaker affinity for the product than the substrate. In a carrier protein system in particular, one might expect the carrier protein to direct the substrate along a particular enzymatic route. Perhaps the conformation of the carrier protein would change depending on what is conjugated to it, and this would mean it could only bind to the right enzyme. Such a mechanism has been proposed for the non-ribosomal peptide synthetase system (Frueh et al., 2008).

For the Sox system, SoxB has the same affinity for substrate and product, making such a mechanism unlikely. Instead, from the SPR data of substrate-loaded and non-substrate-loaded SoxYZ binding to SoxB (Figure 3.5E), and comparison of our crystal structure with previous SoxB structure, we can suggest a mechanism of kinetic discrimination (Figure 3.16). In this mechanism, when SoxYZ binds to SoxB the highly conserved SoxB moving loop is pushed back by a number of steric clashes with SoxY (Figures 3.13C and 3.16C). These clashes involve absolutely conserved residues, such as SoxY Ile67. If nothing stabilises a position of the SoxB moving loop away from SoxY, the steric clashes will quickly force SoxYZ from the active site. A related mechanism also disfavours binding of small molecules, such as thiosulfate and sulfate, which would be present in the periplasm at reasonable concentrations, to the SoxB active site. The binding of thiosulfate requires a rearrangement of the active site salt-bridge network which is not favoured by the resting moving loop conformation (Figures 3.13A,B and 3.16A). It is only when the substrate-loaded form of SoxYZ binds to SoxB that these two mechanisms work together. SoxYZ binds and pushes the SoxB moving loop out of the way. This movement rearranges the active site salt-bridge network, releasing Arg416 from an interaction with Asp476 (Figures 3.13D and 3.16C). Arg416 is now able to bind to the thiosulfonate moiety through both its non-polar and charged regions. This interaction stabilises a conformation of the SoxB moving loop where it does not sterically clash with SoxYZ. The overall effect of this mechanism is that both substrate- and non-substrate-loaded SoxYZ will bind to SoxB, but non-substrate-loaded SoxYZ will quickly dissociate allowing binding of substrate-loaded SoxYZ, which will remain bound long enough for the hydrolysis reaction to occur.

With this mechanism in mind we can begin to think about how the Sox system works. Rather than an assembly line mechanism, where the substrate will only be brought to the next enzyme in the system, instead the substrate carrier protein will rapidly iteratively sample every enzyme in the system. Only when a cognate interaction is made, i.e. between an enzyme and SoxYZ conjugated to the substrate for that enzyme, will the dissociation rate be decreased sufficiently to allow the reaction to occur. An analogous mechanism to this has been proposed for type I fatty acid synthase systems (Gipson et al., 2010).

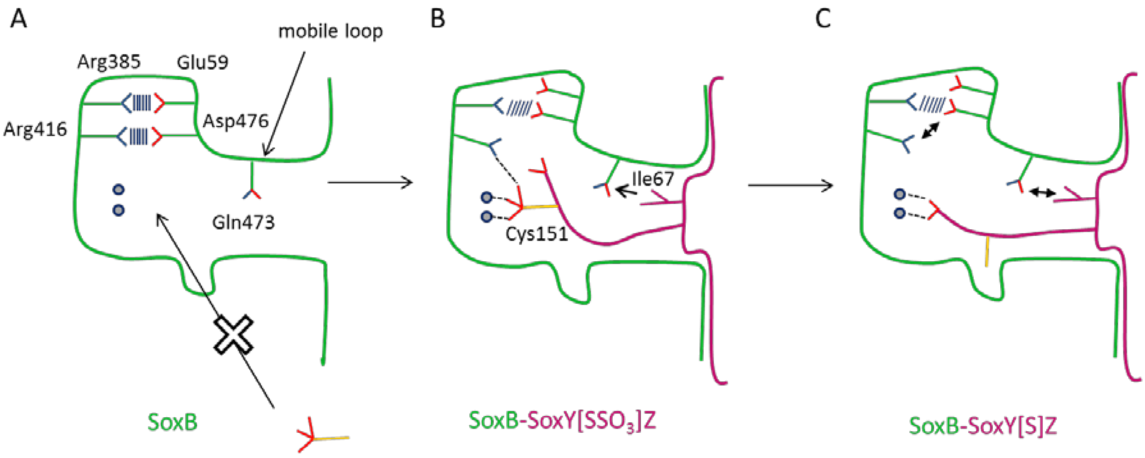

**Figure 3.16 – Mechanism for kinetic discrimination by SoxB during catalysis.** (A) In the resting state small molecules such as thiosulfate are disfavoured from binding because Arg416 is sequestered. (B) Upon binding of SoxYZ, the SoxB moving loop is distorted, particularly through a clash between SoxY Ile67 and SoxB Gln473. This rearranges the active site salt bridge network to free Arg416 to bind to the substrate thiosulfonate moiety. This prevents the SoxB moving loop from ejecting SoxYZ. (C) When the thiosulfonate moiety is hydrolysed, nothing stabilises the high energy moving loop conformation, and SoxYZ will be ejected.

### 3.7.4 Other Sox enzymes

As the structures and sequences of the other Sox enzymes are known, it is possible to speculate as to whether they have similar interactions with SoxYZ as we have shown for SoxB. Both the *P. pantotrophus* SoxAX and SoxCD enzymes have loops with a similar motif to the SoxB Z-patch motif at the right distance from their active site (Figure 3.17). These all include an unusually solvent-exposed aromatic residue surrounded by acidic residues. It would be interesting to investigate the protein-protein interactions of the other Sox enzymes with SoxYZ to confirm if similar mechanisms are employed in these cases.

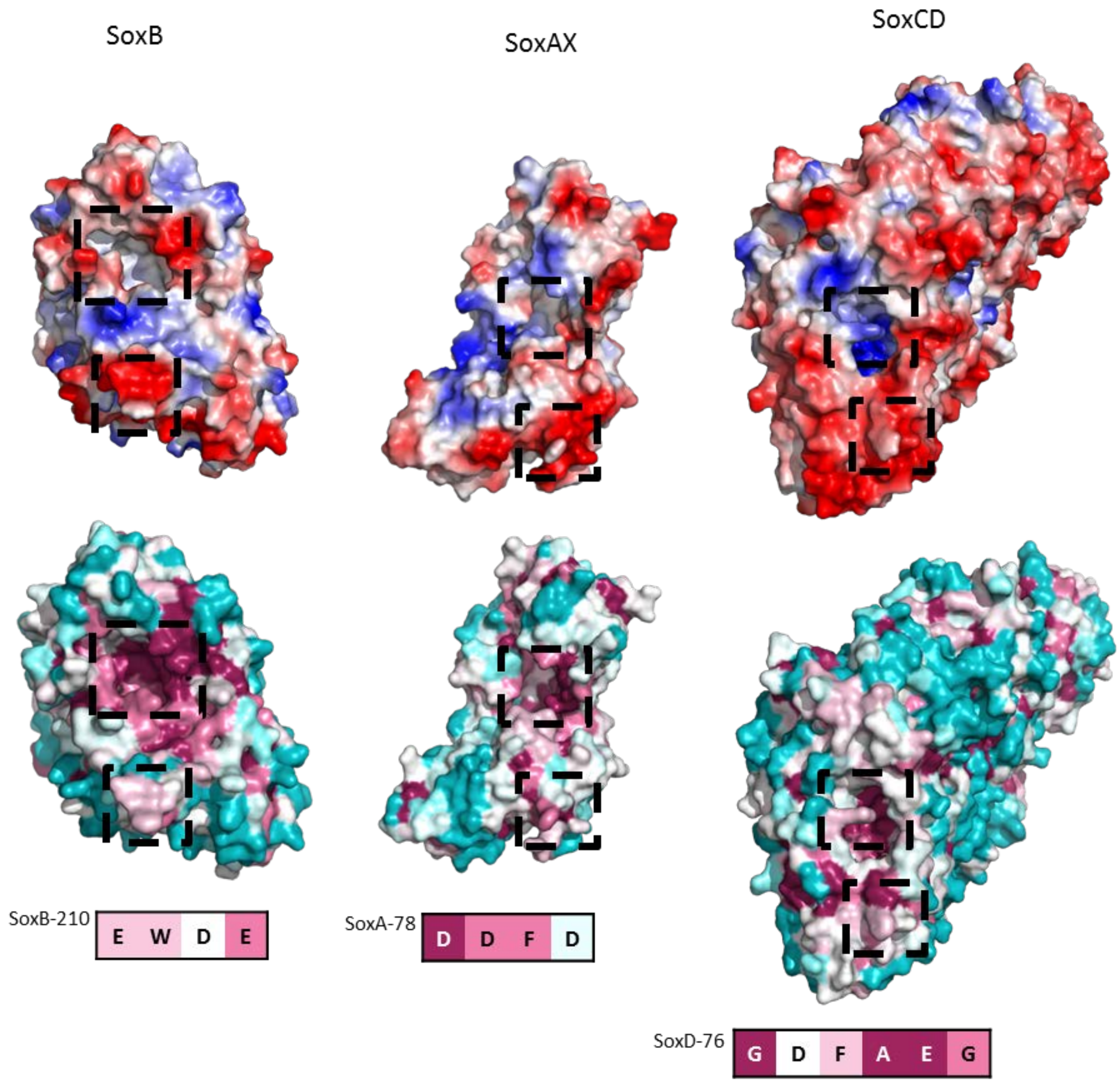

**Figure 3.17 – Possible interaction interfaces for other Sox pathway enzymes.** SoxYZ-interacting enzymes of *P. pantotrophus* are shown in surface representation viewed from the face containing the active site entrance tunnel. The upper panels show the electrostatic surface potential calculated using PyMOL with positive potentials coloured blue and negative potentials red. The lower panels show the same views of each protein but with the surface coloured according to sequence conservation using the program Consurf (Celniker et al., 2013). Magenta indicates areas of highest sequence conservation and cyan the most variable sequences. In each panel the active site entrance is indicated by the upper, larger, box. The known (SoxB) or proposed (SoxAX and SoxCD) SoxZ contact site is indicated by the lower, smaller, box and the sequence of the loop from this contact is shown below at the foot of the figure with residues in Consurf colours. The structures shown are a homology model of SoxB produced using SWISS-MODEL (Arnold et al., 2006) based on the structure of *T. thermophilus* SoxB (PDB: 2WDF) (Sauvé et al., 2009), *P. pantotrophus* SoxAX (PDB:2C1D)(Dambe et al., 2005), and *P. pantotrophus* SoxCD (PDB:2XTS) (Zander et al., 2011).

# Chapter 4: Mechanism of oxidative thiosulfate conjugation catalysed by cysteine-ligated cytochromes

## 4.1 Introduction and aims

### 4.1.1 Aim of chapter

SoxAX is the first enzyme of the Sox thiosulfate oxidation pathway. The structure of SoxAX has been known for some time (Bamford et al., 2002) but no enzyme activity can be detected with the proposed substrates *in vitro*. It has not been possible to determine and demonstrate the mechanism of this enzyme. Recently, Denkmann *et al.* characterised a thiosulfate dehydrogenase, TsdA, from *A. vinosum* (Denkmann et al., 2012), which is homologous to SoxAX but is catalytically active and has simple small-molecule substrates. The aim of the work in this chapter was to use this simpler homologue as model for SoxAX to gain mechanistic insight into both TsdA and SoxAX.

### 4.1.2 Catalytic mechanism of SoxAX

SoxAX is proposed to catalyse oxidative conjugation of thiosulfate to the SoxYZ carrier arm cysteine (Equation 4.1, and see Section 1.2.5).

$$\text{SoxYZ-S}^{-} + {}^{-}\mathbf{S\text{-}SO_3}^{-} \rightarrow \text{SoxYZ-S-}\mathbf{S\text{-}SO_3}^{-} + 2e^{-} \qquad \text{(Equation 4.1)}$$

Several subclasses of SoxAX exist (reviewed in (Kappler and Maher, 2013)), some of which contain an extra subunit or extra structural *c* type heme. All subclasses have an unusual His/Cys ligated *c* type heme at their active site and a His/Met ligated *c* type heme within electron transfer distance of this. EPR spectroscopy of the tri-heme SoxAX from *P. versutus* (Kelly et al., 1997) showed that one of the hemes has a potential low enough not to be reducible by dithionite. The presence of a small high spin signal at $g = 6$ suggested that one heme was accessible to the binding of small substrates.

Cheesman *et al.* used a combination of EPR and magnetic circular dichroism (MCD) spectroscopy on the tri-heme *R. sulfidophilum* SoxAX (Cheesman et al., 2001) to show that one heme had His/Met coordination and the other two had His/thiolate coordination, and one of these hemes existed in at least two forms, postulated to be a native cysteine thiolate and a modified cysteine perthiolate, based on previous mass spectrometry data (Appia-Ayme et al., 2001). The proportion of the different forms was preparation dependent. These inferences were confirmed by a crystal structure of the *R. sulfidophilum* enzyme (Bamford et al., 2002) and later the closely related *P. pantotrophus* SoxAX (Dambe et al., 2005), which showed that the catalytic heme was coordinated by a cysteine perthiolate. The proximity of a conserved arginine to the active site perthiolate led Bamford and co-workers to propose a mechanism based on a comparison with rhodanese (Bamford et al., 2002) (Figure 5.1). Rhodanese catalyses the disproportionation of thiosulfate using a covalent mechanism. First, thiosulfate is bound and positioned by an arginine (Luo and Horowitz, 1994). The catalytic cysteine thiolate then nucleophilically attacks the thiosulfate to form cysteine persulfide and sulfite (Gliubich et al., 1996). The persulfide can then be readily transferred to cyanide. For SoxAX, the arginine-coordinated thiosulfate was proposed to oxidatively react with the catalytic cysteine thiolate to form cysteine-S-thiosulfonate and concomitantly reduce the hemes. This cysteine-S-sulfonate intermediate is then attacked by the SoxYZ cysteine thiolate nucleophile and thiol:disulfide exchange results in the formation of SoxY(SSO$_3$)Z and the unmodified SoxA cysteine thiolate. In this mechanism the persulfide is itself not an intermediate but formed by breakdown of a cysteine-S-thiosulfonate intermediate.

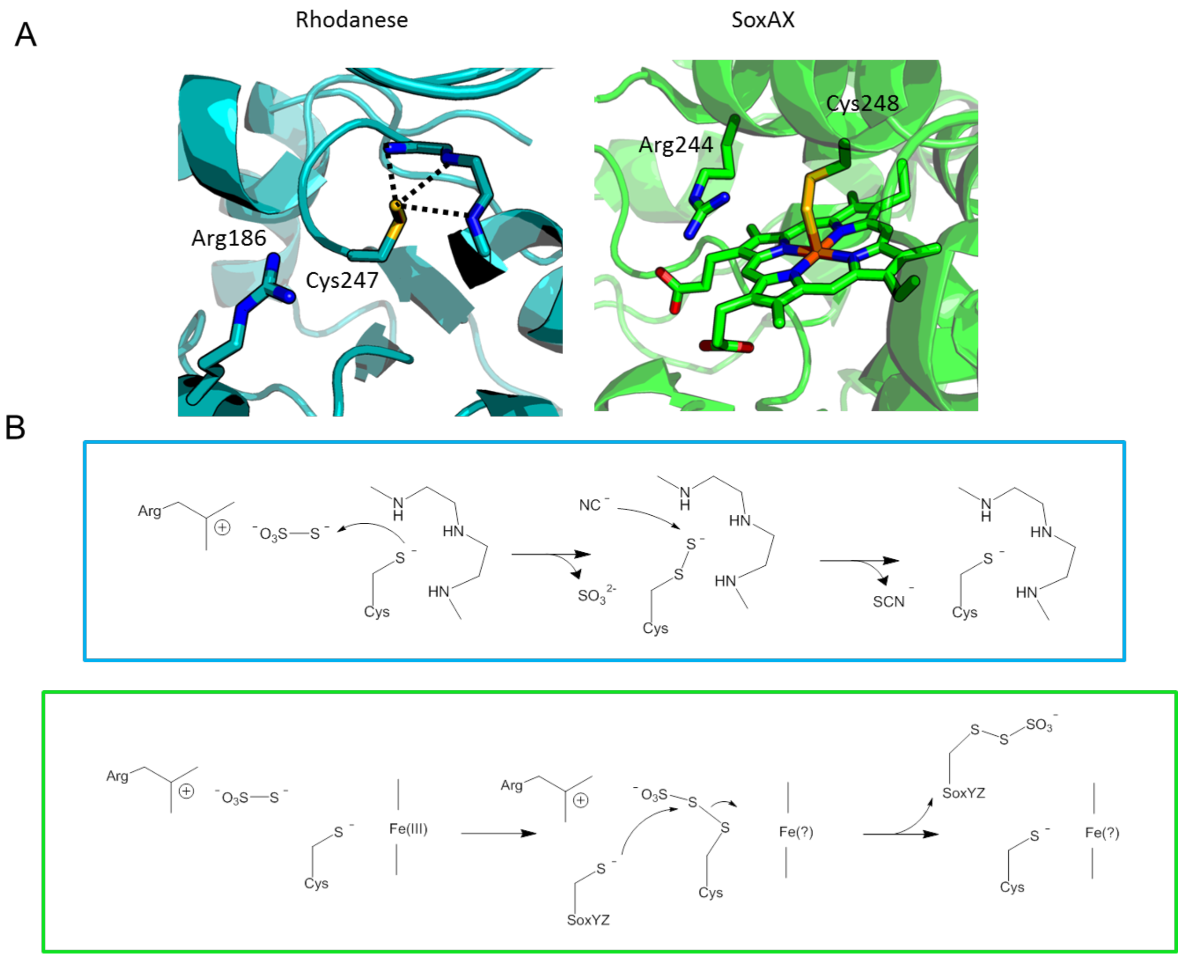

**Figure 4.1 – Proposed catalytic mechanism of SoxAX based on the mechanism of rhodanese.** (A) The left panel shows the crystal structure of the intermediate cysteine persulfide state of bovine rhodanese [PDB code: 1RHS], showing stabilisation of the persulfide by the amide backbone, and the position of the arginine anticipated to coordinate thiosulfate. The right panel shows the active site of SoxAX from *R. sulfidophilum* [PDB code: 1H33]. The catalytic cysteine persulfide coordinates the heme iron, whilst the arginine proposed to coordinate thiosulfate is also shown in stick representation. (B) Proposed mechanisms of rhodanese (top panel) and SoxAX (lower panel). The two SoxAX hemes are expected to be reduced by the first step of the mechanism, but the stage of the mechanism at which the hemes would be re-oxidised is unclear and this is indicated by the question mark symbol.

Kappler and co-workers have used the di-heme SoxAX from *Starkeya novella* for their work. This enzyme does not have the second, catalytically unimportant His/Cys ligated heme, which has overlapping spectral features with the catalytic heme making spectral interpretation difficult (Kappler et al., 2004). They heterologously expressed their protein in *Rhodobacter capsulatus* in an attempt to prevent enzymatic turnover and formation of the active site persulfide (Kappler et al., 2005). Nevertheless, mass spectrometry showed that this SoxAX was still 50% modified with persulfide which was later confirmed by a crystal structure (Kilmartin et al., 2011). They also found that the reactive cysteine could be S-thiosulfonated using DMSO (Kappler et al., 2005), but no explanation for this unexpected chemistry was suggested. Substitution of the active site cysteine heme ligand with methionine resulted in a multi-component EPR spectrum (Kilmartin et al., 2011). This suggests that the methionine ligates the heme in multiple conformations, and this was seen in the crystal structure of the variant.

The redox midpoint potentials of SoxAX hemes have been quantified for the enzymes from *P. pantotrophus* (Reijerse et al., 2007), *S. novella* (Kappler et al., 2008) and *R. sulfidophilum* (Bradley et al., 2012). All these reports show that the catalytic His/Cys heme has a very low potential, e.g. -340 mV vs. SHE for *R. sulfidophilum*, whilst the electron transfer heme has a much higher potential, e.g. +210 mV for *R. sulfidophilum*. Kappler and co-workers suggest that these two hemes would not be able to act as a redox pair and implicated loosely bound copper with a higher redox potential than the catalytic heme as the true active site (Kappler et al., 2008). Bradley *et al.* postulate that if a covalent mechanism occurred (as in Figure 4.1) then the true redox pair would be between ferric thiolate-ligated heme and either ferrous pentacoordinated high-spin heme or cysteine-S-thiosulfonate-ligated heme, either of which, from first principles, would likely have a much higher potential than ferrous thiolate-ligated heme (Bradley et al., 2012). This suggestion is experimentally supported by the observations that the high-spin $g$ = 6 EPR signal is readily reduced by dithionite, whereas the thiolate-ligated heme signal is not (Kelly et al., 1997), and the methionine substituted *S. novella* catalytic heme (which would mimic coordination by the sulfur of cysteine-S-thiosulfonate) has a midpoint potential of +85 mV (Kilmartin et al., 2011).

A serious difficulty in elucidating the mechanism of SoxAX is that it has no demonstrable activity without all other components of the Sox system present (Ogawa et al., 2010; Ben Berks, personal communication). However, Kappler and co-workers have detected activity using a glutathione-based assay (Kappler et al., 2008). This assay uses disulfide formation between two glutathione molecules to reduce cytochrome *c*. They show that supplementing the assay with copper increases the activity. However, similar copper activation also occurs in the absence of SoxAX. The activity only increases 2-fold in the presence of SoxAX, and the dependence on SoxAX is not linear as one would expect for an enzyme catalyst. No copper binding site has been identified in crystal structure of the *S. novella* SoxAX. Kappler and co-workers have also developed an assay with just SoxYZ and thiosulfate (Kilmartin et al., 2011). However, SoxAX has extremely low activity versus background in these assays. Additionally, substitution of the invariant catalytic cysteine with methionine has little effect on the assay. The authors suggest that the labile copper is the true active site.

Recently it was shown that treatment of *R. sulfidophilum* SoxAX with the sulfur-based reductant dithionite ($S_2O_4^{2-}$), but not the non-sulfur reductant europium(II), made the catalytic heme accessible to cyanide coordination (Bradley et al., 2012). The authors suggest that dithionite (or one of its breakdown products) undergoes some chemistry with the catalytic cysteine that is analogous to the physiological reaction and which results in a pentacoordinated heme which can bind cyanide.

### 4.1.3 The SoxAX homologue TsdA

The thiosulfate dehydrogenase TsdA found in the periplasm of some sulfur oxidising bacteria catalyses oxidative conjugation of two thiosulfate molecules to form tetrathionate (Equation 4.2 and see Section 1.2.6.1).

$$^{-}S\text{-}SO_3^{-} + {}^{-}S\text{-}SO_3^{-} \rightarrow {}^{-}O_3S\text{-}S\text{-}S\text{-}SO_3^{-} + 2e^{-} \qquad \text{(Equation 4.2)}$$

This enzyme has recently been characterised by Dahl and co-workers. The native enzyme purified from *A. vinosum* was shown to oxidise thiosulfate with either ferricyanide or yeast cytochrome *c* as an electron acceptor (Hensen et al., 2006). The activity with ferricyanide showed pH-sensitivity with no activity at pH ≥ 7, and maximum activity at pH 4.25. TsdA activity displayed complex Michaelis-Menten kinetics with respect to ferricyanide and thiosulfate concentrations. Additionally, unlike SoxAX, thiosulfate could reduce the enzyme. This reduction only occurred at low pH where the enzyme is catalytically active. The enzyme also catalyses the reverse reaction, the reduction of tetrathionate to thiosulfate, but at a lower rather than in the forward direction (Liu et al., 2013).

The sequence of TsdA shows weak sequence similarity to the catalytic domain of SoxA (Figure 4.2) (Denkmann et al., 2012), particularly the alignment of the cytochrome *c* motif and the catalytic cysteine and conserved arginine residues. TsdA has an additional domain not present in SoxA with a sequence resembling that of His/Met-coordinated mitochondrial cytochrome *c*. This is likely to be an electron-transfer heme with the same role as SoxX. These similarities suggest the enzyme has a mechanism analogous to SoxAX. TsdA also displayed a similar EPR spectrum with features reminiscent of SoxAX, including a more intense, although still relatively weak, high-spin signal. The presence of a small proportion of high-spin ferric heme could also be seen in the UV/visible TsdA spectrum with a small feature at 625 nm. Denkmann *et al.* also showed the enzyme from various bacteria could be expressed in *E. coli*, and all displayed similar pH-dependent activity. Some organisms have another diheme cytochrome-encoding gene, named *tsdB*, in the same operon as *tsdA*. TsdB which is likely to be the physiological electron acceptor of TsdA. TsdB from *Thiomonas intermedia* was expressed and could accept electrons from *A. vinosum* TsdA, with a broader pH optimum. However, there is no TsdB homologue in *A. vinosum.*

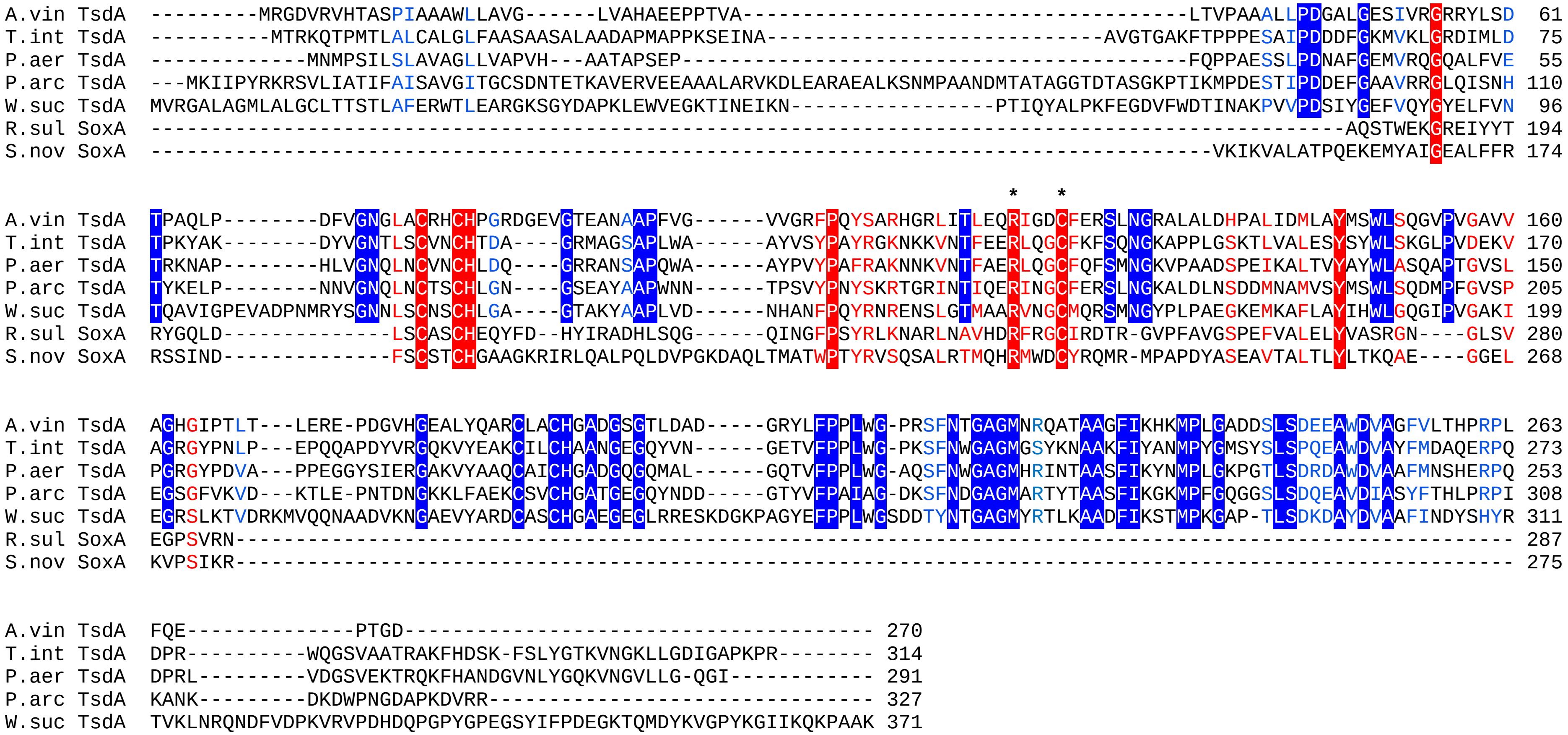

```
A.vin TsdA  ---------MRGDVRVHTASPIAAAWLLAVG------LVAHAEEPPTVA-------------------------------------LTVPAAALLPDGALGESIVRGRRYLSD  61
T.int TsdA  ----------MTRKQTPMTLALCALGLFAASAASALAADAPMAPPKSEINA----------------------------AVGTGAKFTPPPESAIPDDDFGKMVKLGRDIMLD  75
P.aer TsdA  -------------MNMPSILSLAVAGLLVAPVH---AATAPSEP------------------------------------------FQPPAESSLPDNAFGEMVRQGQALFVE  55
P.arc TsdA  ---MKIIPYRKRSVLIATIFAISAVGITGCSDNTETKAVERVEEAAALARVKDLEARAEALKSNMPAANDMTATAGGTDTASGKPTIKMPDESTIPDDEFGAAVRRGLQISNH 110
W.suc TsdA  MVRGALAGMLALGCLTTSTLAFERWTLEARGKSGYDAPKLEWVEGKTINEIKN-----------------PTIQYALPKFEGDVFWDTINAKPVVPDSIYGEFVQYGYELFVN  96
R.sul SoxA  ---------------------------------------------------------------------------------------------------AQSTWEKGREIYYT 194
S.nov SoxA  ----------------------------------------------------------------------------------------VKIKVALATPQEKEMYAIGEALFFR 174

                                                                                       *   *
A.vin TsdA  TPAQLP--------DFVGNGLACRHCHPGRDGEVGTEANAAPFVG------VVGRFPQYSARHGRLITLEQRIGDCFERSLNGRALALDHPALIDMLAYMSWLSQGVPVGAVV 160
T.int TsdA  TPKYAK--------DYVGNTLSCVNCHTDA----GRMAGSAPLWA------AYVSYPAYRGKNKKVNTFEERLQGCFKFSQNGKAPPLGSKTLVALESYSYWLSKGLPVDEKV 170
P.aer TsdA  TRKNAP--------HLVGNQLNCVNCHLDQ----GRRANSAPQWA------AYPVYPAFRAKNNKVNTFAERLQGCFQFSMNGKVPAADSPEIKALTVYAYWLASQAPTGVSL 150
P.arc TsdA  TYKELP--------NNVGNQLNCTSCHLGN----GSEAYAAPWNN------TPSVYPNYSKRTGRINTIQERINGCFERSLNGKALDLNSDDMNAMVSYMSWLSQDMPFGVSP 205
W.suc TsdA  TQAVIGPEVADPNMRYSGNNLSCNSCHLGA----GTAKYAAPLVD------NHANFPQYRNRENSLGTMAARVNGCMQRSMNGYPLPAEGKEMKAFLAYIHWLGQGIPVGAKI 199
R.sul SoxA  RYGQLD--------------LSCASCHEQYFD--HYIRADHLSQG------QINGFPSYRLKNARLNAVHDRFRGCIRDTR-GVPFAVGSPEFVALELYVASRGN----GLSV 280
S.nov SoxA  RSSIND--------------FSCSTCHGAAGKRIRLQALPQLDVPGKDAQLTMATWPTYRVSQSALRTMQHRMWDCYRQMR-MPAPDYASEAVTALTLYLTKQAE----GGEL 268

A.vin TsdA  AGHGIPTLT---LERE-PDGVHGEALYQARCLACHGADGSGTLDAD-----GRYLFFPLWG-PRSFNTGAGMNRQATAAGFIKHKMPLGADDSLSDEEAWDVAGFVLTHPRPL 263
T.int TsdA  AGRGYPNLP---EPQQAPDYVRGQKVYEAKCILCHAANGEGQYVN------GETVFFPLWG-PKSFNWGAGMGSYKNAAKFIYANMPYGMSYSLSPQEAWDVAYFMDAQERPQ 273
P.aer TsdA  PGRGYPDVA---PPEGGYSIERGAKVYAAQCAICHGADGQGQMAL------GQTVFFPLWG-AQSFNWGAGMHRINTAASFIKYNMPLGKPGTLSDRDAWDVAAFMNSHERPQ 253
P.arc TsdA  EGSGFVKVD---KTLE-PNTDNGKKLFAEKCSVCHGATGEGQYNDD-----GTYVFPAIAG-DKSFNDGAGMARTYTAASFIKGKMPFGQGGSLSDQEAVDIASYFTHLPRPI 308
W.suc TsdA  EGRSLKTVDRKMVQQNAADVKNGAEVYARDCASCHGAEGEGLRRESKDGKPAGYEFPPLWGSDDTYNTGAGMYRTLKAADFIKSTMPKGAP-TLSDKDAYDVAAFINDYSHYR 311
R.sul SoxA  EGPSVRN---------------------------------------------------------------------------------------------------------- 287
S.nov SoxA  KVPSIKR---------------------------------------------------------------------------------------------------------- 275

A.vin TsdA  FQE--------------PTGD--------------------------------------- 270
T.int TsdA  DPR----------WQGSVAATRAKFHDSK-FSLYGTKVNGKLLGDIGAPKPR-------- 314
P.aer TsdA  DPRL---------VDGSVEKTRQKFHANDGVNLYGQKVNGVLLG-QGI------------ 291
P.arc TsdA  KANK---------DKDWPNGDAPKDVRR-------------------------------- 327
W.suc TsdA  TVKLNRQNFDVDPKVRVPDHDQPGPYGPEGSYIFPDEGKTQMDYKVGPYKGIIKQKPAAK 371
```

**Figure 5.2 Alignment of TsdA proteins from different organisms with the catalytic domain of SoxA.** Residues which are strictly conserved between TsdA and the SoxA catalytic domain are highlighted in red, whilst conserved residue characteristics have red type. Residues which are only strictly conserved in TsdA are highlighted in blue, whilst conserved residue characteristics are shown in blue type. The putative catalytic cysteine and arginine are highlighted with asterisks. A.vin, *Allochromatium vinosum DSM 180*$^T$; T.int, *Thiomonas intermedia K12*; P.aer, *Pseudomonas aeruginosa PA-01*; P.arc, *Psychrobacter arcticus 273-4*; W.suc, *Wolinella succigones DSM 1740*; R.sul SoxA, *Rhodovulum sulfidophilum* SoxA(180-287); S.nov SoxA, *Starkeya novella* SoxA(149-275).

### 4.1.4 Other His/Cys coordinated *c*-type hemes

A number of other cytochromes with His/Cys coordination have been discovered. However, the function of the His/Cys heme in these proteins is not known. One example is DsrJ, which is part of the DsrJKMOP complex discussed in Section 1.2.3 (Pires et al., 2005). This protein has three *c*-type hemes with His/Met, His/His and His/Cys coordination (Grein et al., 2010). DsrJ is located on the periplasmic side of the membrane so it is not thought to be involved in the catalysis of sulfite reduction, which occurs on the cytoplasmic side of the membrane. The expected heme-coordinating cysteine is Cys46, and substitution of this residue heavily impaired *in vivo* sulfur oxidation. The arrangement of this cysteine and the cytochrome c motif is different to SoxAX and TsdA and there is no equivalent arginine residue. The His/Cys heme in the purified complex appears to be largely in the high-spin state suggesting the cysteine has dissociated from the heme.

As well as perhaps catalysing sulfur chemistry, His/Cys hemes have other interesting properties, such as very low redox potentials, and the possibility of the cysteine ligand dissociating when the heme is in the ferrous state (Pazicni et al., 2005). Other examples of His/Cys c-type cytochromes are: PsbV2, which is possibly involved in photosynthesis in *Thermosynechococcus elongatus* (Suga et al., 2013); PufC, which is involved in photosynthesis in *R. sulfidophilum* (Alric et al., 2004); green heme protein (GHP) perhaps involved in the stress response in *Halochromatium salexigens* (Van Driessche et al., 2006); and NaxLS which may be involved in anaerobic ammonium oxidation (Ukita et al., 2010). It has been suggested that the role of the His/Cys heme in each case is related to its unusually low redox potential.

## 4.2 Production of soluble recombinant TsdA

### 4.2.1 Screening *tsdA* genes

We aimed to use TsdA as a catalytically accessible model for understanding the mechanism of the SoxAX family of enzymes using biochemical, biophysical and structural techniques. To do this we first needed to source milligram quantities of TsdA protein. Denkmann *et al.* were able to produce recombinant strep-tagged TsdA in *E. coli* from a number of sources (*A. vinosum, T. intermedia* and *Pseudomonas stutzeri*) only encountering some issues with TsdA from *Psychrobacter arcticus* (Denkmann et al., 2012). Thus we screened *tsdA* genes from a range of bacterial species for high level functional expression in *E. coli*. *Wolinella succinogenes* is an epsilon-proteobacterium, very closely related to two human pathogens: *Helicobacter pylori* and *Campylobacter jejuni*. *W. succinogenes* genomic DNA was kindly provided by Jörg Simon (TU Darmstadt). *Pseudomonas aeruginosa* is an opportunistic human pathogen and is closely related to *Pseudomonas fluorescens*, a rare opportunistic human pathogen which can also be used to promote plant growth. Genomic DNA from both these pseudomonads was obtained in collaboration with Gail Preston (Plant Sciences, Oxford University). This screening work was performed largely by a summer student, Bianca Eisel, under my supervision.

The *tsdA* genes were initially cloned with their native signal peptides and a C-terminal his$_6$ tag into pET-22b+ under the control of a T7 promoter. Expression tests were performed at varying temperatures, IPTG concentrations and in a range of *E. coli* BL21 (DE3) derivative expression strains, each with a pEC86 plasmid, which constitutively expresses the cytochrome *c* maturation system of *E. coli* (Arslan et al., 1998). Some expression of heme-staining protein was seen with *P. aeruginosa* and *P. fluorescens* TsdA using L56 (pEC86) cells. However, no thiosulfate dehydrogenase activity was detected, and the large majority of the protein was insoluble. This insoluble protein was solubilised and purified in urea, but attempts to refold the protein were unsuccessful. In case misfolding was due to the interaction of the his$_6$-tag with the protein metal centres, expression was also attempted using a strep-tagged *P. aeruginosa* TsdA construct in a pQE80L expression vector with a T5 promoter. Again, the protein was insoluble.

### 4.2.2 Production of strep-tagged *A. vinosum* TsdA

To determine if we had been unfortunate with our *tsdA* gene selection or whether there was an issue with the way we were trying to express TsdA, we next attempted to express TsdA from *A. vinosum* with a C-terminal strep tag and its native signal peptide, as described by Dahl and co-workers (Denkmann et al., 2012). The cloning strategy is detailed in Figure 4.3 and resulted in plasmid pQE80L-AvTsdA-strep. Expression was screened in a range of conditions. The periplasmic fractions of expression tests with a 20$^{o}$C overnight induction using BL21 star, JM109 and L56 expression strains were faintly orange and by SDS-PAGE showed a heme-staining band of the correct size. Additionally, all these periplasmic extracts had thiosulfate dehydrogenase activity. The pattern of heme-staining bands for the BL21 star strain and L56 strain looked slightly different, so larger scale expression tests were attempted using each strain. Both purified proteins had identical behaviour on ion-exchange chromatography and SDS-PAGE, and displayed the same oxidised and reduced UV/visible spectrum and enzymatic activity. The L56 strain produced twice as much protein as BL21 star, so was used for all further protein expression.

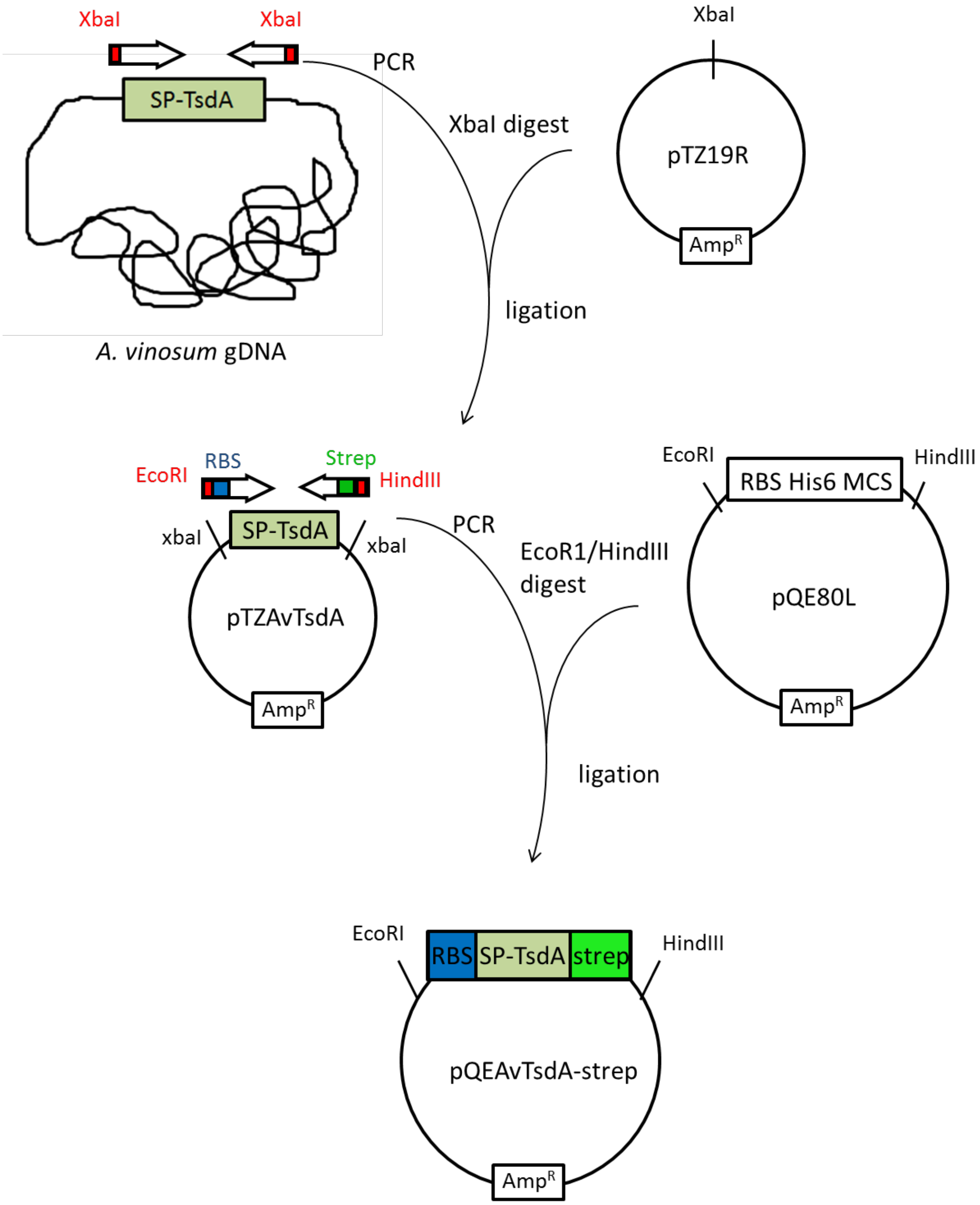

**Figure 4.2 – Cloning strategy for production of recombinant strep-tagged *A. vinosum* TsdA.** TsdA with its native signal peptide was amplified from *A. vinosum* genomic DNA by PCR and inserted into a pTZ19R storage vector by non-directional restriction cloning. Primers for the next cloning stage were designed to introduce a C-terminal strep(II) tag and upstream ribosome binding site (RBS). This product was cloned into pQE80L using directional restriction cloning and resulting in the replacement of the RBS and his$_6$ tag encoded by the plasmid. The procedure resulted in expression plasmid pQE-*Av*TsdA-strep.

To produce pure TsdA, L56 (pEC86) cells expressing TsdA were lysed using a French Press, and purified by Strep-tactin affinity chromatography according to the manual. TsdA was pure as judged by SDS-PAGE following affinity chromatography (Figure 4.4A). In order to ensure homogeneous TsdA with respect to heme maturation, the eluate was diluted five-fold in water to reduce the ionic strength of the buffer and subjected to ion-exchange chromatography using a MonoQ HR 5/5 column (GE Healthcare). TsdA eluted in a single peak, and had less heme-staining contaminants than before ion-exchange chromatography as judged by SDS-PAGE (Figure 4.4B). Final purification was achieved by size-exclusion chromatography in storage buffer (30 mM Tris-HCl pH 8.0 160 mM NaCl).

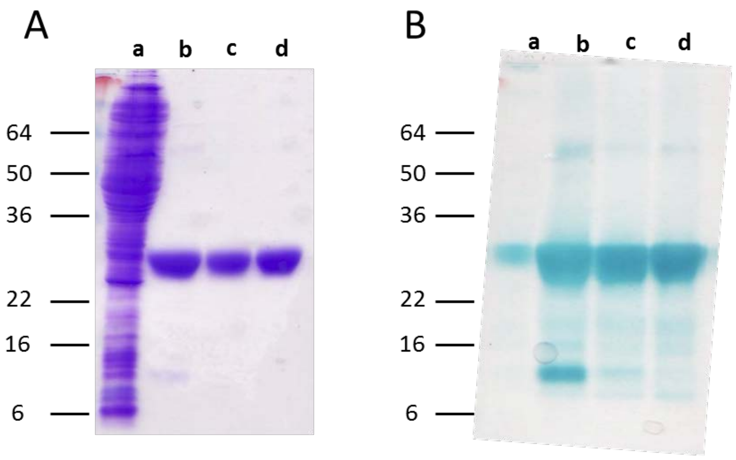

**Figure 4.3 – Purification of *A. vinosum* TsdA.** Samples at each stage of the TsdA purification were analysed by 15% SDS-PAGE. Each sample was loaded twice and analysed either by Coomassie staining to detect total protein, or heme staining to detect proteins with covalently attached heme. **a**) Soluble fraction after cell lysis, **b**) after Streptactin affinity chromatography **c**) after ion-exchange chromatography, **d**) after size-exclusion chromatography. The numbers on the side indicate the position of molecular weight marker bands in kDa.

ESI-MS of purified TsdA showed a single peak at 28,228 Da, consistent with the predicted mass of 28,226 Da for the strep-tagged protein with two covalently bound type *c* hemes and no additional cysteine modifications. SEC-MALS using a Superdex 75 size-exclusion column showed the protein to be a homogeneous monomer of about 26 kDa at all loading concentrations (10, 20 and 40 µM). The protein concentration was determined by the pyridine hemochrome method, which gave the expected signal for a *c*-type cytochrome. The protein was further analysed by UV/visible spectroscopy. The oxidised and dithionite-reduced spectra showed features identical to those previously reported (Denkmann et al., 2012). The specific thiosulfate dehydrogenase activity of the enzyme preparation was assayed by ferricyanide reduction in 100 mM ammonium acetate pH 4.25 to be 8200 U/mg, three times lower than the specific activity of 25000 U/mg at pH 4.2 determined by Denkmann *et al*. The reason for this discrepancy is unclear; however, we note that Denkmann *et al.* determined protein concentration by the BCA assay rather than the more accurate pyridine hemochrome method used here.

## 4.3 Reactivity of Cys123

The first step in determining the mechanism of TsdA was to verify whether the reaction proceeds *via* a covalent intermediate bound to the putative heme iron ligand Cys123, as proposed by Berks and co-workers for SoxAX (Bamford et al., 2002) but disputed by Kappler and co-workers (Kappler et al., 2008). A possible mechanism for the reaction catalysed by TsdA proceeding *via* a covalent intermediate is shown in Figure 4.5. Firstly, thiosulfate is oxidatively conjugated to Cys123. The sulfonate moiety of the cysteine-S-thiosulfonate would then either coordinate the heme iron or Arg119. The next thiosulfate molecule would release Cys123 by thiol:disulfide exchange resulting in production of tetrathionate. It is not clear when re-oxidation of the hemes would occur (Figure 4.5, step e). As a simplification of this mechanism, there are two main reversible catalytic steps which I will largely refer to for the remainder of this chapter: 1) Redox disulfide formation between Cys123 and thiosulfate to form Cys123-S-thiosulfonate (Figure 4.5, steps a and b), and 2) thiol:disulfide exchange between Cys123-S-thiosulfonate and thiosulfate to form tetrathionate (Figure 4.5, steps c and d).

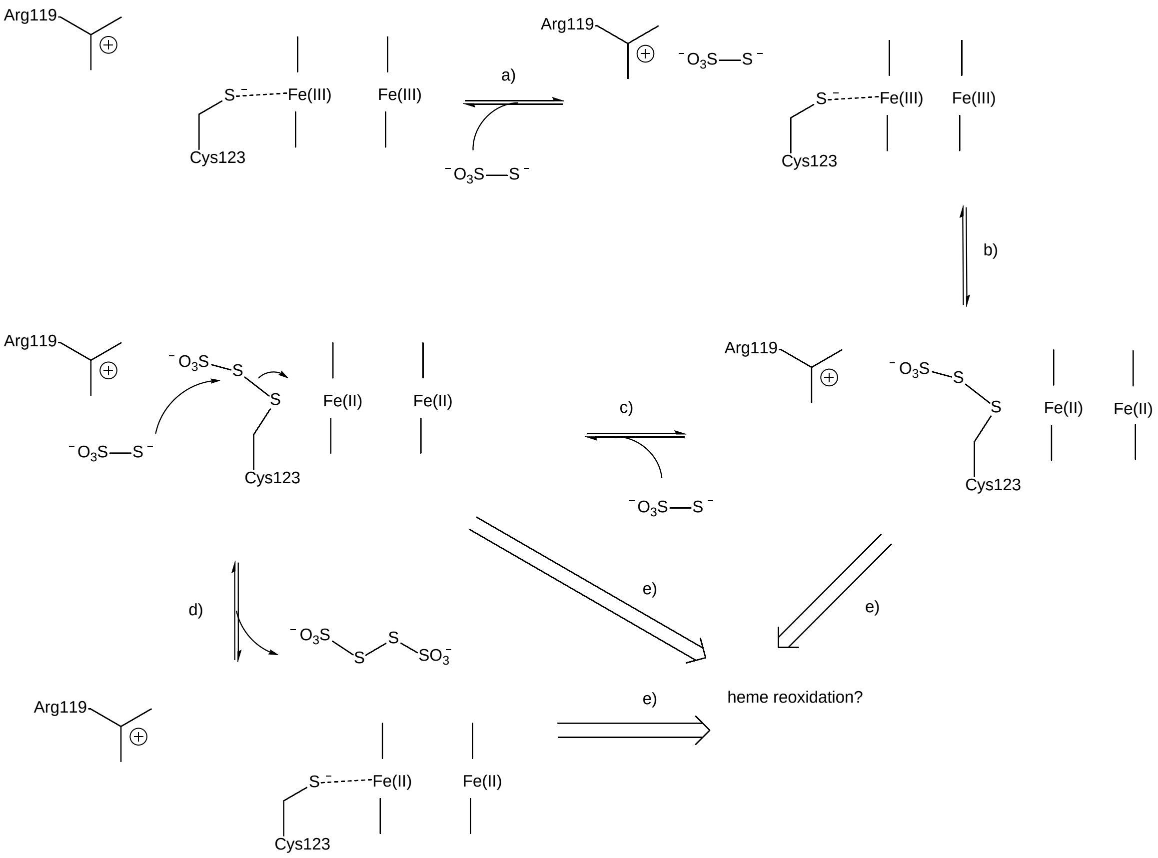

**Figure 4.4 – A possible enzyme mechanism for TsdA based on the proposed catalytic mechanism for SoxAX (Bamford et al., 2002).** Both hemes begin in their oxidised state. a) Thiosulfate binds and is stabilised by Arg119. b) Disulfide formation between thiosulfate and Cys123 to form the covalent cysteine-S-thiosulfonate intermediate. No mechanistic detail has been suggested for this step. c) Binding of the second thiosulfate. d) Reversible thiol:disulfide exchange between second thiosulfate and cysteine-S-thiosulfonate forms tetrathionate and regenerates Cys123 thiolate. e) It is not clear at which stage electrons would be transferred to the downstream electron acceptor. Residue numbering refers to *A. vinosum* TsdA. Each step is assumed to be reversible.

### 4.3.1 Cys123 is accessible to alkylation

The first step of the TsdA-catalysed reverse reaction is a thiol:disulfide exchange reaction which requires nucleophilic attack by TsdA Cys123 on tetrathionate. For this step to be possible, Cys123 must be able to dissociate from the heme iron and thus should be reactive to electrophilic thiolate labelling agents. The alkylating agent iodoacetate reacts with cysteine thiolate nucleophiles to produce cysteine-S-carboxymethyl. This agent is particularly useful for studying the active site chemistry of TsdA because it not only labels reactive thiolates, but the labelled thiolate (S-$CH_2$-$CO_2^-$) is a chemically stable analogue of the putative cysteine-S-thiosulfonate intermediate (S-S-$SO_3^-$). This stable analogue can then in theory be characterised to provide insight into the cysteine-S-thiosulfonate intermediate as well as diagnostic spectra to identify S-thiosulfonation of Cys123. The reactive cysteine of SoxAX is modified to cysteine persulfide. Iodoacetate will react with cysteine perthiolate and so can be used to trap this modification in case the persulfide is lost during sample acidification for ESI-MS, and this is why it is not detected for TsdA.

Incubation of TsdA with 20 mM sodium iodoacetate at pH 8.0 for one hour either in the presence or absence of 2 mM DTT resulted in complete inhibition of thiosulfate:ferricyanide oxidoreductase activity and a single peak in the ESI-MS spectrum of TsdA at +56 Da (Figure 4.6A), consistent with cysteine S-carboxymethylation. Cys123 is the only cysteine in TsdA not covalently linked to heme. This experiment also demonstrates that no cysteine modifications are present in the native enzyme: cysteine persulfide would react with iodoacetate to produce a modification of +90 (58 + 32) Da, whilst other plausible modifications or protonation would either make the thiolate inaccessible or not be removed by S-carboxymethylation.

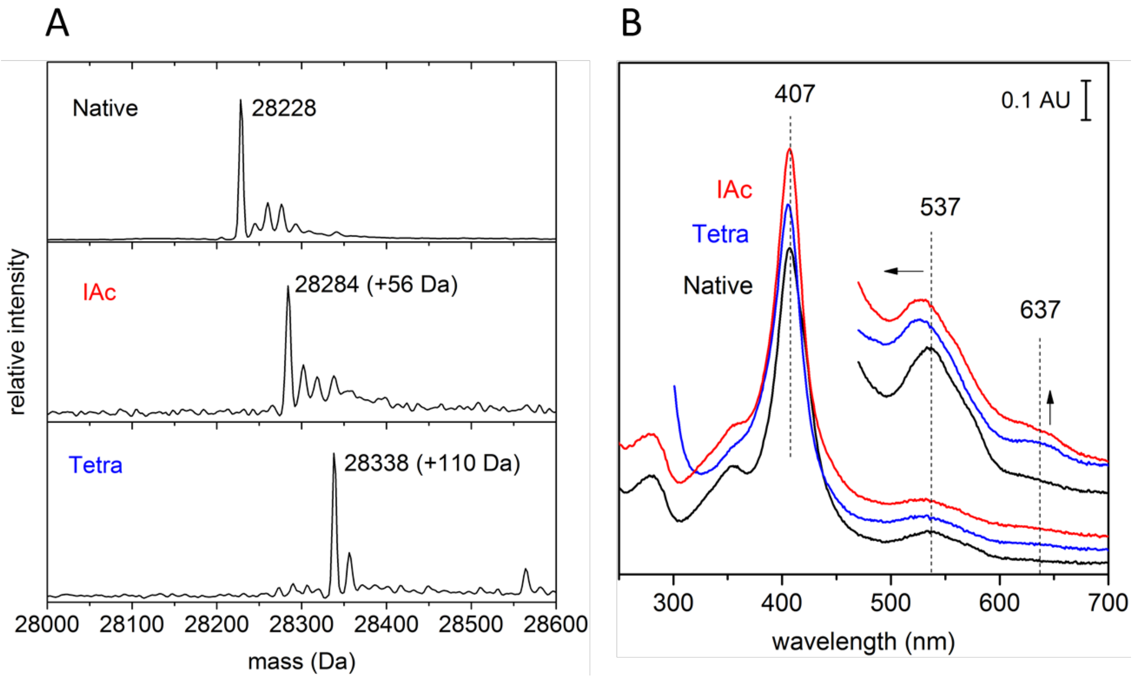

**Figure 4.5 – Modification of Cys123 with electrophiles.** (A) TsdA as described for panel A was diluted in 0.1% TFA, desalted by reverse-phase chromatography and analysed by ESI-MS. (B) UV/visible spectra of 4 μM TsdA, overlaid with spectra of 20 μM TsdA. TsdA was in 30 mM Tris-HCl pH 8.0 160 mM NaCl. Spectra are presented off-set in the Y-axis for clarity. Native – as-isolated protein. Tetra – TsdA after incubation with 50 mM sodium tetrathionate for one hour. IAc – TsdA was treated with 20 mM sodium iodoacetate for one hour and then desalted by size-exclusion chromatography.

A UV/visible spectrum of S-carboxymethylated TsdA (Figure 4.6B) showed three main differences compared to native TsdA: a broadening of the Soret band to lower wavelengths, a shift of the broad oxidised α and β bands to lower wavelength, and an increase at 637 nm. All these features are characteristic of formation of ferric high-spin *c*-type heme (Fedurco et al., 2004). Heme iron becomes high-spin when the heme is either pentacoordinated or if there is a weak-field sixth ligand such as water. These spectral features suggest that modification of the active site cysteine prevents it from coordinating the heme iron analogously to methionine. However, His/carboxylate-ligated hemes are also high spin (Nicola and Leach, 1977), so such an arrangement cannot be ruled out at this stage. Like the native protein, S-carboxymethyl TsdA could be fully reduced by dithionite (Figure 4.7). When compared to the native dithionite-reduced protein, dithionite-reduced S-carboxymethyl TsdA showed slight red shifting of the α band and soret band. A very weak peak at 650 nm could also be distinguished (Figure 4.7, inset).

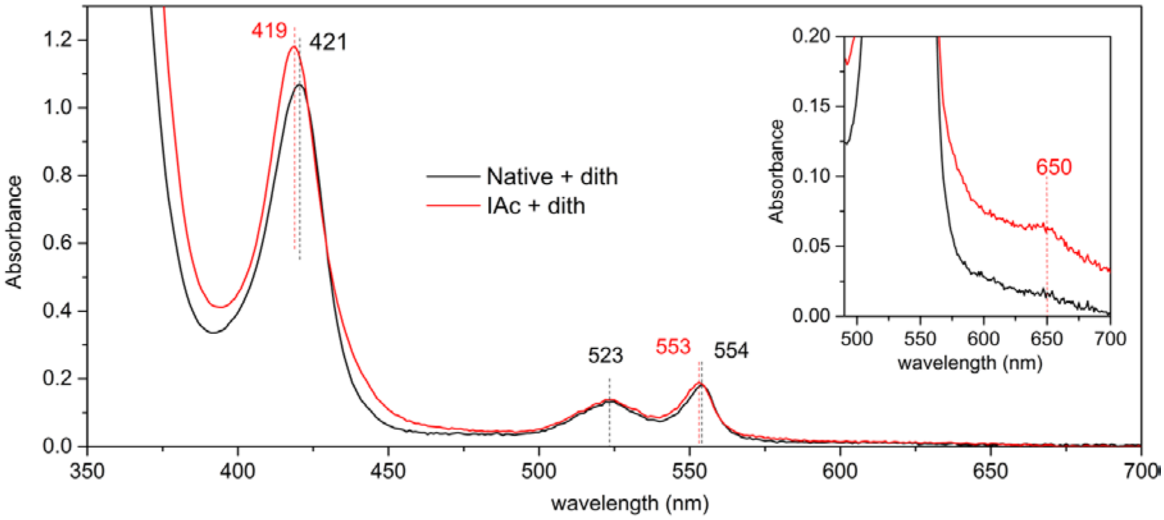

**Figure 4.6 – UV/visible spectra of dithionite-reduced native and modified TsdA.** Main picture shows UV/visible spectra of 4 μM TsdA, whilst the inset shows spectra of 20 μM TsdA. TsdA was in 30 mM Tris-HCl pH 8.0 160 mM NaCl. Native – as-isolated protein. IAc – TsdA was treated with 20 mM sodium iodoacetate for one hour and then desalted by size-exclusion chromatography. Both native and iodoacetate-treated TsdA were reduced with a few crystals of sodium dithionite. Slight scattering due to minor precipitation results in the offset which can be seen in the inset.

### 4.3.2 Cysteine-S-thiosulfonate: a covalent intermediate?

It is known that tetrathionate can modify accessible thiolates to cysteine-S-thiosulfonate by a thiol:disulfide exchange reaction (Sauvé et al., 2009). Furthermore, we know that TsdA catalysis is reversible, and the first step of the reverse reaction would be this very reaction. Electrons from cytochrome *c* would then reduce this cysteine-S-thiosulfonate modification to form thiosulfate and a free cysteine thiolate. However, if no electron donor is present, and the enzyme is in the oxidised state, the reaction would be stalled after cysteine modification. Incubation of TsdA at pH 8.0 with sodium tetrathionate indeed resulted in a modification of +110 Da, as judged by ESI-MS (Figure 4.6A). This is consistent with cysteine-S-thiosulfonation. All ESI-MS samples in this chapter were prepared by acid quenching samples through dilution in

0.1% TFA, which would unfold the protein and therefore prevent any further catalysis occurring. The UV/visible spectrum of tetrathionate modified TsdA (Figure 4.6B) is similar to TsdA-cysteine-S-carboxymethyl. It is therefore likely that the modification is a group with similar physicochemical properties to cysteine-S-carboxymethyl.

The thiosulfonation reaction at pH 8.0 took at least an hour to go to completion even with 50 mM tetrathionate. In contrast, at pH 4.25 the reaction of TsdA with tetrathionate was instantaneous even at an equimolar concentration of tetrathionate (25 μM). A similar increase at 637 nm was observed to that seen with excess tetrathionate at pH 8.0 in the UV/visible spectrum (Figure 4.8D). However, partial reduction of the TsdA also occurred, as evident by the increase in absorption at 554 nm. The reaction of tetrathionate with TsdA would release thiosulfate. At pH 4.25, thiosulfate reduces TsdA, and this is likely to be the cause of the reduction seen here. ESI-MS showed complete thiosulfonation of TsdA at pH 4.25 (Figure 4.8A). It was clear from ESI-MS of thiosulfate- or dithionite-reduced TsdA that the reduction of TsdA interfered with ESI-MS analysis. Therefore, all ESI-MS samples with some proportion of reduced TsdA were oxidised by treatment with a 10:1 excess of potassium ferricyanide after quenching in TFA.

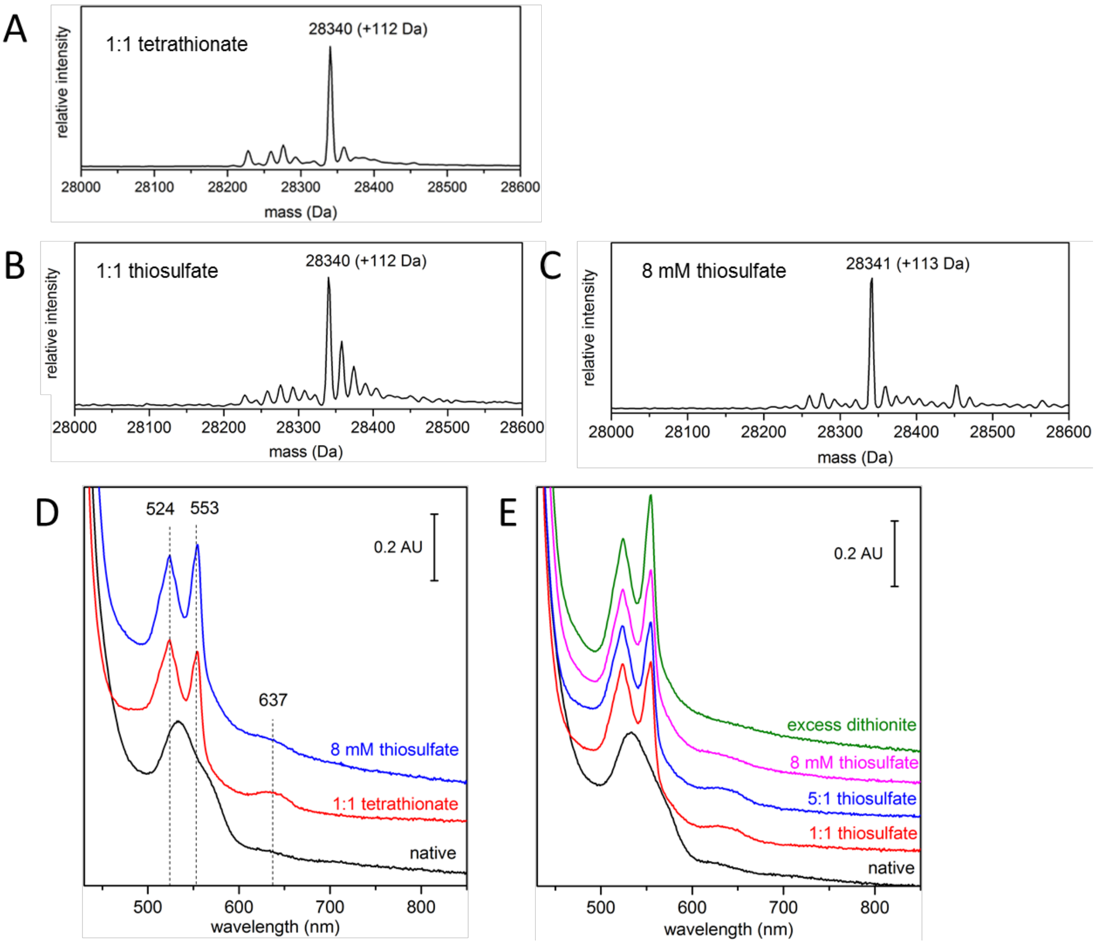

**Figure 4.7 – Reactivity of TsdA with its substrate and product at pH 4.25.** (A-C) ESI-MS of TsdA after the indicated treatment for three minutes at pH 4.25 followed by dilution in 0.1% TFA, oxidation with 10:1 ferricyanide and desalting followed by ESI-MS. (D-E) UV/visible spectra of 25 μM TsdA in 100 mM ammonium acetate pH 4.25. Note that minor precipitation of TsdA due to instability at pH 4.25 occurs during the experiment resulting in an increasingly sloped baseline. All spectra in either panel D or E are of the same sample following treatment with sodium thiosulfate, sodium tetrathionate or sodium dithionite as indicated. Spectra were recorded straight after addition of the sulfur compound.

We next attempted to generate the covalent intermediate by a stalled forward reaction. In this case, an intermediate would form but then may be lost in the second step of the reaction. Whether the intermediate is lost depends on the relative rates of reaction of the first and second steps, where the equilibrium lies for the second step of the reaction and whether the second step is gated by the need for re-oxidation of the catalytic heme. It would be expected that at a 1:1 TsdA:thiosulfate molar ratio, thiosulfate would be oxidatively conjugated to TsdA, and no more thiosulfate would be present to react with the cysteine-S-thiosulfonate by thiol:disulfide exhange in the second step of the reaction. ESI-MS showed that incubation of TsdA with equimolar thiosulfate at pH 4.3 resulted in complete modification of the sample with cysteine-S-thiosulfonate (Figure 4.8B). It would be anticipated that a large excess of thiosulfate would drive the equilibrium of the thiol:disulfide exchange to the right, removing the cysteine-S-thiosulfonate modification. However, incubation of TsdA with 8 mM thiosulfate still resulted in complete thiosulfonation (Figure 4.8C).

One possible explanation for our inability to remove the thiosulfonate group is that the second step of the reaction cannot occur when the heme is reduced. Indeed, the reduced form has decreased positive charge and would be less likely to ligate a cysteine thiolate. Another possibility is that the modification is not actually an intermediate of the reaction. Thiosulfate reduction was also studied by UV/visible spectroscopy. This showed the formation of a small amount of the oxidised high-spin form at 1:1 and 5:1 thiosulfate:TsdA ratios, but this was largely removed by 8 mM thiosulfate (Figure 4.8E). The presence of an oxidised high-spin peak could either be due to turnover of some thiosulfate to tetrathionate which modifies some of the oxidised native enzyme, or due to electron redistribution with unmodified ferric TsdA as an electron acceptor for the reduced modified enzyme.

Further work was undertaken to confirm that the intermediate forms during normal catalysis. Firstly, the protein was modified to TsdA-$SSO_3$ by incubation with tetrathionate followed by desalting. This modification is stable as judged by ESI-MS. A thiosulfate:ferricyanide assay was performed on this sample which was found to be at least as active as a control without tetrathionate incubation. This shows that S-thiosulfonation does not inhibit the reaction, unlike S-carboxymethylation, suggesting it an intermediate which is removed during the reaction. It was also possible to generate the cysteine-S-thiosulfonate intermediate by incubation of TsdA with equimolar tetrathionate at pH 4.25 and then to remove the oxidised high-spin signal at 637 nm with excess (8 mM) thiosulfate (Figure 4.8D). The loss of signal at 637 nm correlates with an increase in the proportion of reduced heme, as shown by an increase in the ratio of the peak at 553 nm compared to the peak at 524 nm. In our proposed mechanism (Figure 4.5), thiosulfate is only able to reduce unmodified TsdA. For thiosulfate to have reduced S-thiosulfonated TsdA, the cysteine-S-thiosulfonate must have first reacted with thiosulfate to generate tetrathionate. Next, we attempted to quench the reaction during turnover and determine whether Cys123 is modified during turnover. A standard thiosulfate:ferricyanide reaction assay was set up, but at pH 6.5 rather than pH 4.3, so that the rate would be decreased. Before the reaction had finished an aliquot was quenched into 0.1% TFA. ESI-MS of this sample showed complete modification to cysteine-S-thiosulfonate. This shows the covalent intermediate is formed under normal turnover conditions. The fact that no free cysteine is visible by ESI-MS corroborates what was seen for the half-reaction with excess thiosulfate.

None of the above experiments directly show that the thiosulfonate is a reaction intermediate, as they do not directly demonstrate turnover of this intermediate to the unmodified enzyme. To test whether the covalent intermediate turns over during catalysis we utilised iodoacetate. This experiment is explained in Figure 4.9A. The enzyme was first modified with 50 mM tetrathionate at pH 8.0 to produce the oxidised S-thiosulfonated enzyme and then tetrathionate was removed using a PD-10 desalting column (GE Healthcare). Sodium iodoacetate (10 mM) was then added to the enzyme. This will quickly react with free thiolates. The S-thiosulfonated enzyme has no free thiolates, and as expected after 10 minutes no alkylation was seen by ESI-MS. If the cysteine-S-thiosulfonate is turned over during the catalytic cycle, then Cys123 will be accessible to alkylation for some proportion of the catalytic cycle. This means that the reaction will be increasingly inhibited by iodoacetate once ferricyanide and thiosulfate are added. This is indeed what was seen (Figure 4.9B), showing that during turnover the cysteine-S-thiosulfonate modification is removed.

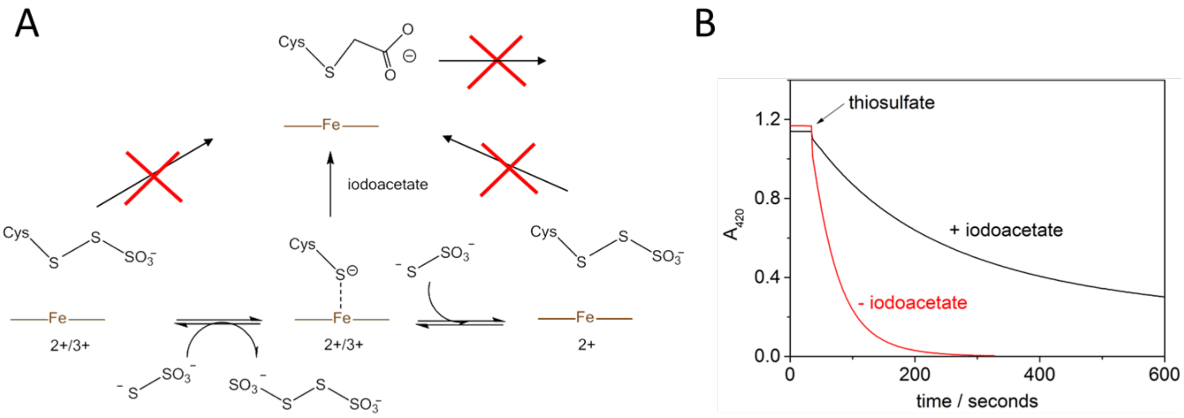

**Figure 4.8 – Experiment to demonstrate the second step of the TsdA mechanism.** (A) Description of the experiment. The starting material was the reaction intermediate, which forms after the first step of the TsdA mechanism. Iodoacetate is used to show that during turnover this covalent intermediate is removed, making the cysteine accessible to alkylation. The alkylated enzyme is irreversibly inhibited. (B) 8 mM ferricyanide was added to S-thiosulfonated oxidised TsdA in 100 mM ammonium acetate pH 4.25 either with or without 20 mM iodoacetate present. The reaction was initiated with 8 mM thiosulfate. In the presence of iodoacetate the rate of reaction increasingly slows.

### 4.3.3 Spontaneous hydrolysis of the covalent intermediate

In initial ESI-MS experiments, samples were prepared in water rather than 0.1% TFA and left at 4$^{o}$C for at least 12 hours. In these experiments there was no cysteine-S-thiosulfonate peak, but one instead at +32 Da, suggestive of a persulfide modification. This means the cysteine-S-thiosulfonate group breaks down over time. To investigate this, TsdA-$SSO_3$ was generated by incubation with tetrathionate and desalting into pH 8.0 storage buffer. This sample was then incubated with 20 mM sodium iodoacetate for an hour at 37$^{o}$C. ESI-MS of this sample (Figure 4.10) showed two peaks – a minor species at +110 Da, cysteine-S-thiosulfonate, and a major species at +88 Da which matches the mass increase for an S-carboxymethylated cysteine persulfide. This confirms slow hydrolysis, or alternatively reductive cleavage, of cysteine-S-thiosulfonate to cysteine persulfide. This could explain why purified SoxAX usually has a cysteine persulfide at the active site. Cysteine persulfurated TsdA was as active as native TsdA and could be reduced with equimolar thiosulfate at pH 4.25.

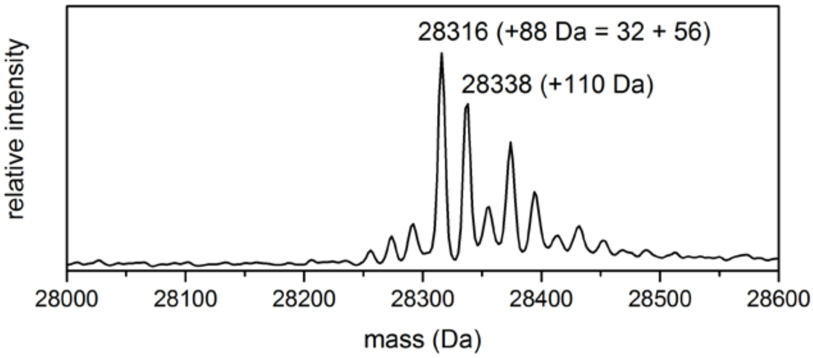

**Figure 4.9 – The cysteine-S-thiosulfonate group breaks down over time.** ESI-MS spectrum of TsdA-$SSO_3$ incubated with iodoacetate to trap free thiolates for one hour followed by dilution in 0.1% TFA. Thiosulfonation of the cysteine increases the mass of the protein by 112 Da. The largest peak at 28316 Da corresponds to an increase of 32 Da from a cysteine persulfide, with an additional 56 Da from trapping by iodoacetate to form cysteine-S-S-carboxymethyl.

## 4.4 Structural insight into the mechanism of TsdA

The most direct way to understand the specific details of the TsdA catalytic mechanism is to obtain structural data of the enzyme active site, preferably with ligands or intermediates bound. To this end, we attempted to crystallise native TsdA and TsdA-$SSO_3$. All indexing, phasing and refinement in this section was performed by Paul Chappell with help from Steven Johnson, both in the group of Susan Lea.

### 4.4.1 Crystallisation trials and issues with structure of native TsdA

Crystallisation trials were attempted with purified TsdA in 10 mM tris-HCl pH 8.0 at 4, 8 and 12 mg/mL. Initial trials were performed by the sitting drop method solely using the Stura Macrosol commercial screen (Molecular Dimensions). The best crystals were obtained at a protein concentration of 12 mg/mL. Large orange crystals grew in a condition containing 200 mM ammonium sulfate 12% PEG 8K. These crystals were in space group $P_1$ and diffracted to 1.6 Å resolution. The dataset was phased by molecular replacement using a model composed of the catalytic domain of SoxA and the cytochrome *c* domain from *Pseudoalteromonas haloplanktis* nitrite reductase. There were two immediate issues with the structure. Firstly, the non-catalytic heme did not have a clear second axial ligand, and secondly there was a large amount of confusing and difficult to fit density near the catalytic cysteine, Cys123. To combat the second issue, crystal trials were repeated in the presence of 2 mM DTT to prevent any oxidative modifications of Cys123.

### 4.4.2 Crystallisation trials and structure of TsdA-DTT

TsdA in the presence of 2 mM DTT did not form large, singular crystals in the same condition as native TsdA. Better crystals were formed in a condition containing 0.1 M ammonium acetate pH 4.5 9% PEG 10K. We screened around this condition to produce large, well separated crystals which it was hoped would diffract to higher resolution and be able to resolve the active site and second heme ligand well. The pH was varied from 4.0 to 5.0 and the percentage of PEG 10K was varied from 6.0% to 10.25%. The crystals which grew in 100 mM ammonium acetate pH 4.6, 7.5% PEG 10K diffracted to 1.5 Å resolution in space group $C_{121}$.

### 4.4.3 Overall architecture of TsdA and structure of the electron transfer heme

As predicted from sequence, the structure consists of two cytochrome *c* like domains connected by a long extended structure linker (Figure 4.11). The domains pack against each bringing the two hemes close together.

The N-terminal cytochrome *c* domain contains the His/Cys ligated heme, and so is assigned as the catalytic domain. This domain aligns well with the either of the duplicated cytochrome domains of di-heme SoxA (1.84 Å RMSD with *R. sulfidophilum* SoxA non-catalytic domain, residues 74-175, and 2.35 Å RMSD with the catalytic domain, residues 177-282). The other domain has a standard mitochondrial cytochrome *c* fold, with highest structural homology to cytochrome *c*L (MoxG) from *Methylobacterium extorquens* (3.36 Å RMSD). All RMSD values were determined using the BioXGEM server.

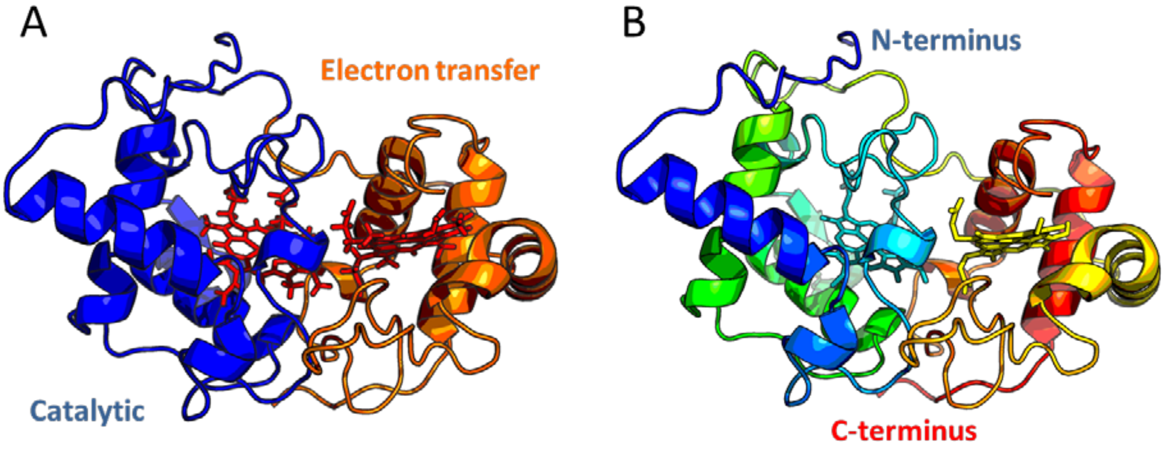

**Figure 4.10 – Structure of TsdA.** TsdA is in cartoon representation with the heme groups in stick representation. (A) The catalytic domain and electron transfer domains are indicated, whilst both hemes are coloured in red. (B) TsdA coloured by sequence starting at blue for the N-terminus, through cyan, green, yellow, orange and finally red for the C-terminus. The hemes are coloured according to the part of the chain they are covalently linked to.

The overall architectures of SoxAX and TsdA can be compared by aligning the catalytic domain of each (Figure 4.12A). TsdA has no part which corresponds to the non-catalytic domain of SoxA. It is likely that this domain assists in interactions with the substrate-carrier protein SoxYZ (see Chapter 3, Section 3.7.4). The same face of the catalytic domain of TsdA and SoxA is packed against the electron transfer domain (SoxX for SoxAX). However, the arrangement of the electron transfer domain relative to the catalytic domain differs for each protein. This alters the relative arrangement of the two hemes in each protein (Figure 4.12B). The hemes in TsdA are well within electron transfer distance with a heme edge to edge distance of 8.1 Å. The difference in packing means that this distance is closer than the corresponding value of 10.7 Å for the two hemes in SoxAX. The electron transfer rate between two hemes is related to the distance between the hemes. This means that TsdA will have a faster rate of electron transfer than SoxAX. The electron transfer heme in SoxX is relatively planar (Figure 4.12C), whilst the electron transfer heme in TsdA is heavily distorted from planarity. This distortion is common for cytochrome *c* hemes and is known as heme ruffling. Heme ruffling may reduce the electron transfer rate to the heme (Sun et al., 2014) and reduce the redox potential of the heme (Can et al., 2011).

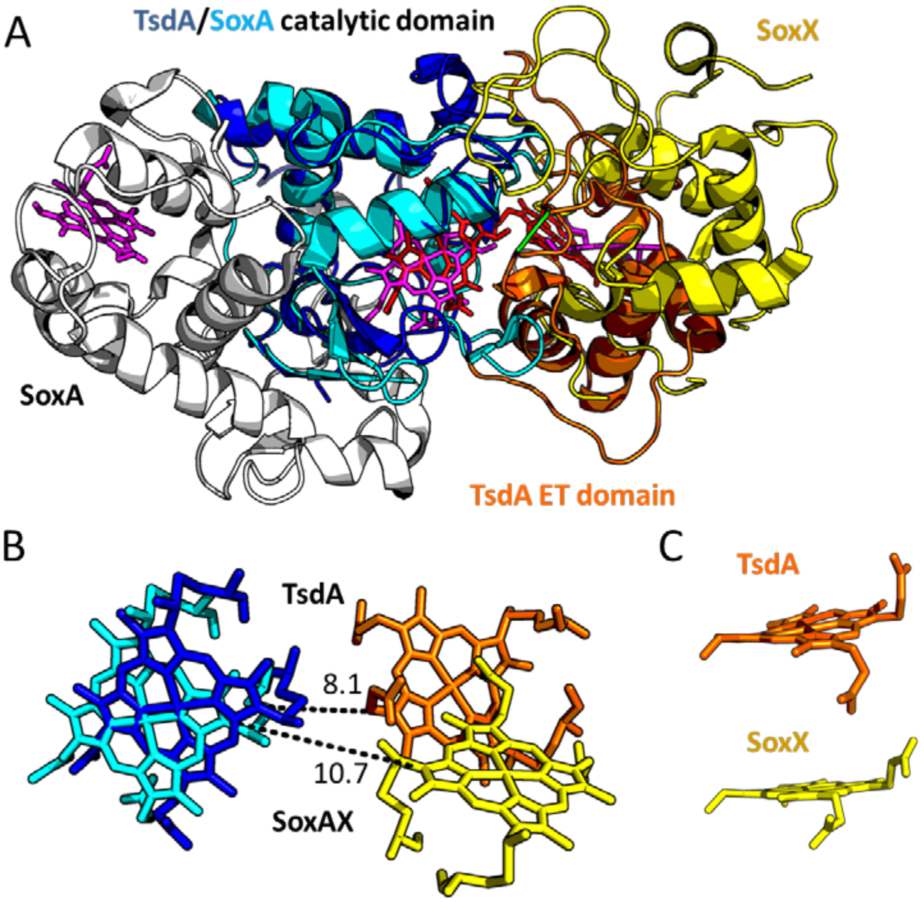

**Figure 4.11 – Comparison of the architecture and heme positions for TsdA and SoxAX.** (A) SoxAX and TsdA are aligned by superposition of the catalytic domains of each. The colours of each domain are indicated. The heme groups of SoxAX are coloured in purple, whilst those of TsdA are in red. (B) Comparison of the arrangement and distances between the two heme pairs, which are coloured according to the domain they are found in. The distances between the hemes are indicated in Angstroms and show the edge-to-edge distance between the heme groups. (C) Comparison of the extent of heme ruffling for the hemes in SoxX and the TsdA electron transfer domain.

Denkmann et al predicted that either of the conserved methionines Met222 or Met236 would serve as the axial ligand to the C-terminal heme (Denkmann et al., 2012). Our structure shows that Met236 plays this role. Met222 is positioned directly in between the two hemes, as is another conserved hydrophobic residue, Phe231. Phe231 is rather close to the C-terminal heme itself, and may be affecting the redox potential of this heme. These two residues could possibly transmit redox or ligation changes between the two hemes. However, the catalytic rate of the enzyme is much faster than would be expected if any conformational changes occurred. Another possibility is that these hydrophobic residues alter the dielectric constant of the electron transfer pathway between the two hemes, and thus increase the rate of electron transfer between the hemes.

The loop which the axial ligand of the electron transfer heme, Met236, is part of displays high B-factors relative to the rest of the TsdA structure (Figure 4.13A). This loop forms part of the solvent-accessible surface which is closest in distance to the heme-edge of the electron transfer heme. This surface also displays high sequence conservation (Figure 4.13B) and is expected to form the interface with the physiological redox transfer partner of TsdA. Flexibility at electron-transfer interfacial sites has previously been shown to be important for the electron transferring flavoprotein (Leys et al., 2003). The identity of the physiological electron transfer partner protein of TsdA is not known in *A. vinosum*. The protein in the *A. vinosum* genome with the highest homology to TsdB from other organisms is the diheme cytochrome *c*, Cyt $c_4$. The residues which form the putative interaction surface on TsdA are alanines, prolines, leucines and a phenylalanine, all residues with non-polar character (Figure 4.13C). This non-polarity of the possible TsdA interaction surface is further displayed by the surface potential of TsdA, showing that this area is uncharged (Figure 4.13D). The non-polarity of the possible TsdA interaction surface would fit well with Cyt $c_4$ being its downstream electron acceptor as the lower potential heme of Cyt $c_4$ is surrounded by a non-polar surface (Kadziola and Larsen, 1997). To understand the role of the flexibility of the predicted TsdA interaction interface it would be necessary to either determine the physiological redox partner of *A. vinosum* TsdA, or do a more detailed structure-led study of TsdA and TsdB from an organism with both proteins.

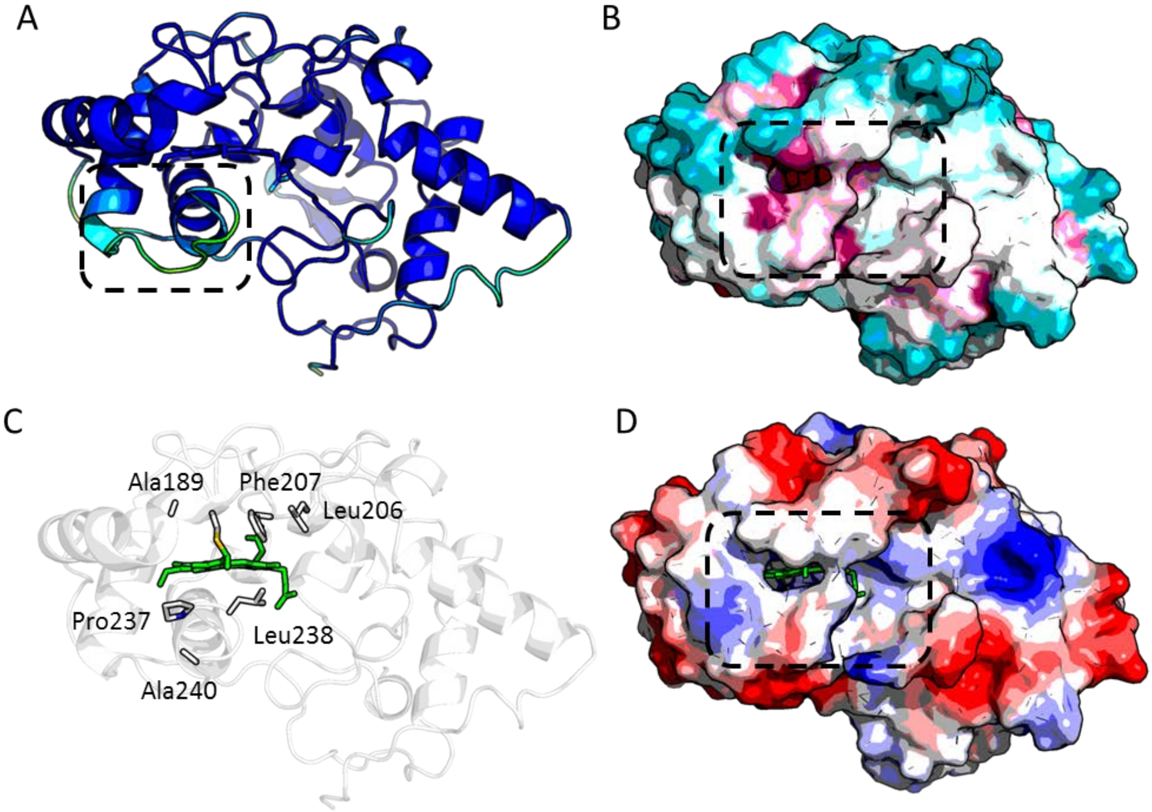

**Figure 4.12 – Characteristics of a possible interaction site with the downstream electron acceptor.** (A) TsdA in cartoon representation coloured by b-factor. Low b-factors are coloured in blue, whilst warmer colours represent higher b-factors. (B) Residues at the possible interface site are shown in stick representation. The electron transfer heme is shown in green. (C) Surface representation of TsdA coloured by conservation. Cyan indicates low conservation, white indicates medium conservation, and magenta indicates high conservation. The surface conservation was calculated using the Consurf server (Celniker et al., 2013). (D) The surface potential of TsdA calculated in PyMOL. Positively charged regions are coloured in blue, negatively charged regions in red, and uncharged regions in white.

### 4.4.4 The TsdA active site

In comparison to SoxAX, the active site pocket of TsdA is very small and the catalytic cysteine is inaccessible to bulky substrates (Figure 4.14A). The main reason for this is the differing arrangements of the electron transfer domains of each protein. For TsdA, the electron transfer domain occludes the main channel and pocket present in SoxAX, as shown in Figure 4.14B. It would be expected that SoxAX has a much larger active site, as it has to accommodate the C-terminal carrier arm of SoxY, similarly to SoxB (see Chapter 3). The TsdA active site only has to accommodate thiosulfate. However, it is strange that the catalytic cysteine is inaccessible to thiosulfate. One explanation for this is that there is a lot of flexibility in the residues which surround the active site. This is particularly true of the heme propionate group, which has a minor flipped conformation, where it would no longer block the active site.

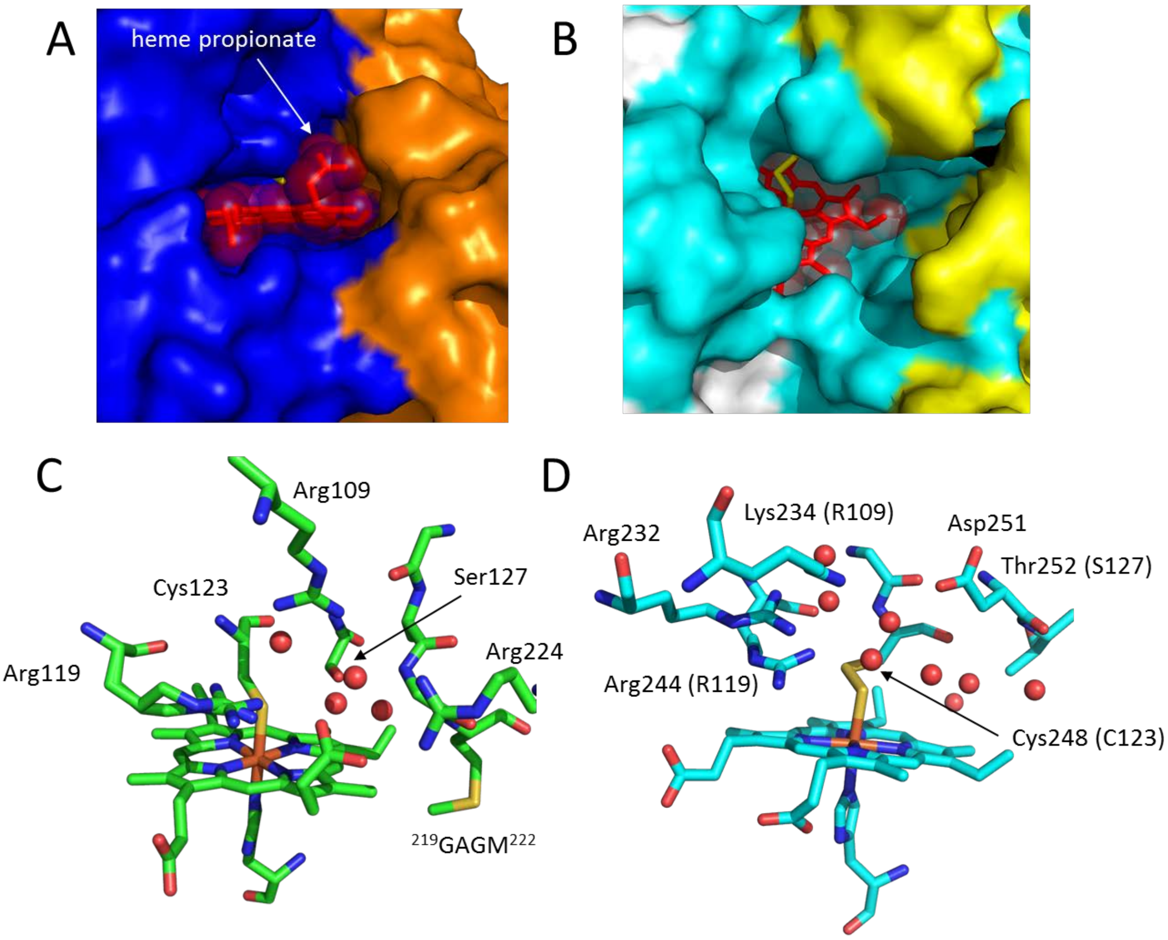

**Figure 4.13 – The active sites of TsdA and SoxAX.** (A) The TsdA active site shown as surface representation with the same colour scheme as Figure 4.11. The catalytic cysteine is shown in stick representation in yellow, whilst the heme is shown in red with transparent spheres indicating the Van der Waals radius of each atom. (B) The active site of *R. sulfidophilum* SoxAX (PDB:1H33) displayed with the same representation as A. (C) The active site of TsdA and (D) the active site of SoxAX. Residues discussed in the text are highlighted, and ordered water molecules shown as small spheres. SoxA residues which are conserved in SoxAX and TsdA are shown with the *A. vinosum* TsdA residue numbering in brackets.

Similarly to SoxAX, the active site is highly positively charged, due to three arginines in the immediate vicinity of Cys123: Arg109 and Arg119 from the N-terminal domain and Arg224 from the C-terminal domain. Arg119 is absolutely conserved in TsdA and SoxA. Arg109 can be a lysine in TsdA but is not conserved as a basic residue in SoxA. In SoxA the arginine two residues before the equivalent to TsdA Arg109 (SoxA Arg232) is conserved and may have a similar role to TsdA Arg109 (Figure 4.14C,D). Arg224 is not absolutely conserved in TsdA, although it is the most common residue at this position. Arg119 is expected to play the role equivalent to the catalytic arginine in rhodanese. The other arginines may have less direct roles in catalysis. They could greatly influence the electrostatic potential of the active site, which could affect the $pK_a$ values of catalytic residues, the electrochemical potential of the catalytic heme, or simply favour rapid binding of the anionic substrate thiosulfate. Arg109 is the second closest arginine to the catalytic cysteine. Arg224 forms a salt-bridge with the alternative conformation of the heme propionate. Arg109 and Arg224 are very disordered, whilst Arg119 is in multiple conformations. This is surprising if these residues are involved in binding and positioning the substrates or intermediate. They may become more ordered upon binding of substrates.

Aside from these arginines, another interesting conserved residue in the active site is Ser127. This is the closest residue to Cys123, along with Arg119, and coordinates one of the ordered water molecules in the active site. This water is also coordinated by the amide backbone of Gly221 and Met222 (the methionine positioned in between the two hemes). This water is within hydrogen bonding distance of a second ordered water molecule, which is coordinated by Arg119. In SoxAX there is no conserved residues equivalent to Ser127, Gly221 or Met222.

The density for the catalytic cysteine, Cys123, is not well-defined (Figure 4.15). The most intense density reflects the sulfur atom, which is able to reach to coordinate the heme iron without an additional persulfide sulfur atom, as is present in SoxAX structures (Bamford et al., 2002). However there is broad density above the sulfur atom. This may be due to a subset of cysteine being oxidised to cysteine-sulfinic acid (Cys-$SO_2^-$) during the timespan of crystallisation. Another possibility is that the cysteine is in three alternative conformations; however the density appears to be too strong for this option. Attempts to obtain ESI-MS data for crystals proved unsuccessful due to difficulty in removing PEG. We also tried to generate an anomalous sulfur difference map using a higher wavelength X-ray beam. This map did not have the resolution required to unambiguously assign the density.

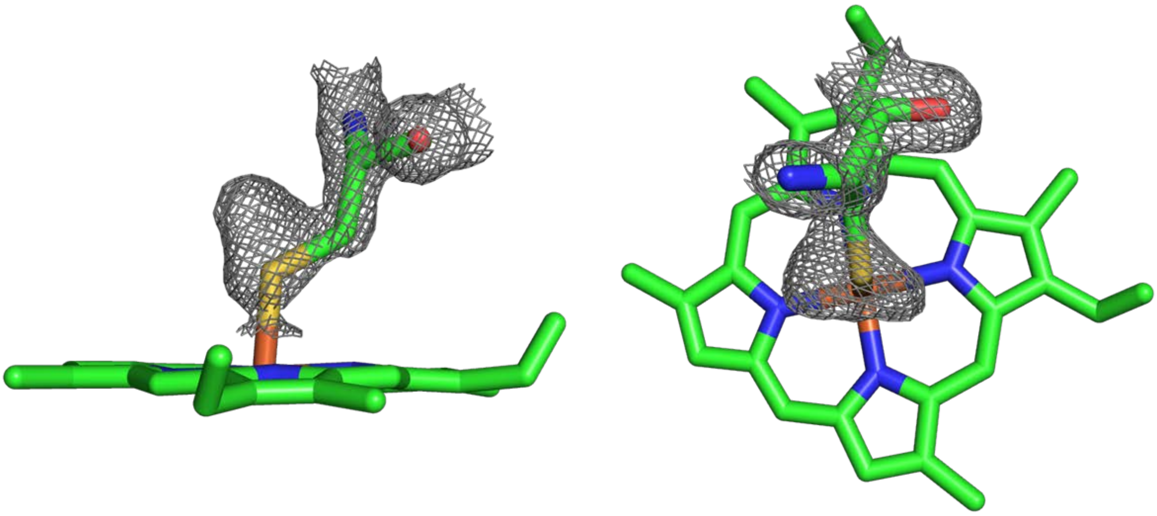

**Figure 4.14 – Electron density of the catalytic cysteine, Cys123.** The ambiguous electron density ($2F_c$-$F_o$) of Cys123 is shown from two angles, contoured at 2.0 $\sigma$.

### 4.4.5 Attempts to crystallise TsdA with cysteine adducts – structure of TsdA-persulfide

For the initial attempts to crystallise TsdA with cysteine adducts TsdA was cocrystallised with either 2 or 5 mM thiosulfate or tetrathionate. As became clear from biochemical studies, the cysteine-S-thiosulfonate adduct would be likely to break down in the time required for crystallisation. These trials were performed using the same ammonium acetate/PEG 10K screen as for TsdA-DTT. Cocrystallisation with either thiosulfate or tetrathionate resulted in much larger crystals than with DTT, and also at slightly higher pHs – around 4.6 rather than 4.1 for TsdA-DTT. Crystals of TsdA-tetra and TsdA-thios were shot and phased using TsdA-DTT as a molecular replacement model. TsdA-tetra was solved at 1.3 Å resolution and TsdA-thios at 1.55 Å resolution. Both structures were very similar, but the density was clearer in the TsdA-tetra structure, so only this structure will be discussed.

**Table 4.1 – TsdA-tetra X-ray data collection statistics**

| | |
|---|---|
| X-ray source | Diamond - i03 (0.920 Å) |
| Space group | C2 |
| Cell dimensions | *a* = 79.28 Å, *b* = 70.42 Å, *c* = 57.91 Å<br>$\alpha$ = 90.00°, $\beta$ = 129.34°, $\gamma$ = 90.00° |
| Resolution (Å) | 44.52 -1.29 (1.32-1.29) |
| Total reflections | 170161 |
| Number of unique reflections | 60432 |
| Completeness (%) | 97.8 (98.0) |
| Multiplicity | 2.8 |
| $R_{merge}$ | 0.034 (0.47) |
| I / δ (I) | 15.5 (2.3) |
| **Refinement statistics** | |
| R (%) | 14.83 (24.70) |
| $R_{free}$ (%) | 16.40 (26.40) |
| **Root mean square deviation from idealized covalent geometry** | |
| Bond length (Å) | 0.03 |
| Bond angles (°) | 2.42 |
| Average B value (Å$^2$) | 22.52 |
| Ramachandran outliers (%) | 0.42 |
| Residues modelled | 234 |
| Non-protein molecules | 202 waters, 2 hemes & 1 thiosulfate |
| Molprobity score | 1.22 |

In the TsdA-tetra structure the active site cysteine is not modified with S-thiosulfonate, but instead with a persulfide sulfur atom. This persulfide is likely to result from hydrolysis of the thiosulfonate intermediate as discussed in Section 4.3.3. This is accommodated in place of a coordinating cysteine thiolate, in the same manner as the cysteine perthiolate of SoxA. The density for both sulfur atoms of the cysteine persulfide is much cleaner than the density for the cysteine sulfur in the TsdA-DTT structure. The position of Ser127 and the ordered water coordinated by Ser127 are unchanged in this structure. However, new density has appeared almost on top of the second ordered water. This could be fitted as a thiosulfate molecule at 50%

occupancy with the ordered water also at 50% occupancy. Thiosulfate would be formed by the reaction of TsdA with the tetrathionate. The sulfane sulfur is coordinated by Arg119, whilst Arg109 is likely to coordinate both the sulfane sulfur and a sulfonate oxygen. In this structure the density for Arg119 and particularly Arg109 is clearer than for the TsdA-DTT structure. This indicates that these arginine residues become more ordered upon substrate binding. The amide backbone of Gly221 also hydrogen bonds to a sulfonate oxygen. The heme propionate group is largely in the flipped conformation, allowing access to the active site.

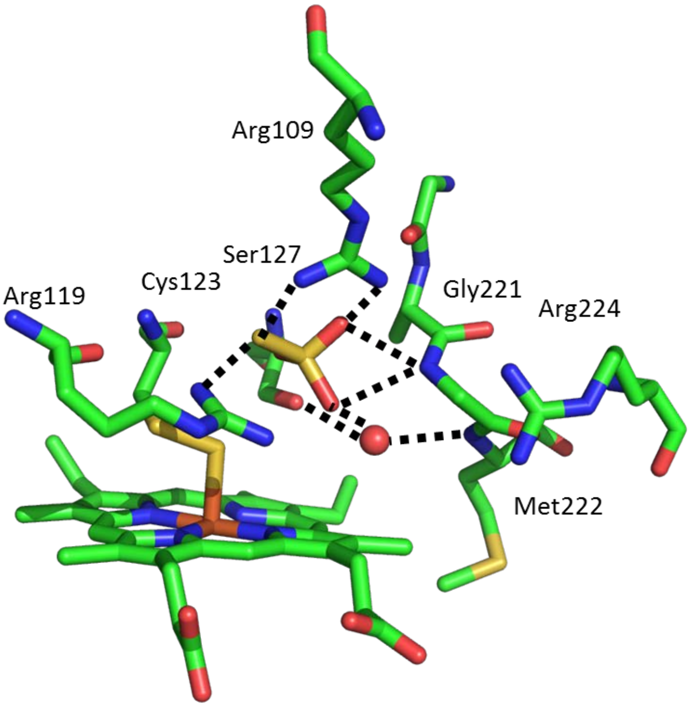

**Figure 4.15 – Structure of the active site of TsdA co-crystallised with tetrathionate.** The same residues are shown as in Figure 4.13C. Hydrogen-bonding between active site residues and the thiosulfate molecule and ordered active site water molecule are indicated.

### 4.4.6 Attempts to obtain a structure of thiosulfonated TsdA

To gain a clear structural understanding of the intermediate state, we needed a structure of the non-hydrolysed intermediate. Two approaches were used to attain this. Firstly, crystallisation trials were set up using the S-carboxymethylated protein. In theory this should be unable to hydrolyse. TsdA-IAc did not form as large and singular crystals as the native protein and the best TsdA-IAc crystals only diffracted to 2.3 Å resolution. The density in the active site was not clear. There was no clear density for an S-carboxymethyl group. This may be because the group was too disordered to see at this resolution, or was hydrolysing over time, or perhaps was decarboxylated due to radiation damage. It was difficult to ascertain the long-term stability of TsdA-IAc at low pH because the protein precipitated after several hours. We therefore abandoned this approach.

To decrease the extent of S-thiosulfonate breakdown we grew TsdA crystals in the presence of 2 mM DTT and then soaked these crystals in a cryoprotectant solution containing sodium tetrathionate. With 10 mM tetrathionate and time periods under 10 minutes no additional density was seen in the TsdA active site. This may be due to the heme propionate group occluding the active site in the cyrstallised TsdA-DTT form. When the concentration was increased to 50 mM and soaking performed over 2 hours new density appeared in the active site, however this was largely the persulfide break-down product. A small amount of density covalently linking the cysteine sulfur atom to the thiosulfate group could be seen in this structure. However, this density had sufficiently low occupancy that we abandoned this approach, and instead tried to understand the role of the active site residues by site-directed mutagenesis.

## 4.5 Mutagenesis of residues implicated in the mechanism by the crystal structures

The crystal structures and sequence conservation implicate a number of residues in the enzymatic mechanism of TsdA. We therefore alanine-substituted some of these residues to determine their exact role in each step of the mechanism. The substitutions investigated were: Arg119Ala, Ser127Ala, Arg109Ala and Arg224Ala. Arg119 appears to position the thiosulfate substrate for the oxidative disulfide bond formation step. Ser127 is absolutely conserved in TsdA, but not present in SoxAX. This would be consistent with a role of Ser127 in the second step of the mechanism, which involves a substrate with very different physicochemical properties for SoxAX compared to TsdA. Arg109 is very close to the active site and appears to coordinate the thiosulfate substrate. However, this residue is not well conserved and shows a lot of disorder. Arg224 is not present in SoxAX, and appears to stabilise the flipped conformation of one of the heme propionate groups. One possibility is that this negatively-charged propionate-group mimics the second thiosulfate group, and so Arg224 is involved in positioning the substrate in the second step of the mechanism.

All variants expressed well and were purified using the same method as used for the native protein.

### 4.5.1 Enzymatic activity of TsdA variants

Under standard thiosulfate dehydrogenase activity conditions (8 mM thiosulfate, 1 mM ferricyanide), the R224A variant only showed a small decrease in activity to about 70% of wild-type. The activity of the R109A and S127A variants were respectively 53% and 36% of wild-type activity whilst the thiosulfate dehydrogenase activity of the R119A variant was about 3% of wild-type activity. This result shows that Arg119 has an important catalytic role.

The thiosulfate dehydrogenase activity of TsdA displays complex Michaelis-Menten kinetics (Hensen et al., 2006). The two substrate steps result in a substrate vs. rate curve which is most easily modelled as positive cooperativity using the Hill equation. A further complication is that the concentration of ferricyanide has a large impact on the kinetic behaviour. At the standard condition of 1 mM ferricyanide, the enzyme has a relatively high $K_M$ value for thiosulfate of 1.1 mM. As the concentration of ferricyanide is decreased this $K_M$ decreases, indicating that the effective affinity of the enzyme for substrate increases at lower ferricyanide concentrations. However, the opposite effect is observed with the $k_{cat}$, which decreases at lower ferricyanide concentrations.

We determined the $K_M$ and $k_{cat}$ values of the wild-type enzyme and each variant under low (0.2 mM) and high (1 mM) ferricyanide conditions.

**Table 4.2 – Kinetic behaviour of TsdA variants.** All measurements are at pH 4.25. Relative activity refers to the activity with 8 mM thiosulfate and 1 mM ferricyanide compared to wild-type TsdA. Error values show the standard error of the mean for fits of curves with duplicate points.

| Variant | Relative activity (%) | 0.2 mM ferricyanide | | | 1 mM ferricyanide | | |
|---|---|---|---|---|---|---|---|
| | | $K_M$ (mM) | $k_{cat}$ ($s^{-1}$) | $n$ | $K_M$ (mM) | $k_{cat}$ ($s^{-1}$) | $n$ |
| Wild-type | 100 | 0.22 ± 0.03 | 920 ± 50 | 1.4 ± 0.25 | 2.2 ± 0.3 | 4280 ± 150 | 1.52 ± 0.25 |
| S127A | 36 | 4.4 ± 0.5 | 1530 ± 150 | 2.4 ± 0.7 | 10.7 ± 6.2 | 3060 ± 920 | 1.1 ± 0.4 |
| R119A | 3 | 17 ± 2 | 378 ± 20 | 1.2 ± 0.1 | 47 ± 7 | 640 ± 40 | 1.0 ± 0.05 |
| R109A | 53 | 1.11 ± 0.25 | 780 ± 95 | 1.6 ± 0.5 | 5.8 ± 0.8 | 3210 ± 310 | 1.7 ± 0.3 |
| R224A | 69 | 0.44 ± 0.05 | 870 ± 50 | 1.3 ± 0.2 | 2.5 ± 0.8 | 3670 ± 460 | 1.14 ± 0.26 |

The R224A substitution results in a small increase in the $K_M$ value under low ferricyanide conditions and affects no other parameters. It is therefore unlikely that Arg224 is directly involved in substrate binding and positioning or transition state stabilisation. The small apparent weakening of affinity under low ferricyanide conditions may reflect the need for overall positive charge in the active site to favour binding of substrates.

The R109A substitution increases the $K_M$ values at both low and high ferricyanide concentration, without strongly affecting the $k_{cat}$ values. Our structural studies show that Arg109 and Arg119 bind to thiosulfate. Our structure probably reflects the binding site of thiosulfate in the first step of the mechanism. Arg109 and Arg119 are also likely to bind to the thiosulfonate group of the cysteine-S-thiosulfonate intermediate, as there is no reason why this would not remain bound to Arg109 and Arg119 after disulfide formation. This means Arg109 is involved in both steps of the mechanism and so its effect on the kinetic parameters is difficult to deconvolute. Simplistically, an increase in $K_M$ is consistent with the role of Arg109 in binding to thiosulfate.

The R119A substitution decreases the $k_{cat}$ values and substantially increases the $K_M$ values at both ferricyanide concentrations. This is consistent with Arg119 being involved in a catalytic step, such as transition state stabilisation, as well as binding to the substrate. Similarly to Arg109, the effect of the substitution on the kinetics will be complicated as Arg119 is probably involved in both steps of the mechanism.

The S127A substitution results in many changes to the kinetic parameters of TsdA. At low ferricyanide concentration there is a 20-fold increase in $K_M$ but also a two-fold increase in $k_{cat}$. This is similar to the effect of increasing ferricyanide concentration. Also noteworthy, is the increase in the Hill coefficient, $n$. The error on this value is large, but the increase here to 2.4 is quite substantial. At high ferricyanide concentrations the substitution causes a 5-fold increase in $K_M$ with no large effect on $k_{cat}$. Without developing a complete model to mathematically describe the enzyme mechanism and effect of ferricyanide it is very difficult to assign these changes in parameters to specific effects on different steps of the mechanism. It does at least show that Ser127 is important in the enzyme mechanism, and has a distinct role to Arg109 and Arg119.

### 4.5.2 Effect of substitutions on enzymatic half-reactions

A perhaps simpler way to determine the role of each residue it to study the effect of each alanine substitution on the half reactions described in Section 4.3.2. It should be noted that the turnover rate of the enzyme is much faster than UV/visible spectra can be recorded by a standard setup. So a significant effect is required to be noticeable without a stopped-flow setup and diode-array spectrophotometer. However, the concentrations of substrates used in these experiments are much lower than the $K_M$ values determined above which should decrease the rate to some extent.

The variant enzymes showed some differences in their visible spectra compared to wild-type TsdA before treatment with sulfur compounds (Figure 4.17A). The R109A and R224A variants have larger high-spin heme peaks at 625 nm, whilst the S127A variant has a slightly smaller peak at this position. The 625 nm peak is larger for the R119A and R109A variants, but otherwise has a similar shape to the wild-type enzyme. It is noticeable that the position of the peak is not the same as the tetrathionate modified wild-type enzyme, which has a peak at 637 nm (Figure 4.17B black spectrum).

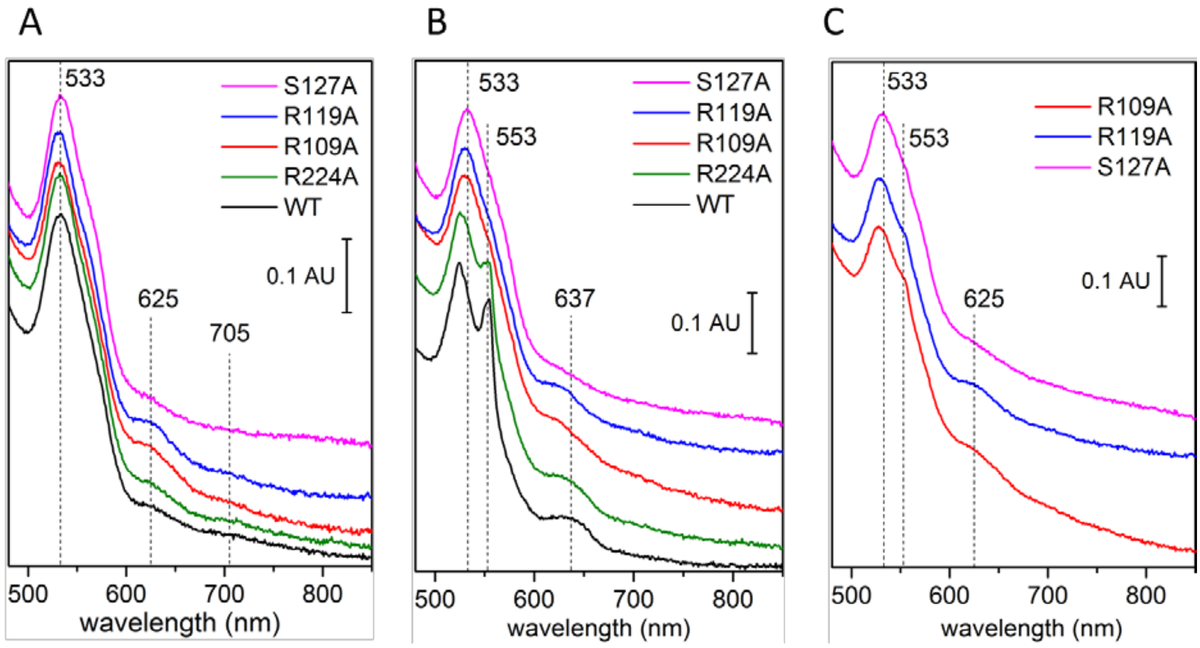

**Figure 4.16 – UV/visible spectral characteristics of the TsdA variants.** TsdA is at a concentration of 25 μM in 100 mM ammonium acetate pH 4.25. (A) Spectra of the TsdA variants as-isolated compared to wild-type TsdA show differences in the size of the peak at 625 nm. The R109A variant was relatively unstable at pH 4.25 resulting in minor precipitation and therefore a slightly sloped background. (B) The samples in panel A were treated with 25 μM sodium tetrathionate. An increase in peaks at 637 nm and 553 nm indicating high-spin oxidised heme and reduced heme respectively are only seen for the wild-type enzyme and the R224A variant. (C) Selected samples from panel B exposed to 125 μM tetrathionate shows a slight increase in the peak at 553 nm indicating reduction.

The first half-reaction for the wild-type enzyme is modification of the enzyme with tetrathionate at pH 4.25, resulting in an instantaneous increase in high-spin heme signal, as well as formation of thiosulfate which reduces a portion of the unmodified protein resulting in an increase in absorption at 553 nm. The same behaviour was seen for the R224A variant (Figure 4.17B). However, when equimolar tetrathionate (25 μM) was added to the R119A, R109A and S127A variants no increase in high-spin signal or reduction was observed (Figure 4.17B). Only when a 5-fold excess of tetrathionate (125 μM) was added could a small amount of reduction be seen (Figure 4.17C), which increased over time, showing that the half-reaction had occurred to generate thiosulfate which can reduce the enzyme. The R109A variant showed the most reduction, followed by the R119A variant and the S127A variant with the least reduction.

We can assume the mechanism of this half reaction involves binding of tetrathionate and nucleophilic attack by Cys123 to result in a cysteine-S-thiosulfonate. If we assume the thiosulfonate group of the cysteine-S-thiosulfonate binds to Arg109 and Arg119, then it is likely that the corresponding thiosulfonate group of tetrathionate also binds to Arg109 and Arg119. From this experiment and the kinetic data we can discount the possibility that Arg224 binds to the other half of tetrathionate. It is possible that Ser127 performs this function, although the properties of its side-chain are not suited for this role in the same way as an arginine residue. Alternatively, there is no binding site for this thiosulfonate group. This would also have implications for the forward reaction. The thiosulfate nucleophile in the second step of the mechanism would be expected to bind in the same place as the second thiosulfonate group of tetrathionate. This may mean there is no specific binding site for this thiosulfate group. This could explain the high $K_{\mathrm{M}}$ of 2 mM for this reaction under high ferricyanide conditions. There would not be millimolar concentrations of thiosulfate in the environment, and this step may simply follow first-order kinetics under physiological thiosulfate concentrations.

Next, the TsdA variants were tested for reduction in the forward half-reaction. Addition of equimolar thiosulfate at pH 4.25 to all the variants resulted in instantaneous reduction, as judged by the peak at 553 nm (Figure 4.18). Judging from the $k_{\mathrm{cat}}$ value determined in Section 4.6.1, this reduction should occur on a sub millisecond time-scale for the wild-type enzyme, and so a stopped-flow setup would be required to detect differences in the rate of reduction of each variant, even if they are impaired 1000-fold in reduction rate. The fact that the variants can decrease the rate of the reverse half-reaction sufficiently to see the effect without a stopped-flow setup is consistent with the $k_{\mathrm{cat}}$ of the reverse reaction being 1000-fold lower than the $k_{\mathrm{cat}}$ of the forward reaction (Liu et al., 2013).

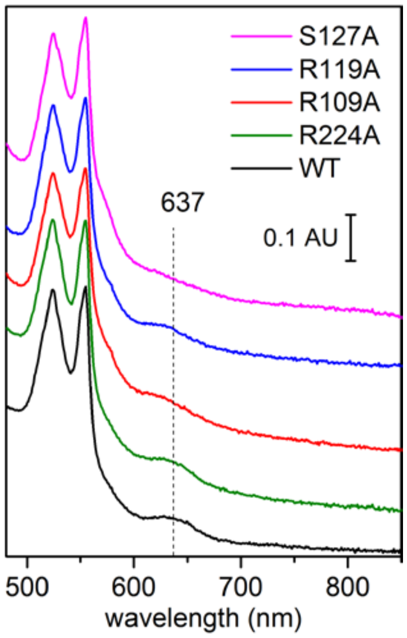

**Figure 4.17 – Reduction of TsdA variants with equimolar thiosulfate.** 25 μM sodium thiosulfate was added to 25 μM TsdA in 100 mM ammonium acetate pH 4.25. A UV/visible spectrum was recorded straight after addition.

### 4.5.3 Role of active site residues in stabilisation of the cysteine-S-thiosulfonate group

One way to determine which residues are binding to the cysteine-S-thiosulfonate group, without structural data, is to see if any of the substitutions affect the stability of this group. This could be investigated using ESI-MS (Figure 4.19). We used two approaches to attempt to generate the cysteine-S-thiosulfonate intermediate. One approach was to incubate the variants with equimolar thiosulfate at pH 4.25. As all the variants are reduced, this means they must form the cysteine-S-thiosulfonate intermediate as this is the first step of the reaction. For the wild-type enzyme under these conditions the cysteine is completely modified to form cysteine-S-thiosulfonate (Figure 4.8B). The second approach was to use our standard cysteine thiosulfonation protocol, which involves incubating the proteins with 50 mM tetrathionate at pH 8.0 for one hour.

All the variants had a mass difference from the wild-type as expected from each substitution. As in all other assays, the R224A variant behaved similarly to the wild-type enzyme, with complete cysteine-S-thiosulfonate formation under both conditions. For each variant at 50 mM tetrathionate an additional two sets of peaks was seen at +224 Da and +448 Da (not shown) compared to the main set of peaks. These affect every peak and probably arise from non-specifically bound tetrathionate. Similar peaks are also seen for the wild-type enzyme (Figure 4.6A)

Different behaviour was exhibited by the S127A variant. Complete thiosulfonation was observed using tetrathionate at pH 8.0. It should be noted that excess tetrathionate is present to regenerate the cysteine-S-thiosulfonate modification and that no catalytic events occur at this pH. However, when the S127A variant was reduced with thiosulfate at pH 4.25, the resulting spectrum showed substantial heterogeneity. The major species are the unmodified cysteine and cysteine persulfide (+32 Da), but other species are present at intervals of +16 Da from the unmodified cysteine to +144 Da. It is difficult to assign all of these species. The +144 Da species may be Cys-S-**S-S-SO**$_3^-$, and the remainder are probably various breakdown products. The mechanism of the enzyme means that reduction must result in formation of cysteine-S-thiosulfonate. At the catalytic pH of 4.25 and under reduced conditions, this intermediate appears to be largely unstable for the S127A variant.

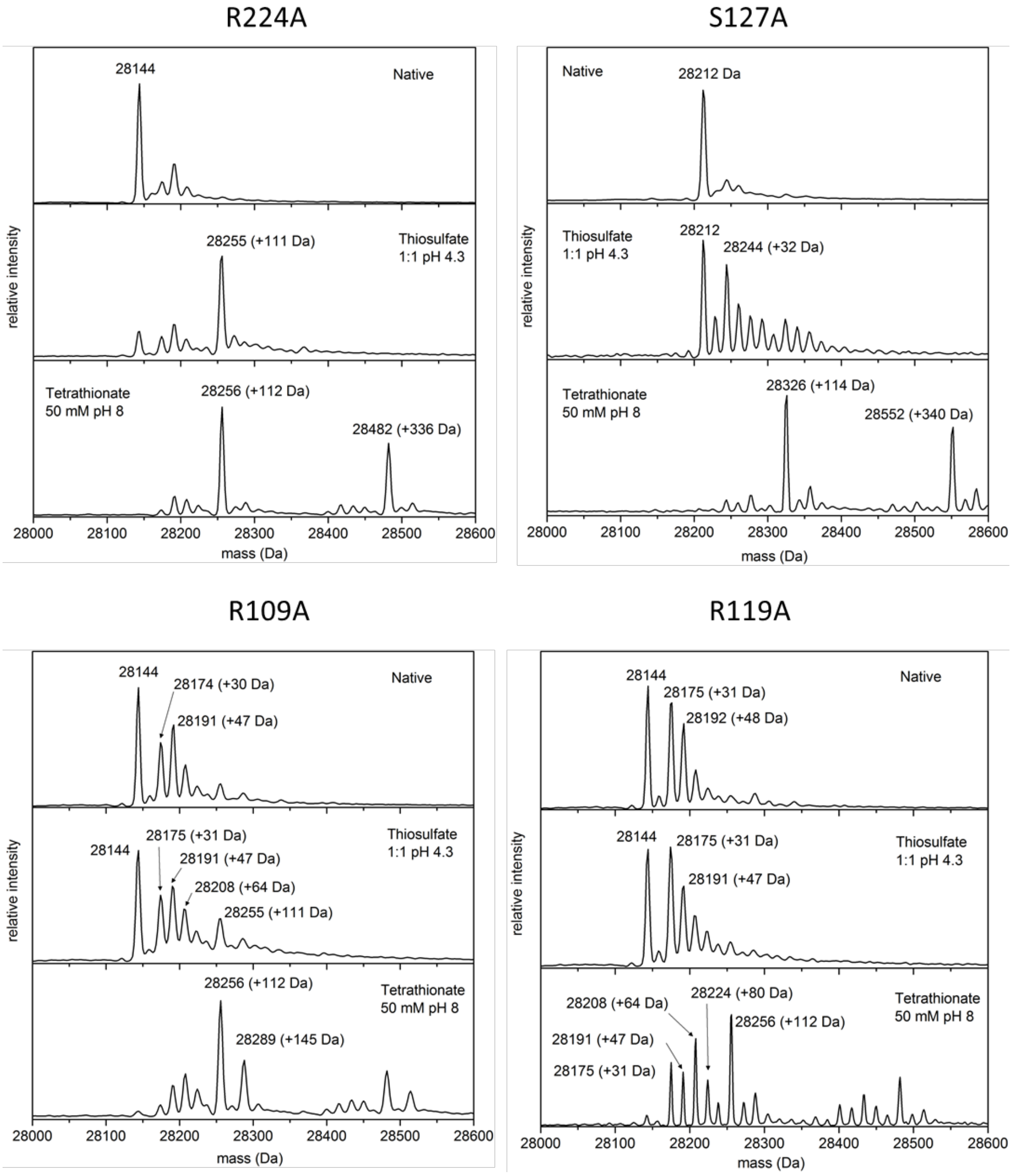

**Figure 4.18 – Stability of cysteine-S-thiosulfonate for each variant as shown by ESI-MS.** Samples of the variants, as indicated, were either not treated, treated with equimolar thiosulfate at low pH for three minutes, or treated with excess tetrathionate for one hour at high pH. Samples were diluted into 0.1% TFA, and oxidised with 10:1 ferricyanide and then desalted and subject to ESI-MS analysis. Some peaks have not been labelled for the sake of clarity, but all peaks are separated by approximately either 16 or 32 Da.

The R109A and R119A variants showed heterogeneity in their as-isolated forms, with additional peaks present at +32 Da and +48 Da. One sulfur atom cannot be distinguished from two oxygen atoms, meaning it is difficult to assign these species. It is possible that these species result in the large high-spin peak at 625 nm seen for both these variants. These ESI-MS peaks are present as very minor species for the wild-type enzyme (Figure 4.6A). The mass spectrum of both variants is largely unchanged by reduction with thiosulfate. Both proteins exhibit a slight increase in the proportion of higher mass modification such as +64 Da and +112 Da, but it should be noted that ESI-MS is not especially quantitative. Unlike the S127A variant, these variants did not form cysteine-S-thiosulfonate as a sole major species upon treatment with 50 mM tetrathionate at pH 8.0. The R109A variant only showed two major species, +112 Da (Cys-S-**S-SO$_3$**$^-$) and +145 Da (Cys-S-**S-S-SO$_3$**$^-$). The longer species may form either by direct reaction of cysteine with tetrathionate, with sulfate as the product, or by breakdown of cysteine-S-thiosulfonate to form cysteine persulfide, and reaction of this with tetrathionate. The R119A variant has different products, with peaks at +32 Da (Cys-S-**S**$^-$), +64 Da (possibly Cys-S-**S-S**$^-$) and +112 Da (Cys-S-**S-SO$_3$**$^-$) as the major species. The Cys-S-**S-S**$^-$ species could form from hydrolysis of Cys-S-**S-S-SO$_3$**$^-$.

The clearest conclusion from these data is that the protein environment heavily influences the reactivity of Cys123 and the stability of its modifications. The wild-type enzyme appears to specifically stabilise the cysteine-S-thiosulfonate form of the enzyme, over the longer cysteine-S-S-thiosulfonate modification, and prevent uncontrolled hydrolysis of any modifications. Arg109 and Arg119 are required for homogeneous generation of a cysteine-S-thiosulfonate group. These residues must be positioned to specifically coordinate and stabilise this modification so it is preferably formed over other modifications. These residues also preserve the version of the enzyme with an unmodified cysteine during expression and purification.

Ser127 has a different role to Arg109 and Arg119. At pH 8.0 a cysteine-S-thiosulfonate group can be stabilised in the S127A variant in the presence of tetrathionate. However, at pH 4.25, where the enzyme is active, all control is lost and no particular species is stabilised. Although interesting, this data is not enough to assign a particular role to Ser127. One possibility is that Ser127 orders the water molecules in the active site to control side-reactivity. A general conclusion is that the residues involved in the TsdA mechanism must not only perform catalysis of the thiosulfate reaction, but also prevent any non-specific reactivity which could occur at any point during this mechanism.

## 4.6 A TsdA mechanism

Although disulfide bond formation is a common reaction in biology, this often involves transfer of a disulfide bond from one protein to another by a thiol:disulfide exchange reaction (Sevier and Kaiser, 2002; Nakamoto and Bardwell, 2004). There are two well-characterised enzyme types which catalyse *de novo* disulfide bond formation. One family uses an FAD cofactor and has two cysteines in close proximity to this (Argyrou and Blanchard, 2004). The Sox pathway enzyme SoxF is an example of this enzyme family (Chapter 1) (Rother et al., 2001), as is dihydrolipoamide dehydrogenase, which functions in central metabolic carrier protein systems. The enzyme DsbB differs from this family and uses a ubiquinone rather than FAD cofactor, but again has two cysteines in close proximity (Inaba et al., 2006). For both enzyme groups, one cysteine forms a charge-transfer complex with the cofactor. A covalent bond between the cysteine and cofactor is then thought to form, with electrons stored on the cofactor. Then the second cysteine thiolate attacks in a nucleophilic substitution with the cofactor as the leaving group. DsbB notably uses an essential arginine to stabilise the deprotonated cysteine and the charge transfer complex (Inaba et al., 2006).

Another enzyme type which catalyses disulfide bond formation is typified by ferredoxin:thioredoxin reductase (Jameson et al., 2003) and heterodisulfide reductase

(Hedderich et al., 2005). These enzymes have an unusual catalytic [4Fe4S] cluster. It has been proposed that this mechanism proceeds through two one-electron reduction steps. A thiyl radical is stabilised by coordination to the [4Fe4S] cluster resulting in one unusual pentacoordinated iron and the cluster in the 3+ state. The two thiolate groups are bridged by iron, which allows an isomerisation reaction to occur, resulting in formation of a disulfide bond. A metal bridging two thiolate ligands is the usual pathway of disulfide formation in metal complexes, particular copper complexes which are a good catalyst for disulfide formation (Pecci et al., 1997; Thomas et al., 2013).

Although TsdA uses a metal cofactor, our structural studies provide no evidence that the iron serves as a bridging ligand for the cysteine thiolate and thiosulfate molecule. It is more likely that the reaction proceeds similarly to the FAD- and ubiquinone-dependent disulfide formation enzymes. However, the cysteine thiolate cannot form a covalent bond with the iron atom, and a single iron atom can only store one electron, not two. Another difference is that only one cysteine is present. However, this simply means that an intermediate step in the mechanism is skipped – formation of a cystine disulfide before nucleophilic attack on this disulfide by the first thiosulfate molecule.

Our structure of the thiosulfate bound state of the enzyme is likely to show the first step of the mechanism. The thiosulfate group is bound and positioned by the side-chains of Arg119 and Arg109, a water molecule, and the amide group of Gly221. Alanine-substitution of Arg109 increases the $K_M$ of the enzyme for thiosulfate, confirming a role for Arg109 in binding thiosulfate. Arg119 is absolutely conserved in TsdA and SoxAX, and alanine-substitution of this residue greatly increases the $K_M$ and decreases the $k_{cat}$, suggesting a direct role for Arg119 in catalysis. This direct role is supported by structural studies which show that Arg119 is in an intermediary position between the thiosulfate molecule and perthiolate of Cys123 (2.87 Å from the thiosulfate and 3.14 Å from the thiolate), and is positioning the sulfane group of the thiosulfate (Figure 4.20). The relative positions of Cys123 and the thiosulfate are very close to that of a linear thiol:disulfide exchange transition state (Bach et al., 2007). There is a distance of 3.79 Å between the thiosulfate sulfane the cysteine persulfide sulfane. The persulfide is 2.30 Å from the heme iron. The angle of the thiosulfate relative to the cysteine is 73°, whilst the angle of the cysteine to the thiosulfate is 81°, although this would be lower if this was a cysteine rather than a cysteine persulfide. From this state a small rotation of the thiosulfate and cysteine towards each other would result in 90° angles and distances of around 2.6 Å as expected for a linear thiol:disulfide exchange transition state. Such a transition state could be stabilised by Arg119.

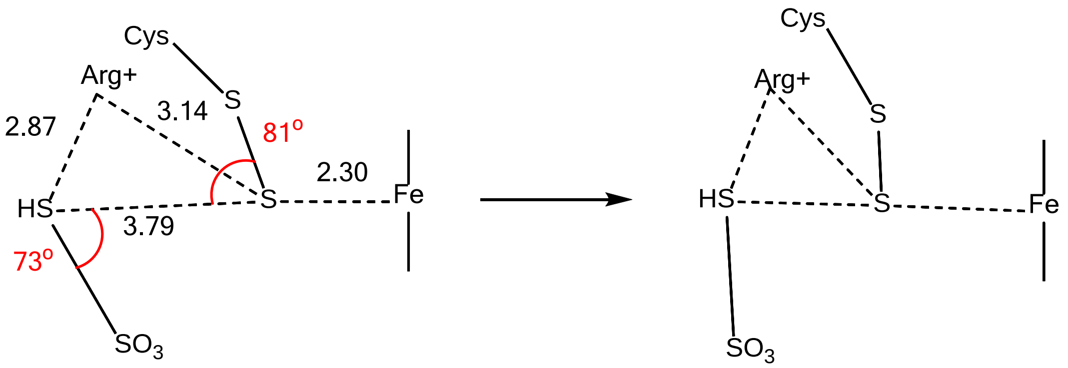

**Figure 4.19 – Geometry of the substrate-bound state of TsdA in relation to a thiol:disulfide transition state.** A schematic of Arg119, the thiosulfate and the cysteine persulfide in the TsdA-tetra crystal structure and comparison to a linear thiol:disulfide exchange transition state.

The exact electronic mechanism of this reaction step is difficult to know. The heme iron is unlikely to be doubly reduced to the 1+ state. Another possibility is that there is a free radical intermediate such as a thyl radical. Regardless, the electron transfer rate between the two hemes of TsdA is expected to be very fast, so whatever the nature of this intermediate it would be very short-lived.

The first step of the mechanism results in a cysteine-S-thiosulfonate group which is not coordinating the iron, resulting in a high-spin state. In the next step a second thiosulfate nucelophilically attacks this group in a thiol:disulfide exchange reaction. We have no direct structural data of this second step of the mechanism. It is likely that Arg119 and Arg109 are binding to the thiosulfonate intermediate. This intermediate is a stable state of the enzyme. However, this is no longer the case when Arg109 or Arg119 are alanine substituted. This suggests that these residues are binding to and stabilising the thiosulfonate group. A surface representation of the active site gives some indication of how the second step could proceed. The only space for a second thiosulfate group is in place of the water which is coordinated by Ser127 (Figure 4.21). Alanine-substitution of Ser127 results in complicated changes to the kinetics which is different to the effect of substitution of Arg119. As the reaction involves three substrates, including ferricyanide which accepts one electron rather than two as the physiological electron acceptor would be expected to do, and steps can probably occur non-specifically it is very difficult to model the kinetics of this enzyme. However, we can say that Ser127 is catalytically important and has a different role to Arg119. Furthermore, Ser127 is absolutely conserved in TsdA, but there is no equivalent residue in SoxAX. SoxAX is likely to share the same initial oxidation reaction with TsdA, but instead of a second thiosulfate reacting with the cysteine-S-thiosulfonate, the SoxYZ carrier arm cysteine residue would react with it. Not only does a cysteine residue have different reactivity to a thiosulfate, but the binding would be governed by protein-protein interactions between SoxAX and SoxYZ. Therefore the second step of the SoxAX mechanism is likely to display differences relative to the second step of the TsdA mechanism. For TsdA, we propose that another thiol:disulfide transition state forms. Here, the thiolate leaving group is stabilised by the iron, the cysteine-S-thiosulfonate is stabilised by Arg109 and Arg119, and the incoming thiosulfate is positioned and stabilised by Ser127.

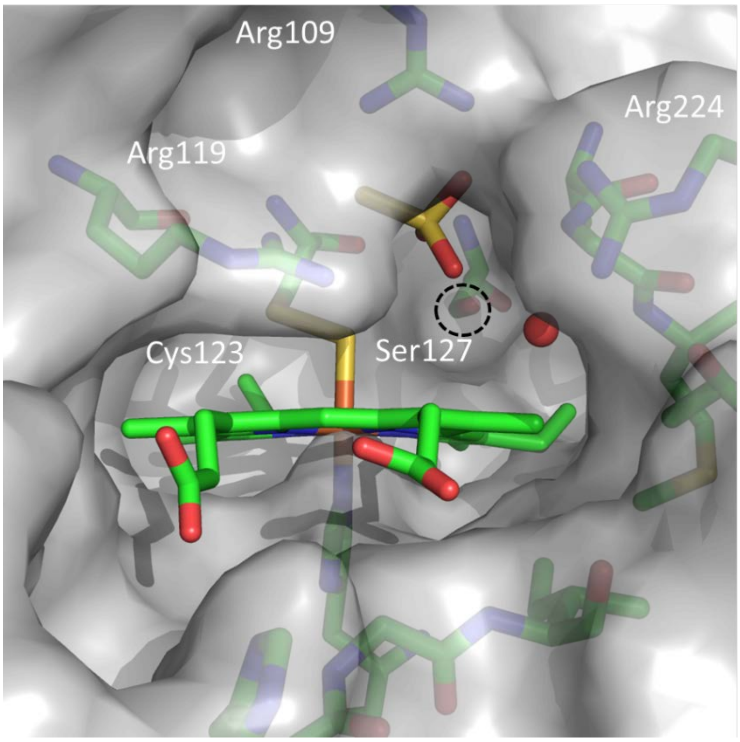

**Figure 4.20 – Accessibility of the active site of TsdA with bound thiosulfate.** The TsdA-tetra structure is shown in surface representation, with the heme, thiosulfate and Cys123 in stick representation, and the active site water molecule as a small red sphere. This shows that the only space to position a second thiosulfate is in front of Ser127.

One final issue is when are the hemes re-oxidised, and does it matter. We cannot force the second step of the reaction forward with excess thiosulfate. When excess thiosulfate is present, the enzyme is reduced. We know the second step can proceed when the enzyme is oxidised, because the oxidised high-spin peak can be removed and reduced by excess thiosulfate. One possibility is that the second step is gated by re-oxidation of the catalytic heme. Due to the difference in charge, ligation of the ferric state by the cysteine thiolate product would be more favourable than ligation of the ferrous state by the cysteine thiolate product.

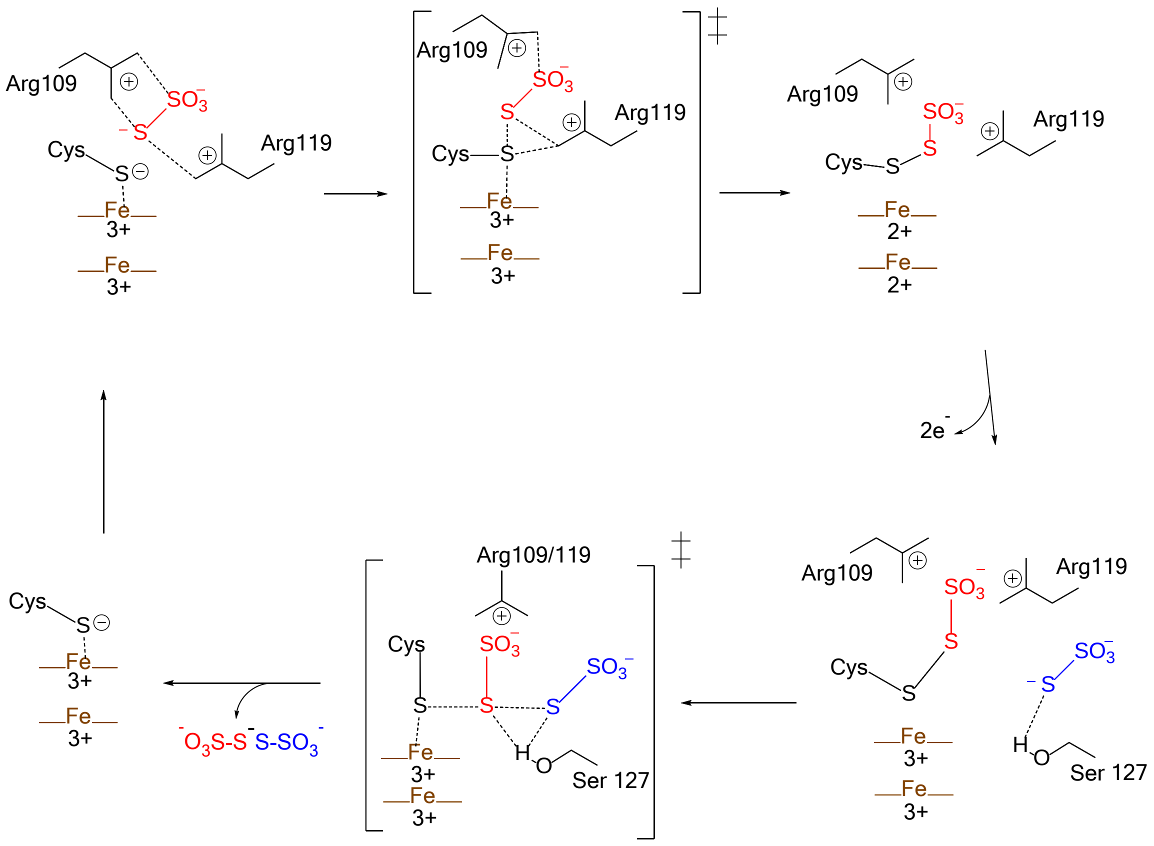

**Figure 4.21 – A possible reaction mechanism for TsdA.** The first thiosulfate (red) is positioned by Arg109 and Arg119. A linear oxidation transition state is favoured by binding to Arg119 and results in cysteine-S-thiosulfate. The thiosulfonate group is stabilised by Arg109 and Arg119. TsdA is reoxidised. The second thiosulfate (blue) attacks the thiosulfonate group in a thiol:disulfide exchange reaction. The leaving group (Cys123) is stabilised by the heme iron(III) whilst the transition state is stabilised by Ser127.

## 4.7 What can we learn about the mechanism of SoxAX?

Comparisons with SoxAX have been drawn throughout this chapter. TsdA and SoxAX appear closely related. The main differences are the lack of a residue equivalent to Ser127 in SoxAX and the arrangement and nature of the electron transfer domains. The electron transfer domains heavily influence the structure of the active sites. In TsdA, the active site is very small, largely due to the presence of conserved residues: Gly219, Ala220, Gly221, Met222 and Arg224. These residues may be involved in binding the second thiosulfate molecule. However, alanine-substitution of Arg224 only has a small negative effect on catalysis. For SoxAX, SoxX provides no residues equivalent to these. Instead there is a large amount of empty space in the active site. Notably, this space is on the Ser127 side of Cys123, suggesting that the SoxYZ cysteine for SoxAX attacks from the same side as the thiosulfate for TsdA. SoxYZ is likely to form protein-protein interactions with SoxAX (see Chapter 3), so will have different requirements for active site recognition compared to TsdA. It would be interesting to combine the approaches used in this chapter and Chapter 3 to gain a detailed understanding of the mechanism of SoxAX.

# Chapter 5: Optimising an IR spectroscopic method to provide insight into the mechanism of iron-sulfur protein nitrosylation

## 5.1 Nitrosylation of iron-sulfur proteins

Nitric oxide (NO) is a toxic free-radical gas which reacts with biological material. As discussed in Section 1.3, the reactivity of NO with iron-sulfur proteins is important for the survival of bacteria attacked by the mammalian immune system. The reactions of iron-sulfur proteins with NO may be a major contributor to the bacteriostatic effect of NO. Additionally, many intracellular pathogens have NO-sensing iron-sulfur proteins which are sensitive to reaction with NO, producing a signalling state of the protein. It is challenging to study the *in vivo* nitrosylation of iron-sulfur proteins during a mammalian immune response. One way to investigate the immunological role of NO is to study what NO reactivity is possible with isolated iron-sulfur proteins, and then use this to infer what NO might do *in vivo*. To understand the proteinaceous systems it is often useful to refer to studies on the well-characterised reactivity of small-molecule model systems which mimic protein-bound iron-sulfur clusters and their nitrosylated iron products.

### 5.1.1 Iron-sulfur clusters

Iron-sulfur clusters are an evolutionary-ancient stable form of iron and sulfide. Under anaerobic conditions, the most stable form is the cubane [4Fe4S] cluster (Figure 5.1). However, with the introduction of $O_2$ into the biosphere, the oxygen-tolerant [2Fe2S] cluster (Figure 5.1) became more common-place. There also exist [4Fe3S] clusters and more unusual clusters with very specific functions. Iron-sulfur clusters are often used for electron transfer, but can also be used for catalysis and sensing of reactive molecules such as $O_2$, superoxide and NO, as discussed here.

### 5.1.2 The NO chemistry of small-molecule model systems

NO displays interesting coordination chemistry and this was studied long before any biological interest in NO emerged (Eisenberg and Meyer, 1975). When the biological significance of the reactivity of iron-sulfur clusters and NO became clear (Reddy et al., 1983; Assreuy et al., 1994), much of the study of NO coordination chemistry focused on synthesising model complexes to understand this reactivity. A characteristic EPR signal at a *g* value of 2.03 is seen after exposure of biological material to NO, and from comparison to synthetic complexes this led to early identification of an important nitrosylation product, a dinitrosyl iron complex (DNIC) (Figure 5.1) (Woolum et al., 1968). The oxidation state of the iron in this complex is not easily described due to covalence and delocalisation of the Fe-NO bond. A notation developed by Enemark and Feltham, $(Fe(NO)_x)^n$, is generally used to describe iron-nitrosyl species (Enemark and Feltham, 1974). In this notation, 'n' refers to the total number of electrons in the metal d orbital and NO $\pi^*$ orbital (see Section 5.2.2), whilst 'x' refers to the number of NO molecules coordinating each iron. EPR-active DNIC is an $(Fe(NO)_2)^9$ species.

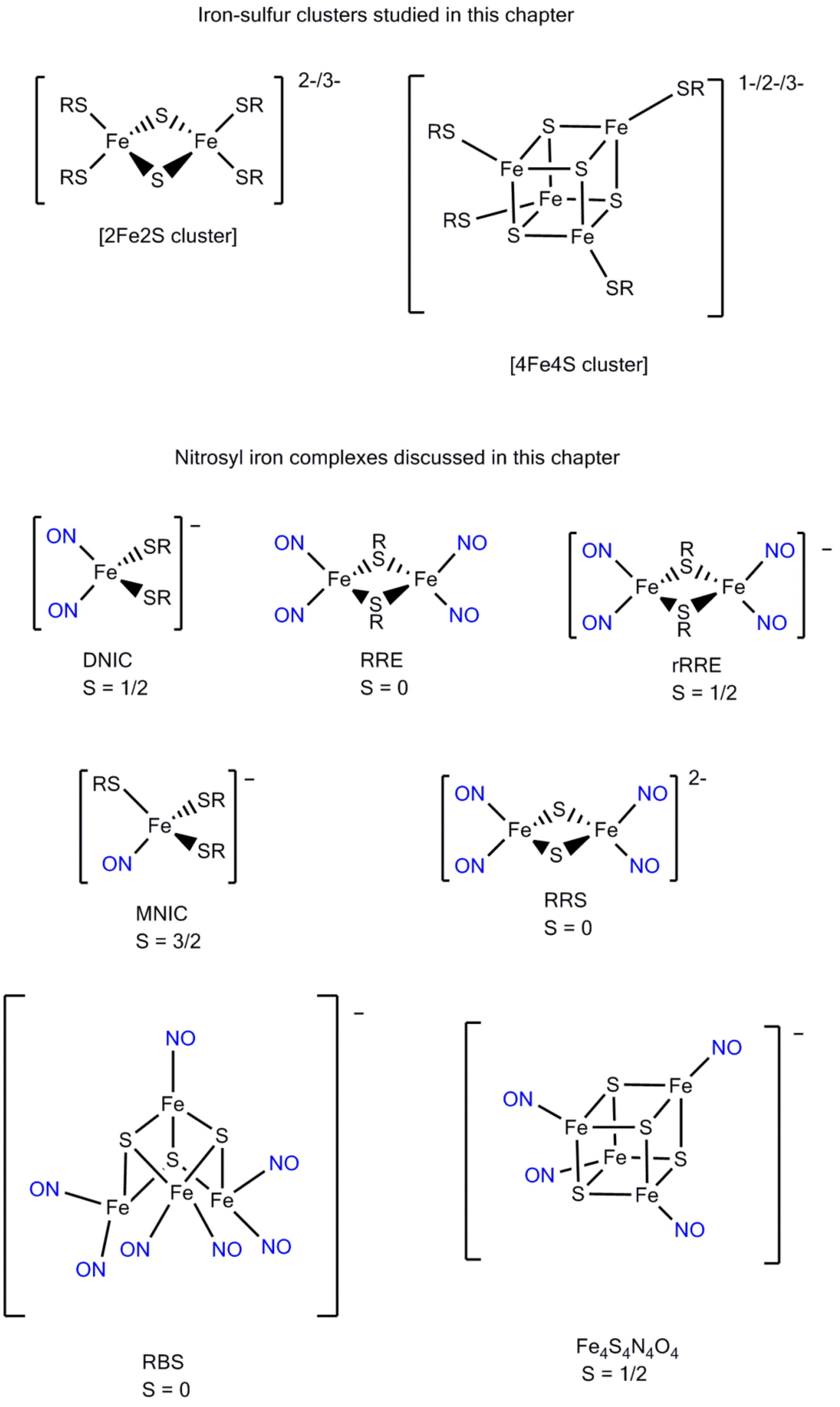

Iron-sulfur clusters studied in this chapter

[2Fe2S cluster]

[4Fe4S cluster]

Nitrosyl iron complexes discussed in this chapter

DNIC
S = 1/2

RRE
S = 0

rRRE
S = 1/2

MNIC
S = 3/2

RRS
S = 0

RBS
S = 0

$Fe_4S_4N_4O_4$
S = 1/2

**Figure 5.1 – Complexes discussed in this chapter.**

DNIC species can be easily synthesised by either substituting NO into an iron complex with carbon monoxide ligands (Caulton, 1975), or by simply mixing iron(II) sulfate with excess thiols and an NO donor (McDonald et al., 1965). It was shown that by decreasing the ratio of thiols to $Fe(NO)_2$ it is possible to synthesise a different product, Roussin's Red Ester (RRE) (Figure 5.1) (Costanzo et al., 2001). RRE can be described as a $(Fe(NO)_2)^9$-$(Fe(NO)_2)^9$ species, and is EPR-silent due to antiferromagnetic coupling between the two Fe atoms. Interestingly, this product displayed a UV/visible spectrum similar to nitrosylated iron-sulfur proteins with a peak at 362 nm (Cruz-Ramos et al., 2002). This RRE can undergo a single electron reduction to produce reduced RRE (rRRE) (Figure 5.1), which has a characteristic EPR signal with a *g* value of 2.01 (Tsou et al., 2007). Such an EPR signal had also been seen for nitrosylated iron-sulfur proteins upon dithionite reduction (Kennedy et al., 1997; Foster and Cowan, 1999).

Mononitrosyl (MNIC) species (Figure 5.1) have been synthesised by exposing model $Fe(RS^-)_4$ centres to a single equivalent of NO (Harrop et al., 2006; Lu et al., 2006). These EPR-active compounds can be described as $(Fe(NO))^7$ centres. These have never been identified as products of iron-sulfur protein nitrosylation, but are suggested to be an early intermediate in the nitrosylation pathway (Fujikawa et al., 2014).

It is also possible to synthesise larger multinuclear iron-nitrosyl complexes with no thiolate ligands. By reacting synthetic [2Fe2S] and [4Fe4S] clusters with controlled stoichiometries of NO, Lippard and co-workers were able to form either DNIC or the cubane EPR-silent $Fe_4S_3(NO)_7$ Roussin's Black Salt (RBS) (Figure 5.1) (Harrop et al., 2008). Lippard and co-workers later showed that by using different cluster ligands they could stabilise a potential intermediate of the reaction of [4Fe4S] clusters with NO, a $Fe_4S_4(NO)_4$ cluster (Figure 5.1) (Victor and Lippard, 2014). Importantly, this cluster has a very similar EPR spectrum to DNIC, which led Lippard and co-workers to suggest that this species may be a product of iron-sulfur protein nitrosylation but has been incorrectly assigned as DNIC. A different intermediate to RBS formation can also be obtained by starting with Roussin's Red Salt (RRS), which is similar to RRE but with bridging sulfides rather than thiolates (Figure 5.1) (Beck et al., 1981). Liaw and co-workers used RRS as a starting material to stabilise an unusual nitroxyl-bridged $Fe_4S_2(NO)_8$ (Yeh et al., 2014) nitrosyl-iron-sulfur cluster.

### 5.1.3 Iron-sulfur protein nitrosylation chemistry

The reactivity of protein-bound iron-sulfur clusters with NO is much less well understood than the small-molecule systems described above. This is largely because the two best methods to identify and characterise nitrosyl iron species are infrared (IR) spectroscopy and X-ray crystallography, and both of these methods are much more challenging to apply to protein-bound systems than to small-molecule systems. Instead, iron-sulfur protein nitrosylation reactions have largely been studied by EPR spectroscopy, UV/visible spectroscopy and indirectly *via* the quantification of released sulfur. NO-sensing and non-sensing [2Fe2S], [4Fe4S] and [3Fe4S] iron-sulfur proteins all form DNIC to some extent upon nitrosylation, as judged by EPR spectroscopy (Sellers et al., 1996; Kennedy et al., 1997; Foster and Cowan, 1999; Ding and Demple, 2000; Cruz-Ramos et al., 2002; Duan et al., 2009; Crack et al., 2010; Tinberg et al., 2010). EPR spectroscopy is quantitative, and in most of the studies listed above the yield of DNIC was relatively low (5-20%), although yields closer to 100% DNIC have been obtained for the [4Fe4S] enzyme IlvD (Duan et al., 2009). A variety of evidence has led people to believe that much of the remaining product is the EPR-silent RRE species. The UV/visible spectra of nitrosylated iron-sulfur proteins more closely resemble those of small-molecule RRE rather than DNIC, as first described for the [4Fe4S] redox state/NO-sensing protein FNR (Cruz-Ramos et al., 2002), whilst dithionite reduction of nitrosylated [4Fe4S] high potential iron-sulfur protein (HiPIP) (Foster and Cowan, 1999) and a [2Fe2S] rieske protein (Tinberg et al., 2010) resulted in an EPR spectrum similar to small-molecule rRRE. Further evidence for RRE formation came from the stoichiometry of the reaction of the [4Fe4S] NO-sensing protein WhiD with NO and quantitative sulfur analysis (Crack et al., 2010).

By investigating the pre-steady state kinetics of iron-sulfur protein nitrosylation using UV/visible spectroscopy (Crack et al., 2010; Crack et al., 2013; Fujikawa et al., 2014), it has been suggested that the reactions proceed *via* mononitrosyl intermediates but this has never been proven. Recently, it has been shown by mass spectrometry and UV/visible spectroscopy that sulfur can be retained to form cysteine-persulfide coordinated DNIC clusters (Crack et al., 2013).

The only method used to study iron-sulfur protein nitrosylation able to directly detect different nitrosyl species is nuclear resonance vibrational spectroscopy (NRVS). This method requires isotopic labelling of proteins with $^{57}$Fe and a synchrotron source. Signal to noise is generally poor, but nevertheless this technique has identified formation of RRE upon nitrosylation of a [2Fe2S] rieske protein (Tinberg et al., 2010) and RBS upon nitrosylation of a [4Fe4S] ferredoxin (Tonzetich et al., 2010). This is the only study which has identified the EPR-silent RBS as a product of iron-sulfur protein nitrosylation.

## 5.2 Infrared spectroscopy as a tool to study FeS protein nitrosylation

The simplest direct method to study iron-sulfur protein nitrosylation is IR spectroscopy. The power of IR spectroscopy to distinguish different iron-nitrosyl species can be understood from a brief introduction to its theoretical basis.

### 5.2.1 Infrared spectroscopy theory

IR spectroscopy detects vibrational transitions, such as bond stretching and deformation, of a molecule which is usually in its electronic ground state. Unlike Raman spectroscopy, which detects vibrational transitions by inelastic scattering, IR spectroscopy measures direct absorption of IR light. IR spectroscopy can only detect vibrational transitions with a change in the dipole moment. This means that the vibrational mode of symmetric molecules, like $N_2$, cannot be detected but the stretching vibration of NO can. The number of vibrational bands arising from a molecule can be predicted from the number of vibrational degrees of freedom, and so linear molecules have 3N – 5 modes, whilst non-linear molecules have 3N – 6 modes (where N is the number of atoms). In more complex molecules one can calculate the possible number of vibrational modes, and then use group theory and knowledge of the symmetry of the molecule to determine how many of these modes will be IR-active. For example, a $C_{2v}$ DNIC species has two ν(NO) vibrational modes, whilst a $C_{2v}$ RRE species has three ν(NO) vibrational modes. This is one way in which IR spectroscopy is very sensitive to the structure of the molecule under study.

The energy at which absorptions occur is also sensitive to the structure of the molecule. The energy of a diatomic vibration can be calculated by approximating the system as a harmonic oscillator (**Equation 5.1**).

$$\nu = \frac{1}{2\pi}\sqrt{\frac{k}{\mu}} \qquad \textbf{Equation 5.1}$$

Here, $\nu$ is the frequency of oscillation, $k$ is the force constant of the bond and $\mu$ is the reduced mass of the molecule. In the case of NO, this equation means that the energy of the ν(NO) stretching mode will be highly sensitive to the strength of the N-O bond. The dependency on the reduced mass of the molecule means that the energy of the ν(NO) stretching mode is sensitive to the use of different nitrogen and oxygen isotopes.

### 5.2.2 Coordination of metals by NO

The best way to understand how coordination of NO to a metal will affect the ν(NO) stretching frequency is to use molecular orbital theory. The electronic configuration of an atom can be described by atomic orbital theory, where each orbital and its energy are described by a quantum wavefunction. Orbitals are then filled by one or two electrons. Formation of a covalent bond can be modelled as a linear combination of these atomic orbital wavefunctions to create molecular orbitals. Only orbitals with the correct symmetry to interact will combine to form, for example, σ or π interactions. These interactions can either result in constructive interference and a bonding interaction or destructive interference and an antibonding interaction. Placing electrons into bonding or antibonding orbitals will either increase or decrease the strength of the bond, respectively. The bonding in a NO molecule as described by molecular orbital theory is shown in Figure 5.2A. The highest energy electrons are associated with the nitrogen atom and this is the end of the molecule which will interact with the metal ligand. Importantly, the highest energy occupied NO molecular orbital is a π* antibonding orbital with a single unpaired electron.

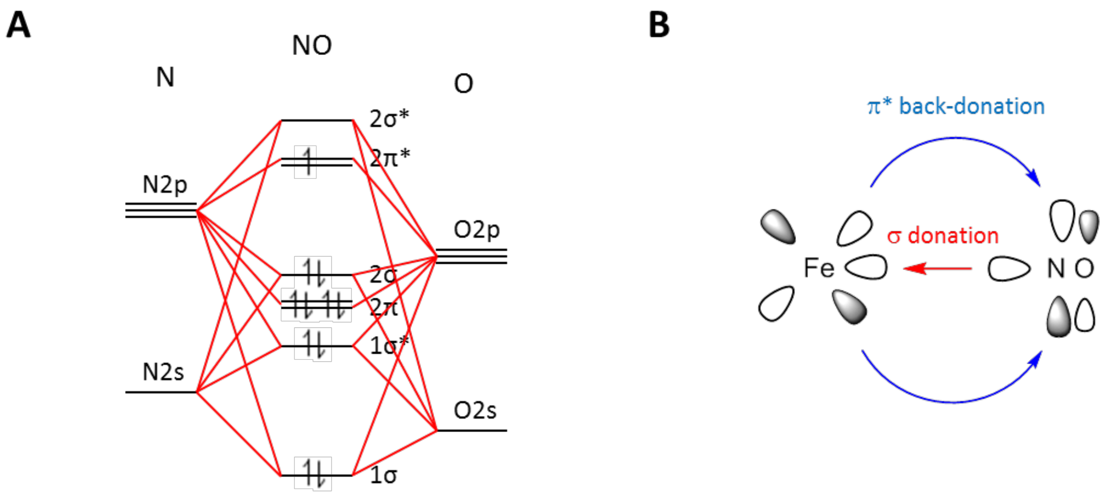

**Figure 5.2 – Description of bonding in NO and a Fe-NO interaction using molecular orbital theory.** (A) A molecular orbital bonding diagram of the interaction between nitrogen and oxygen in an NO molecule. (B) A simplistic description of the Fe-NO interaction based on the Chatt-Dewar-Duncanson model for bonding between a transition metal and an unsaturated ligand; π* back-donation occurs into the NO 2π* molecular orbital in (A), whilst σ donation is from the NO 2σ molecular orbital. These interactions are with the Fe d-orbitals.

The interaction between NO and a metal can be described as a synergistic σ-donor, π-acceptor interaction (Figure 5.2 B). The 2σ NO orbital will donate electrons to a metal σ-acceptor orbital. This will increase the electron density on the metal. Depending on the electron configuration of the metal, a certain amount of π back-donation will occur, and this will be into the 2π* antibonding orbital of NO. Thus, the strength of the N-O bond is highly sensitive to the electronic state of the metal it is coordinating. Whether electrons are accommodated on the metal or the NO molecule will also affect the formal oxidation states of the metal and NO, as well as the geometry of the interaction. When electrons are accommodated on the metal, then NO can be described as $NO^+$ and coordinates in a linear configuration. When electrons are accommodated on NO, NO can be described as $NO^-$ and has a bent coordination configuration. This all means that energy of the ν(NO) stretching mode is extremely sensitive to the electronic state of the metal the NO is coordinating, which will be affected by other ligands to the iron, and the oxidation state of the iron. For example, reduction of the iron from 3+ to 2+ will increase the charge on the iron, and therefore increase the extent of back-donation into the NO

$\pi^*$ antibonding orbital. This will decrease the strength of the N-O bond, and therefore decrease the energy of the $\nu$(NO) band. Myoglobin in the Fe(III)-NO state has a $\nu$(NO) band at 1927 cm$^{-1}$ (Miller et al., 1997), whilst in the Fe(II)-NO state it has a $\nu$(NO) band at 1614 cm$^{-1}$ (Thomas et al., 2001).

Different iron-nitrosyl species will have different numbers of NO molecules in different symmetries, different iron oxidation states, and the irons will have different coordination environments. This means IR spectroscopy can distinguish the various iron-nitrosyl complexes described in the previous sections.

## 5.3 Developing an IR spectroscopic method to study FeS protein nitrosylation

IR spectroscopy has previously been applied to study NO binding to protein-bound metal centres, and so there is no intrinsic reason why it should not be possible to apply this technique to iron-sulfur protein nitrosylation. One difficulty arises from the detection limit of IR spectroscopy; molecules need to be in the millimolar concentration range to be detectable. When there is only one iron-nitrosyl species formed in each protein this means the protein has to be at a high concentration to detect these species. The technique therefore can consume a lot of protein and also requires that the protein is very soluble. The specific problem with detecting NO species is that the $\nu$(NO) bands which can be used to detect and characterise protein-bound NO species overlap with the very strongly absorbing protein amide bands and water bands. This means that a difference spectroscopy approach is needed to see any $\nu$(NO) bands.

One approach is to use a flash of light to photolyse the NO ligand, and subtract the pre-flash spectrum from the post-flash spectrum. This has been applied to investigate binding of NO to heme proteins, such as myoglobin (Thomas et al., 2001). Binding of NO to protein-bound iron sites has been detected using a non-destructive IR spectroscopy method for the non-heme iron protein Fur (D'Autréaux et al., 2004). Here, the authors detect formation of nitrosyl iron complexes by subtraction of spectra taken before NO exposure from spectra taken after NO exposure.

Liaw and co-workers have extended their small-molecule iron-nitrosyl work to systems bound to oligopeptides (Lin et al., 2011). As well as gaining insight into the reactivity of more physiologically relevant DNIC and RRE systems, they were able to record IR spectra of these products. Their spectra provide good references for assigning IR spectra of nitrosylated iron-sulfur proteins.

### 5.3.1 Aim of Chapter

The aim of this work was to develop a simple non-destructive IR spectroscopic method with a low sample requirement which can detect and distinguish different products of iron-sulfur protein nitrosylation.

### 5.3.2 Spinach ferredoxin – a model iron-sulfur protein

To optimise our IR method we needed an iron-sulfur protein we could easily obtain in large quantities. To increase ease of handling, this iron-sulfur protein would ideally not be oxygen-sensitive. For most of this work we used *Spinacia oleracea* Ferredoxin I (Fd). This well-characterised protein has a [2Fe2S] cluster which is rapidly oxidised by oxygen to its oxidised $[2Fe2S]^{2+}$ form. As only two Fe atoms are present in the cluster, this means that no nitrosylation products larger than RRE can form, which simplifies identification of products.

Spinach cDNA was obtained by reverse transcription of spinach mRNA, which was obtained by phenol extraction from a few leaves of spinach. The gene encoding Fd without its chloroplastic signal peptide was obtained by PCR of spinach cDNA (see Section 2.2) and inserted into expression vector pASK-IBA-13+ (IBA), which introduces an N-terminal Strep II tag, to make pASK-StrepFd. *E. coli* strain BL21-star (Invitrogen) was transformed with this plasmid for expression. The expression and purification protocol are described in Section 2.3. Once loaded on a 5 mL streptactin (IBA) column, the protein was only washed with one column volume of washing buffer. This was because the protein did not bind strongly to the column. This decreased the purity of the protein, so additional purification steps were added to the protocol before size-exclusion chromatography with a Superdex 75 10/300 (GE Healthcare). First, contaminants were precipitated by addition of 2.5 M ammonium sulfate and removed by centrifugation at 16000 x *g* for 10 minutes. The supernatant was loaded on a 1 mL phenyl sepharose HP column (GE Healthcare) equilibrated in 30 mM tris-HCl pH 7.5, 2.5 M ammonium sulfate, and washed with 10 volumes of the same buffer. Ferredoxin was eluted with a gradient from 2.5 to 0.5 M ammonium sulfate over 20 column volumes. Ferredoxin-containing fractions were diluted to reduce the ammonium sulfate concentration and then concentrated by ultrafiltration with a 10 kDa cut-off concentrator (Millipore) to 500 µL, before final purification by size-exclusion chromatography. The buffer for the final step was varied as will be discussed later, but for method development the final buffer was 15 mM HEPES pH 7.5, 200 mM NaCl. The protein was pure as judged by SDS-PAGE and the ratio of the $A_{280}$ protein absorption to the $A_{420}$ absorption from the [2Fe2S] cluster. The concentration of Fd was determined by optical absorption using an $\varepsilon_{420}$ of 9680 $M^{-1}cm^{-1}$.

### 5.3.3 Nitrosyl iron complexes absorb in a difficult region of the spectrum

All the species described in Section 5.1.2 have ν(NO) bands between 1830 and 1550 $cm^{-1}$. Both water and amide have broad absorption bands centred at 1650 $cm^{-1}$ (Figure 5.3A,B), and in an aqueous protein-bound system the concentrations of peptide bonds and water will be much higher than the concentration of the iron-nitrosyl species. It is very challenging to identify small peaks on a sloping baseline and therefore a difference method is required to achieve a flat baseline, as previously discussed. An alternative approach is to use $D_2O$ instead of $H_2O$. This shifts the water absorption outside of the area of interest. Similarly, $^{15}N$ and $^{13}C$ labelling the protein can shift the amide I band outside the region of interest. Isotopic labelling of the protein is very expensive and is still likely to result in at least 10% of the unlabelled protein. We attempted to use $D_2O$ but had issues with deuterium-hydrogen exchange occurring over the timescale of the experiment, resulting in baseline changes which were very hard to account for by simple subtraction. Furthermore, use of $H_2O$ is more physiologically relevant as $D_2O$ will alter the hydrogen bonding within the protein.

Another overlapping feature arises from water vapour (Figure 5.3C). When molecules are in the gas-phase it is possible to see the rotational fine-structure in their IR spectra. If the water vapour content of the air in the path of the IR beam changes during an experiment this will result in large sharp peaks or troughs in the region of interest. This is particularly a problem if there are large gaps in time between the recording of the two spectra used to make the difference spectrum.

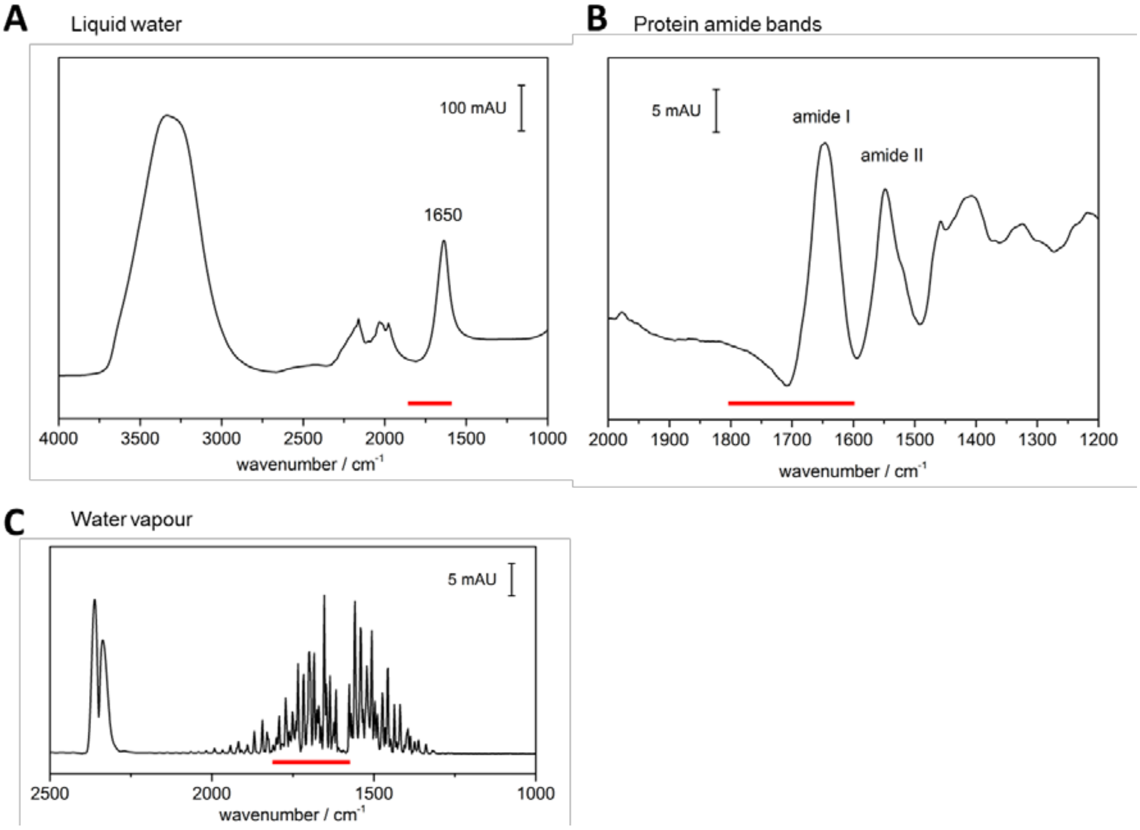

**Figure 5.3 – Nitrosyl iron complexes absorb in a difficult region of the spectrum.** The thick red lines indicate the region of the IR spectrum where nitrosyl iron complexes are expected to absorb (1800 - 1600 cm$^{-1}$). (A) Spectrum of milli-Q water. The peaks at 2000 - 2200 cm$^{-1}$ are due to diamond absorptions preventing light from reaching the detector (B) Spectrum of 0.8 mM *E. coli* fumarate and nitrate reductase regulator (see Section 5.5.2) processed against a water background. A slight decrease in water absorption is also apparent in this spectrum. (C) Difference spectrum in an empty transmission-mode experiment recording an undefined increase in the amount of laboratory air inside the sample compartment. Peaks arise from $CO_2$ (2400 - 2250 cm$^{-1}$) and water vapour (2000 - 1250 cm$^{-1}$).

### 5.3.4 An ATR-IR approach

It is difficult to use transmission-mode IR spectroscopy for the ν(NO) region of the spectrum in non-deuterated aqueous solution because all of the IR light is absorbed and cannot reach the detector. An alternative approach is attenuated-total reflectance (ATR)-IR spectroscopy. Here, the sample is loaded on a prism which has a higher refractive index than the sample. An IR beam is directed at the prism/sample interface at an angle larger than the critical angle so that total internal reflection will occur. This reflection creates an evanescent wave which effectively samples the area just above the prism/sample interface. The effective path-length relates to the penetration of the evanescent wave into the sample. This is on the order of 1 $\mu$m, which greatly reduces absorption by the solvent compared to transmission-mode IR spectroscopy. Additionally, it requires only 5 $\mu$L of sample to cover the entire prism, so this method is ideal to conserve material. However, this method is less sensitive than transmission-mode IR spectroscopy.

Initial experiments were performed using the DuraSamplIR II (SensIR Technologies) ATR accessory, which has an in-built single-reflection diamond ATR prism. A gas-tight cell was designed to clamp onto the prism (Figure 5.4), with septum-sealed ports which could be used to inject the sample and to flush the cell with $N_2$ to maintain anaerobicity. Maintaining an anaerobic environment is extremely important because NO reacts with $O_2$ to form $NO_x$ species, which are very soluble, decrease the pH of the solution and are very reactive. Additionally, certain iron-nitrosyl products such as DNIC are oxygen sensitive (Costanzo et al., 2001). Such a cell also prevents evaporation of the sample. To achieve high signal to noise it is necessary to record an average spectrum over an extended period of time, which means each spectrum can take 3-10 minutes to record. The sample would dry on to the prism in this time-frame without a sealed cell.

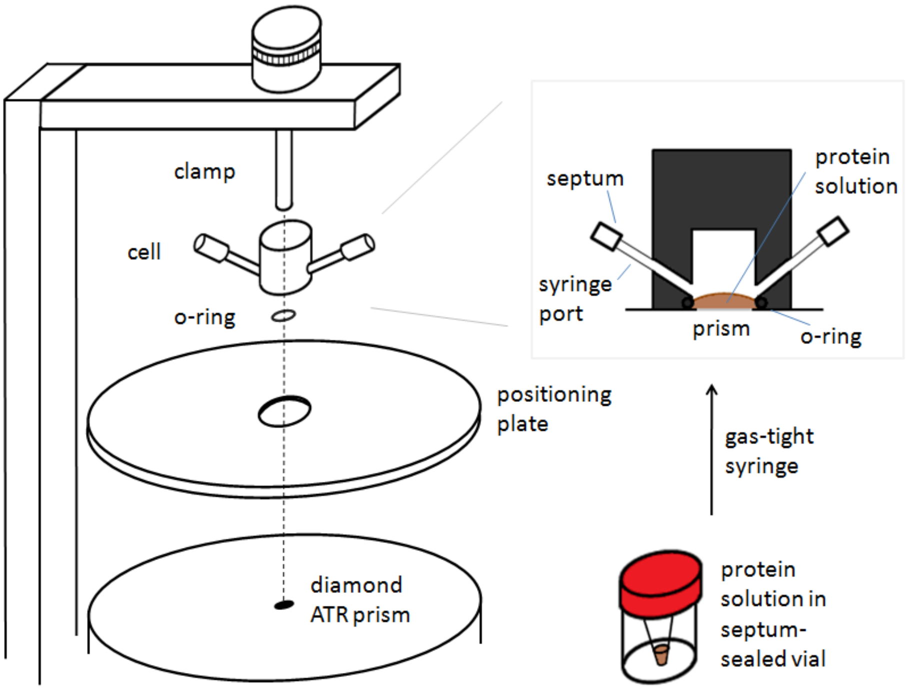

**Figure 5.4 – Schematic representation of our first ATR-IR method.** The schematic shows a custom-built gas-tight cell which can clamp onto a DuraSamplIR II accessory to allow anaerobic ATR-IR spectra of a protein sample to be recorded. Samples were exposed to well-defined NO gas concentrations for defined lengths of time inside septum-sealed vials before loading into the cell.

Fd at a concentration of 0.8 mM was put inside septum-sealed vials inside a glove box (Figure 5.4). These vials were flushed with 10% NO gas (in $N_2$, BOC) outside of the glove box, but all lines were pre-flushed to maintain anaerobicity. The prism was cleaned with ethanol, nitric acid and water. The cell was clamped on to the prism and flushed with $N_2$, and then the sample was injected with a gas-tight Hamilton syringe. A spectrum of unexposed Fd was recorded for subtraction from the spectra of exposed Fd.

### 5.3.5 Fd reacts with NO to form RRE under microaerobic conditions

Upon exposure of Fd to 10% NO we could detect a species with bands at 1783 and 1757 cm$^{-1}$ (Figure 5.5A). These bands correspond well with those recorded for oligopeptide-bound RRE (Lin et al., 2011) at 1788 and 1763 cm$^{-1}$. The weak band that they observe at 1819 cm$^{-1}$ would be difficult to observe due to the signal-to-noise of the initial method. To confirm assignment of the peaks to a protein-bound RRE, we tested whether the species was indeed protein-bound. We first generated the species through reaction of Fd with 10% NO, and measured an IR spectrum of an aliquot of the sample to confirm presence of RRE (Figure 5.5B). The remainder of the sample was then subjected to multiple rounds of dilution and concentration using a centrifugal concentrator with a 3 kDa cut-off. This process removes low-molecular weight species, but retains protein-bound species. After concentration back to the starting volume, and therefore approximately the initial concentration, the IR spectrum was measured again (Figure 5.5B). This spectrum showed RRE peaks, confirming that the species is protein-bound. As all manipulations were performed in a $N_2$ atmosphere with no NO, this experiment also demonstrates that the RRE species is stable in the absence of NO.

To confirm that the bands were due to $\nu$(NO) modes we used isotopically labelled $^{15}$NO gas. To generate this gas, we mixed equimolar ascorbic acid with $^{15}$N-sodium nitrite at the bottom of the sample-containing vial. From Equation 5.1, it can be expected that by increasing the mass of the NO molecule from 30 to 31 Da, the bands would be expected to shift from 1783 and 1757 cm$^{-1}$ to 1754 and 1728 cm$^{-1}$. Both bands were shifted (Figure 5.5C), but it was difficult to see the lower wavenumber band as it moved closer to the amide region. The 1783 cm$^{-1}$ band shifted to 1747 cm$^{-1}$, which is a larger shift than calculated but within the range expected from similar experiments with small-molecule systems (Tonzetich et al., 2010).

The size of the RRE bands varied in an irreproducible manner, but correlated with loss of the red-brown colour of the protein. Sometimes the protein would precipitate, and these samples would have very large RRE bands. It was noticed that the size of the RRE bands correlated well with a broad band at 1240 cm$^{-1}$ (Figure 5.5D), which also shifted to lower energies when $^{15}$NO gas was used. This band can be assigned to nitrous acid, which forms when NO and $O_2$ react in solution. It was therefore clear both that the RRE species was favoured by the presence of $O_2$ and that our initial methods were not sufficiently anaerobic.

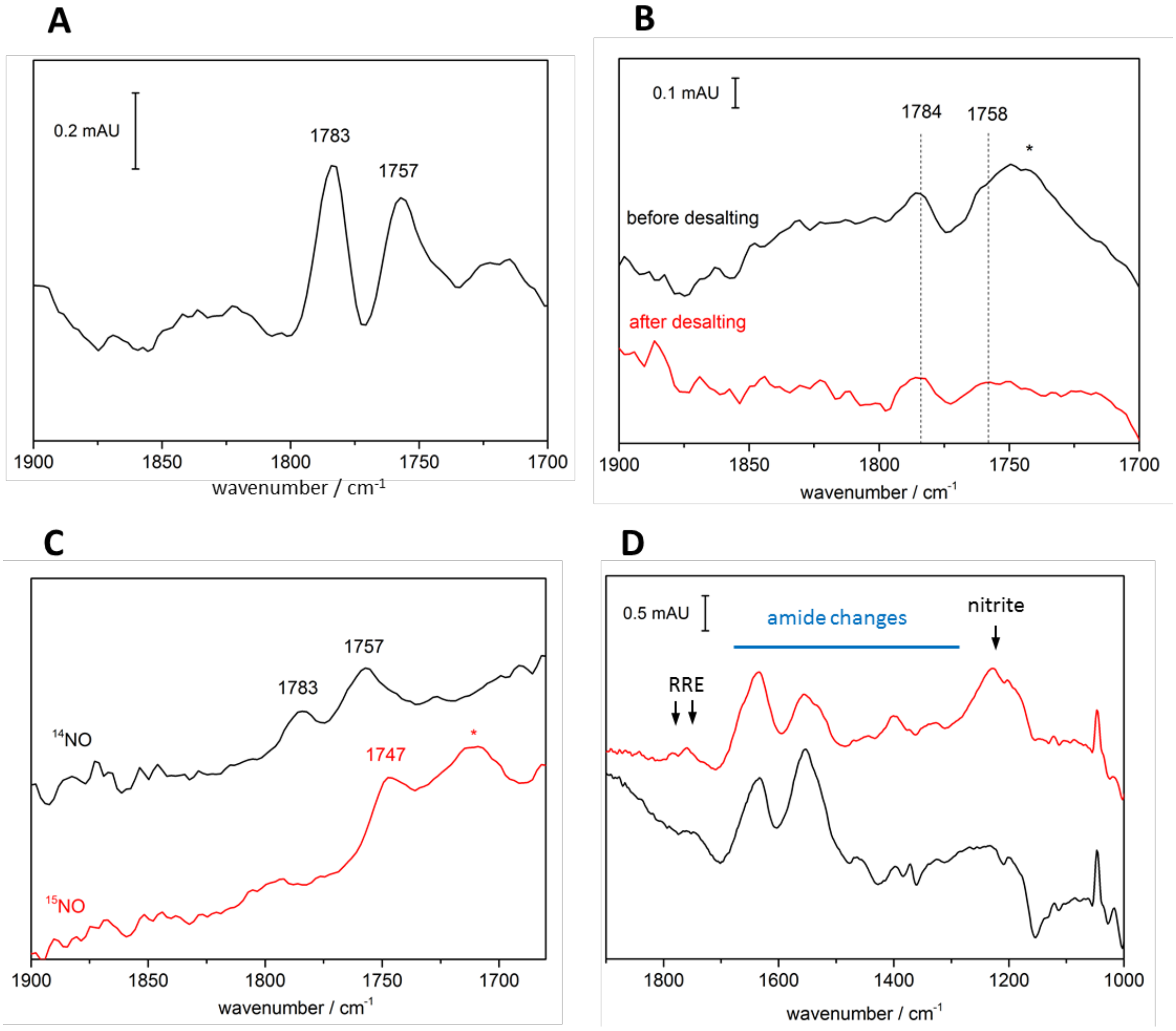

**Figure 5.5 – Characterisation of Fd-RRE using IR spectroscopy.** All panels show IR spectra of 0.8 mM Fd in 15 mM HEPES pH 7.5, 200 mM NaCl exposed to 1% or 10% NO using methods described in Section 5.3.3 processed against a background of unexposed Fd. (A) Spectrum of Fd exposed to 1% NO until significant sample yellowing. (B) Fd was exposed to 10% NO for 30 minutes. A sample was taken to record the IR spectrum shown in black. The remainder of the sample was desalted in a glove box by multiple rounds of dilution and concentration, concentrated back to its original volume and an IR spectrum taken. The asterisk shows that the spectrum is distorted by a peak at 1744 cm$^{-1}$, due to surface contamination as described in Section 5.3.6. (C) Fd was exposed to NO gas generated by mixing of $^{14}$N or $^{15}$N-labelled (as indicated) sodium nitrite and ascorbic acid. The 1783 cm$^{-1}$ peak shifts to 1747 cm$^{-1}$. The potential peak labelled with an asterisk is probably due to a baseline subtraction issue, and this may obscure the actual shifted 1757 cm$^{-1}$ peak. (D) Two samples of Fd were separately exposed to 10% NO for approximately 3 hours. One sample contains RRE (red line) and the other sample (black line) does not. This correlates with the size of the nitrite peak.

### 5.3.6 Technical problems we encountered when using a diamond ATR prism

ATR-IR is a surface sensitive technique due to the limited penetration depth of the evanescent wave and is highly sensitive to molecules adsorbing on the prism surface. This presented a large difficulty for studying iron-sulfur protein nitrosylation. Firstly, when the sample was left on the diamond prism, the amide bands increased in size. This indicates that the protein was adsorbing onto the prism. This occurred significantly within a single measurement (120 s). This meant that it was very difficult to have two separate spectra with the similarly sized amide bands, which resulted in poor baselines after subtraction. Furthermore, proteins can unfold when adsorbing to carbon surfaces, which would mean a large proportion of the signal we were seeing could be from denatured protein. Washing the prism with nitric acid, followed by milli-Q water, would in theory polarise the surface and decrease adsorption. This decreased the rate of adsorption, but did not prevent it entirely.

The second issue with the diamond ATR approach was that it was very difficult to remove residual adsorbed “dirt” from the prism. In particular a band at 1744 $cm^{-1}$ was often present in our difference spectra (Figure 5.6). At first we thought this was a $\nu$(NO) band arising from a mononitrosyl iron species. The band was very irreproducible and sometimes occurred when difference spectra were recorded using two different unexposed Fd samples. The band was present in sweat and it is probable that it arises from the carboxylate group of lactate, which is present in skin dust as well as sweat. Washing the prism with multiple rounds of ethanol and nitric acid decreased this problem but never completely. It should also be noted that the DuraSamplIR II accessory was shared between multiple groups, and was often contaminated with strongly IR-absorbing powders.

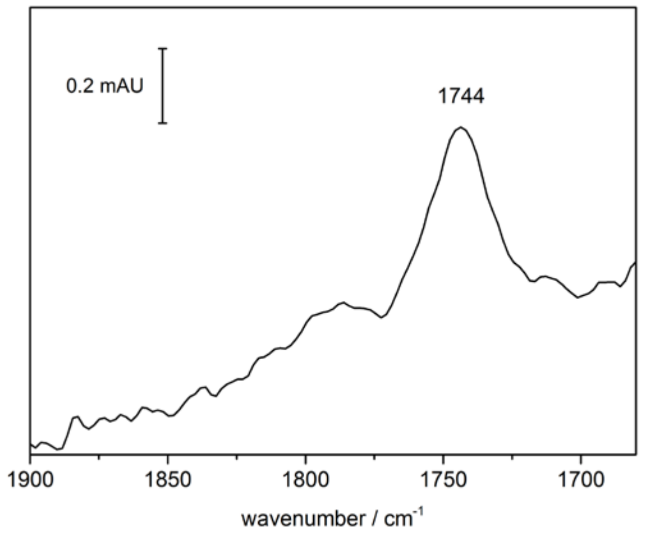

**Figure 5.6 – Adsorbed contaminants absorbing in the ν(NO) region.** The IR spectrum of Fd exposed to 0.1% NO for 3 hours processed against unexposed Fd shows a peak at 1744 cm$^{-1}$.

### 5.3.7 An optimised ATR difference method

We needed to design a setup which could overcome both of the major issues encountered using the diamond ATR in a laboratory atmosphere. To prevent surface contamination issues, we stopped using the diamond ATR accessory and instead used a GladiATR ATR accessory (PIKE Technologies). The benefit of this accessory is that the prism is detachable, so any prism material can be used and it can be cleaned intensely. We used a silicon prism which has no bands in the ν(NO) region and did not adsorb any protein. By removing the prism between each spectrum and cleaning by sonication in concentrated sulfuric acid followed by concentrated nitric acid, then rinsing in milli-Q water, we were able to prevent any anomalous or irreproducible changes in absorption at 1744 cm$^{-1}$.

To improve our anaerobic methods we performed gas exposure and spectroscopy in the same dedicated anaerobic chamber. As NO can disproportionate in the cylinder and form $NO_x$ species we also used a stainless steel column packed with Ascarite® II (20-30 mesh, Sigma-Aldrich) after the cylinder in our setup (Lim et al., 2005). Any $N_2$ which was used was first passed through an $O_2$ scrubber. The flow rate and mixing of gases was controlled with mass flow controllers (Brooks). The mixed gases then entered the glove-box and were bubbled through 5 M sodium hydroxide to both moisture-saturate the gas and ensure complete removal of $NO_x$ species. The anaerobic chamber also provided a dry atmosphere, with a dew point below -85$^{o}$C. This minimised issues with water vapour. Essentially the same method of exposure and sample loading was used as with the diamond ATR method, except the sample was injected onto the prism before the gas-tight cell was clamped on top as there was no risk of oxygen exposure inside the anaerobic chamber.

## 5.4 Insight into the mechanism of [2Fe2S] protein nitrosylation

With this new method in place we now aimed to understand the factors which influence the nitrosylation of Fd to form RRE, as observed with our previous method. Our first specific aim was to investigate the role of $O_2$ in this nitrosylation reaction. The role of $O_2$ in iron-sulfur protein nitrosylation has not been directly studied despite the fact that the immune response will expose bacterial iron-sulfur proteins to NO in an aerobic, highly oxidising environment. One possibility for the action of $O_2$ is that it reacts with NO to form nitrous acid and the drop in pH alters the reactivity of Fd. A study in 1992 showed that Fd undergoes a conformational change below pH 7.0 which increases the solvent exposure of buried hydrophobic residues (Kieleczawa et al., 1992). We postulated that such an opening up of the protein may increase the reactivity of the cluster. This correlates with two previous reports on Fd nitrosylation. A study at pH 8.1 showed that Fd is unreactive towards NO (Sellers et al., 1996), whilst a study at pH 7.0 showed slight reactivity to form 8-10% DNIC as judged by EPR spectroscopy (Fujikawa et al., 2014). This study was published after we had done all the work that will be described below. Our method development work had been performed at pH 7.5, so our second specific aim was to investigate the pH-dependency of the nitrosylation reaction. We increased the buffer concentration in all our reactions to reduce pH changes during reaction with NO. Reactions were performed in either 25 mM MES-NaOH or HEPES-NaOH, depending on the pH used, each with 160 mM NaCl.

### 5.4.1 Role of dioxygen

When Fd at pH 7.5 was exposed to 10% NO gas overnight with no $O_2$ or $NO_x$ species present, no peaks were detectable by IR spectroscopy (Figure 5.7, spectrum i), consistent with the previous report at pH 8.1 (Sellers et al., 1996). To test the effect of $O_2$, Fd was flushed with 10% NO (in $N_2$) gas for 15 minutes and then pure $O_2$ was injected into the vial to different final concentrations. When more than approximately 0.06% $O_2$ was added, the protein rapidly precipitated and the red-brown colour of the protein was lost. At concentrations below 0.03% $O_2$, no colour change was observed after overnight exposure. When approximately 0.05% $O_2$ was added, the solution did not precipitate but underwent a colour change from red-brown to yellow. An IR spectrum after overnight exposure showed substantial RRE formation (Figure 5.7, spectrum ii). In this spectrum it is possible to see a third very minor peak at 1815 $cm^{-1}$, which absolutely confirms the identity of the species as an RRE (Wang et al., 2009).

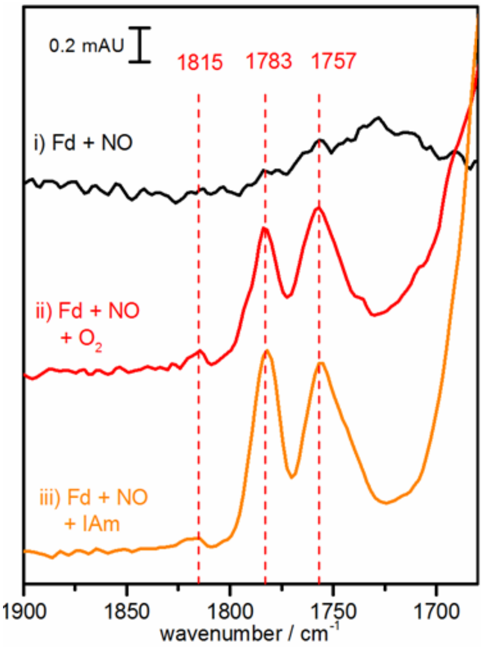

**Figure 5.7 – IR spectra showing the reactivity of Fd towards NO and thiolate sequestration reagents at pH 7.5.** All spectra are of 0.8 mM Fd in 25 mM HEPES pH 7.5, 160 mM NaCl, and are recorded against a background of unexposed Fd. i) Spectrum of Fd after overnight exposure to 10% NO gas under anaerobic conditions. ii) Spectrum of Fd after overnight exposure to a gas mixture containing 10% NO and 0.05% $O_2$. iii) Spectrum of Fd in the presence of 24 mM sodium iodoacetamide after overnight exposure to 10% NO gas.

A mechanistic pathway for nitrosylation of an oxidised [2Fe2S] cluster has been proposed (Figure 5.8) (Lin et al., 2011). In these pathways, the sulfide ligands of the iron are first substituted by NO to form two DNIC products. Loss of two cysteine thiolates would then be required to convert these two DNIC species into an RRE product. In small-molecule systems, DNIC can be converted to RRE by removing thiolates through oxidation by $O_2$ or hydrogen peroxide (Costanzo et al., 2001). Incomplete oxidative sequestration of thiolates by disulfide formation has been shown by mass spectrometry for small-molecule systems (Fitzpatrick et al., 2013), and it has been suggested that oxidative modification of cysteines to sulfenic acids may account for the remainder of the sequestered thiolates. It is therefore possible that in our protein-bound system the role of oxygen is to favour formation of the RRE product by oxidative sequestration of two cysteine thiolates.

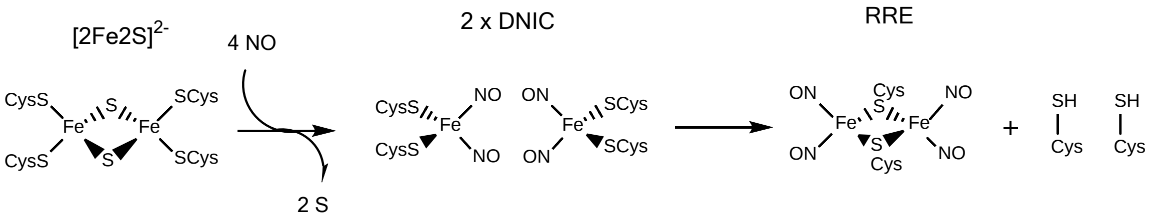

**Figure 5.8 – Possible nitrosylation pathway of an oxidised [2Fe2S] cluster to form an RRE *via* a DNIC intermediate (Lin et al., 2011).**

To examine whether cysteine thiolate sequestration is important in increasing the reactivity of Fd towards NO, we substituted $O_2$ for a specific thiolate-reactive agent, iodoacetamide, which alkylates thiolates through a nucleophilic substitution reaction. Under anaerobic conditions at room temperature and at a pH value of 7.5, iodoacetamide reacts specifically with thiolates and should not cross-react with other residues or NO. We added a 10-fold molar excess of iodoacetamide over free cysteines (assuming complete reaction to form RRE) to Fd and exposed this mixutre to 10% NO. After overnight exposure, the sample had become yellow, and an IR spectrum showed substantial RRE formation (Figure 5.7, spectrum iii). This suggests that thiolate sequestration increases the reactivity of Fd with NO to result in RRE formation. It is therefore likely that oxidative thiolate sequestration is the role that $O_2$ plays in the reaction of Fd with NO.

There are alternative mechanisms by which $O_2$ could be acting. One alternative is that $O_2$ reacts with NO either in the aqueous phase or gas phase and the reaction products react with Fd to result in RRE-formation. In solution, NO and $O_2$ react to form nitrous acid. We measured the pH of a solution just containing the reaction buffer which had been exposed to the same conditions as the RRE-forming Fd, and saw no significant change in pH. We also added excess sodium nitrite to Fd either with or without NO and saw no RRE formation. In the gas phase NO and $O_2$ react to form $NO_2$, and this reacts with further NO and $O_2$ to form various $NO_x$ species. The cross-reactivity of all $NO_x$ gases makes it very difficult to study the specific effects of just one. A cylinder of $NO_2$ gas would contain some NO and higher $NO_x$ species. The simplest way we could determine whether $NO_x$ species are sufficient to nitrosylate Fd was to pre-mix 0.05% $O_2$ and 0.05% NO in $N_2$ in a vial, and then to inject Fd into this vial. This mixture might be expected to generate similar levels of $NO_x$ species as 10% NO, 0.05% $O_2$, but have much less NO. If NO is the reactive species then the reaction of Fd with 0.05% NO, 0.05% $O_2$ will be much slower than in 10% NO, 0.05% $O_2$, whilst if $NO_x$ species are the nitrosylating agents the reaction should occur similarly with each gas mixture. We saw no RRE formation after overnight exposure of Fd to 0.05% NO, 0.05% $O_2$. It is still not possible to distinguish whether it is $O_2$ or $NO_x$ species which favour RRE formation in the presence of NO. One $NO_x$ species which would form is $N_2O_3$. This is known to nitrosylate cysteine thiolates (Ali et al., 2013), which would have the same effect as oxidative sequestration of thiolates by $O_2$. In a phagolysosome, where bacteria will be exposed to NO, there will be multiple thiolate-reactive species (Xia and Zweier, 1997), such as peroxynitrite, superoxide, $O_2$ and $N_2O_3$, so the principle is perhaps more important than the exact identity of the thiolate-reactive species in our case.

A final possibility is that oxidation of the iron in an intermediate cluster is required for RRE formation. As we start with Fd in its oxidised state and do not require a change in oxidation state of the iron to form RRE, it is not clear what this change would be. To investigate this possibility we added excess potassium ferricyanide to Fd and then exposed this mixture to 10% NO. Ferricyanide would not oxidise cysteine thiolates but would oxidise iron. We again saw no RRE formation under these conditions.

From these experiments, we can conclude that the most probable role of $O_2$ is the sequestration of cysteine thiolates.

### 5.4.2 Role of pH

We next wanted to investigate whether the [2Fe2S] cluster of Fd is more reactive towards NO at lower pH values because of the conformational changes which occur below pH 7.0, as discussed earlier. Fd was prepared at a range of pH values – 6.0 and 6.5 in MES buffer and 7.0 and 7.5 in HEPES buffer. All samples were exposed to 10% NO gas overnight under anaerobic conditions. An IR spectrum of each sample was recorded (Figure 5.9). A number of peaks are present in these spectra, indicating that Fd is indeed more reactive toward NO at pH 7.0 and below. A peak is present in each spectrum at 1783 cm$^{-1}$. This is likely to be due to RRE formation. The mechanism by which RRE can form without addition of a thiolate sequestering reagent is not clear. Perhaps a structural change could occur which moves the cysteine thiolates away from the cluster, effectively sequestering them. Unlike the RRE spectra described in the previous sections, the second RRE peak at 1757 cm$^{-1}$ is much larger than the peak at 1783 cm$^{-1}$ and distorted such that the centre of the peak is shifted to 1760 cm$^{-1}$. There also appears to be a third peak at 1726 cm$^{-1}$. The 1726 cm$^{-1}$ peak is most clear when Fd was exposed to NO at pH 6.0. The spectrum at pH 6.0 also has the smallest peak at 1783 cm$^{-1}$ relative to the size of the peak at 1760 cm$^{-1}$. The peak at 1726 cm$^{-1}$ for Fd at pH 6.0 was reproducible (Figure 5.10A, spectrum i). Subtraction of 15% of the RRE spectrum (Figure 5.7, spectrum ii) from the pH 6.0 spectrum (Figure 5.10A, spectrum i) reveals a spectrum with peaks at 1762 and 1726 cm$^{-1}$ (Figure 5.10A, spectrum ii). These peak positions are similar to those recorded for small-molecule DNIC species, particularly the oligopeptide-bound DNIC, which has peaks at 1767 and 1722 cm$^{-1}$ (Lin et al., 2011).

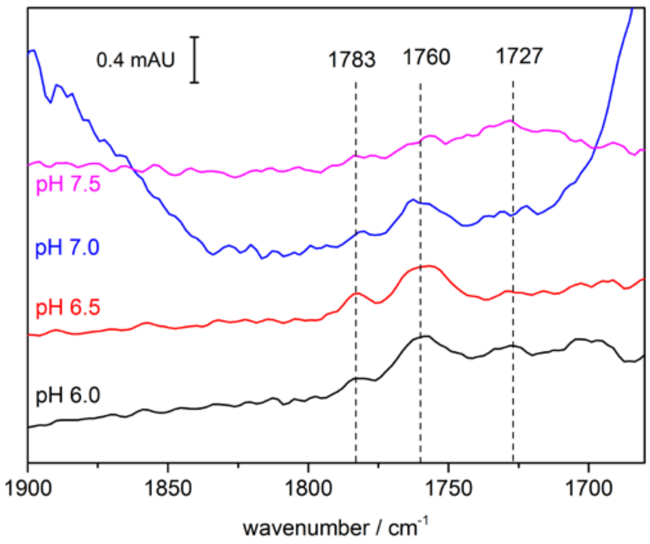

**Figure 5.9 – Effect of pH on the anaerobic reaction of Fd with NO.** IR spectra of 0.8 mM Fd exposed to 10% NO overnight processed against a background of unexposed Fd. Fd was in either a MES or HEPES buffer at the pH values indicated.

The appearance of a different nitrosylation product, DNIC, at low pH gave us an opportunity to investigate the Fd nitrosylation pathway. If the scheme suggested by Liaw and co-workers is correct (Figure 5.8)(Lin et al., 2011), this DNIC should be converted to RRE by removal of thiolates, which we propose is the role of $O_2$. To detect transformations we ideally needed to determine how much cluster remained in its unreacted [2Fe2S] state, and to quantitatively determine the amounts of each product formed. This required correlating our IR spectra with other spectroscopic techniques. We therefore used sufficient Fd in each reaction that one aliquot could be used for IR spectroscopy, one for UV/visible spectroscopy and one for EPR spectroscopy. The UV/visible spectrometer was housed in an anaerobic chamber linked to the one used for NO exposure. EPR samples were prepared and flash frozen in liquid $N_2$ in this linked chamber as well. This meant we could be sure anaerobic conditions were maintained across all three spectroscopic measurements.

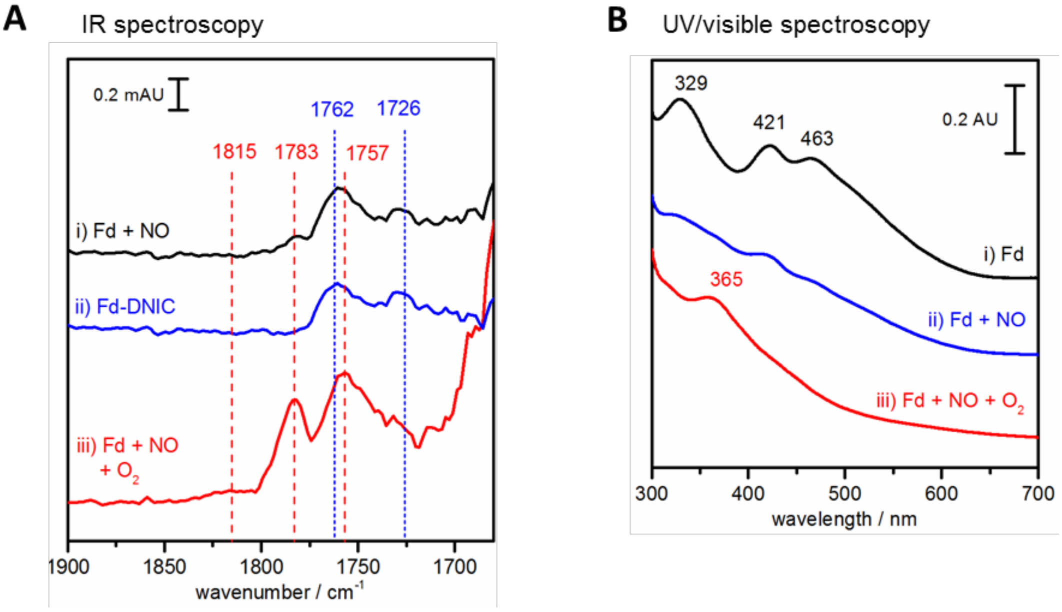

**Figure 5.10 – Reactivity of Fd towards NO at pH 6.0.** (A) IR spectra of 0.8 mM Fd in MES pH 6.0, 160 mM NaCl processed against unexposed Fd. i) Spectrum of Fd exposed to 10% NO overnight. ii) Spectrum i with the RRE component removed by subtraction of 15% of spectrum ii from Figure 5.7. This shows peaks arising from the DNIC component. iii) Fd exposed to 10% NO overnight followed by exposure to a mixture of 10% NO and 0.05% $O_2$ for two hours. (B) UV/visible spectra of 40 µM of the same Fd samples described for panel A processed against a background of buffer alone. i) Unexposed Fd. ii) Fd exposed to 10% NO overnight. iii) Fd exposed to 10% NO overnight followed by exposure to a mixture of 10% NO and 0.05% $O_2$ for two hours.

A UV/visible spectrum of native Fd shows characteristic features of an oxidised [2Fe2S] cluster (Figure 5.10B, spectrum i). When Fd was exposed to 10% NO at pH 6.0 overnight, the resulting UV/visible spectrum showed partial loss of the [2Fe2S] features (Figure 5.10B, spectrum ii). This spectrum is relatively featureless so it is not obvious what new species have formed; the spectral features of iron nitrosyl species are broad and overlap with those of [2Fe2S] features, which are also broad. This is the major problem with using UV/visible spectroscopy to study iron-sulfur protein nitrosylation.

We now wanted to see if $O_2$ would convert DNIC product to RRE product. Our first approach was to add 0.05% $O_2$ to a sample that had already been exposed to 10% NO overnight. In this case there was a clear yellowing of the sample within a few hours. IR spectroscopy showed substantial RRE formation (Figure 5.10A, spectrum iii). UV/visible spectroscopy of this sample showed that absorption features arising from the native [2Fe2S] cluster had been lost and were replaced by a single broad peak at 367 nm (Figure 5.10B, spectrum iii). This peak at 367 nm is consistent with RRE formation (Costanzo et al., 2001).

### 5.4.3 Probing the mechanism of Fd nitrosylation with EPR

It is possible to detect and quantify DNIC formation by EPR because DNIC is an EPR-active species with a spin, S = ½. Although the oxidised Fd [2Fe2S] cluster and RRE are both EPR-silent, it is possible to reduce these species with dithionite to S = ½ EPR-active states. Double integration of an EPR signal quantifies the number of "spins" which give rise to that signal. By taking a spectrum of a copper(II)-EDTA standard, which has the same spin system as the species under study, at a known concentration, it is possible to correlate the number of spins with the actual concentration of the sample. Thus, it is possible to quantify the yields of each transformation. There are, however, two issues with this method. Firstly, it depends on the sample being completely stable during freezing. It is possible for ice crystals formed during the freezing process to destroy biological material. Secondly, the dithionite reduction approach depends on there being no further reactivity with dithionite apart from reduction. This is particularly an issue because dithionite is unstable and its reactivity is difficult to predict. Additionally the clusters may have further reactivity when reduced. All EPR spectroscopy and data analysis detailed in this section were performed by Dr. Will Myers (CAESR Facility, Department of Chemistry, University of Oxford).

Reduced native Fd is EPR-active. However, reduction of Fd at pH 6.0 with excess dithionite resulted in no EPR signal. This may have been because the reduced cluster is unstable at pH 6.0. To investigate this idea, Fd at pH 6.0 was reduced with excess dithionite, and dithionite was subsequently removed by washing out low molecular-weight compounds with a spin concentrator column. UV/visible spectra at each stage of this process reveal the instability of the reduced Fd [2Fe2S] cluster (Figure 5.11). Fd is largely reduced by dithionite (Figure 5.11B). During the subsequent desalting process, the colour of Fd slowly faded. A UV/visible spectrum of desalted Fd shows that the ratio of the absorbance of the [2Fe2S] cluster between 300 and 700 nm compared to the absorbance of the protein at 280 nm had greatly decreased (Figure 5.11C). This suggests that most of the cluster has been lost. Furthermore, the remaining absorption is from an oxidised, not reduced, cluster, and can probably be attributed to incomplete dithionite reduction. Instability of the reduced Fd cluster has not previously been reported in the literature, although this has not been studied at low pH, and we did not witness this effect when working at pH 7.5. These results agree with the idea that the Fd [2Fe2S] cluster is less stable at lower pH. The relevance of this to quantification is that we were unable to quantify the unreacted native Fd signal at pH 6.0 by EPR spectroscopy.

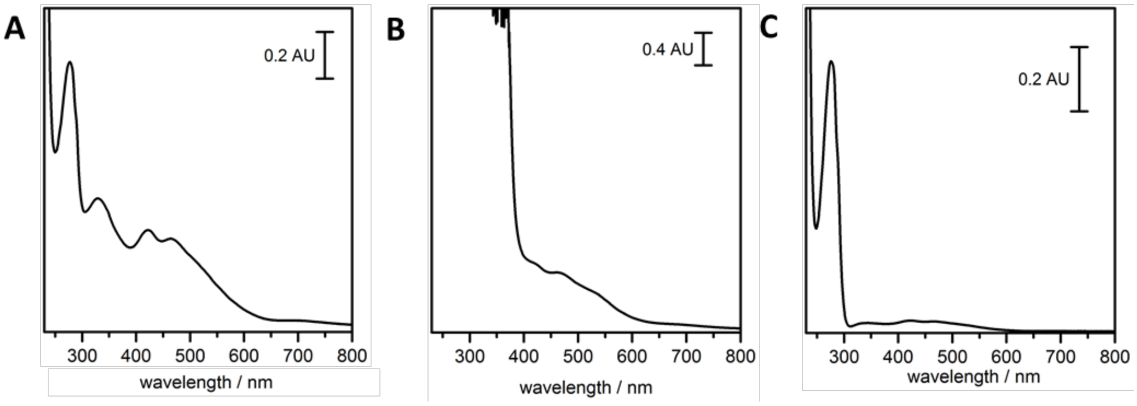

**Figure 5.11 – UV/visible spectra showing that dithionite-reduced Fd at pH 6.0 is unstable.** All spectra show Fd in 25 mM MES, pH 6.0, 160 mM NaCl. (A) Spectrum of 40 μM oxidized Fd as prepared. (B) Spectrum of 128 μM Fd recorded straight after reduction with excess sodium dithionite. The spectrum is shown scaled by protein concentration to spectrum A. (C) Spectrum of sample of Fd reduced by excess sodium dithionite following a desalting step to remove dithionite shows that the majority of the cluster is no longer present, and the remaining cluster is in the oxidised form, probably due to initial incomplete reduction. Spectrum(C) is presented scaled to the $A_{280}$ peak of (A) to account for changes in concentration during desalting. All manipulations were performed under anaerobic conditions. Spectra of both oxidized and reduced Fd have been reported at pH 7.8 (Tagawa and Arnon, 1962).

EPR spectroscopy was first applied to Fd at pH 6.0 exposed to 10% NO overnight. An EPR spectrum of this sample showed a single species with a $g_{av}$ = 2.03 (Figure 5.12A). This is characteristic of a DNIC species. Spin counting showed that this accounts for 16-18% of the total protein. However, as two DNIC species can in theory form per Fd protein, this is only 8-9% of the potential DNIC which could form. Reduction of the sample with excess sodium dithionite resulted in an EPR spectrum characteristic of an rRRE, with a minor DNIC component (Figure 5.12B). Simulation of the individual components, and spin integration, showed that RRE accounted for 10% of the total iron or protein (as one rRRE would be expected to form per protein), whilst the DNIC component was now at 1.5% of total iron. The decrease in the DNIC component caused by dithionite is consistent with partial reduction of protein-bound DNIC by dithionite, which has been observed previously (Tinberg et al., 2010). In summary, the EPR confirms what was seen by IR and UV/visible spectroscopy: incomplete nitrosylation of the Fd [2Fe2S] cluster under anaerobic conditions to form a mixture of DNIC and RRE.

EPR spectroscopy was next performed to quantify the conversion of DNIC to RRE observed by IR spectroscopy (Figure 5.10A) after introduction of 0.05% $O_2$ to the Fd sample exposed to 10% NO overnight. Compared to the sample before $O_2$ addition, there was a decrease in DNIC signal from 9% to 4% of total Fe after $O_2$ addition. The sample was reduced with sodium dithionite and another EPR spectrum recorded. EPR spin quantitation showed an increase in rRRE signal relative to NO exposure alone, from 10% to 17%. This is a smaller increase than would be expected from the IR and UV/visible spectra (Figure 5.10). This may be due to the issues with EPR discussed previously, such as the rRRE being destroyed by the freezing process or reactivity between the rRRE and dithionite. In summary, the presence of $O_2$ causes transformation of DNIC to RRE, but the overall yield remains relatively low.

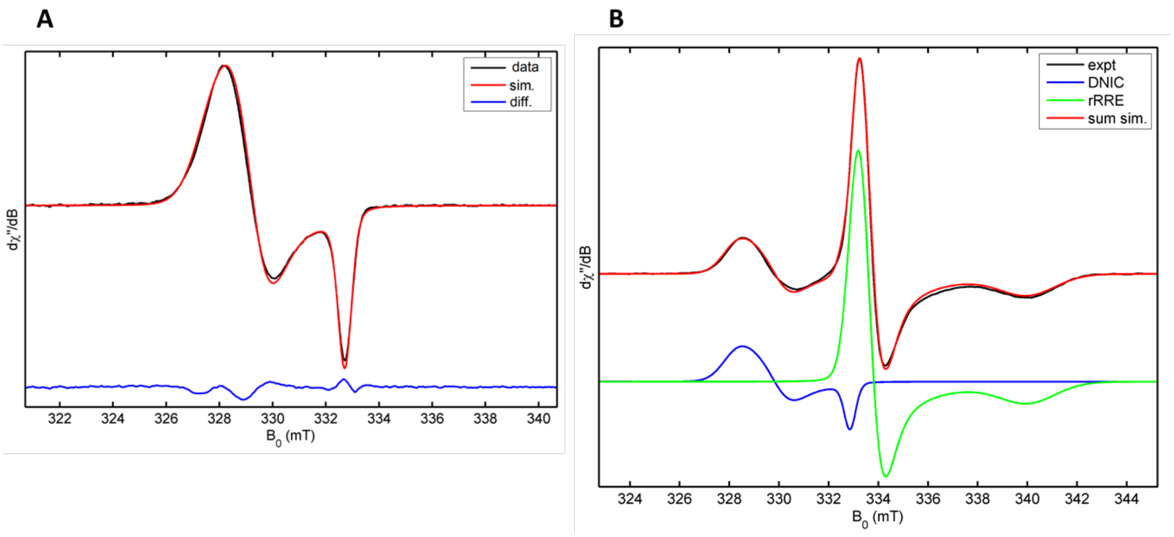

**Figure 5.12 – Characterisation of the Fd nitrosylation products formed at pH 6.0 using EPR spectroscopy.** (A) Continuous wave (CW) EPR spectrum of 250 µL of 160 µM Fd I in 25 mM MES, pH 6.0, 160 mM NaCl, measured at X-band (black). A simulation of this spectrum is shown in red, whilst the residuals between the data and the simulation are shown in blue. By spin quantitation the DNIC signal doubly-integrates to 26 µM, equivalent to 8% of total Fe in the sample. In the EPR simulation, the g-values were obtained as $g_x$=2.043, $g_y$=2.035 $g_z$=2.014. (B) CW-EPR spectrum of the sample in A after reduction with a few crystals of sodium dithionite (Tinberg et al., 2010). A simulation of the spectrum is shown in red. This simulation is a sum of 22% dinitrosyl iron complex (DNIC), shown in blue, and 78% reduced Roussin's red ester (rRRE), shown in green. For the DNIC component, simulation parameter values were $g_x$=2.041, $g_y$=2.032, and $g_z$=2.013. For the rRRE component, simulation parameter values were $g_x$=2.011, $g_y$=2.008, and $g_z$=1.970. EPR spin quantitation shows that the concentration of total spins is 16.6 µM, which means that DNIC and rRRE account for 1.5% and 10% respectively of total Fe.

Exposing Fd to a mixture of NO and $O_2$ is difficult to interpret because a) NO and $O_2$ react to form $NO_x$ species and b) the new RRE which forms may not result from the DNIC which is lost, as new RRE can be formed from the native Fd [2Fe2S] cluster. If the scheme shown in Figure 5.8 is correct, then DNIC can be converted to RRE without additional NO if two DNIC species are present in one protein molecule. To test this we exposed Fd to 10% NO overnight, then removed the NO by flushing the vial with $N_2$ for two hours, and then introduced 0.05% $O_2$. EPR spin quantitation of the sample after $O_2$ exposure showed that the DNIC content had decreased from 8% to 2% of total Fe. However, the IR spectrum of this sample was not clear due to water vapour and baseline issues. It would be interesting to follow up this line of study in the future.

### 5.4.4 Protein structural changes upon nitrosylation

Bacterial NO-sensing iron-sulfur proteins must undergo a conformational change upon reaction with NO to allow them to signal the presence of NO. IR spectroscopy can be used to study the secondary structure of proteins (Barth, 2007). The amide I region of the spectrum is due to the amide C=O stretching vibration. This vibrational band is very sensitive to hydrogen bonding. Protein secondary structures have defined hydrogen bonding. The amide I band is composed of multiple defined C=O bands in different secondary structures, and much work has been performed to assign secondary structures to particular C=O band positions. By taking a second derivative of the spectrum it is possible to identify these bands and quantify the ratio of different secondary structure elements in a protein.

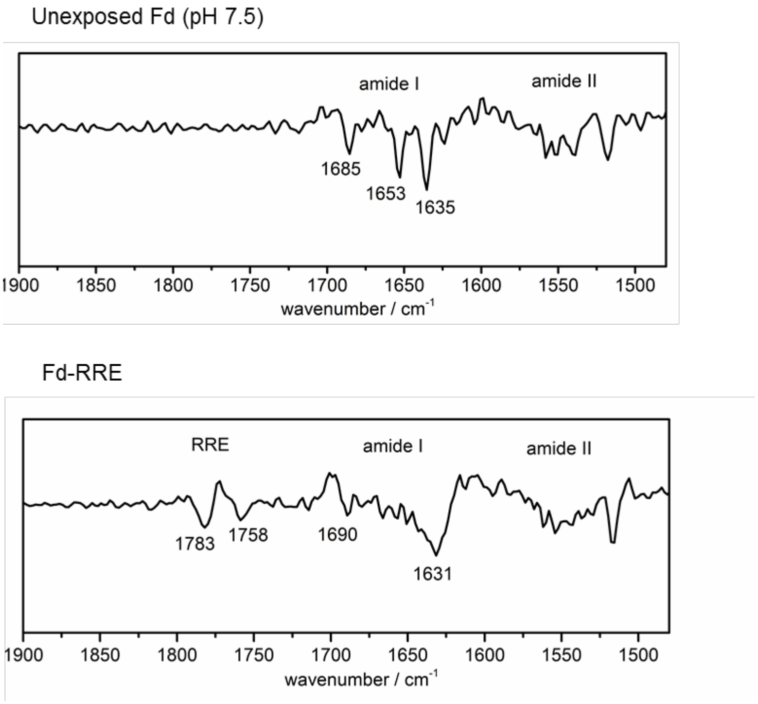

**Figure 5.13 – Protein structural changes associated with nitrosylation of Fd to form RRE.** Second derivatives were taken of IR spectra of the indicated proteins processed against a water background. Fd-RRE is Fd at pH 7.5 exposed to 10% NO, 0.05% $O_2$ until complete sample yellowing.

In the case of Fd, the second derivative of an IR spectrum of the unexposed Fd shows defined peaks (Figure 5.13, upper panel); the peak at 1653 $cm^{-1}$ is due to $\alpha$-helix, whilst the peaks at 1685 and 1635 $cm^{-1}$ are due to $\beta$-strand (Barth, 2007). The second derivative of the IR spectrum of Fd-RRE (Fd at pH 7.5 exposed to 10% NO, 0.05% $O_2$) shows a rather different profile (Figure 5.13, lower panel). The defined peaks are no longer present, and instead the spectrum is broad with features at 1690 and 1631 $cm^{-1}$. Such a second derivative spectrum is consistent with protein unfolding (Susi and Byler, 1986). Fd is a small protein and its fold is stabilised by the presence of its iron-sulfur cluster. Formation of RRE from a [2Fe2S] cluster requires loss of two cysteine thiolates (Figure 5.8), and the other two cysteine thiolates move from terminal coordination geometry to bridging positions. It is therefore expected that protein unfolding may be required to accommodate this large structural change. This highlights the importance of the chelating effect of the protein and the importance of studying iron-sulfur cluster nitrosylation in the context of the protein to which the cluster is bound.

## 5.5 Extending the technique to [4Fe4S] proteins

### 5.5.1 HiPIP

Now that we had a method which worked reproducibly, and had gained some insight into the mechanism of [2Fe2S] iron-sulfur protein nitrosylation, we wanted to extend the method and mechanistic insight to [4Fe4S] proteins. In general, [4Fe4S] proteins are more sensitive to $O_2$ than [2Fe2S] proteins. We chose *Acidithiobacillus ferrooxidans* HiPIP as our model [4Fe4S] protein. This protein has a cluster with a sufficiently high potential that it is not oxidised by $O_2$, and so is oxygen-stable. Furthermore, HiPIP is used by the group of Ben Berks as a model substrate for the twin-arginine translocation (Tat) system. I therefore had access to a HiPIP expression strain. This strain contained a plasmid in which HiPIP has its native Tat signal peptide, and a C-terminal hexahistidine tag. The strain is a BL21 derivative with a Tat system knock-out. The Tat system translocates folded proteins into the periplasm. In this construct HiPIP is produced in the cytoplasm as normal, but not exported to the periplasm. The only issue with this expression strategy is that the HiPIP signal peptide is not cleaved, but this is anticipated to be an unstructured peptide chain which will have no effect on the reactivity of the HiPIP [4Fe4S] cluster.

Cells were induced with IPTG in LB medium. The protein was purified by the standard methods for purification of SoxYZ as described in Section 2.3, but without the heat-treatment step. The soluble lysate was loaded on a 5 mL histrap HP (GE Healthcare) and eluted with a gradient of imidazole. Final purification was achieved by size-exclusion chromatography with a Superdex 75 10/300 column (GE Healthcare) into reaction buffer – 25 mM HEPES-NaOH, 160 mM NaCl pH 7.5.

Experiments with HiPIP were performed using the setup described for Fd, with a GladiATR accessory housed inside the same glove box as the gas exposure system. There is a much larger range of products which could form from nitrosylation of a [4Fe4S] protein compared to a [2Fe2S] protein (Figure 5.1). Furthermore, there have been no reports on nitrosylation of oligopeptide-bound [4Fe4S] systems which could provide accurate estimates of band positions for expected products. Sergio Kogikoski, a DPhil student in our group, is working on nitrosylation of oligopeptide-bound [4Fe4S] systems, and so some comparisons will be made to his unpublished work on this.

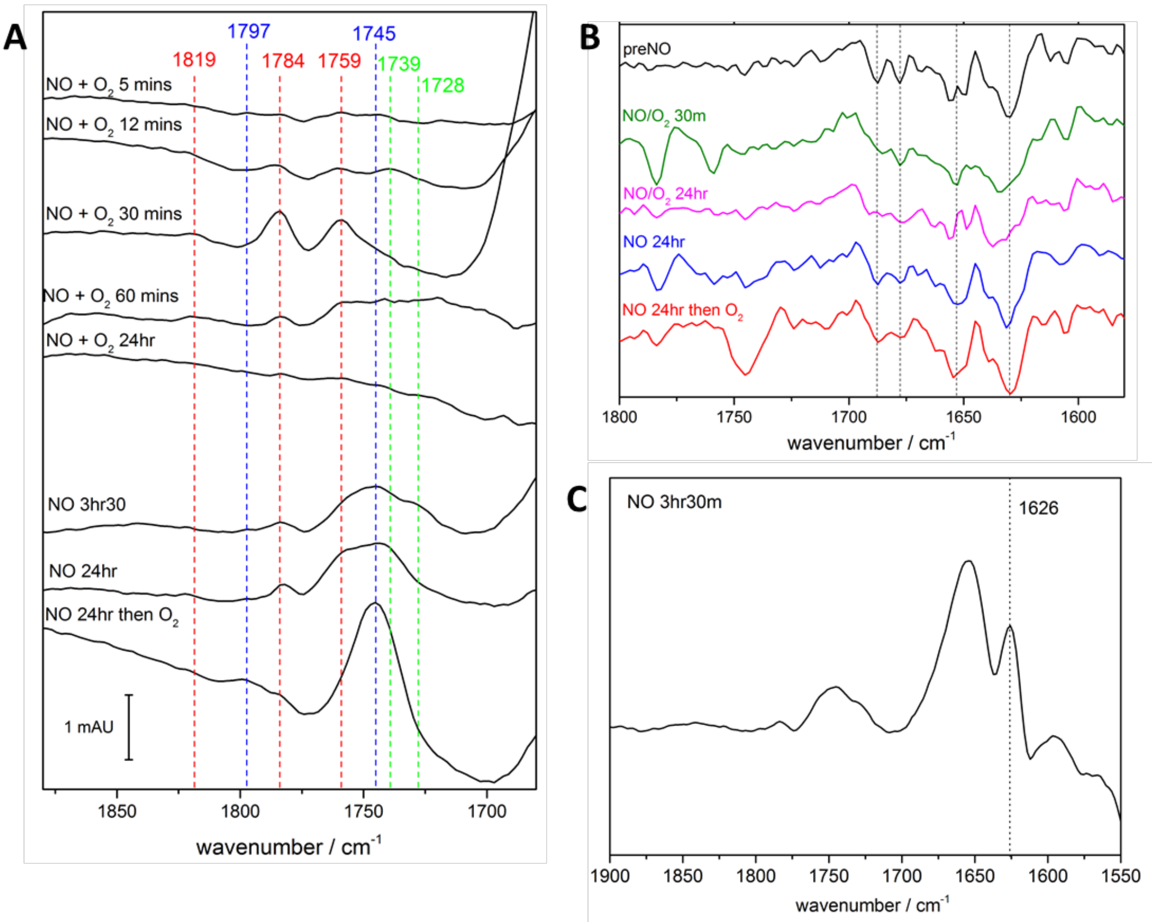

**Figure 5.14 – IR spectroscopic study of the reaction of the [4Fe4S] HiPIP protein with NO.** All panels show IR spectra of 0.8 mM HiPIP exposed to NO and recorded using the methods described in Section 5.3.5. Spectra in panels (A) and (C) are processed against a spectrum of unexposed HiPIP, whilst spectra in (B) are second deriviatives of the spectra shown in (A) processed against water as a background. In (A), peaks which may be assigned to RRE are labelled with red dashed lines, peaks which may be assigned to RBS are labelled with blue dashed lines, and unassigned peaks are indicated with green dashed lines.

We first studied nitrosylation of HiPIP by a mixture of 10% NO, 0.05% $O_2$ (Figure 5.14). The reaction was remarkably similar to Fd with the same gas mixture. After 30 minutes, substantial RRE product had formed. HiPIP-RRE had bands at 1819 (weak), 1784 and 1759 cm$^{-1}$, compared to 1815 (weak), 1783 and 1757 cm$^{-1}$ for Fd-RRE. However, whereas Fd-RRE was stable for long exposure times to this gas mixture, the HiPIP-RRE product began to disappear after 30 minutes and the RRE bands are barely detectable in a spectrum taken after overnight exposure of HiPIP to 10% NO, 0.05% $O_2$. The protein had become colourless by this point. In the early time points there were other possible $\nu$(NO) bands in the 1700-1800 cm$^{-1}$ region of the spectrum. These peaks may arise from intermediate species in the [4Fe4S] nitrosylation reaction. As with Fd, there were large changes in the amide region during this reaction (Figure 5.14B). Second derivatives of the amide I region of the spectra shows broadening and shifting of the peaks after gas exposure. This suggests that, like Fd, HiPIP unfolds during RRE formation. The protein remains unfolded when the RRE is lost. HiPIP is very small (5 kDa) and the presence of a [4Fe4S] cluster may be required to stabilise the protein fold.

We also performed anaerobic nitrosylation experiments. There were no obvious colour changes during any anaerobic nitrosylation experiments with HiPIP. However, after exposure of HiPIP to 10% NO in $N_2$ for 3.5 hours there were clear peaks in the IR spectrum (Figure 5.14). A peak at 1784 $cm^{-1}$ and shoulder at 1759 $cm^{-1}$ can be tentatively assigned as RRE. There are also peaks at 1745 and 1728 $cm^{-1}$. A peak was also present at 1626 $cm^{-1}$ (Figure 5.14C), which looks much larger than a usual secondary structure change. Interestingly, Sergio Kogikoski has synthesised an oligopeptide-bound iron-nitrosyl species with a similar peak. After a further 20 hours of exposure to 10% NO, the peaks at 1728 and 1626 $cm^{-1}$ were no longer present. One possibility is that the 1728 $cm^{-1}$ peak arises from a $Fe_4S_4(NO)_4$ intermediate (Figure 5.1). A previous study has shown that this species exhibits a single peak at 1725 $cm^{-1}$ (Victor and Lippard, 2014). As a final experiment, 0.05% $O_2$ was added to the vial in which HiPIP had been exposed to 10% NO for 24 hours. Remarkably, the tentative RRE peaks decreased, and the spectrum became dominated by the peak at 1745 $cm^{-1}$. A new minor peak was also present at 1797 $cm^{-1}$. In all these experiments there were no obvious changes to the amide region (Figure 5.14B) suggesting the protein remained folded throughout.

The cubane iron-nitrosyl species, RBS (Figure 5.1), is expected to have two minor peaks at 1727 and 1797 $cm^{-1}$, and one major peak at 1745 $cm^{-1}$ (Victor and Lippard, 2014). It is not unexpected that we would not be able to detect the 1727 $cm^{-1}$ peak as we generally have trouble detecting peaks below 1730 $cm^{-1}$ when we do not have very flat baseline (see Section 5.3.4 on $^{15}NO$

labelling of Fd-RRE), it is likely that the 1745 and 1797 cm$^{-1}$ peaks we detect arise from RBS. RBS has previously been detected as a major product of nitrosylation of a [4Fe4S] ferredoxin in a study using NRVS (Tonzetich et al., 2010). Interestingly, this RBS species is not bound by cysteine thiolates. HiPIP appears to be unstable without any bound cluster, as judged by the amide I region after removal of the [4Fe4S] cluster by overnight NO and $O_2$ exposure. As the protein remains folded after substantial RBS formation, as judged by the amide I region (Figure 5.14B), it seems likely that the RBS is non-covalently bound inside the protein. It is unclear why a 10% NO, 0.05% $O_2$ mixture promotes rapid RBS formation after overnight exposure to NO, but promotes RRE formation when HiPIP has not been pre-incubated with NO. This result is reproducible. One possibility is that $O_2$ is oxidising a reduced RBS species which is hidden in the amide region of the spectrum. This could be tested by determining whether either the oxidising agent ferricyanide or the cysteine-sequestration reagent iodoacetamide can substitute for $O_2$ to promote RBS formation.

### 5.5.2 An NO-sensing [4Fe4S] protein

The long-term aim of this method development was to study the nitrosylation reactions of NO-sensing proteins. Our collaborators in the University of East Anglia are interested in the nitrosylation of the *E. coli* Fumarate and Nitrate Reductase Regulator (FNR) [4Fe4S] protein. The [4Fe4S] cluster of this protein is broken down in the presence of oxygen. This results in a conformational change of the protein which prevents dimerisation of the protein and stops it binding to its cognate DNA promoter region. A similar effect is induced by NO. Our collaborators have shown that FNR forms a mixture of DNIC and RRE upon nitrosylation (Cruz-Ramos et al., 2002) and that some of the released sulfide may be retained as cysteine persulfide such that the iron-nitrosyl clusters are ligated by cysteine perthiolates (Crack et al., 2013). For our studies we used a Leu28His variant of FNR (Bates et al., 2000). This substitution makes the protein more oxygen-stable which eases handling, but does not affect the rate of reaction of the protein with NO (Jason Crack, personal communication). This protein was expressed and purified by Jason Crack in the group of Nick Le Brun. The protein was prepared in 25mM HEPES pH 7.5, 100mM NaCl, 600mM KCl, 5% Glycerol. We have only performed experiments with this protein whilst we were using the diamond ATR setup, and so our preliminary data have issues with anaerobicity and prism surface effects.

FNR was much more reactive towards NO than Fd was. The reaction of FNR with 10% NO had finished before we could measure the sample. Unlike Fd, FNR could be nitrosylated by 0.1% NO, which is equivalent to *ca.* 2 $\mu$M NO in solution. The clearest spectra were obtained from a time-course using 0.5% NO (Figure 5.15A). The spectrum after 200 minutes exposure shows a product with a major peak at 1744 $cm^{-1}$, and minor peaks at 1796 and 1711 $cm^{-1}$. By comparison to HiPIP, this can be tentatively assigned to an RBS species. The peak at 1744 $cm^{-1}$ was retained after desalting the exposed protein to remove low-molecular weight species (Figure 5.15C), suggesting that the RBS is protein-bound even if it is not coordinated by cysteine residues. A peak at 1653 $cm^{-1}$ grew at the same rate as the RBS peaks. This position corresponds exactly with the amide I peak for $\alpha$-helix. We exposed FNR to $^{15}$NO using the nitrite and ascorbate method described in Section 5.3.4. Whilst the 1745 $cm^{-1}$ peak clearly shifted to 1708 $cm^{-1}$, the peak at 1653 $cm^{-1}$ was unaffected (Figure 5.15B). This confirms that this peak does not arise from NO but is likely due to a conformational change leading to an increase in $\alpha$-helix. A previous report has used circular dichroism spectroscopy to show that the conformational change of FNR induced by $O_2$ exposure results in an increase in $\alpha$-helix content. The presence of a peak at 1783 $cm^{-1}$ in these spectra which shifts to 1747 $cm^{-1}$ when $^{15}$NO is used suggests that RRE can also form as a product of FNR nitrosylation. It is likely that the NO produced using the nitrite and ascorbate method is heavily contaminated with $NO_x$ species.

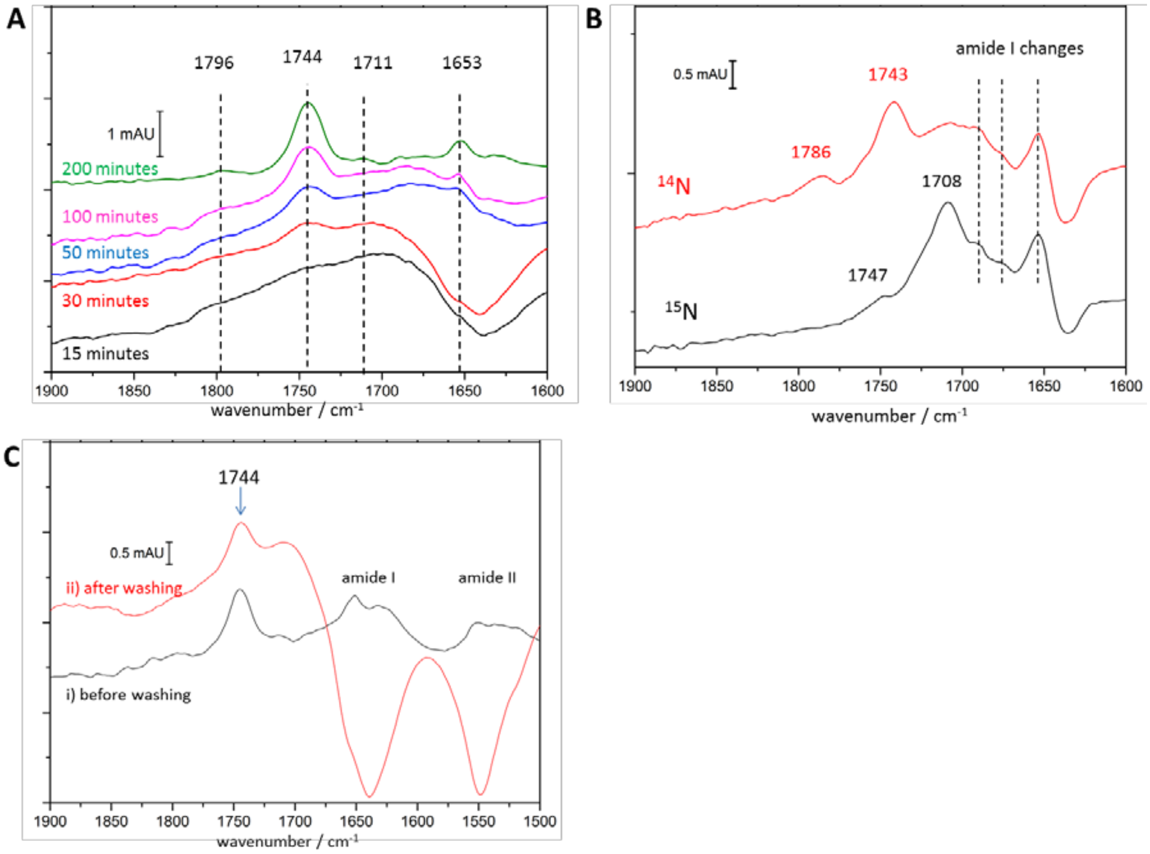

**Figure 5.15 – FNR nitrosylation studied using IR spectroscopy.** All panels show IR spectra, recorded using the diamond ATR DurasamplIR II method, of 0.8 mM FNR after exposure to NO processed against a background of unexposed FNR. (A) FNR was exposed to 0.5% NO (in $N_2$) and samples were taken at the indicated time-points for IR spectroscopy. (B) FNR was nitrosylated by NO generated through mixing either $^{14}$N- or $^{15}$N-sodium nitrite (as indicated) and ascorbic acid at the bottom of the reaction vial. (C) FNR was exposed to 10% NO for one hour. A sample was taken to record IR spectrum i. The rest of the NO-exposed FNR was removed from the vial in an anaerobic chamber. Multiple rounds of dilution and concentration using a spin concentrator column were performed to wash low-molecular weight species from the sample. The sample was concentrated back to approximately the same volume and IR spectrum recorded. Both spectra are shown as difference spectra processed against unexposed FNR. The slight decrease in the 1744 cm$^{-1}$ peak after washing compared to before washing is consistent with the decrease in the amide bands after washing, suggesting that the protein is slightly more dilute than before the washing process.

## 5.6 *In situ* IR experiments

The biggest advantage of IR spectroscopy as a method to study iron-sulfur protein nitrosylation, when compared to NRVS or EPR, is that experiments can be done *in situ*. This means continuous measurements can be performed on a single sample whilst this sample is exposed to varying conditions. An example of such a method is to collect IR spectra of proteins under electrochemical control. Our ideal experiment to study iron-sulfur protein nitrosylation is to put unexposed protein on the ATR prism in a gas-tight cell, and then introduce different gas mixtures into the cell and record spectra of the nitrosylation reactions as they occur. Such a method may be able to detect early reaction intermediates, such as a mononitrosyl iron complex. Such a method would also be ideal for studying the nitrosylation of HiPIP. In both the anaerobic and aerobic pathways different species are made and lost during the time points I measured. Due to the stringency in prism cleaning it is only possible to collect one IR spectrum every two hours in the method we have optimised. This makes it very difficult to do detailed time-course studies.

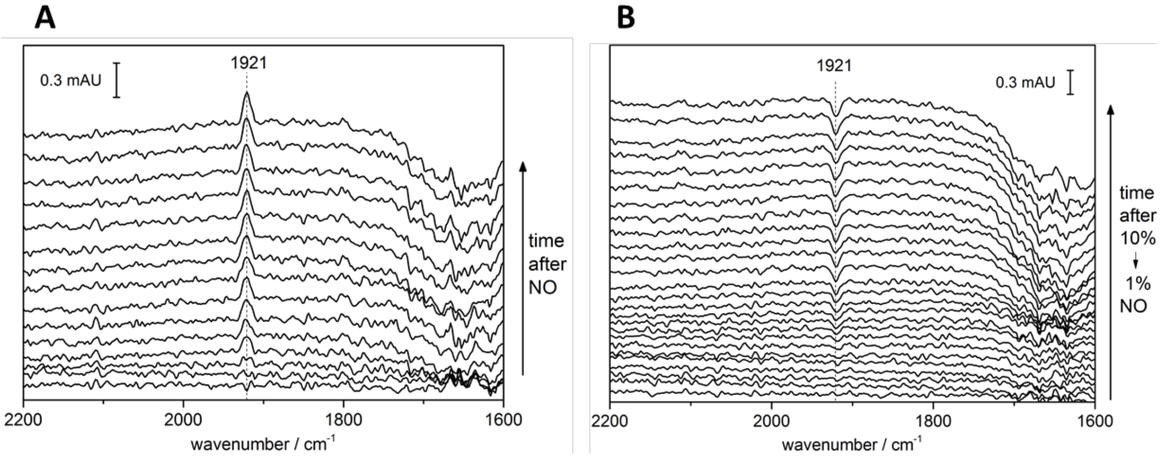

**Figure 5.16 – *In situ* IR spectroscopy of NO binding and dissociating from Mb(III).** NO gas was flushed through the sample cell at 2.2 mL minute$^{-1}$. Mb(III) was at a concentration of 4 mM in 15 mM HEPES pH 7.5, 200 mM NaCl. Each spectrum is an average of 100 scans recorded over 45 seconds, directly after the preceding spectrum. All spectra are processed against the spectrum recorded just before the indicated gas change. The lowest spectrum shows the first spectrum after the indicated gas change. (A) The cell had previously been flushed with $N_2$ gas. All the lines leading to the cell had been flushed with 10% NO gas. The taps leading to the cell were opened to expose the sample to a continuous flow of 10% NO gas. The time taken for the NO gas to flush the line after the tap and the cell results in the small lag phase before an increase in the Mb(III)-NO signal at 1921 cm$^{-1}$. (B) The cell was being continuously flushed with 10% NO gas (in $N_2$). The concentration was changed to 1% NO gas (in $N_2$) using mass flow controllers. A larger lag phase and equilibration time is seen here because of the line between the mass flow controllers and the sample cell. NO binds to Mb(III) reversibly, so a decrease in the concentration of NO in solution causes NO to dissociate form Mb(III) resulting in the negative peak at 1921 cm$^{-1}$.

In theory, this experiment should be relatively easy. We can load the protein on the ATR prism and seal it in a gas-tight cell to prevent evaporation. The protein does not adsorb to the prism and spectra recorded over time show little change. Then, instead of flushing gas through the vial with protein, we would flush gas through the gas-tight cell. We first attempted the experiment as described using oxidised myoglobin (Mb). Continuous spectra were recorded whilst gas was constantly flushed through the cell. Mass flow controllers were used to switch from pure $N_2$ to 10% NO in $N_2$. The resulting spectra are shown in Figure 5.16A as difference spectra processed against Mb being flushed with $N_2$. In Figure 5.16A a peak at corresponding to Mb(III)NO can be seen forming within 3 scans. Mb should bind NO reversibly. The NO gas concentration was decreased to 1% NO. Spectra recorded after this change are shown as difference spectra processed against a spectrum before the gas concentration decrease. The Mb(III)NO peak decreases in size when the NO concentration is decreased (Figure 5.16B), as would be anticipated for a reversible binding event. A change from 10% to 1% NO gas would be equivalent to a decrease in dissolved NO concentration from *ca.* 200 μM to 20 μM. That most of the NO dissociates after this concentration decrease correlates well with the $K_D$ for the binding of NO to Mb(III) being *ca.* 100 μM (Brucker et al., 1998).

This *in situ* method should be readily applicable to HiPIP and FNR because they react anaerobically with NO at reasonable rates. It is also not necessary to keep a constant flow of gas if the cell is gas-tight. This would prevent problems with disturbance of the protein on the prism and evaporation, which result in the relatively poor baseline in the amide region during the Mb experiments (Figure 5.16).

## 5.7 Possible mechanistic pathways of iron-sulfur protein nitrosylation

Our data provide us with some insight into the specific mechanistic pathways for the nitrosylation of [2Fe2S] and [4Fe4S] iron-sulfur proteins are. The data for our [2Fe2S] model system, Fd, are nearly consistent with a pathway where sulfides are substituted for NO to form two DNIC species (Figure 5.17A) (Lin et al., 2011). A rearrangement of these species into an RRE is then favoured by sequestration of the two released thiolates. One important detail is that there is no anaerobic reactivity at pH 7.5, but relatively fast reactivity in the presence of thiolate-reactive reagents. This would suggest that the thiolate sequestration step is limiting the rate of the nitrosylation pathway. However, if the mechanism shown in Figure 5.17A were true then under these conditions you would anticipate a large build-up of the intermediate before RRE formation, the DNIC species, which is not the case. One explanation for this behaviour is that all the steps are in equilibrium until the thiolates are sequestered and this drives the entire reaction pathway forward. However, there is no evidence that DNIC formation is reversible.

Another mechanism is possible which is more consistent with our data (Figure 5.17B). In this mechanism DNIC is not an intermediate to RRE formation and the formation pathways to DNIC and RRE are distinct. In this case the first step of the RRE formation pathway requires loss of two thiolates to form a mononitrosyl intermediate. The steps to RRE formation after thiolate sequestration would then be very rapid so that these intermediates are not detected. DNIC formation would occur as in Figure 5.17A with substitution of sulfides by NO first. The DNIC which is formed could also be converted to RRE by thiolate-reactive reagents, as in the pathway shown in Figure 5.17A, but this would not be the major RRE formation pathway. In the mechanism of RRE formation shown in Figure 5.17B it is not clear why both pairs of cysteine thiolates would not be substituted to form the sulfide-bridged RRS cluster (Figure 5.1).

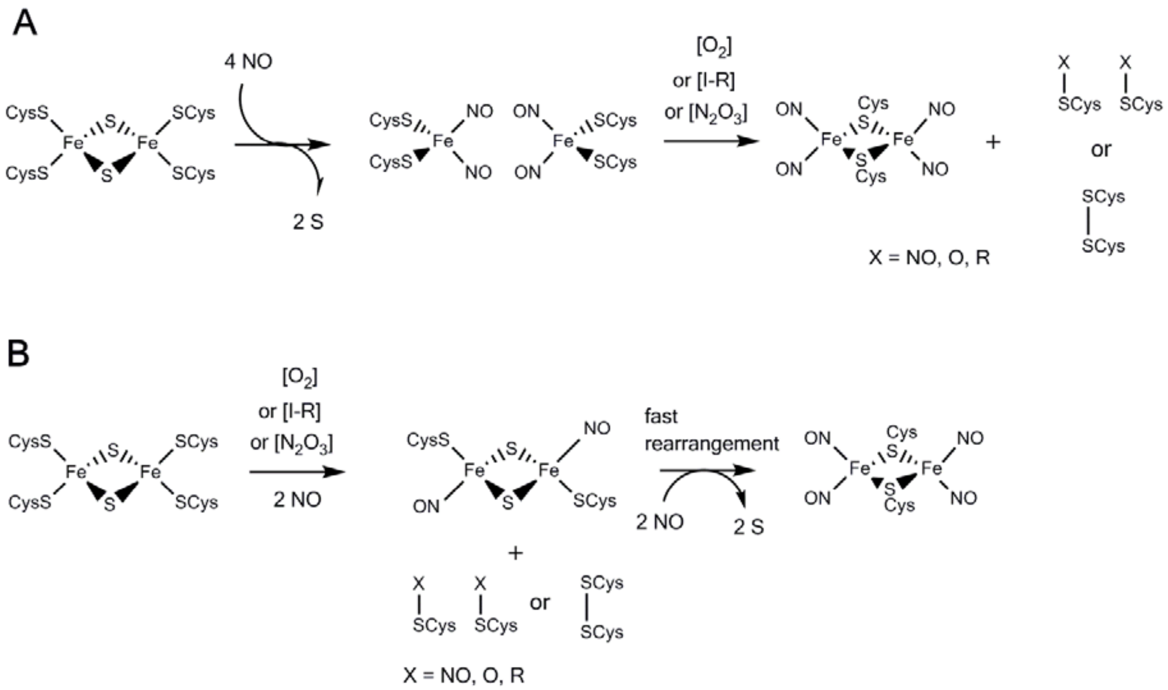

**Figure 5.17 – Possible mechanisms of [2Fe2S] iron-sulfur protein nitrosylation.** [I-R] refers to iodoacetamide. No mechanistic detail is provided for the rearrangements which would be required to form RRE in each case. (A) Pathway for DNIC formation and then subsequent RRE formation. (B) An alternative pathway to RRE formation where the initial step requires a thiolate sequestration reagent. Here, NO substitution of cysteine thiolates would lead to RRE formation, whilst NO substitution of sulfides would lead to DNIC formation as in panel A.

We do not have sufficient data at this stage to propose pathways for [4Fe4S] protein nitrosylation. Interestingly, formation of either RRE or RBS from a [4Fe4S] cluster would require substituting cysteine thiolate ligands for NO. It is therefore strange in this case that the presence of $O_2$ would favour RRE formation over RBS formation. It would be interesting to see if similar results are obtained with the specific thiolate sequestration agent iodoacetamide.

## 5.8 Conclusions and outlook

In this chapter we have successfully optimised an IR spectroscopic method to study iron-sulfur protein nitrosylation reactions. When great care is taken over cleaning of the prism and maintenance of an anaerobic environment, it is possible to record reproducible spectra. With sub-millimolar protein concentrations our technique is sufficiently sensitive to detect peaks which derive from less than 10% yields of product. The major limitation in the technique is the ability to detect bands at wavenumbers below 1730 $cm^{-1}$, unless one is fortunate with the amide and water subtraction so that the baseline is completely flat (see Figures 5.6C, 5.9, 5.10A and 5.15A which are all aiming to detect species between 1730 and 1700 $cm^{-1}$). Another problem is that the cleaning procedure is long enough to make it very difficult to record more than four spectra in a single day. A potential solution to both of these problems is to apply *in situ* methods to study iron-sulfur protein nitrosylation. However, it is necessary to first record discrete spectra to know what species form under what conditions and gain an idea about what the rate of the reaction is before attempting to do more sophisticated *in situ* experiments. Using *in situ* methods to study HiPIP nitrosylation is our next immediate aim in this project.

IR spectroscopy is a very powerful technique to study iron-sulfur protein nitrosylation. It has allowed us to do more than simply identify the major products of iron-sulfur protein nitrosylation. We have been able to gain an understanding of the nitrosylation pathways of protein-bound iron-sulfur clusters which is more on par with the understanding of small-molecule systems. The relatively low sample requirements mean we have been able to screen a range of conditions to favour formation of different products. We can identify minor products and show conversion from one product to another.

The most important conclusion from the work in this chapter is that the presence of $O_2$ markedly affects iron-sulfur protein nitrosylation. This finding may be important in understanding the cytotoxic effects of NO towards bacteria. Previously, from anaerobic studies, it was thought that buried iron-sulfur proteins are not a major target for NO toxicity. We have shown that relatively NO-unreactive iron-sulfur proteins, such as Fd and HiPIP, will react rapidly with NO if thiolate reactive reagents are available. In a phagolysosome there will be multiple thiolate reactive species present. The presence of $O_2$ also alters the products which are formed upon iron-sulfur protein nitrosylation. This effect may be significant in understanding bacterial NO toxicity, as well as how bacteria repair NO damage and sense of NO. The anaerobic reaction of [4Fe4S] proteins with NO appears to lead to RBS formation. RBS may be able to dissociate from the protein and is a very potent antimicrobial agent if it does (Hamilton-Brehm et al., 2009). There has been an *in vivo* study on the effect of $O_2$ on the repair of nitrosylated iron-sulfur proteins (Ren et al., 2008). In this study it was shown that a nitrosylated [4Fe4S] iron-sulfur protein was not repaired under anaerobic conditions, but was repaired in the presence of oxygen. We have seen with the [4Fe4S] protein HiPIP that if the cluster is nitrosylated in the presence of $O_2$ then the nitrosylated cluster is lost from the protein. This may enable quick repair of the protein, which may not be the case if the anaerobically-formed RBS is stably bound to the protein. Finally, the NO-sensing protein FNR forms some RRE upon nitrosylation under aerobic conditions, but forms RBS under anaerobic conditions. It is likely that these different products induce different structural changes and result in different signalling events. A similar situation could occur with [2Fe2S] NO-sensing proteins where either DNIC or RRE would form upon nitrosylation depending on the anaerobicity. If the repair pathways for each product are different, then each protein-bound product could have a different lifetime. This would affect the downstream signalling from the NO-sensing protein.

# Chapter 6: Conclusions and future directions

Many bacteria use inorganic nitrogen and sulfur compounds for energy metabolism. These compounds are often toxic and so bacteria must adapt to survive their deleterious effects. In order to metabolise, sense and detoxify these compounds, bacteria use specific proteins. In this thesis, protein interactions with inorganic nitrogen and sulfur compounds have been examined at the mechanistic level. This type of detailed reductionist study increases our understanding of the microbiological processes in which these proteins participate and can be applied to understanding the mechanistic detail of related proteins or the design of novel systems.

## 6.1 The Sox sulfur oxidation pathway

In the Sox sulfur oxidation pathway intermediates are attached to the carrier arm of a substrate-carrier protein SoxYZ. One aim of this thesis was to understand the issues that must be overcome by an enzyme when its substrate is attached to a carrier protein. In the specific case of the Sox pathway enzyme SoxB, the system has evolved to overcome three issues. Firstly, the nature of the protein-protein interactions between SoxB and SoxYZ allows for specific but promiscuous interactions. Specific interactions form between the Z-patch on SoxZ and a distal surface loop on SoxB. Any enzyme could gain specificity for SoxY-conjugated substrates by mutation of a few residues on a surface loop to form a Z-patch interaction motif. This surface motif would have to be same distance from the active site channel as the distance between the SoxY carrier arm and the Z-patch. The second issue is how a Sox enzyme which has defined protein-protein interactions with SoxYZ can differentiate between different SoxYZ-conjugated intermediates. We have shown that for SoxB this differentiation is through kinetic specificity, which we propose is mediated by a substrate-stabilised conformational change in a loop in the active site. Thirdly, SoxB must distinguish the SoxY-conjugated substrate moiety from similar functional groups on SoxYZ, such as the SoxY C-terminal carboxylate. We have shown that the active site has evolved to “read” the context of the substrate moiety by recognising the hydrophobicity of the site of attachment of the substrate to SoxYZ.

With this knowledge of the SoxB-SoxYZ interaction it would be relatively easy to investigate if similar principles underlie the interactions between SoxYZ and the other Sox pathway enzymes. As shown in Section 3.7.4, if we assume the Z-patch is important for the other SoxYZ-Sox enzyme interactions, we can identify putative interfaces between SoxYZ and its other cognate enzyme partners. To confirm such interactions we would first need to identify whether protein-protein interactions between SoxYZ and SoxAX or SoxCD exist, using native PAGE, analytical gel filtration or ITC. Following this, we could test the authenticity of the putative Z-patch interfaces by determining the effect of disruptive mutagenesis on the protein-protein interactions. We would then attempt to generate SoxYZ-conjugated substrate and product analogues for each enzyme and test whether kinetic discrimination occurs using SPR as we have shown for SoxB. The long-term aim would be to crystallise the SoxYZ-SoxAX and SoxYZ-SoxCD complexes and compare the molecular details of each interaction with the details of the SoxYZ-SoxB interaction.

To do the experiments described above with SoxYZ, SoxAX and SoxCD, we need to recombinantly express these proteins from the same organism. The experiments in Chapter 3 used *T. thermophilus* SoxYZ and SoxB expressed in *E. coli*. The advantage of proteins from thermophilic organisms is that they are often easier to express and crystallise. Additionally, the only successful recombinant expression of SoxB which has been reported to date has used the *soxB* gene from *T. thermophilus* (Sauvé et al., 2009). To continue our studies using *T. thermophilus sox* genes, we would need to recombinantly express SoxAX and SoxCD from this organism. One problem with this approach is that there are a number of differences between the *T. thermophilus sox* genes and those of the model organism for studying the Sox pathway, *P. pantotrophus*. Unlike in *P. pantotrophus*, thiosulfate-utilisation and the presence of an expressed Sox pathway have never been experimentally tested in *T. thermophilus*. It is therefore difficult to know what the functional significance is of the differences between the *T. thermophilus* and *P. pantotrophus sox* genes.

The *T. thermophilus soxC* gene encodes a protein with a predicted C-terminal flexible cysteine-containing arm which bears some resemblance to the SoxY carrier arm. This SoxC arm is only present in *Thermus* species and some but not all *Meiothermus* species. Preliminary expression tests show that *T. thermophilus* SoxCD readily forms disulfide-linked oligomers due to the cysteine on this arm when reductant is not present. The reactive carrier-arm cysteine or reductant would interfere with assays which also include SoxYZ. It would be possible to use mutagenesis to remove the carrier arm from SoxCD, but this arm is likely to be important for the function of SoxCD in *T. thermophilus*.

Unlike many organisms with a Sox pathway, *T. thermophilus* has two sets of *soxAX* genes. These *soxAX* genes are more related to each other than to non-*Thermus soxAX* genes, so it is not clear whether there is any significance in the presence of two sets of genes. It should be noted that the SoxA protein encoded by *TT_C1050* has a Z-patch motif (**E**T**F**GI) which aligns with the Z-patch motif proposed for *P. pantotrophus* (**D**D**F**DN)(Figure 3.17), with the increased hydrophobic character consistent with the increased hydrophobic character of the Z-patch from *T. thermophilus* SoxZ compared to *P. pantotrophus* SoxZ (Figure 3.11). However, the SoxA protein encoded by *TT_C1054* has a **S**T**A**GI Z-patch motif, missing both the conserved aromatic and acidic residues. This suggests that this SoxAX protein does not interact with SoxYZ. It may be possible that the substrate of this SoxAX could be the cysteine on the carrier arm of SoxC.

An alternative to using *T. thermophilus* SoxYZ, SoxAX and SoxCD would be to use the proteins from the well-studied Sox model organism *P. pantotrophus*. *P. pantotrophus* SoxYZ and SoxAX are functionally expressed in *E. coli* (Rother and Friedrich, 2002; Sauvé et al., 2007). SoxCD from the species *R. sulfidophilum* can be expressed in *E. coli*, albeit with a poor yield (Sauvé, 2008).

However, SoxYZ from *R. sulfidophilum* cannot be recombinantly expressed in *E. coli* (Sauvé, 2008).

A number of SoxYZ and SoxY homologues with no known function exist. These are distinguished from true SoxYZ by sequence differences, such as an absence of the conserved residues around the carrier arm cysteine and the conserved Ile67 which we showed to have an important role in the protein-protein interactions between SoxYZ and SoxB. These SoxYZ homologues are also often found encoded in the genomes of bacteria which do not encode other Sox components. One SoxYZ homologue is the fused SoxY-SoxZ which is found in methylotrophic bacteria. In fused SoxYZ, the SoxY carrier arm still contains a cysteine but the arm forms part of a linker with N-terminus of SoxZ. This would be expected to limit the conformational flexibility of the arm. I have generated a strain of *P. denitrificans* with a chromosomal deletion of the gene which encodes this protein. I have shown that the protein is induced under methylotrophic growth conditions, but I have not found conditions where deletion of the gene has an effect on the growth of the organism. I suspect that this protein is involved in periplasmic formaldehyde detoxification and I aim to purify this protein natively from *P. denitrificans* to determine whether any potential intermediates are conjugated to the carrier arm cysteine.

As alluded to in the introduction, the Sox pathway reactions have never been directly demonstrated. This means we cannot be certain of the identity of the substrates and products of the Sox pathway enzymes. However, we now know that SoxB discriminates between the substrate-bound and unloaded states of SoxYZ, as judged by kinetic and thermodynamic differences detected by SPR and ITC. This means that we can generate the putative SoxB substrates and see in each case whether the substrate moiety or the C-terminal carboxylate bind to the dimanganese centre in SoxB. As well as doing this indirectly by ITC, we are trying a more direct approach. By using $^{13}$C-labelled SoxYZ we can directly detect the interaction between the C-terminal carboxylate and the dimanganese centre using pulsed EPR techniques.

The Friedrich model states that SoxB has two substrates – SoxYZ with a cysteine-S-thiosulfonate, and SoxYZ with a cysteine-S-sulfonate. Our preliminary data suggests that the cysteine-S-sulfonate modified SoxYZ is not a true SoxB substrate. This can be correlated with the sulfide activation of SoxYZ (Quentmeier et al., 2007). If the active form of SoxYZ has a cysteine persulfide or a longer sulfur chain on the cysteine, then there would be no need for a SoxYZ cysteine-S-sulfonate intermediate in the Sox pathway. I am attempting to confirm this model by complementing the SoxYZ-depleted reconstituted *P. pantotrophus* Sox pathway with putative Sox pathway intermediates.

## 6.2 The thiosulfate oxidation mechanism of cysteine-ligated cytochromes

In Chapter 4 we investigated the mechanism of the thiosulfate dehydrogenase TsdA. We used structural and biochemical data to propose a mechanism which includes a cysteine-S-thiosulfonate intermediate. This work may be useful for understanding other enzymes involved in bacterial sulfur metabolism which use active site cysteines. This work is also useful for understanding the types of possible heme-catalysed chemistry. Heme-analogues are an important part of biomimetic organometallic chemistry. It would be useful to do more experiments with TsdA to confirm the proposed mechanism. We have not carried out EPR and magnetic circular dichroism experiments so far, and these experiments would provide a lot of electronic and structural information for the heme iron in the cysteine-S-thiosulfonate intermediate and the various variants. By linking EPR and magnetic circular dichroism spectroscopy to electrochemistry we would also be able to determine the mid-point potentials of the TsdA hemes. Preliminary attempts to determine the mid-point potentials of the TsdA hemes by protein film electrochemistry were unsuccessful. We would ideally like to determine a structure of the cysteine-S-thiosulfonate intermediate. We hoped that mutating the active site residues might stabilise this intermediate but these substitutions appear to have the opposite effect. It is possible that the interaction between the heme propionate and Arg224 in crystallised native TsdA prevents the access of tetrathionate in our crystal soaking experiments. We would therefore like to retry these experiments with the R224A variant.

One main interest in the mechanism of TsdA is the relevance of it to the mechanism of SoxAX. Therefore, our future work in this area is likely to be related to performing similar experiments with SoxAX. Ideally, we would like to perform experiments inspired by those in Chapter 3 and Chapter 4 for SoxAX. This would mean trying to form covalent adducts on the SoxAX catalytic cysteine using the substrate, thiosulfate; the product analogue, tetrathionate; or the product, SoxYZ cysteine-S-thiosulfonate. Preliminary experiments show that ESI-MS does not give good quality data for *P. pantotrophus* SoxAX. Thus, it may be useful to attempt to express *T. thermophilus* SoxAX and see if we can obtain high quality ESI-MS data for this protein. Thermophilic SoxAX may also be useful for future crystallographic work if we are able to stabilise a SoxYZ-SoxAX complex.

## 6.3 The reactivity of iron-sulfur proteins with NO

In Chapter 5, we investigated the reactions of iron-sulfur proteins with NO. IR spectroscopy is a simple method which has low sample requirements and can distinguish different protein-bound iron-nitrosyl species. In this work we established experimental methodology to detect the products of the reaction of three iron-sulfur proteins with NO. Using this methodology we have shown that iron-sulfur proteins react to form a range of products, such as DNIC, RRE and RBS. We have demonstrated that the presence of trace $O_2$ greatly increases the reactivity of iron-sulfur proteins with NO and favours the formation of RRE regardless of the type of cluster in the native protein. We propose that the effects of $O_2$ are due to cysteine thiolate sequestration. In the immune system, bacteria are exposed to NO in the presence of thiolate-reactive species, such as superoxide and $N_2O_3$. We have shown that the [2Fe2S] protein spinach ferredoxin, which was assumed to be unreactive towards NO, reacts rapidly with NO when cysteine-reactive reagents are present. We have also demonstrated that when [4Fe4S] proteins react with NO, different species are formed in the presence or absence of cysteine-reactive reagents. These products are likely to have different effects on the structure of signalling proteins, such as FNR. Furthermore, these products probably have different life-times, and may require different repair pathways to remove and replace the nitrosyl iron complex with the native cluster. This may mean that bacterial sensing of NO in the presence of thiolate reactive reagents is distinct to the sensing of NO in the absence of such reagents.

With our methodology demonstrated, we are now in a position to make significant progress in understanding the reactivity of iron-sulfur proteins with NO. We aim to perform an in-depth characterisation of the reactions of [4Fe4S] proteins with NO, with a similar approach to that which we used for spinach ferredoxin. Here, we would expose [4Fe4S] proteins to NO in combination with oxidising agents or thiolate sequesteration agents and study the ensuing reactions using IR, UV/visible and EPR spectroscopy. Understanding the reactions of [4Fe4S] proteins with NO also relies on generating oligopeptide model complexes to aid in assigning IR peaks to particular species. We would like to perform more experiments with NO-sensing proteins. We hope to characterise the relationship between which nitrosylation product forms inside an NO-sensing protein and how the conformation of the protein changes. We aim to do this by simultaneously inspecting the $\nu$(NO) bands and the amide I band. We could also use different conditions to form different products and then test how these products affect the binding of the NO-sensing protein to its cognate protein or DNA partner. A long-term aim would be to use infrared microscopy to visualise which nitrosyl iron products are formed *in vivo* when bacteria are exposed to NO, and how these are repaired. At first this would involve over-expressing a model iron-sulfur protein in *E. coli* cells.

We also aim to further optimise our IR methods to gain greater mechanistic insight into iron-sulfur protein nitrosylation. One aim would be to develop *in situ* methods. By recording IR spectra whilst exposing samples to NO we may be able to detect reaction intermediates. We could also use spectroelectrochemistry methods. By determining the redox properties of the reaction products and by detecting the positions of the $\nu$(NO) in different redox states we could better assign the chemical nature of these products. It would also be useful to know what effect the redox state of the cluster in the starting material has on the reactions which occur.

# Bibliography

Abu-Soud, H.M. and Stuehr, D.J. (1993) Nitric oxide synthases reveal a role for calmodulin in controlling electron transfer. *Proceedings of the National Academy of Sciences USA*, **90**, 10769-10772.

Ali, A.A., Coulter, J.A., Ogle, C.H., Migaud, M.M., Hirst, D.G., Robson, T. and McCarthy, H.O. (2013) The contribution of $N_2O_3$ to the cytotoxicity of the nitric oxide donor DETA/NO: an emerging role for S-nitrosylation. *Bioscience Reports*, **33**, 333-349.

Alric, J., Tsukatani, Y., Yoshida, M., Matsuura, K., Shimada, K., Hienerwadel, R., Schoepp-Cothenet, B., Nitschke, W., Nagashima, K.V.P. and Verméglio, A. (2004) Structural and functional characterization of the unusual triheme cytochrome bound to the reaction center of *Rhodovulum sulfidophilum*. *Journal of Biological Chemistry*, **279**, 26090-26097.

Appia-Ayme, C. and Berks, B.C. (2002) SoxV, an orthologue of the CcdA disulfide transporter, is involved in thiosulfate oxidation in *Rhodovulum sulfidophilum* and reduces the periplasmic thioredoxin SoxW. *Biochemical and Biophysical Research Communications*, **296**, 737-741.

Appia-Ayme, C., Little, P.J., Matsumoto, Y., Leech, A.P. and Berks, B.C. (2001) Cytochrome complex essential for photosynthetic oxidation of both thiosulfate and sulfide in *Rhodovulum sulfidophilum*. *Journal of Bacteriology*, **183**, 6107-6118.

Argyrou, A. and Blanchard, J.S. (2004) Flavoprotein disulfide reductases: advances in chemistry and function. *Progress in Nucleic Acid Research and Molecular Biology*, **78**, 89-142.

Arnold, K., Bordoli, L., Kopp, J. and Schwede, T. (2006) The SWISS-MODEL workspace: a web-based environment for protein structure homology modelling. *Bioinformatics*, **22**, 195-201.

Arslan, E., Schulz, H., Zufferey, R., Künzler, P. and Thöny-Meyer, L. (1998) Overproduction of the *Bradyrhizobium japonicum* *c*-type cytochrome subunits of the *cbb*$_3$ oxidase in *Escherichia coli*. *Biochemical and Biophysical Research Communications*, **251**, 744-747.

Assreuy, J., Cunha, F.Q., Epperlein, M., Noronha-Dutra, A., O'Donnell, C.A., Liew, F.Y. and Moncada, S. (1994) Production of nitric oxide and superoxide by activated macrophages and killing of *Leishmania major*. *European Journal of Immunology*, **24**, 672-676.

Aussignargues, C., Giuliani, M.-C., Infossi, P., Lojou, E., Guiral, M., Giudici-Orticoni, M.-T. and Ilbert, M. (2012) Rhodanese functions as sulfur supplier for key enzymes in sulfur energy metabolism. *Journal of Biological Chemistry*, **287**, 19936-19948.

Babior, B.M., Lambeth, J.D. and Nauseef, W. (2002) The neutrophil NADPH oxidase. *Archives of Biochemistry and Biophysics*, **397**, 342-344.

Bach, R.D., Dmitrenko, O. and Thorpe, C. (2007) Mechanism of thiolate−disulfide interchange reactions in biochemistry. *The Journal of Organic Chemistry*, **73**, 12-21.

Baker, N.A., Sept, D., Joseph, S., Holst, M.J. and McCammon, J.A. (2001) Electrostatics of nanosystems: Application to microtubules and the ribosome. *Proceedings of the National Academy of Sciences USA*, **98**, 10037-10041.

Bamford, V.A., Bruno, S., Rasmussen, T., Appia-Ayme, C., Cheesman, M.R., Berks, B.C. and Hemmings, A.M. (2002) Structural basis for the oxidation of thiosulfate by a sulfur cycle enzyme. *EMBO Journal*, **21**, 5599-5610.

Bardischewsky, F., Fischer, J., Höller, B. and Friedrich, C.G. (2006a) SoxV transfers electrons to the periplasm of *Paracoccus pantotrophus* – an essential reaction for chemotrophic sulfur oxidation. *Microbiology*, **152**, 465-472.

Bardischewsky, F., Quentmeier, A. and Friedrich, C.G. (2006b) The flavoprotein SoxF functions in chemotrophic thiosulfate oxidation of Paracoccus pantotrophus in vivo and in vitro. *FEMS Microbiology Letters*, **258**, 121-126.

Barth, A. (2007) Infrared spectroscopy of proteins. *Biochimica et Biophysica Acta (BBA) – Bioenergetics*, **1767**, 1073-1101.

Bates, D.M., Popescu, C.V., Khoroshilova, N., Vogt, K., Beinert, H., Münck, E. and Kiley, P.J. (2000) Substitution of leucine 28 with histidine in the *Escherichia coli* transcription factor FNR results in increased stability of the $[4Fe\text{-}4S]^{2+}$ cluster to oxygen. *Journal of Biological Chemistry*, **275**, 6234-6240.

Beck, W., Grenz, R., Götzfried, F. and Vilsmaier, E. (1981) Zur Kenntnis der „Säure" des Roten Roussinschen salzes, $(ON)_2Fe(SH)_2Fe(NO)_2$ und ihrer Derivate. *Chemische Berichte*, **114**, 3184-3187.

Beller, H.R., Chain, P.S.G., Letain, T.E., Chakicherla, A., Larimer, F.W., Richardson, P.M., Coleman, M.A., Wood, A.P. and Kelly, D.P. (2006) The genome sequence of the obligately chemolithoautotrophic, facultatively anaerobic bacterium *Thiobacillus denitrificans*. *Journal of Bacteriology*, **188**, 1473-1488.

Bertani, G. (1951) Studies on lysogenesis I: The mode of phage liberation by lysogenic *Escherichia coli*. *Journal of Bacteriology*, **62**, 293-300.

Bertero, M.G., Rothery, R.A., Palak, M., Hou, C., Lim, D., Blasco, F., Weiner, J.H. and Strynadka, N.C.J. (2003) Insights into the respiratory electron transfer pathway from the structure of nitrate reductase A. *Nature Structural Biology*, **10**, 681-687.

Bhat, S.A., Singh, N., Trivedi, A., Kansal, P., Gupta, P. and Kumar, A. (2012) The mechanism of redox sensing in *Mycobacterium tuberculosis*. *Free Radical Biology and Medicine*, **53**, 1625-1641.

Binkerd, E.F. and Kolari, O.E. (1975) The history and use of nitrate and nitrite in the curing of meat. *Food and Cosmetics Toxicology*, **13**, 655-661.

Blanc, E., Roversi, P., Vonrhein, C., Flensburg, C., Lea, S.M. and Bricogne, G. (2004) Refinement of severely incomplete structures with maximum likelihood in BUSTER-TNT. *Acta Crystallographica D Biological Crystallography*, **60**, 2210-2221.

Boon, C. and Dick, T. (2002) *Mycobacterium bovis BCG* response regulator essential for hypoxic dormancy. *Journal of Bacteriology*, **184**, 6760-6767.

Bradley, J.M., Marritt, S.J., Kihlken, M.A., Haynes, K., Hemmings, A.M., Berks, B.C., Cheesman, M.R. and Butt, J.N. (2012) Redox and chemical activities of the hemes in the sulfur oxidation pathway enzyme SoxAX. *Journal of Biological Chemistry*, **287**, 40350-40359.

Brandl, H. (2008) Microbial leaching of metals. *Biotechnology Set, 2$^{nd}$ Ed, Wiley-VCH Verlag GmbH*, 191-224.

Brito, J.A., Sousa, F.L., Stelter, M., Bandeiras, T.M., Vonrhein, C., Teixeira, M., Pereira, M.M. and Archer, M. (2009) Structural and functional insights into sulfide:quinone oxidoreductase. *Biochemistry*, **48**, 5613-5622.

Bruce, B.D., Fuller, R.C. and Blankenship, R.E. (1982) Primary photochemistry in the facultatively aerobic green photosynthetic bacterium *Chloroflexus aurantiacus*. *Proceedings of the National Academy of Sciences USA*, **79**, 6532-6536.

Brucker, E.A., Olson, J.S., Ikeda-Saito, M., Phillips, G.N. and George, N. (1998) Nitric oxide myoglobin: crystal structure and analysis of ligand geometry. *Proteins: Structure, Function, and Genetics*, **30**, 352-356.

Brune, D.C. (1989) Sulfur oxidation by phototrophic bacteria. *Biochimica et Biophysica Acta (BBA) – Bioenergetics*, **975**, 189-221.

Buckel, W. and Thauer, R.K. (2013) Energy conservation *via* electron bifurcating ferredoxin reduction and proton/$Na^+$ translocating ferredoxin oxidation. The evolutionary aspects of bioenergetic systems. *Biochimica et Biophysica Acta (BBA) – Bioenergetics,* **1827**, 94-113.

Can, M., Zoppellaro, G., Andersson, K.K. and Bren, K.L. (2011) Modulation of ligand-field parameters by heme ruffling in cytochromes *c* revealed by EPR Spectroscopy. *Inorganic Chemistry*, **50**, 12018-12024.

Cao, W., Bao, C. and Lowenstein, C.J. (2003) Inducible nitric oxide synthase expression inhibition by adenovirus E1A. *Proceedings of the National Academy of Sciences USA*, **100**, 7773-7778.

Carlson, H.K., Vance, R.E. and Marletta, M.A. (2010) H-NOX regulation of c-di-GMP metabolism and biofilm formation in *Legionella pneumophila*. *Molecular Microbiology*, **77**, 930-942.

Case, D.A., Darden, T.A., Cheatham, T.E., Simmerling, C.L., Wang, J., Duke, R.E., Luo, R., Walker, R.C., Zhang, W., Merz, K.M., Roberts, B., Hayik, S., Roitberg, A., Seabra, G., Swails, J., Götz, A.W., Kolossváry, I., Wong, K.F., Paesani, F., Vanicek, R.M., Wolf, J., Liu, J., Wu, X., Brozell, S.R., Steinbrecher, T., Gohlke, H., Cai, Q., Ye, X., Wang, J., Hsieh, M.-J., Cui, G., Roe, D.R., Mathews, D.H., Seetin, M.G., Salomon-Ferrer, R., Sagui, C., Babin, V., Luchko, T., Gusarov, S., Kovalenko, A. and Kollman, P.A. (2012) AMBER 12.

Caulton, K.G. (1975) Synthetic methods in transition metal nitrosyl chemistry. *Coordination Chemistry Reviews*, **14**, 317-355.

Celniker, G., Nimrod, G., Ashkenazy, H., Glaser, F., Martz, E., Mayrose, I., Pupko, T. and Ben-Tal, N. (2013) ConSurf: Using Evolutionary Data to Raise Testable Hypotheses about Protein Function. *Israel Journal of Chemistry*, **53**, 199-206.

Chakravortty, D., Hansen-Wester, I. and Hensel, M. (2002) *Salmonella* pathogenicity island 2 mediates protection of intracellular *Salmonella* from reactive nitrogen intermediates. *The Journal of Experimental Medicine*, **195**, 1155-1166.

Chakravortty, D. and Hensel, M. (2003) Inducible nitric oxide synthase and control of intracellular bacterial pathogens. *Microbes and Infection*, **5**, 621-627.

Chandra, T.S. and Friedrich, C.G. (1986) Tn5-induced mutations affecting sulfur-oxidizing ability (Sox) of *Thiosphaera pantotropha*. *Journal of Bacteriology*, **166**, 446-452.

Chawla, M., Parikh, P., Saxena, A., Munshi, M., Mehta, M., Mai, D., Srivastava, A.K., Narasimhulu, K.V., Redding, K.E., Vashi, N., Kumar, D., Steyn, A.J.C. and Singh, A. (2012) *Mycobacterium tuberculosis* WhiB4 regulates oxidative stress response to modulate survival and dissemination *in vivo*. *Molecular Microbiology*, **85**, 1148-1165.

Cheesman, M.R., Little, P.J. and Berks, B.C. (2001) Novel heme ligation in a c-type cytochrome involved in thiosulfate oxidation: EPR and MCD of SoxAX from *Rhodovulum sulfidophilum*. *Biochemistry*, **40**, 10562-10569.

Chim, N., Johnson, P.M. and Goulding, C.W. (2014) Insights into redox sensing metalloproteins in *Mycobacterium tuberculosis*. *Journal of Inorganic Biochemistry*, **133**, 118-126.

Choi, H.-S., Rai, P.R., Chu, H.W., Cool, C. and Chan, E.D. (2002) Analysis of nitric oxide synthase and nitrotyrosine expression in human pulmonary tuberculosis. *American Journal of Respiratory and Critical Care Medicine*, **166**, 178-186.

Church, J.S. and Evans, D.J. (2008) A spectroscopic investigation into the reaction of sodium tetrathionate with cysteine. *Spectrochimica Acta Part A: Molecular and Biomolecular Spectroscopy*, **69**, 256-262.

Cort, J.R., Selan, U., Schulte, A., Grimm, F., Kennedy, M.A. and Dahl, C. (2008) *Allochromatium vinosum* DsrC: solution-state NMR structure, redox properties, and interaction with DsrEFH, a protein essential for purple sulfur bacterial sulfur oxidation. *Journal of Molecular Biology*, **382**, 692-707.

Costanzo, S., Ménage, S., Purrello, R., Bonomo, R.P. and Fontecave, M. (2001) Re-examination of the formation of dinitrosyl-iron complexes during reaction of S-nitrosothiols with Fe(II). *Inorganica Chimica Acta*, **318**, 1-7.

Crack, J.C., Smith, L.J., Stapleton, M.R., Peck, J., Watmough, N.J., Buttner, M.J., Buxton, R.S., Green, J., Oganesyan, V.S., Thomson, A.J. and Le Brun, N.E. (2010) Mechanistic insight into the nitrosylation of the [4Fe–4S] cluster of WhiB-like proteins. *Journal of the American Chemical Society*, **133**, 1112-1121.

Crack, J.C., Stapleton, M.R., Green, J., Thomson, A.J. and Le Brun, N.E. (2013) Mechanism of [4Fe-4S](Cys)$_4$ cluster nitrosylation is conserved amongst NO-responsive regulators. *Journal of Biological Chemistry*, **288**, 11492-11502.

Crane, B.R., Arvai, A.S., Gachhui, R., Wu, C., Ghosh, D.K., Getzoff, E.D., Stuehr, D.J. and Tainer, J.A. (1997) The structure of nitric oxide synthase oxygenase domain and inhibitor complexes. *Science*, **278**, 425-431.

Crankshaw, M.W. and Grant, G.A. (2001) Modification of cysteine. *Current Protocols in Protein Science. John Wiley & Sons, Inc., Unit 15.1.*

Crosby, J. and Crump, M.P. (2012) The structural role of the carrier protein - active controller or passive carrier. *Natural Product Reports*, **29**, 1111-1137.

Cruz-Ramos, H., Crack, J., Wu, G., Hughes, M.N., Scott, C., Thomson, A.J., Green, J. and Poole, R.K. (2002) NO sensing by FNR: regulation of the *Escherichia coli* NO-detoxifying flavohaemoglobin, Hmp. *EMBO Journal*, **21**, 3235-3244.

Cryle, M.J. and Schlichting, I. (2008) Structural insights from a P450 Carrier Protein complex reveal how specificity is achieved in the P450$_{\text{BioI}}$ ACP complex. *Proceedings of the National Academy of Sciences USA*, **105**, 15696-15701.

Cunningham-Bussel, A., Zhang, T. and Nathan, C.F. (2013) Nitrite produced by *Mycobacterium tuberculosis* in human macrophages in physiologic oxygen impacts bacterial ATP consumption and gene expression. *Proceedings of the National Academy of Sciences USA*, **110**, E4256-E4265.

D'Autreaux, B., Tucker, N.P., Dixon, R. and Spiro, S. (2005) A non-haem iron centre in the transcription factor NorR senses nitric oxide. *Nature*, **437**, 769-772.

D'Autréaux, B., Horner, O., Oddou, J.-L., Jeandey, C., Gambarelli, S., Berthomieu, C., Latour, J.-M. and Michaud-Soret, I. (2004) Spectroscopic description of the two nitrosyl−iron complexes responsible for Fur inhibition by nitric oxide. *Journal of the American Chemical Society*, **126**, 6005-6016.

Daff, S. (2010) NO synthase: Structures and mechanisms. *Nitric Oxide*, **23**, 1-11.

Dahl, C., Franz, B., Hensen, D., Kesselheim, A. and Zigann, R. (2013) Sulfite oxidation in the purple sulfur bacterium *Allochromatium vinosum*: identification of SoeABC as a major player and relevance of SoxYZ in the process. *Microbiology*, **159**, 2626-2638.

Dambe, T., Quentmeier, A., Rother, D., Friedrich, C. and Scheidig, A.J. (2005) Structure of the cytochrome complex SoxXA of *Paracoccus pantotrophus*, a heme enzyme initiating chemotrophic sulfur oxidation. *Journal of Structural Biology*, **152**, 229-234.

Darrah, P.A., Hondalus, M.K., Chen, Q., Ischiropoulos, H. and Mosser, D.M. (2000) Cooperation between reactive oxygen and nitrogen intermediates in killing of *Rhodococcus equi* by activated macrophages. *Infection and Immunity*, **68**, 3587-3593.

de Jong, G.A.H., Hazeu, W., Bos, P. and Kuenen, J.G. (1997) Polythionate degradation by tetrathionate hydrolase of *Thiobacillus ferrooxidans*. *Microbiology*, **143**, 499-504.

Denkmann, K., Grein, F., Zigann, R., Siemen, A., Bergmann, J., van Helmont, S., Nicolai, A., Pereira, I.A.C. and Dahl, C. (2012) Thiosulfate dehydrogenase: a widespread unusual acidophilic *c*-type cytochrome. *Environmental Microbiology*, **14**, 2673-2688.

Di Salle, A., D’Errico, G., La Cara, F., Cannio, R. and Rossi, M. (2006) A novel thermostable sulfite oxidase from *Thermus thermophilus*: characterization of the enzyme, gene cloning and expression in *Escherichia coli*. *Extremophiles*, **10**, 587-598.

Ding, H. and Demple, B. (2000) Direct nitric oxide signal transduction via nitrosylation of iron-sulfur centers in the SoxR transcription activator. *Proceedings of the National Academy of Sciences USA*, **97**, 5146-5150.

Duan, X., Yang, J., Ren, B., Tan, G. and Ding, H. (2009) Reactivity of nitric oxide with the [4Fe–4S] cluster of dihydroxyacid dehydratase from *Escherichia coli*. *Biochemical Journal*, **417**, 783-789.

Eisenberg, R. and Meyer, C.D. (1975) Coordination chemistry of nitric oxide. *Accounts of Chemical Research*, **8**, 26-34.

Emsley, P., Lohkamp, B., Scott, W.G. and Cowtan, K. (2010) Features and development of Coot. *Acta Crystallographica D Biological Crystallography*, **66**, 486-501.

Enemark, J.H. and Feltham, R.D. (1974) Principles of structure, bonding, and reactivity for metal nitrosyl complexes. *Coordination Chemistry Reviews*, **13**, 339-406.

Enning, D., Venzlaff, H., Garrelfs, J., Dinh, H.T., Meyer, V., Mayrhofer, K., Hassel, A.W., Stratmann, M. and Widdel, F. (2012) Marine sulfate-reducing bacteria cause serious corrosion of iron under electroconductive biogenic mineral crust. *Environmental Microbiology*, **14**, 1772-1787.

Fang, F.C. (2004) Antimicrobial reactive oxygen and nitrogen species: concepts and controversies. *Nature Reviews Microbiology*, **2**, 820-832.

Fedurco, M., Augustynski, J., Indiani, C., Smulevich, G., Antalík, M., Bánó, M., Sedlák, E., Glascock, M.C. and Dawson, J.H. (2004) The heme iron coordination of unfolded ferric and ferrous cytochrome *c* in neutral and acidic urea solutions. Spectroscopic and electrochemical studies. *Biochimica et Biophysica Acta - Proteins and Proteomics*, **1703**, 31-41.

Finster, K. (2008) Microbiological disproportionation of inorganic sulfur compounds. *Journal of Sulfur Chemistry*, **29**, 281-292.

Fitzpatrick, J., Kalyvas, H., Shearer, J. and Kim, E. (2013) Dioxygen mediated conversion of $\{Fe(NO)_2\}^9$ dinitrosyl iron complexes to Roussin's red esters. *Chemical Communications*, **49**, 5550-5552.

Flatley, J., Barrett, J., Pullan, S.T., Hughes, M.N., Green, J. and Poole, R.K. (2005) Transcriptional responses of *Escherichia coli* to S-nitrosoglutathione under defined chemostat conditions reveal major changes in methionine biosynthesis. *Journal of Biological Chemistry*, **280**, 10065-10072.

Foster, M.W. and Cowan, J.A. (1999) Chemistry of nitric oxide with protein-bound iron sulfur centers. insights on physiological reactivity. *Journal of the American Chemical Society*, **121**, 4093-4100.

Friedrich, C.G., Quentmeier, A., Bardischewsky, F., Rother, D., Kraft, R., Kostka, S. and Prinz, H. (2000) Novel genes coding for lithotrophic sulfur oxidation of *Paracoccus pantotrophus GB17*. *Journal of Bacteriology*, **182**, 4677-4687.

Friedrich, C.G., Quentmeier, A., Bardischewsky, F., Rother, D., Orawski, G., Hellwig, P. and Fischer, J. (2008) Redox control of chemotrophic sulfur oxidation of *Paracoccus pantotrophus*, *Microbial Sulfur Metabolism, Springer Berlin Heidelberg,* 139-150.

Friedrich, C.G., Rother, D., Bardischewsky, F., Quentmeier, A. and Fischer, J. (2001) Oxidation of reduced inorganic sulfur compounds by bacteria: emergence of a common mechanism? *Applied and Environmental Microbiology*, **67**, 2873-2882.

Frisch, M.J., Trucks, G.W., Schlegel, H.B., Scuseria, G.E., Robb, M.A., Cheeseman, J.R., Montgomery, J., J. A., Vreven, T., Kudin, K.N., Burant, J.C., Millam, J.M., Iyengar, S.S., Tomasi, J., Barone, V., Mennucci, B., Cossi, M., Scalmani, G., Rega, N., Petersson, G.A., Nakatsuji, H., Hada, M., Ehara, M., Toyota, K., Fukuda, R., Hasegawa, J., Ishida, M., Nakajima, T., Honda, Y., Kitao, O., Nakai, H., Klene, M., Li, X., Knox, J.E., Hratchian, H.P., Cross, J.B., Bakken, V., Adamo, C., Jaramillo, J., Gomperts, R., Stratmann, R.E., Yazyev, O., Austin, A.J., Cammi, R., Pomelli, C., Ochterski, J.W., Ayala, P.Y., Morokuma, K., Voth, G.A., Salvador, P., Dannenberg, J.J., Zakrzewski, V.G., Dapprich, S., Daniels, A.D., Strain, M.C., Farkas, O., Malick, D.K., Rabuck, A.D., Raghavachari, K., Foresman, J.B., Ortiz, J.V., Cui, Q., Baboul, A.G., Clifford, S., Cioslowski, J., Stefanov, B.B., Liu, G., Liashenko, A., Piskorz, P., Komaromi, I., Martin, R.L., Fox, D.J., Keith, T., Al-Laham, M.A., Peng, C.Y., Nanayakkara, A., Challacombe, M., Gill, P.M.W., Johnson, B., Chen, W., Wong, M.W., Gonzalez, C. and Pople, J.A. (2004) Guassian 03, Revision C.02, Guassian Inc., Wallingford CT.

Frueh, D.P., Arthanari, H., Koglin, A., Vosburg, D.A., Bennett, A.E., Walsh, C.T. and Wagner, G. (2008) Dynamic thiolation-thioesterase structure of a non-ribosomal peptide synthetase. *Nature*, **454**, 903-906.

Fujikawa, M., Kobayashi, K. and Kozawa, T. (2014) Mechanistic studies on formation of the dinitrosyl iron complex of the [2Fe-2S] cluster of SoxR protein. *Journal of Biochemistry*, **156**, 163-172.

Fülöp, V., Moir, J.W.B., Ferguson, S.J. and Hajdu, J. (1995) The anatomy of a bifunctional enzyme: Structural basis for reduction of oxygen to water and synthesis of nitric oxide by cytochrome $cd_1$. *Cell*, **81**, 369-377.

Gardner, A.M., Helmick, R.A. and Gardner, P.R. (2002) Flavorubredoxin, an Inducible Catalyst for Nitric Oxide Reduction and Detoxification in *Escherichia coli*. *Journal of Biological Chemistry*, **277**, 8172-8177.

Gardner, P.R., Costantino, G., Szabó, C. and Salzman, A.L. (1997) Nitric oxide sensitivity of the aconitases. *Journal of Biological Chemistry*, **272**, 25071-25076.

Gayon, U. and Dupetit, G. (1886) Recherches sur la réduction des nitrates par les infiniment petits. *Mémoires de la Société des Sciences Physiques et Naturelles de Bordeaux*, **3**, 201-307.

Ghosh, W. and Dam, B. (2009) Biochemistry and molecular biology of lithotrophic sulfur oxidation by taxonomically and ecologically diverse bacteria and archaea. *FEMS Microbiology Reviews*, **33**, 999-1043.

Giardina, G., Rinaldo, S., Johnson, K.A., Di Matteo, A., Brunori, M. and Cutruzzolà, F. (2008) NO sensing in *Pseudomonas aeruginosa*: Structure of the transcriptional regulator DNR. *Journal of Molecular Biology*, **378**, 1002-1015.

Gipson, P., Mills, D.J., Wouts, R., Grininger, M., Vonck, J. and Kühlbrandt, W. (2010) Direct structural insight into the substrate-shuttling mechanism of yeast fatty acid synthase by electron cryomicroscopy. *Proceedings of the National Academy of Sciences USA*, **107**, 9164-9169.

Gliubich, F., Gazerro, M., Zanotti, G., Delbono, S., Bombieri, G. and Berni, R. (1996) Active site structural features for chemically modified forms of rhodanese. *Journal of Biological Chemistry*, **271**, 21054-21061.

Goddard, A.D., Moir, J.W.B., Richardson, D.J. and Ferguson, S.J. (2008), Interdependence of two NarK domains in a fused nitrate/nitrite transporter. *Molecular Microbiology*, **70**, 667-681.

Gomes, C.M., Giuffrè, A., Forte, E., Vicente, J.B., Saraiva, L.g.M., Brunori, M. and Teixeira, M. (2002) A novel type of nitric-oxide reductase: *Escherichia coli* flavorubredoxin. *Journal of Biological Chemistry*, **277**, 25273-25276.

Goubern, M., Andriamihaja, M., Nübel, T., Blachier, F. and Bouillaud, F. (2007) Sulfide, the first inorganic substrate for human cells. *The FASEB Journal*, **21**, 1699-1706.

Greenberg, J.T., Monach, P., Chou, J.H., Josephy, P.D. and Demple, B. (1990) Positive control of a global antioxidant defense regulon activated by superoxide-generating agents in *Escherichia coli*. *Proceedings of the National Academy of Sciences USA*, **87**, 6181-6185.

Grein, F., Ramos, A.R., Venceslau, S.S. and Pereira, I.A.C. (2013) Unifying concepts in anaerobic respiration: Insights from dissimilatory sulfur metabolism. The evolutionary aspects of bioenergetic systems. *Biochimica et Biophysica Acta – Bioenergetics*, **1827**, 145-160.

Grein, F., Venceslau, S.S., Schneider, L., Hildebrandt, P., Todorovic, S., Pereira, I.A.C. and Dahl, C. (2010) DsrJ, an essential part of the DsrMKJOP transmembrane complex in the purple sulfur bacterium *Allochromatium vinosum*, is an unusual triheme cytochrome *c*. *Biochemistry*, **49**, 8290-8299.

Gusarov, I. and Nudler, E. (2005) NO-mediated cytoprotection: Instant adaptation to oxidative stress in bacteria. *Proceedings of the National Academy of Sciences USA*, **102**, 13855-13860.

Gusarov, I., Shatalin, K., Starodubtseva, M. and Nudler, E. (2009) Endogenous nitric oxide protects bacteria against a wide spectrum of antibiotics. *Science*, **325**, 1380-1384.

Hamilton-Brehm, S.D., Schut, G.J. and Adams, M.W.W. (2009) Antimicrobial activity of the iron-sulfur nitroso compound roussin's black salt [$Fe_4S_3(NO)_7$] on the hyperthermophilic archaeon *Pyrococcus furiosus*. *Applied and Environmental Microbiology*, **75**, 1820-1825.

Hanson, T. and Tabita, F.R. (2003) Insights into the stress response and sulfur metabolism revealed by proteome analysis of a *Chlorobium tepidum* mutant lacking the Rubisco-like protein. *Photosynthesis Research*, **78**, 231-248.

Harrop, T.C., Song, D. and Lippard, S.J. (2006) Interaction of nitric oxide with tetrathiolato iron(II) complexes: relevance to the reaction pathways of iron nitrosyls in sulfur-rich biological coordination environments. *Journal of the American Chemical Society*, **128**, 3528-3529.

Harrop, T.C., Tonzetich, Z.J., Reisner, E. and Lippard, S.J. (2008) Reactions of synthetic [2Fe-2S] and [4Fe-4S] clusters with nitric oxide and nitrosothiols. *Journal of the American Chemical Society*, **130**, 15602-15610.

Hausladen, A., Gow, A. and Stamler, J.S. (2001) Flavohemoglobin denitrosylase catalyzes the reaction of a nitroxyl equivalent with molecular oxygen. *Proceedings of the National Academy of Sciences USA*, **98**, 10108-10112.

Hausladen, A., Privalle, C.T., Keng, T., DeAngelo, J. and Stamler, J.S. (1996) Nitrosative stress: activation of the transcription factor OxyR. *Cell*, **86**, 719-729.

Hedderich, R., Hamann, N. and Bennati, M. (2005) Heterodisulfide reductase from methanogenic archaea: a new catalytic role for an iron-sulfur cluster. *Biological Chemistry*, **386**, 961-970.

Henares, B.M., Higgins, K.E. and Boon, E.M. (2012) Discovery of a nitric oxide responsive quorum sensing circuit in *Vibrio harveyi*, *ACS Chemical Biology*, **7**, 1331-1336.

Hensel, M., Hinsley, A.P., Nikolaus, T., Sawers, G. and Berks, B.C. (1999) The genetic basis of tetrathionate respiration in *Salmonella typhimurium*. *Molecular Microbiology*, **32**, 275-287.

Hensen, D., Sperling, D., Trüper, H.G., Brune, D.C. and Dahl, C. (2006) Thiosulphate oxidation in the phototrophic sulphur bacterium *Allochromatium vinosum*. *Molecular Microbiology*, **62**, 794-810.

Hess, B., Kutzner, C., van der Spoel, D. and Lindahl, E. (2008) GROMACS 4: Algorithms for highly efficient, load-balanced, and scalable molecular simulation. *Journal of Chemical Theory and Computation*, **4**, 435-447.

Hino, T., Matsumoto, Y., Nagano, S., Sugimoto, H., Fukumori, Y., Murata, T., Iwata, S. and Shiro, Y. (2010) Structural basis of biological $N_2O$ generation by bacterial nitric oxide reductase. *Science*, **330**, 1666-1670.

Honaker, R.W., Dhiman, R.K., Narayanasamy, P., Crick, D.C. and Voskuil, M.I. (2010) DosS responds to a reduced electron transport system to induce the *Mycobacterium tuberculosis* DosR regulon. *Journal of Bacteriology*, **192**, 6447-6455.

Hornak, V., Abel, R., Okur, A., Strockbine, B., Roitberg, A. and Simmerling, C. (2006) Comparison of multiple Amber force fields and development of improved protein backbone parameters. *Proteins: Structure, Function, and Bioinformatics*, **65**, 712-725.

Houtman, J.C.D., Brown, P.H., Bowden, B., Yamaguchi, H., Appella, E., Samelson, L.E. and Schuck, P., (2007) Studying multisite binary and ternary protein interactions by global analysis of isothermal titration calorimetry data in SEDPHAT: Application to adaptor protein complexes in cell signaling. *Protein Science*, **16**, 30-42.

Hutchings, M.I., Shearer, N., Wastell, S., van Spanning, R.J.M. and Spiro, S. (2000) Heterologous NNR-mediated nitric oxide signaling in *Escherichia coli*. *Journal of Bacteriology*, **182**, 6434-6439.

Ikeuchi, Y., Shigi, N., Kato, J.-i., Nishimura, A. and Suzuki, T. (2006) Mechanistic insights into sulfur relay by multiple sulfur mediators involved in thiouridine biosynthesis at tRNA wobble positions. *Molecular Cell*, **21**, 97-108.

Imlay, J.A. and Linn, S. (1988) DNA damage and oxygen radical toxicity. *Science*, **240**, 1302-1309.

Inaba, K., Takahashi, Y.-h., Ito, K. and Hayashi, S. (2006) Critical role of a thiolate-quinone charge transfer complex and its adduct form in *de novo* disulfide bond generation by DsbB. *Proceedings of the National Academy of Sciences USA*, **103**, 287-292.

Iovine, N.M., Pursnani, S., Voldman, A., Wasserman, G., Blaser, M.J. and Weinrauch, Y. (2008) Reactive nitrogen species contribute to innate host defense against *Campylobacter jejuni*. *Infection and Immunity*, **76**, 986-993.

Ivanov, M. and Freney, J. (1983) The global biogeochemical sulphur cycle, *SCOPE Series, Wiley & sons.*

Jameson, G.N.L., Walters, E.M., Manieri, W., Schürmann, P., Johnson, M.K. and Huynh, B.H. (2003) Spectroscopic evidence for site specific chemistry at a unique iron site of the [4Fe−4S] cluster in ferredoxin:thioredoxin reductase. *Journal of the American Chemical Society*, **125**, 1146-1147.

John, G.S., Brot, N., Ruan, J., Erdjument-Bromage, H., Tempst, P., Weissbach, H. and Nathan, C. (2001) Peptide methionine sulfoxide reductase from *Escherichia coli* and *Mycobacterium tuberculosis* protects bacteria against oxidative damage from reactive nitrogen intermediates. *Proceedings of the National Academy of Sciences USA*, **98**, 9901-9906.

Jorgensen, W.L., Chandrasekhar, J., Madura, J.D., Impey, R.W. and Klein, M.L. (1983) Comparison of simple potential functions for simulating liquid water. *The Journal of Chemical Physics*, **79**, 926-935.

Jormakka, M., Yokoyama, K., Yano, T., Tamakoshi, M., Akimoto, S., Shimamura, T., Curmi, P. and Iwata, S. (2008) Molecular mechanism of energy conservation in polysulfide respiration. *Nature Structural and Molecular Biology*, **15**, 730-737.

Jung, J.-Y., Madan-Lala, R., Georgieva, M., Rengarajan, J., Sohaskey, C.D., Bange, F.-C. and Robinson, C.M. (2013) The intracellular environment of human macrophages that produce nitric oxide promotes growth of *Mycobacteria*. *Infection and Immunity*, **81**, 3198-3209.

Kadziola, A. and Larsen, S. (1997) Crystal structure of the dihaem cytochrome $c_4$ from *Pseudomonas stutzeri* determined at 2.2 A resolution. *Structure*, **5**, 203-216.

Kakishima, K., Shiratsuchi, A., Taoka, A., Nakanishi, Y. and Fukumori, Y. (2007) Participation of nitric oxide reductase in survival of *Pseudomonas aeruginosa* in LPS-activated macrophages. *Biochemical and Biophysical Research Communications*, **355**, 587-591.

Kappler, U. (2011) Bacterial sulfite-oxidizing enzymes. *Biochimica et Biophysica Acta – Bioenergetics*, **1807**, 1-10.

Kappler, U., Aguey-Zinsou, K.-F., Hanson, G.R., Bernhardt, P.V. and McEwan, A.G., 2004. Cytochrome $c_{551}$ from *Starkeya novella*: characterization, spectroscopic properties, and phylogeny of a diheme protein of the SoxAX family. *Journal of Biological Chemistry*, **279**, 6252-6260.

Kappler, U., Bennett, B., Rethmeier, J., Schwarz, G., Deutzmann, R., McEwan, A.G. and Dahl, C. (2000) Sulfite:cytochrome c oxidoreductase from *Thiobacillus novellus*: purification, characterization, and molecular biology of a heterodimeric member of the sulfite oxidase family. *Journal of Biological Chemistry*, **275**, 13202-13212.

Kappler, U., Bernhardt, P.V., Kilmartin, J., Riley, M.J., Teschner, J., McKenzie, K.J. and Hanson, G.R. (2008) SoxAX cytochromes, a new type of heme copper protein involved in bacterial energy generation from sulfur compounds. *Journal of Biological Chemistry*, **283**, 22206-22214.

Kappler, U., Hanson, G.R., Jones, A. and McEwan, A.G. (2005) A recombinant diheme SoxAX cytochrome – Implications for the relationship between EPR signals and modified heme-ligands. *FEBS letters*, **579**, 2491-2498.

Kappler, U. and Maher, M. (2013) The bacterial SoxAX cytochromes. *Cellular and Molecular Life Sciences*, **70**, 977-992.

Karlinsey, J.E., Bang, I.-S., Becker, L.A., Frawley, E.R., Porwollik, S., Robbins, H.F., Thomas, V.C., Urbano, R., McClelland, M. and Fang, F.C. (2012) The NsrR regulon in nitrosative stress resistance of *Salmonella enterica* serovar Typhimurium. *Molecular Microbiology*, **85**, 1179-1193.

Kelly, D., Shergill, J., Lu, W.-P. and Wood, A. (1997) Oxidative metabolism of inorganic sulfur compounds by bacteria. *Antonie van Leeuwenhoek*, **71**, 95-107.

Kelly, D.P. and Wood, A.P. (1994) Synthesis and determination of thiosulfate and polythionates. *Methods in Enzymology*, **243**, 475-501.

Kennedy, M.C., Antholine, W.E. and Beinert, H. (1997) An EPR investigation of the products of the reaction of cytosolic and mitochondrial aconitases with nitric oxide. *Journal of Biological Chemistry*, **272**, 20340-20347.

Kieleczawa, J., France, L.L., Sutherland, J.C. and Hind, G. (1992) pH-induced conformational changes in spinach ferredoxin: Steady-state and time-resolved fluorescence studies. *Archives of Biochemistry and Biophysics*, **298**, 63-69.

Kilmartin, J.R., Maher, M.J., Krusong, K., Noble, C.J., Hanson, G.R., Bernhardt, P.V., Riley, M.J. and Kappler, U. (2011) Insights into structure and function of the active site of SoxAX cytochromes. *Journal of Biological Chemistry*, **286**, 24872-24881.

Kinkel, T.L., Roux, C.M., Dunman, P.M. and Fang, F.C. (2013) The *Staphylococcus aureus* SrrAB two-component system promotes resistance to nitrosative stress and hypoxia. *mBio*, **4**, e00696-13

Knofel, T. and Strater, N. (1999) X-ray structure of the *Escherichia coli* periplasmic 5'-nucleotidase containing a dimetal catalytic site. *Nature Structural Biology*, **6**, 448-453.

Koh, M., Meyer, T.E., De Smet, L., Van Beeumen, J.J. and Cusanovich, M.A. (2003) Characterization of the interaction of *Rhodobacter capsulatus* cytochrome *c* peroxidase with charge reversal mutants of cytochrome $c_2$. *Archives of Biochemistry and Biophysics*, **410**, 230-237.

Kolmert, Å., Wikström, P. and Hallberg, K.B. (2000) A fast and simple turbidimetric method for the determination of sulfate in sulfate-reducing bacterial cultures. *Journal of Microbiological Methods*, **41**, 179-184.

Kumar, A., Toledo, J.C., Patel, R.P., Lancaster, J.R. and Steyn, A.J.C. (2007) *Mycobacterium tuberculosis* DosS is a redox sensor and DosT is a hypoxia sensor. *Proceedings of the National Academy of Sciences USA*, **104**, 11568-11573.

Kusai, A. and Yamanaka, T. (1973) Cytochrome *c* (553, *Chlorobium thiosulfatophilum*) is a sulphide-cytochrome c reductase. *FEBS Letters*, **34**, 235-237.

Laemmli, U.K. (1970) Cleavage of structural proteins during the assembly of the head of bacteriophage T4. *Nature*, **227**, 680-685.

Lange, C. and Hunte, C. (2002) Crystal structure of the yeast cytochrome *bc*$_1$ complex with its bound substrate cytochrome *c*. *Proceedings of the National Academy of Sciences USA*, **99**, 2800-2805.

Langer, G., Cohen, S.X., Lamzin, V.S. and Perrakis, A. (2008) Automated macromolecular model building for X-ray crystallography using ARP/wARP version 7. *Nature protocols*, **3**, 1171-1179.

Leimkühler, S., Wuebbens, M.M. and Rajagopalan, K.V. (2011) The history of the discovery of the molybdenum cofactor and novel aspects of its biosynthesis in bacteria. *Molybdenum*, **255**, 1129-1144.

Lengeler, J., Drews, G. and Schlegel, H. (1998) Oxidation of inorganic compounds by chemolithotrophs. *Biology of the Prokaryotes, Blackwell Science Ltd, 234-260*

Lepoivre, M., Fieschi, F., Coves, J., Thelander, L. and Fontecave, M. (1991) Inactivation of ribonucleotide reductase by nitric oxide. *Biochemical and Biophysical Research Communications*, **179**, 442-448.

Leys, D., Basran, J., Talfournier, F., Sutcliffe, M.J. and Scrutton, N.S. (2003) Extensive conformational sampling in a ternary electron transfer complex. *Nature Structural and Molecular Biology*, **10**, 219-225.

Liamleam, W. and Annachhatre, A.P. (2007) Electron donors for biological sulfate reduction. *Biotechnology Advances*, **25**, 452-463.

Libiad, M., Yadav, P.K., Vitvitsky, V., Martinov, M. and Banerjee, R. (2014) Organization of the human mitochondrial $H_2S$ oxidation pathway. *Journal of Biological Chemistry*, *in press*.

Lim, M.D., Lorković, I.M. and Ford, P.C. (2005) The preparation of anaerobic nitric oxide solutions for the study of heme model systems in aqueous and nonaqueous media: some consequences of $NO_x$ impurities. *Methods in Enzymology*, **396**, 3-17.

Lin, Z.-S., Lo, F.-C., Li, C.-H., Chen, C.-H., Huang, W.-N., Hsu, I.J., Lee, J.-F., Horng, J.-C. and Liaw, W.-F. (2011) Peptide-bound dinitrosyliron complexes (DNICs) and neutral/reduced-form roussin's red esters (RREs/rRREs): Understanding nitrosylation of [Fe–S] clusters leading to the formation of DNICs and RREs using a *de novo* design strategy. *Inorganic Chemistry*, **50**, 10417-10431.

Liu, L., Hausladen, A., Zeng, M., Que, L., Heitman, J. and Stamler, J.S. (2001) A metabolic enzyme for S-nitrosothiol conserved from bacteria to humans. *Nature*, **410**, 490-494.

Liu, Y.-W., Denkmann, K., Kosciow, K., Dahl, C. and Kelly, D.J. (2013) Tetrathionate stimulated growth of *Campylobacter jejuni* identifies a new type of bi-functional tetrathionate reductase (TsdA) that is widely distributed in bacteria. *Molecular Microbiology*, **88**, 173-188.

Lu, T.-T., Chiou, S.-J., Chen, C.-Y. and Liaw, W.-F. (2006) Mononitrosyl tris(thiolate) iron complex $[Fe(NO)(SPh)_3]^-$ and dinitrosyl iron complex $[(EtS)_2Fe(NO)_2]^-$: formation pathway of dinitrosyl iron complexes (DNICs) from nitrosylation of biomimetic rubredoxin $[Fe(SR)_4]^{2-/1-}$ (R = Ph, Et). *Inorganic Chemistry*, **45**, 8799-8806.

Lu, W.-P. and Kelly, D.P. (1983a). Purification and some properties of two principal enzymes of the thiosulphate-oxidizing multi-enzyme system from *Thiobacillus A2*. *Journal of General Microbiology*, **129**, 3549-3564.

Lu, W.-P. and Kelly, D.P. (1983b) Rhodanese: an enzyme not necessary for thiosulphate oxidation by *Thiobacillus A2*. *FEMS Microbiology Letters*, **18**, 289-292.

Lu, W.-P. and Kelly, D.P. (1984) Properties and role of sulphite: cytochrome c oxidoreductase purified from *Thiobacillus versutus* (A2). *Journal of General Microbiology*, **130**, 1683-1692.

Lu, W.-P., Swoboda, B.E.P. and Kelly, D.P. (1985) Properties of the thiosulphate-oxidizing multi-enzyme system from *Thiobacillus versutus*. *Biochimica et Biophysica Acta - Protein Structure and Molecular Enzymology*, **828**, 116-122.

Lundberg, B.E., Wolf, R.E., Dinauer, M.C., Xu, Y. and Fang, F.C. (1999) Glucose 6-phosphate dehydrogenase is required for *Salmonella typhimurium* virulence and resistance to reactive oxygen and nitrogen intermediates. *Infection and Immunity*, **67**, 436-438.

Luo, G.X. and Horowitz, P.M. (1994) The sulfurtransferase activity and structure of rhodanese are affected by site-directed replacement of Arg-186 or Lys-249. *Journal of Biological Chemistry*, **269**, 8220-8225.

M. Bradbrook, G., Gleichmann, T., J. Harrop, S., Habash, J., Raftery, J., Kalb, J., Yariv, J., H. Hillier, I. and R. Helliwell, J. (1998) X-Ray and molecular dynamics studies of concanavalin-A glucoside and mannoside complexes Relating structure to thermodynamics of binding. *Journal of the Chemical Society, Faraday Transactions*, **94**, 1603-1611.

Maier, T., Leibundgut, M. and Ban, N. (2008) The crystal structure of a mammalian fatty acid synthase. *Science*, **321**, 1315-1322.

Marletta, M.A., Yoon, P.S., Iyengar, R., Leaf, C.D. and Wishnok, J.S. (1988) Macrophage oxidation of L-arginine to nitrite and nitrate: nitric oxide is an intermediate. *Biochemistry*, **27**, 8706-8711.

Martin, W. and Russell, M.J. (2003) On the origins of cells: a hypothesis for the evolutionary transitions from abiotic geochemistry to chemoautotrophic prokaryotes, and from prokaryotes to nucleated cells. *Philosophical Transactions of the Royal Society of London. Series B: Biological Sciences*, **358**, 59-85.

Masoudi, A., Raetz, C.R.H., Zhou, P. and Pemble IV, C.W., 2014. Chasing acyl carrier protein through a catalytic cycle of lipid A production. *Nature*, **505**, 422-426.

McCoy, A.J., Grosse-Kunstleve, R.W., Adams, P.D., Winn, M.D., Storoni, L.C. and Read, R.J. (2007) Phaser crystallographic software. *Journal of Applied Crystallography*, **40**, 658-674.

McDonald, C.C., Phillips, W.D. and Mower, H.F. (1965) An electron spin resonance study of some complexes of iron, nitric oxide, and anionic ligands. *Journal of the American Chemical Society*, **87**, 3319-3326.

Meyer, B., Imhoff, J.F. and Kuever, J. (2007) Molecular analysis of the distribution and phylogeny of the *soxB* gene among sulfur-oxidizing bacteria – evolution of the Sox sulfur oxidation enzyme system. *Environmental Microbiology*, **9**, 2957-2977.

Miller, L.M., Pedraza, A.J. and Chance, M.R. (1997) Identification of conformational substates involved in nitric oxide binding to ferric and ferrous myoglobin through difference fourier transform infrared spectroscopy (FTIR). *Biochemistry*, **36**, 12199-12207.

Miroux, B. and Walker, J.E. (1996) Over-production of proteins in *Escherichia coli*: Mutant hosts that allow synthesis of some membrane proteins and globular proteins at high levels. *Journal of Molecular Biology*, **260**, 289-298.

Moncada, S., Palmer, R.M.J. and Higgs, E.A. (1989) Biosynthesis of nitric oxide from L-arginine: A pathway for the regulation of cell function and communication. *Biochemical Pharmacology*, **38**, 1709-1715.

Morgenstern, D.E., Gifford, M.A.C., Li, L.L., Doerschuk, C.M. and Dinauer, M.C. (1997) Absence of respiratory burst in X-linked chronic granulomatous disease mice leads to abnormalities in both host defense and inflammatory response to *Aspergillus fumigatus*. *The Journal of Experimental Medicine*, **185**, 207-218.

Mueller, E.G. (2006) Trafficking in persulfides: delivering sulfur in biosynthetic pathways. *Nature Chemical Biology*, **2**, 185-194.

Mukhopadhyay, P., Zheng, M., Bedzyk, L.A., LaRossa, R.A. and Storz, G. (2004) Prominent roles of the NorR and Fur regulators in the *Escherichia coli* transcriptional response to reactive nitrogen species. *Proceedings of the National Academy of Sciences USA*, **101**, 745-750.

Mukhopadhyaya, P.N., Deb, C., Lahiri, C. and Roy, P. (2000) A *soxA* gene, encoding a diheme cytochrome *c*, and a *sox* locus, essential for sulfur oxidation in a new sulfur lithotrophic bacterium. *Journal of Bacteriology*, **182**, 4278-4287.

Murshudov, G.N., Vagin, A.A. and Dodson, E.J. (1997) Refinement of macromolecular structures by the maximum-likelihood method. *Acta Crystallographica Section D Biological Crystallography*, **53**, 240-255.

Müller, F.H., Bandeiras, T.M., Urich, T., Teixeira, M., Gomes, C.M. and Kletzin, A. (2004) Coupling of the pathway of sulphur oxidation to dioxygen reduction: characterization of a novel membrane-bound thiosulphate:quinone oxidoreductase. *Molecular Microbiology*, **53**, 1147-1160.

Nakamoto, H. and Bardwell, J.C.A. (2004) Catalysis of disulfide bond formation and isomerization in the *Escherichia coli* periplasm. *Biochimica et Biophysica Acta - Molecular Cell Research*, **1694**, 111-119.

Nathan, C. and Shiloh, M.U. (2000) Reactive oxygen and nitrogen intermediates in the relationship between mammalian hosts and microbial pathogens. *Proceedings of the National Academy of Sciences USA*, **97**, 8841-8848.

Nathan, C. and Xie, Q.-w. (1994) Nitric oxide synthases: Roles, tolls, and controls. *Cell*, **78**, 915-918.

Nguyen, C., Haushalter, R.W., Lee, D.J., Markwick, P.R.L., Bruegger, J., Caldara-Festin, G., Finzel, K., Jackson, D.R., Ishikawa, F., O/'Dowd, B., McCammon, J.A., Opella, S.J., Tsai, S.-C. and Burkart, M.D. (2014) Trapping the dynamic acyl carrier protein in fatty acid biosynthesis. *Nature*, **505**, 427-431.

Nicola, N.A. and Leach, S.J. (1977) Structural rearrangements due to ligand binding and haem replacement in myoglobin and leghaemoglobins. *European Journal of Biochemistry*, **78**, 133-140.

Ogawa, T., Furusawa, T., Shiga, M., Seo, D., Sakurai, H. and Inoue, K. (2010) Biochemical studies of a *soxF*-encoded monomeric flavoprotein purified from the green sulfur bacterium *Chlorobaculum tepidum* that stimulates *in vitro* thiosulfate oxidation. *Bioscience, Biotechnology, and Biochemistry*, **74**, 771-780.

Oliveira, T.F., Vonrhein, C., Matias, P.M., Venceslau, S.S., Pereira, I.A.C. and Archer, M. (2008) The crystal structure of *Desulfovibrio vulgaris* dissimilatory sulfite reductase bound to DsrC provides novel insights into the mechanism of sulfate respiration. *Journal of Biological Chemistry*, **283**, 34141-34149.

Palmer, R.M.J., Ferrige, A.G. and Moncada, S. (1987) Nitric oxide release accounts for the biological activity of endothelium-derived relaxing factor. *Nature*, **327**, 524-526.

Palmer, R.M.J., Rees, D.D., Ashton, D.S. and Moncada, S. (1988) L-arginine is the physiological precursor for the formation of nitric oxide in endothelium-dependent relaxation. *Biochemical and Biophysical Research Communications*, **153**, 1251-1256.

Pazicni, S., Cherney, M.M., Lukat-Rodgers, G.S., Oliveriusová, J., Rodgers, K.R., Kraus, J.P. and Burstyn, J.N. (2005) The heme of cystathionine β-synthase likely undergoes a thermally induced redox-mediated ligand switch. *Biochemistry*, **44**, 16785-16795.

Pecci, L., Montefoschi, G., Musci, G. and Cavallini, D. (1997) Novel findings on the copper catalysed oxidation of cysteine. *Amino Acids*, **13**, 355-367.

Perham, R.N. (2000) Swinging arms and swinging domains in multifunctional enzymes: catalytic machines for multistep reactions. *Annual Review of Biochemistry*, **69**, 961-1004.

Pierson, M.D., Smoot, L.A. and Robach, M.C. (1983) Nitrite, nitrite alternatives, and the control of clostridium botulinum in cured meats. *Critical Reviews in Food Science and Nutrition*, **17**, 141-187.

Pires, R.H., Lourenço, A.I., Morais, F., Teixeira, M., Xavier, A.V., Saraiva, L.g.M. and Pereira, I.A.C. (2003) A novel membrane-bound respiratory complex from *Desulfovibrio desulfuricans ATCC 27774*. *Biochimica et Biophysica Acta - Bioenergetics* **1605**, 67-82.

Pires, R.H., Venceslau, S.S., Morais, F., Teixeira, M., Xavier, A.V. and Pereira, I.A.C. (2005) Characterization of the *Desulfovibrio desulfuricans ATCC 27774* DsrMKJOP Complex - a membrane-bound redox complex involved in the sulfate respiratory pathway. *Biochemistry*, **45**, 249-262.

Plate, L. and Marletta, M.A. (2013) Nitric oxide-sensing H-NOX proteins govern bacterial communal behavior. *Trends in Biochemical Sciences*, **38**, 566-575.

Pomowski, A., Zumft, W.G., Kroneck, P.M.H. and Einsle, O. (2011) $N_2O$ binding at a [4Cu:2S] copper-sulphur cluster in nitrous oxide reductase. *Nature*, **477**, 234-237.

Pott, A.S. and Dahl, C. (1998) Sirohaem sulfite reductase and other proteins encoded by genes at the *dsr* locus of *Chromatium vinosum* are involved in the oxidation of intracellular sulfur. *Microbiology*, **144**, 1881-1894.

Quentmeier, A. and Friedrich, C.G. (2001) The cysteine residue of the SoxY protein as the active site of protein-bound sulfur oxidation of *Paracoccus pantotrophus GB17*. *FEBS Letters*, **503**, 168-172.

Quentmeier, A., Hellwig, P., Bardischewsky, F., Grelle, G., Kraft, R. and Friedrich, C.G. (2003) Sulfur oxidation in *Paracoccus pantotrophus*: interaction of the sulfur-binding protein SoxYZ with the dimanganese SoxB protein. *Biochemical and Biophysical Research Communications*, **312**, 1011-1018.

Quentmeier, A., Janning, P., Hellwig, P. and Friedrich, C.G. (2007) Activation of the heterodimeric central complex SoxYZ of chemotrophic sulfur oxidation is linked to a conformational change and SoxY-Y interprotein disulfide formation. *Biochemistry*, **46**, 10990-10998.

Quentmeier, A., Kraft, R., Kostka, S., Klockenkämper, R. and Friedrich, C.G. (2000) Characterization of a new type of sulfite dehydrogenase from *Paracoccus pantotrophus GB17*. *Archives of Microbiology*, **173**, 117-125.

Quentmeier, A., Li, L. and Friedrich, C.G. (2008) Identification of two inactive forms of the central sulfur cycle protein SoxYZ of *Paracoccus pantotrophus. FEBS letters*, **582**, 3701-3704.

Rawlings, D.E. and Johnson, D.B. (2007) The microbiology of biomining: development and optimization of mineral-oxidizing microbial consortia. *Microbiology*, **153**, 315-324.

Reddy, D., Lancaster, J.R. and Cornforth, D.P. (1983) Nitrite inhibition of *Clostridium botulinum*: electron spin resonance detection of iron-nitric oxide complexes. *Science*, **221**, 769-770.

Reijerse, E.J., Sommerhalter, M., Hellwig, P., Quentmeier, A., Rother, D., Laurich, C., Bothe, E., Lubitz, W. and Friedrich, C.G. (2007) The unusal redox centers of SoxXA, a novel *c*-type heme-enzyme essential for chemotrophic sulfur-oxidation of *Paracoccus pantotrophus*. *Biochemistry*, **46**, 7804-7810.

Reinartz, M., Tschäpe, J., Brüser, T., Trüper, H.G. and Dahl, C. (1998) Sulfide oxidation in the phototrophic sulfur bacterium *Chromatium vinosum*. *Archives of Microbiology*, **170**, 59-68.

Ren, B., Zhang, N., Yang, J. and Ding, H. (2008) Nitric oxide-induced bacteriostasis and modification of iron-sulphur proteins in *Escherichia coli*. *Molecular Microbiology*, **70**, 953-964.

Richardson, A.R., Libby, S.J. and Fang, F.C. (2008) A nitric oxide–inducible lactate dehydrogenase enables *Staphylococcus aureus* to resist innate immunity. *Science*, **319**, 1672-1676.

Richardson, Anthony R., Payne, Elizabeth C., Younger, N., Karlinsey, Joyce E., Thomas, Vinai C., Becker, Lynne A., Navarre, William W., Castor, Margaret E., Libby, Stephen J. and Fang, Ferric C. (2011) Multiple targets of nitric oxide in the tricarboxylic acid cycle of *Salmonella enterica* Serovar Typhimurium. *Cell Host & Microbe*, **10**, 33-43.

Richardson, D.J., Berks, B.C., Russell, D.A., Spiro, S. and Taylor, C.J. (2001) Functional, biochemical and genetic diversity of prokaryotic nitrate reductases. *Cellular and Molecular Life Sciences*, **58**, 165-178.

Rohwerder, T. and Sand, W. (2003) The sulfane sulfur of persulfides is the actual substrate of the sulfur-oxidizing enzymes from *Acidithiobacillus* and *Acidiphilium spp*. *Microbiology*, **149**, 1699-1710.

Rollauer, S.E., Tarry, M.J., Graham, J.E., Jaaskelainen, M., Jager, F., Johnson, S., Krehenbrink, M., Liu, S.-M., Lukey, M.J., Marcoux, J., McDowell, M.A., Rodriguez, F., Roversi, P., Stansfeld, P.J., Robinson, C.V., Sansom, M.S.P., Palmer, T., Hogbom, M., Berks, B.C. and Lea, S.M. (2012) Structure of the TatC core of the twin-arginine protein transport system. *Nature*, **492**, 210-214.

Rother, D. and Friedrich, C.G. (2002) The cytochrome complex SoxXA of *Paracoccus pantotrophus* is produced in *Escherichia coli* and functional in the reconstituted sulfur-oxidizing enzyme system. *Biochimica et Biophysica Acta - Proteins and Proteomics*, **1598**, 65-73.

Rother, D., Henrich, H.-J., Quentmeier, A., Bardischewsky, F. and Friedrich, C.G. (2001) Novel genes of the *sox* gene cluster, mutagenesis of the flavoprotein SoxF, and evidence for a general sulfur-oxidizing system in *Paracoccus pantotrophus GB17*. *Journal of Bacteriology*, **183**, 4499-4508.

Sasaki, E., Zhang, X., Sun, H.G., Lu, M.-Y.J., Liu, T.-l., Ou, A., Li, J.-y., Chen, Y.-h., Ealick, S.E. and Liu, H.-w. (2014) Co-opting sulphur-carrier proteins from primary metabolic pathways for 2-thiosugar biosynthesis. *Nature*, **510**, 427-431.

Sauvé, V., Bruno, S., Berks, B.C. and Hemmings, A.M. (2007) The SoxYZ complex carries sulfur cycle intermediates on a peptide swinging arm. *Journal of Biological Chemistry*, **282**, 23194-23204.

Sauvé, V. (2008) Biochemical and structural characterisation of proteins involved in the sulfur oxidation (Sox) system. *DPhil thesis, Oxford University*.

Sauvé, V., Roversi, P., Leath, K.J., Garman, E.F., Antrobus, R., Lea, S.M. and Berks, B.C. (2009) Mechanism for the hydrolysis of a sulfur-sulfur bond based on the crystal structure of the thiosulfohydrolase SoxB. *Journal of Biological Chemistry*, **284**, 21707-21718.

Schapiro, J.M., Libby, S.J. and Fang, F.C. (2003) Inhibition of bacterial DNA replication by zinc mobilization during nitrosative stress. *Proceedings of the National Academy of Sciences USA*, **100**, 8496-8501.

Schippers, A., Glombitza, F., Sand, W. and Rossi, G. (2014) The microbial desulfurization of coal. *Geobiotechnology II, Springer Berlin Heidelberg*, 147-167.

Schneemann, M., Schoedon, G., Hofer, S., Blau, N., Guerrero, L. and Schaffner, A. (1993) Nitric oxide synthase is not a constituent of the antimicrobial armature of human mononuclear phagocytes. *Journal of Infectious Diseases*, **167**, 1358-1363.

Schütz, M., Klughammer, C., Griesbeck, C., Quentmeier, A., Friedrich, C.G. and Hauska, G. (1998) Sulfide-quinone reductase activity in membranes of the chemotrophic bacterium *Paracoccus denitrificans GB17*. *Archives of Microbiology*, **170**, 353-360.

Schütz, M., Maldener, I., Griesbeck, C. and Hauska, G. (1999) Sulfide-quinone reductase from *Rhodobacter capsulatus*: Requirement for growth, periplasmic localization, and extension of gene sequence analysis. *Journal of Bacteriology*, **181**, 6516-6523.

Sellers, V.M., Johnson, M.K. and Dailey, H.A. (1996) Function of the [2Fe−2S] cluster in mammalian ferrochelatase: A possible role as a nitric oxide sensor. *Biochemistry*, **35**, 2699-2704.

Sevier, C.S. and Kaiser, C.A. (2002) Formation and transfer of disulphide bonds in living cells. *Nature Reviews Molecular Cell Biology*, **3**, 836-847.

Shatalin, K., Gusarov, I., Avetissova, E., Shatalina, Y., McQuade, L.E., Lippard, S.J. and Nudler, E. (2008) *Bacillus anthracis*-derived nitric oxide is essential for pathogen virulence and survival in macrophages. *Proceedings of the National Academy of Sciences USA*, **105**, 1009-1013.

Shimizu, T., Tsutsuki, H., Matsumoto, A., Nakaya, H. and Noda, M. (2012) The nitric oxide reductase of enterohaemorrhagic *Escherichia coli* plays an important role for the survival within macrophages. *Molecular Microbiology*, **85**, 492-512.

Simon, J. and Klotz, M.G. (2013) Diversity and evolution of bioenergetic systems involved in microbial nitrogen compound transformations. The evolutionary aspects of bioenergetic systems. *Biochimica et Biophysica Acta – Bioenergetics*, **1827**, 114-135.

Singh, A., Guidry, L., Narasimhulu, K.V., Mai, D., Trombley, J., Redding, K.E., Giles, G.I., Lancaster, J.R. and Steyn, A.J.C. (2007) *Mycobacterium tuberculosis* WhiB3 responds to $O_2$ and nitric oxide via its [4Fe-4S] cluster and is essential for nutrient starvation survival. *Proceedings of the National Academy of Sciences USA*, **104**, 11562-11567.

Smith, L.J., Stapleton, M.R., Fullstone, G.J.M., Crack, J.C., Thomson, A.J., Le Brun, N.E., Hunt, D.M., Harvey, E., Adinolfi, S., Buxton, R.S. and Green, J. (2010) *Mycobacterium tuberculosis* WhiB1 is an essential DNA-binding protein with a nitric oxide-sensitive iron–sulfur cluster. *Biochemical Journal*, **432**, 417-427.

Sousa, E.H.S., Tuckerman, J.R., Gonzalez, G. and Gilles-Gonzalez, M.-A. (2007) DosT and DevS are oxygen-switched kinases in *Mycobacterium tuberculosis*. *Protein Science*, **16**, 1708-1719.

Sousa, F.L., Thiergart, T., Landan, G., Nelson-Sathi, S., Pereira, I.A.C., Allen, J.F., Lane, N. and Martin, W.F. (2013) Early bioenergetic evolution. *Philosophical Transactions of the Royal Society B: Biological Sciences*, **368**.

Spiro, S. (2007) Regulators of bacterial responses to nitric oxide. *FEMS Microbiology Reviews*, **31**, 193-211.

Stern, A.M., Hay, A.J., Liu, Z., Desland, F.A., Zhang, J., Zhong, Z. and Zhu, J. (2012) The NorR regulon is critical for *Vibrio cholerae* resistance to nitric oxide and sustained colonization of the intestines. *mBio*, **3**, e00013-12.

Stern, A.M., Liu, B., Bakken, L.R., Shapleigh, J.P. and Zhu, J. (2013) A novel protein protects bacterial iron-dependent metabolism from nitric oxide. *Journal of Bacteriology*, **195**, 4702-4708.

Stevanin, T.M., Ioannidis, N., Mills, C.E., Kim, S.O., Hughes, M.N. and Poole, R.K. (2000) Flavohemoglobin Hmp affords inducible protection for *Escherichia coli* respiration, catalyzed by cytochromes *bo*′ or *bd*, from nitric oxide. *Journal of Biological Chemistry*, **275**, 35868-35875.

Stevanin, T.M., Moir, J.W.B. and Read, R.C. (2005) Nitric oxide detoxification systems enhance survival of *Neisseria meningitidis* in human macrophages and in nasopharyngeal mucosa. *Infection and Immunity*, **73**, 3322-3329.

Stoffels, L., Krehenbrink, M., Berks, B.C. and Unden, G. (2012) Thiosulfate reduction in *Salmonella enterica* is driven by the proton motive force. *Journal of Bacteriology*, **194**, 475-485.

Stoll, S. and Schweiger, A. (2006) EasySpin, a comprehensive software package for spectral simulation and analysis in EPR. *Journal of Magnetic Resonance*, **178**, 42-55.

Sudhamsu, J. and Crane, B.R. (2009) Bacterial nitric oxide synthases: what are they good for? *Trends in Microbiology*, **17**, 212-218.

Suga, M., Lai, T.-L., Sugiura, M., Shen, J.-R. and Boussac, A. (2013) Crystal structure at 1.5 Å resolution of the PsbV2 cytochrome from the cyanobacterium *Thermosynechococcus elongatus*. *FEBS letters*, **587**, 3267-3272.

Sun, Y., Benabbas, A., Zeng, W., Kleingardner, J.G., Bren, K.L. and Champion, P.M. (2014) Investigations of heme distortion, low-frequency vibrational excitations, and electron transfer in cytochrome *c*. *Proceedings of the National Academy of Sciences USA*, **111**, 6570-6575.

Susi, H. and Byler, D.M. (1986) Resolution-enhanced fourier transform infrared spectroscopy of enzymes. *Methods in Enzymology*, **130**, 290-311.

Tagawa, K. and Arnon, D.I. (1962) Ferredoxins as electron carriers in photosynthesis and in the biological production and consumption of hydrogen gas. *Nature*, **195**, 537-543.

Tanoue, T. and Nishida, E. (2003) Molecular recognitions in the MAP kinase cascades. *Cellular Signalling*, **15**, 455-462.

Tarry, M., Skaar, K., Heijne, G.v., Draheim, R.R. and Högbom, M. (2012) Production of human tetraspanin proteins in *Escherichia coli*. *Protein Expression and Purification*, **82**, 373-379.

Taylor, B.S. and Geller, D.A. (2000) Molecular regulation of the human inducible nitric oxide synthase (iNOS) gene. *Shock*, **13**, 413-424

Tervoort, M.J., Schilder, L.T.M. and Van Gelder, B.F. (1981) The absorbance coefficient of beef heart cytochrome $c_1$. *Biochimica et Biophysica Acta – Bioenergetics*, **637**, 245-251.

Thauer, R.K., Jungermann, K. and Decker, K. (1977) Energy conservation in chemotrophic anaerobic bacteria. *Bacteriological Reviews*, **41**, 100-180.

Thomas, A.M., Lin, B.-L., Wasinger, E.C. and Stack, T.D.P. (2013) Ligand noninnocence of thiolate/disulfide in dinuclear copper complexes: solvent-dependent redox isomerization and proton-coupled electron transfer. *Journal of the American Chemical Society*, **135**, 18912-18919.

Thomas, M.R., Brown, D., Franzen, S. and Boxer, S.G. (2001) FTIR and resonance raman studies of nitric oxide binding to H93G cavity mutants of myoglobin. *Biochemistry*, **40**, 15047-15056.

Tinberg, C.E., Tonzetich, Z.J., Wang, H., Do, L.H., Yoda, Y., Cramer, S.P. and Lippard, S.J. (2010) Characterization of iron dinitrosyl species formed in the reaction of nitric oxide with a biological rieske center. *Journal of the American Chemical Society*, **132**, 18168-18176.

Tong, L. (2013) Structure and function of biotin-dependent carboxylases. *Cellular and Molecular Life Sciences*, **70**, 863-891.

Tonzetich, Z.J., Wang, H., Mitra, D., Tinberg, C.E., Do, L.H., Jenney, F.E., Adams, M.W.W., Cramer, S.P. and Lippard, S.J. (2010) Identification of protein-bound dinitrosyl iron complexes by nuclear resonance vibrational spectroscopy. *Journal of the American Chemical Society*, **132**, 6914-6916.

Tsou, C.-C., Lu, T.-T. and Liaw, W.-F. (2007) EPR, UV−Vis, IR, and X-ray demonstration of the anionic dimeric dinitrosyl iron complex $[(NO)_2Fe(\mu\text{-}S^tBu)_2Fe(NO)_2]^-$: Relevance to the products of nitrosylation of cytosolic and mitochondrial aconitases, and high-potential iron proteins. *Journal of the American Chemical Society*, **129**, 12626-12627.

Tucker, N.P., Hicks, M.G., Clarke, T.A., Crack, J.C., Chandra, G., Le Brun, N.E., Dixon, R. and Hutchings, M.I. (2008) The transcriptional repressor protein NsrR senses nitric oxide directly via a [2Fe-2S] cluster. *PLoS ONE*, **3**, e3623.

Tucker, N.P., Le Brun, N.E., Dixon, R. and Hutchings, M.I. (2010) There's NO stopping NsrR, a global regulator of the bacterial NO stress response. *Trends in Microbiology*, **18**, 149-156.

Ukita, S., Fujii, T., Hira, D., Nishiyama, T., Kawase, T., Migita, C.T. and Furukawa, K. (2010) A heterodimeric cytochrome *c* complex with a very low redox potential from an anaerobic ammonium-oxidizing enrichment culture. *FEMS Microbiology Letters*, **313**, 61-67.

Urich, T., Gomes, C.M., Kletzin, A. and Frazão, C. (2006) X-ray structure of a self-compartmentalizing sulfur cycle metalloenzyme. *Science*, **311**, 996-1000.

Vagin, A. and Teplyakov, A. (2010) Molecular replacement with MOLREP. *Acta Crystallographica Section D Biological Crystallography*, **66**, 22-25.

Valdes, J., Pedroso, I., Quatrini, R., Dodson, R., Tettelin, H., Blake, R., Eisen, J. and Holmes, D. (2008) *Acidithiobacillus ferrooxidans* metabolism: from genome sequence to industrial applications. *BMC Genomics*, **9**, 597.

Van Driessche, G., Devreese, B., Fitch, J.C., Meyer, T.E., Cusanovich, M.A. and Van Beeumen, J.J. (2006) GHP, a new *c*-type green heme protein from *Halochromatium salexigens* and other proteobacteria. *FEBS Journal*, **273**, 2801-2811.

van Sorge, N.M., Beasley, F.C., Gusarov, I., Gonzalez, D.J., von Köckritz-Blickwede, M., Anik, S., Borkowski, A.W., Dorrestein, P.C., Nudler, E. and Nizet, V. (2013) Methicillin-resistant *Staphylococcus aureus* bacterial nitric-oxide synthase affects antibiotic sensitivity and skin abscess development. *Journal of Biological Chemistry*, **288**, 6417-6426.

Vazquez-Torres, A., Jones-Carson, J., Mastroeni, P., Ischiropoulos, H. and Fang, F.C. (2000) Antimicrobial actions of the NADPH phagocyte oxidase and inducible nitric oxide synthase in experimental salmonellosis. I. Effects on microbial killing by activated peritoneal Macrophages *in vitro*. *The Journal of Experimental Medicine*, **192**, 227-236.

Venceslau, S.S., Stockdreher, Y., Dahl, C. and Pereira, I.A.C. (2014) The "bacterial heterodisulfide" DsrC is a key protein in dissimilatory sulfur metabolism. *Biochimica et Biophysica Acta – Bioenergetics*, **1837**, 1148-1164.

Victor, E. and Lippard, S.J. (2014) A tetranitrosyl [4Fe–4S] Cluster forms en route to roussin's black anion: nitric oxide reactivity of $[Fe_4S_4(LS_3)L']^{2-}$. *Inorganic Chemistry*, **53**, 5311-5320.

Visser, J., de Jong, G.H., Robertson, L. and Kuenen, J.G. (1996) Purification and characterization of a periplasmic thiosulfate dehydrogenase from the obligately autotrophic *Thiobacillus sp. W5*. *Archives of Microbiology*, **166**, 372-378.

Wang, J., Wolf, R.M., Caldwell, J.W., Kollman, P.A. and Case, D.A. (2004) Development and testing of a general amber force field. *Journal of Computational Chemistry*, **25**, 1157-1174.

Wang, R., Camacho-Fernandez, M.A., Xu, W., Zhang, J. and Li, L. (2009) Neutral and reduced Roussin's red salt ester $[Fe2(\mu\text{-}RS)_2(NO)_4]$ (R = n-Pr, t-Bu, 6-methyl-2-pyridyl and 4,6-dimethyl-2-pyrimidyl): synthesis, X-ray crystal structures, spectroscopic, electrochemical and density functional theoretical investigations. *Dalton Transactions*, **5**, 777-786.

Wang, Y., Dufour, Y.S., Carlson, H.K., Donohue, T.J., Marletta, M.A. and Ruby, E.G. (2010) H-NOX–mediated nitric oxide sensing modulates symbiotic colonization by *Vibrio fischeri*. *Proceedings of the National Academy of Sciences USA*, **107**, 8375-8380.

Wei, C.-C., Crane, B.R. and Stuehr, D.J. (2003) Tetrahydrobiopterin radical enzymology. *Chemical Reviews*, **103**, 2365-2384.

Weinberg, J.B. (1998) Nitric oxide production and nitric oxide synthase type 2 expression by human mononuclear phagocytes: a review. *Molecular Medicine*, **4**, 557.

Welte, C., Hafner, S., Krätzer, C., Quentmeier, A., Friedrich, C.G. and Dahl, C. (2009) Interaction between Sox proteins of two physiologically distinct bacteria and a new protein involved in thiosulfate oxidation. *FEBS Letters*, **583**, 1281-1286.

Wen, J., Arakawa, T. and Philo, J.S. (1996) Size-exclusion chromatography with on-line light-scattering, absorbance, and refractive index detectors for studying proteins and their interactions. *Analytical Biochemistry*, **240**, 155-166.

Wink, D.A., Kasprzak, K.S., Maragos, C.M., Elespuru, R.K., Misra, M., Dunams, T.M., Cebula, T.A., Koch, W.H., Andrews, A.W., Allen, J.S. and Keefer, L.K. (1991) DNA deaminating ability and genotoxicity of nitric oxide and its progenitors. *Science*, **254**, 1001-1003.

Wodara, C., Bardischewsky, F. and Friedrich, C.G. (1997) Cloning and characterization of sulfite dehydrogenase, two c-type cytochromes, and a flavoprotein of *Paracoccus denitrificans GB17*: essential role of sulfite dehydrogenase in lithotrophic sulfur oxidation. *Journal of Bacteriology*, **179**, 5014-5023.

Woolum, J.C., Tiezzi, E. and Commoner, B. (1968) Electron spin resonance of iron-nitric oxide complexes with amino acids, peptides and proteins. *Biochimica et Biophysica Acta - Protein Structure*, **160**, 311-320.

Xia, Y. and Zweier, J.L. (1997) Superoxide and peroxynitrite generation from inducible nitric oxide synthase in macrophages. *Proceedings of the National Academy of Sciences USA*, **94**, 6954-6958.

Xu, W., Liu, L.Z., Loizidou, M., Ahmed, M. and Charles, I.G. (2002) The role of nitric oxide in cancer. *Cell Research*, **12**, 311-320.

Yanisch-Perron, C., Vieira, J. and Messing, J. (1985) Improved M13 phage cloning vectors and host strains: nucleotide sequences of the M13mpl8 and pUC19 vectors. *Gene*, **33**, 103-119.

Yeh, S.-W., Tsou, C.-C. and Liaw, W.-F. (2014) The dinitrosyliron complex $[Fe_4(\mu_3\text{-}S)_2(\mu_2\text{-}NO)_2(NO)_6]^{2-}$ containing bridging nitroxyls: $15^N$ (NO) NMR analysis of the bridging and terminal NO-coordinate ligands. *Dalton Transactions*, **43**, 9022-9025.

Yu, K., Mitchell, C., Xing, Y., Magliozzo, R.S., Bloom, B.R. and Chan, J. (1999) Toxicity of nitrogen oxides and related oxidants on mycobacteria: *M. tuberculosis* is resistant to peroxynitrite anion. *Tubercule and Lung Disease*, **79**, 191-198.

Yukl, E.T., Elbaz, M.A., Nakano, M.M. and Moënne-Loccoz, P. (2008) Transcription factor NsrR from *Bacillus subtilis* senses nitric oxide with a 4Fe–4S cluster. *Biochemistry*, **47**, 13084-13092.

Zander, U., Faust, A., Klink, B.U., de Sanctis, D., Panjikar, S., Quentmeier, A., Bardischewsky, F., Friedrich, C.G. and Scheidig, A.J. (2011) Structural basis for the oxidation of protein-bound sulfur by the sulfur cycle molybdohemo-enzyme sulfane dehydrogenase SoxCD. *Journal of Biological Chemistry*, **286**, 8349-8360.

Zheng, M., Åslund, F. and Storz, G. (1998) Activation of the OxyR transcription factor by reversible disulfide bond formation. *Science*, **279**, 1718-1722.